PAUL SCHERRER INSTITUT

PSI

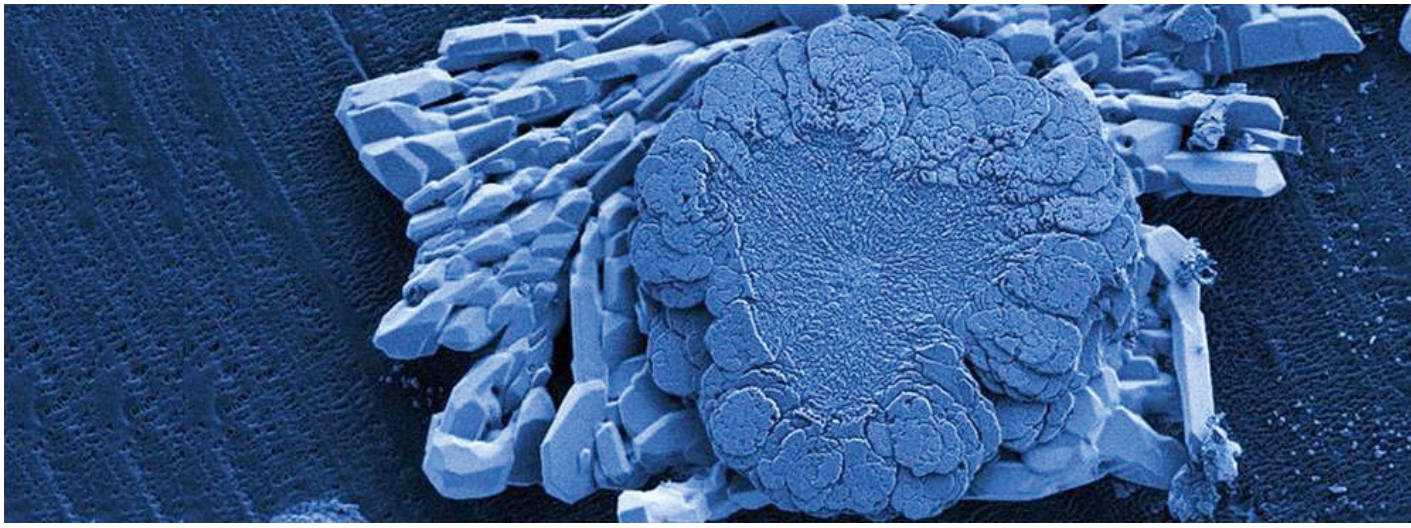

Annual Report 2014

Electrochemistry Laboratory

Cover
Flower-like electrolyte decomposition products on the surface of polypropylene Li-S battery separator.

DOI: 10.3929/ethz-a-007047464

PAUL SCHERRER INSTITUT

Annual Report 2014

Electrochemistry Laboratory

Paul Scherrer Institut
Electrochemistry Laboratory
5232 Villigen PSI
Switzerland

Secretary
Phone +41 56 310 29 19
Fax +41 56 310 44 15

Hardcopies of this report are available from

Cordelia Gloor
cordelia.gloor@psi.ch
Paul Scherrer Institut
5232 Villigen PSI
Switzerland

A full version of this report is also available on the web
http://www.psi.ch/lec

Publisher
Electrochemistry Laboratory
Paul Scherrer Institut
5232 Villigen PSI
Switzerland

Editorial Team
Cordelia Gloor / Peter Lutz
Lorenz Gubler
Thomas J. Schmidt

Printing
Paul Scherrer Institut

ISSN 1661-5379
DOI: 10.3929/ethz-a-007047464
PSI Electrochemistry Laboratory : : Annual Report 2014

CONTENTS

EDITORIAL

In an energy system where more and more renewable power from intermittent resources (e.g., wind and solar) is implemented, sooner or later the demand for proper and efficient energy storage systems will arise, simply due to the high probability of a temporal and local mismatch of power supply and demand. As a consequence of this mismatch, we already see an impact not only within the stability and/or reliability of the power grid, but also on the economics within the electricity market resulting in occasionally negative electricity prizes in countries with high renewable energy penetration, e.g., Germany or Denmark. Energy storage hence is also a key element in Switzerland's Energy Strategy due to the anticipated replacement of nuclear power with renewable sources over the next 20 to 30 years. Storing excess energy in times of low energy demand and making it available in times of high energy demand is not only advantageous from an energetic perspective; it also may create an economic value within the energy market.

The topics worked on in PSI's Electrochemistry Laboratory, viz., *electrochemical energy storage and conversion* play a crucial role in this context. On the one hand, direct electricity storage using *rechargeable batteries* in stationary and mobile applications is of utmost importance due to its high flexibility and storage efficiencies. On the other hand, storing electricity in the chemical bond of hydrogen molecules produced by *water electrolysis,* in principle, allows for large scale energy storage on the GWh-scale for possible use in short-term or seasonal energy storage systems. In addition, a significant value in producing renewable hydrogen through electrolysis lies in its flexible use, e.g., in chemical industries, as enabling feed gas in power-to-gas processes to produce synthetic natural gas, or as blending gas of methane for efficient combustion. In addition, renewable hydrogen can be efficiently reconverted into electricity using *polymer electrolyte fuel cells* (PEFC) in stationary H_2-O_2 PEFCs or in H_2-Air PEFCs in automotive applications, offering a carbon (and CO_2) free energy storage and conversion cycle.

Electrochemical energy storage and conversion, therefore, also plays a central role within the Swiss Competence Centers for Energy Research (SCCER) – Heat & Electricity Storage (hosted at PSI's General Energy Research Department and its Electrochemistry Laboratory) as well as in the SCCER – Mobility (hosted at ETH Zürich), both being operational since beginning of 2014.

As head of PSI's Electrochemistry Laboratory and Director of the Swiss Competence Center for Energy Research (SCCER) – Heat & Electricity Storage, it is my pleasure to coordinate our own work in electrochemical energy storage and conversion and the work of 20 other academic groups from different Swiss Institutions in order to successfully develop energy storage technologies helping to facilitate the transition of the Swiss Energy System to high penetration of renewables.

In this Annual Report 2014, you will not only find details on PSI's Electrochemistry Laboratory and the SCCER – Heat & Electricity Storage, but also some short insights into ongoing projects and activities, summarized in more than 40 short reports authored by our researchers demonstrating some of our contributions to the grand challenge of electrochemical energy storage and conversion. In addition, some key facts and figures from 2014 are given, including a full list of our more than 50 publications.

If the topic of electrochemical energy storage and conversion finds your interest, you are cordially invited to join the annual *SCCER Heat & Electricity Storage Spring Symposium* and the 2015 PSI *Electrochemistry Symposium* with the topic «Electrochemical Energy Storage – A key for Future Energy Systems» being held on May 5 and 6, 2015 at PSI. Both events will bring together international experts from the field sharing their perspectives on topics in line with our own activities.

Thomas J. Schmidt

THE ELECTROCHEMISTRY LABORATORY AT A GLANCE

Our Mission

Advancement of electrochemical energy storage and conversion by

- **developing novel electrochemical materials, cells and devices;**
- **providing insights into electrochemical materials, cells and device properties.**

PSI's Electrochemistry Laboratory is Switzerland's largest Center for Electrochemical Research with around 60 employees. Our mission is to advance the scientific and technological understanding of electrochemical energy storage and conversion specifically in the context of a sustainable energy system, in which renewable energy is required to be stored in secondary batteries or chemicals (as e.g., hydrogen) and (re-)converted into electricity. Our applied fundamental R&D, hence, is focused on devices like secondary batteries – specifically Li-based systems –, supercapacitors, polymer electrolyte fuel cells and electrolyzers, respectively.

As a research institute's laboratory we are bridging the gap between fundamental science and applied engineering by combining both academically as well as industrially relevant questions. For all outlined devices we not only develop fundamental understanding of materials on atomic and molecular level (electrochemical materials sciences and electrocatalysis), but also on the applied development of technical cells and devices, e.g., fuel cell systems.

On all technical complexity levels, we are developing and utilizing advanced *in situ* diagnostic tools to gain insights on properties and processes from the nanometer to the centimeter scale, respectively, often making use of PSI's unique large scale facilities.

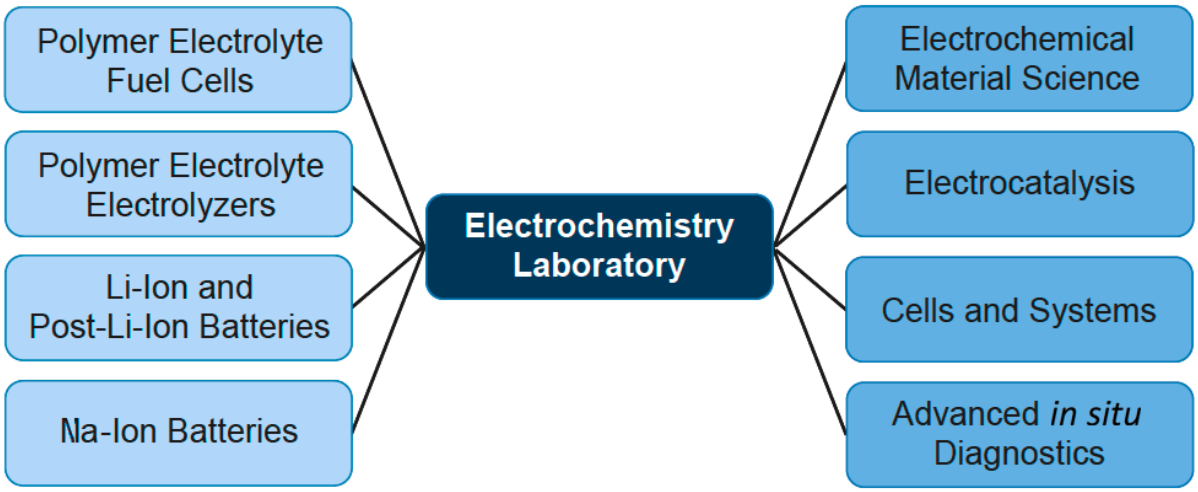

Electrochemical Energy Storage

The vision of the Electrochemical Energy Storage Section is the development of the best energy storage system.

We work on rechargeable batteries, mainly lithium based. The scientific goal is a profound understanding of electrochemical processes in complex nonaqueous systems. In particular, of utmost scientific interest are the numerous interactions of all components of electrochemical energy storage systems (batteries, supercapacitors, and hybrids) determining the safety and life time of such systems.

Multi-channel battery testing facilities.

The work equally considers the synthesis of novel materials for electrochemical energy storage, the modification of known materials (e.g., carbon) and material characterization, keeping in mind the entire span from basic science to industrial applications. To answer the scientific questions, we develop various sophisticated *in situ* methods for use in the field of nonaqueous solid-state electrochemistry and investigate the physical and electrochemical properties of insertion materials and electrochemical interfaces *in situ*. Also, we do electrochemical engineering work on threedimensional electrodes and characterize industrial batteries and battery systems.

Electrochemical Energy Conversion

The Electrochemical Energy Conversion Section is focused on the development and in-depth understanding of materials, processes and devices for the conversion of renewable energy into electricity or chemical energy carriers. Especially in the context of a sustainable energy system utilizing hydrogen as an energy carrier and its electrochemical energy conversion is of particular importance.

In this topical context our goal is the in-depth understanding of technologies like Polymer Electrolyte Fuel Cells (PEFC), Polymer Electrolyte Electrolyzer Cells (PEEC) for water electrolysis and processes like the co-electrolysis of CO_2 and water, respectively.

The R & D strategy involves activities on four pathways:

- system, stack and cell engineering;
- membrane development based on PSI's own radiation-grafting technology and the development of cell components;
- research in electrocatalysis and the reaction kinetics of the important reactions (e.g., the oxygen electrode reactions) for improved understanding of intrinsically limiting factors; and
- the development and application of advanced *in situ* diagnostic tools on stack, cell and component levels including analyses of the electrode-electrolyte interface.

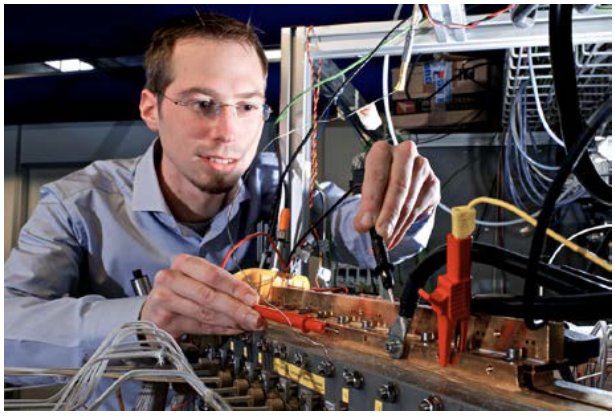

Characterization of a Polymer Electrolyte Fuel Cell with locally resolved analytical tools.

THE SWISS COMPETENCE CENTER FOR ENERGY RESEARCH – HEAT & ELECTRICITY STORAGE

The Swiss Competence Center for Energy Research (SCCER) «Heat & Electricity Storage» (HaE) is one of eight centers, which have been established in the research fields of mobility (SCCER Mobility), efficiency (SCCER FEEB+D, SCCER EIP), power supply (SCCER SoE), grids (SCCER FURIES), biomass (SCCER Biosweet), energy storage (SCCER HaE), as well as economy and environment (SCCER CREST) in light of the Swiss Government's Energy Strategy 2050. The declared aim of this energy strategy is the transition from nuclear power to a power supply system based on renewable sources to meet the CO_2 emission targets. An important factor is to expand and strengthen the knowledge in the energy field through the increase of personnel (e.g., scientists, engineers, technicians) alongside with technology development. The Centers are organized as virtual consortia of industrial and academic institutions (cantonal universities, universities of applied sciences and federal universities and research centers) distributed all across Switzerland with the intension to maximize the outcome by combining the strongest competencies in each area of expertise. To maintain a long-lasting effect on the Swiss power supply system, the competence centers will receive financial support until 2016 with a perspective of a second period until 2020. The SCCER Heat & Electricity Storage is located and managed at PSI with Prof. Thomas J. Schmidt being its Director.

Energy storage is a key element in Switzerland's Energy Strategy since energy, sourced from renewables like wind and solar energy, is only available on an intermittent, stochastic basis. Storing excess energy in times of low energy demand and releasing it in times of high energy demand is not only useful from an energetic perspective; it also may create an economic value within the energy market.

With an increasing contribution of the aforementioned renewable energy sources to the electricity mix, the significance of energy storage increases. This is clearly demonstrated by countries having installed a lot of wind and photovoltaic power, e.g., Germany and Denmark. Large intermittent discrepancies between electricity production and demand are being observed with the consequence of strongly fluctuating electricity prize – causing also challenges to the stability of the power supply system.

In order to stabilize the grid, an increase in short term electricity storage capacity (hrs) with high response time is needed within the next years. In the long run, seasonal storage becomes important to ensure constant electricity supply without conventional fossil based power generation.

Heat, besides of electricity is one of the most required types of energy today. About 50% of the primary energy carriers are transformed to heat by modern industrialized societies – required for space heating, hot water and process heat. Thus, it becomes obvious that a sensible use of energy must not neglect the questions related to heat.

The research and development within the SCCER Heat & Electricity Storage concentrates on five different fields.

In the Battery Section three research directions will be pursued: Lithium-ion-batteries, batteries on the bases of sodium as well as lithium-air-batteries. The second research field concerns itself with the thermal and mechanical storage. Especially, storage for building application and pumped hydroelectric storage as well as compressed-air storage without heat loss to the surrounding areas (adiabatic). The third research field is dedicated to the production and storage of hydrogen, whereas the fourth field is focused on the catalytic conversion of CO_2 into, e.g., synthetic hydrocarbons. The fifth research field will integrate these technologies into already established structures; this area of expertise is the one closest to industry.

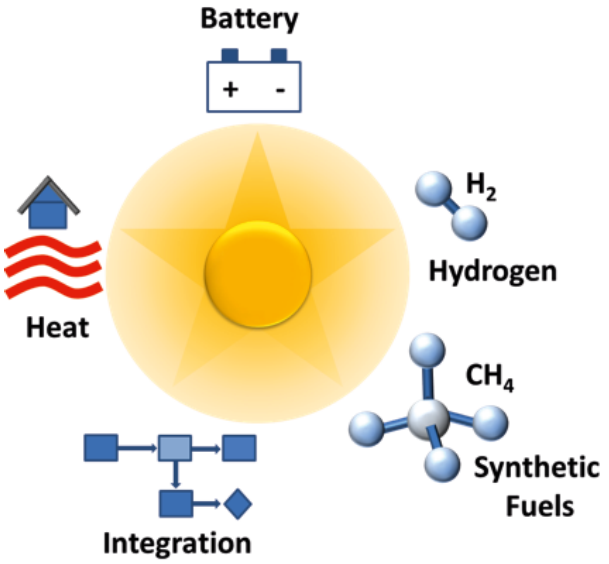

Researchers from PSI's Electrochemistry Laboratory are involved in the R&D of next generation sodium-ion batteries, the electrocatalytic reduction of CO_2 and the electrocatalysis of oxygen electrode reactions for electrolysis applications.

Storage
Swiss Competence Centers for Energy Research

www.sccer-hae.ch

SCIENTIFIC ACHIEVEMENTS 2014

Fuel Cells & Electrolysis –

Systems & Diagnostics

Pulsed gas supply for H_2/O_2 PEFC systems

F.N. Büchi, C. Peter, M. Amman, M. Hofer, T.J. Schmidt, U. Hannesen[1]
phone: +41 56 310 5763, e-mail: felix.buechi@psi.ch

Polymer electrolyte fuel cell systems fed with pure hydrogen and oxygen offer high efficiency and power density [1]. In this system concept, with both gases having a high purity, both gas loops are closed (see schematic in Figure 1) and gases are recycled in the system which offers the following advantages:

- gases are humidified by mixing of fresh gas with off-gas,
- high gas utilization can be achieved for both gases,
- both gas loops can be operated at pressures below ambient.

For gas recirculation often ejectors are used which provide gas recirculation in a passive manner. In the fuel cell application, recirculated gas flow rates equal to the fresh gas stream can be achieved (this corresponds to a stoichiometry of 2 in fuel cell operation). However, recirculation flows are strongly dependent on the fresh gas flow rate. This means that at low fuel cell power the ejector works ineffectively and an additional mechanical recirculation is required.

As components including moving parts such as pumps and compressors are critical for cost, reliability and durability of the system, solutions without provide a substantial benefit for the fuel cell system. Here we report on the development of an ejector only gas recirculation concept.

System set-up

A simplified schematic of a H_2/O_2 system is shown in Figure 1. Gas recirculation by the ejector is effective when the gas velocity in the orifice is near sonic speed. The ejector is designed that this is near full load. At low load no gas is recirculated by the ejector and the pump is required for recirculation.

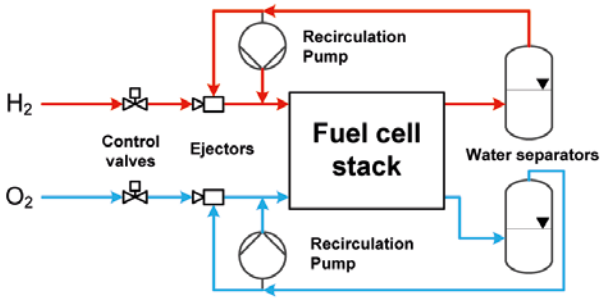

Figure 1: *Simplified schematic of H_2/O_2 fuel cell system showing gas recirculation loops.*

Concept

For eliminating the pumps, the ejectors have therefore to be operated always at maximum gas speed. Hence, the control valve is operated in pulsed mode. The pressure in the stack at different loads is regulated by adapting the opening frequency. Due to the pulses gas travels at full speed through the ejector and thus optimum recirculation is achieved during that period. Figure 2 shows the gas pressure at the stack-in and outlets for a 5 ms gas puls (i.e., opening time of the valve).

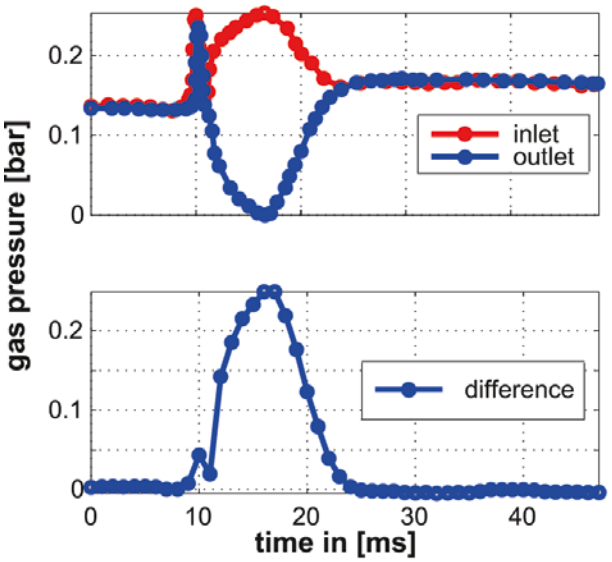

Figure 2: *Top: stack-inlet and stack-outlet pressure during 5 ms gas pulse; bottom: pressure difference between in- and outlet manifold during gas pulse; data for hydrogen at pressure level of 2.5 bar(abs).*

Results

The pulsing gas supply concept has been tested with a 38-cell stack (with 200 cm^2 active area per cell). Figure 3 shows the pressure differences between in- and outlet manifold for gas pulse durations between 5 and 30 ms. At the anode pressure differences of 250 to 300 mbar are reached while at the cathode the values are in between 150 and 200 mbar. These pressure differences are expected to be sufficient to remove product water from the cells.

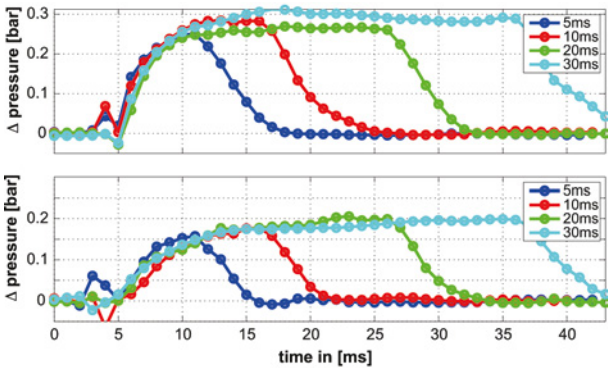

Figure 3: *Pressure difference for gas pulses with 38-cell stack for pulse lengths between 5 and 30 ms; top: anode and bottom: cathode.*

[1] Belenos Clean Power Holding, Biel/Bienne

The performance of a system with a 38-cell test stack (system shown in Figure 5) was investigated for power and durability. In Figure 4 the performance is shown as i/E and i/power curves for different gas pressures. Stable operation between idling and a current density of 2 A/cm² For all gas pressures a stack power of at least 10 kW (i.e > 265 W/cell) is obtained with a specific power density at maximum load of about 1.4 W/cm².

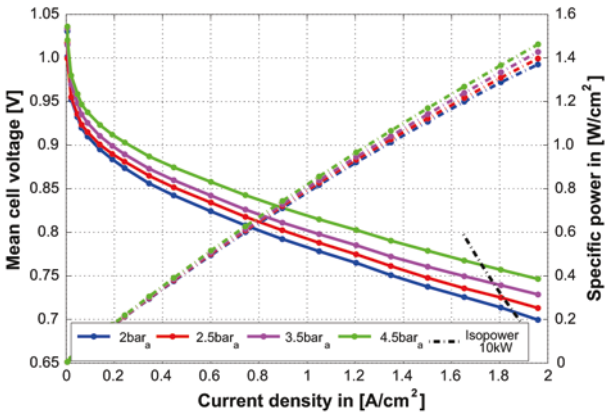

Figure 4: *I/E and i/power curves for 10 kW system (38-cell stack) at stack temperature of 74 °C for different gas pressures.*

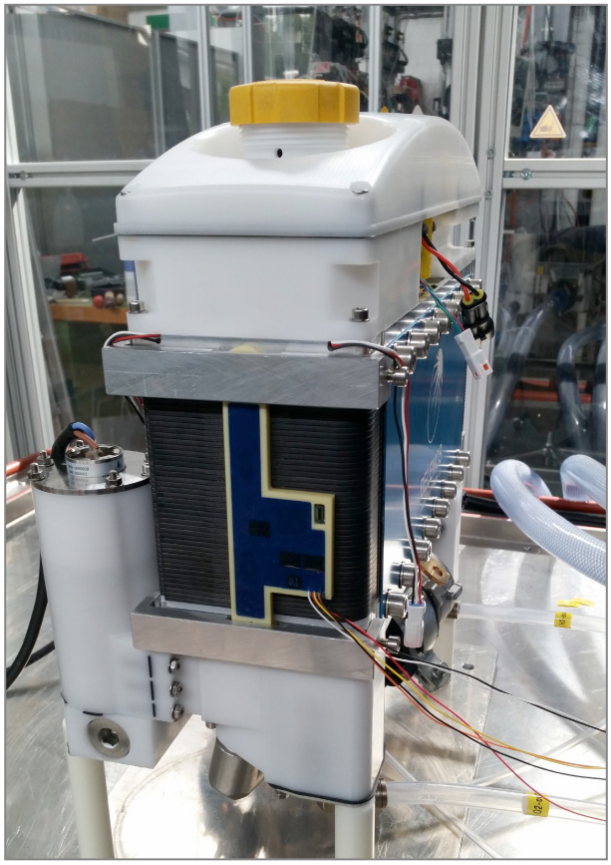

Figure 5: *Picture of H_2/O_2 polymer electrolyte fuel cell system with 38-cell stack; rated power 10 kW.*

The high number of gas pressure pulses, though only in the range 150–300 mbar may be considered as a degradation issue. Therefore the system with the 38-cell stack was operated for a 300 h durability test. The test was performed with a dynamic current profile with changes between the levels of 34, 67 and 168 A (0.17, 0.34 and 0.84 A/cm²). One cycle of the profile has a duration of about 70 s (details see [1]), so in one hour about 50 cycles are performed. Figure 6 shows the temporal development of the voltage at 168 A, the degradation rate and the fluorine concentration in the product water at anode and cathode side.

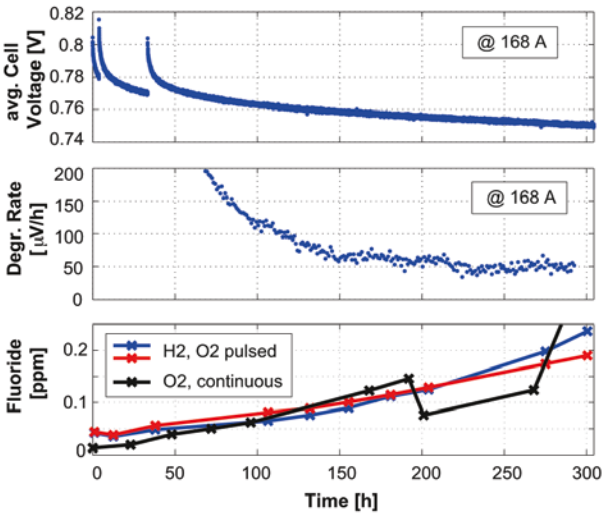

Figure 6: *Durability test with cyclic current protocol (see text) with 38-cell stack at stack temperature of 74 °C; top: average stack voltage; middle: average voltage degradation over 20 h; bottom: fluoride emission compared to short stack with continuous gas supply.*

The average cell voltage of the stack shows the typical behavior with an initial fast decay (which is reversible and possibly caused by sulfate adsorption on the catalyst) and then a constant voltage decrease at about 50 µV/h. The fluoride concentration in the product water (an indicator for membrane degradation) is at the same level as for operation with continuous gas supply. The test data indicates that the pulsed gas supply does not lead to increased degradation.

Conclusions & outlook

It is demonstrated that fuel cell systems can be operated with pulsed gas supply over a wide load range (between idling and 2 A/cm²) without the need of mechanical recirculation pumps in the system. The completely passive gas recirculation system potentially increases robustness and reliability of the system.

The gas supply concept will be tested with larger stack sizes of up to 60 kW.

Acknowledgement

Funding by Belenos Clean Power is gratefully acknowledged.

References

[1] F.N. Büchi, M. Hofer, C. Peter, U.D. Cabalzar, J. Bernard, U. Hannesen, T.J. Schmidt, A. Closset, P. Dietrich, *RSC Adv.* **4**, 56139–56146 (2014).

Determination of local saturation in GDLs during imbibition and drainage

A. Lamibrac, J. Roth, M. Toulec, F. Marone, F.N. Büchi
phone: +41 56 310 5768, e-mail: adrien.lamibrac@psi.ch

For automotive applications, low temperature proton exchange fuel cells (PEFC) have to perform over a wide range of operating conditions regarding temperature, humidity or current. At high current density, water produced at the cathode may condense in or close to the catalyst layer (CL) and obstruct the access for the gas to the reaction sites which results in significant performance loss. Understanding and improvement of the liquid water transport mechanisms from the catalyst layer to the flow field channels via the gas diffusion layer (GDL) are therefore essential to meet automotive applications requirements.

Even though *in situ* observations with X-ray tomographic microscopy (XTM) imaging provide important information about the liquid water location in a single cell [1, 2], no conclusion can be drawn regarding the efficiency of the water removal through the GDL. The reason behind is that the driving forces responsible for the water movement are not controlled: the water production is not homogeneously distributed on the active area, condensation may appear in different locations and the water pressure cannot be monitored during the invasion of the GDL.

A thorough characterization can be achieved using an *ex situ* imbibition/drainage experiment which has the advantage of well defined boundary conditions [3, 4]. Quantitative results obtained for different materials are presented here.

Experimental

For the imbibition and drainage experiments the GDL sample is mounted in a sample holder and sandwiched between a hydrophilic (bottom) and a hydrophobic (top) membrane. The hydrophilic membrane ensures a homogenous invasion of water at the bottom of the GDL. The hydrophobic membrane avoids water to leave the GDL so that imbibition can be pursued even after breakthrough has been achieved. Water is forced in the GDL using a syringe pump and the differential pressure between water and ambient air or capillary pressure is directly measured by a pressure sensor (accuracy ± 1 mbar) connected to a parallel water column (see Figure 1).

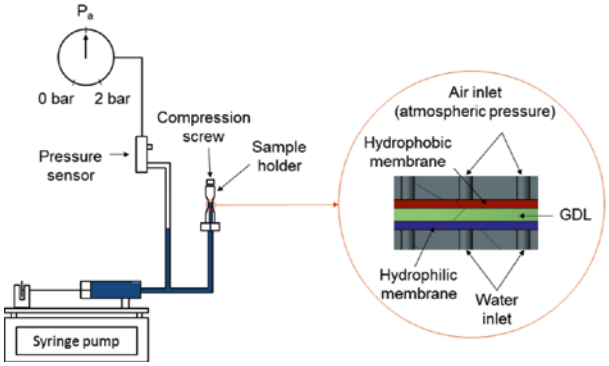

Figure 1: *Experimental setup used for the GDL imbibition/drainage imaging.*

To access global as well as local saturation, XTM imaging has been carried out at the TOMCAT beamline of the Swiss Light Source. The beam energy was set to 13.5 keV, exposure time to 15 ms (2001 projections) and the 2–4 x microscope was used (pixel size of 2.2 µm). The samples were compressed by about 20 % and experiments were carried out at ambient temperature.

Results

In Figure 2, the stepwise increase of the capillary pressure induces an increase of the saturation for all GDLs. However the saturations achieved at a given capillary pressure are different due to the void structures of these GDLs which present different characteristic dimensions. The SGL 24BA and Toray TGP-H060 have a rather homogeneous pore size distribution across their thicknesses while the SGL 24BC can be divided in three layers: the micro-porous layer (MPL) made of very small pores (submicrometre size) and cracks, the interfacial region between MPL and GDL and the GDL. Water can only penetrate the MPL through the cracks which are relatively easy to imbibe since they are several tenths of micrometres large and hundreds of micrometres long. The interfacial region has very small pores that require high capillary pressure to be filled. Once the necessary capillary pressure is achieved the further flooding of the GDL is instantaneous in the through plane direction. In in-plane direction flooding appears to be very limited possibly due to locally deeper penetration of the MPL in the GDL.

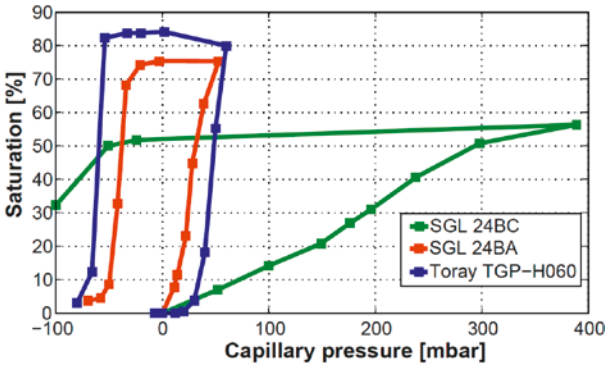

Figure 2: *Global saturation as a function of the capillary pressure applied for SGL 24BA, Toray TGP-H060, and SGL 24BC.*

The larger and more homogeneous void structures of the SGL 24BA and Toray TGP-H060 compared to the 24BC enable an easier imbibition (Figure 2). Still, these two GDLs have heterogeneous water transport between in- and through plane directions. Water columns with an always smaller cross-section from the bottom to the top of the GDL are observed and result in water profiles across the GDL thickness such as those shown in Figure 3. The pore structure was analysed by local thickness defined for each point of the void as the diameter of the largest disc including the point and fitting inside the void structure. This has been calculated for both in- and

through-plane 2D-slices. The distribution of local thickness for the through-plane slices appears to be much smaller than for the in-plane ones (Figure 4) which is in good agreement with a preferred through-plane and capillary controlled transport of liquid water.

Compared to the SGL 24BA, a higher capillary pressure is required to fill the Toray TGP-H060 in Figure 2. The breakthrough corresponding to the time when water reached the opposite side of the GDL is already achieved at 22 mbar in the case of the SGL 24BA while more than 30 mbar are necessary for the Toray TGP-H060. The comparison between the local thickness distributions of the in-plane slices for these two GDLs shows that in average the void structure is larger for the SGL than for the Toray. This observation is consistent with an easier and capillary dominated imbibition of the SGL material.

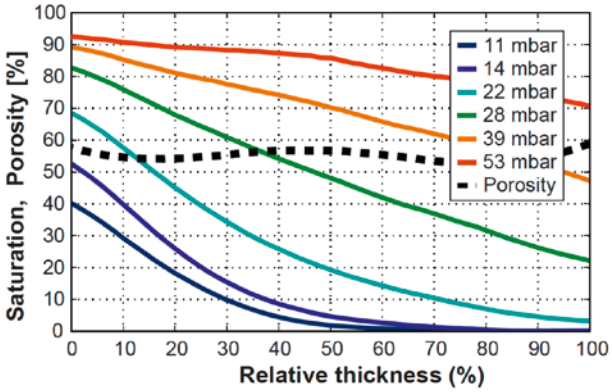

Figure 3: *Local saturation as a function of the position across the GDL thickness during imbibition for SGL 24BA.*

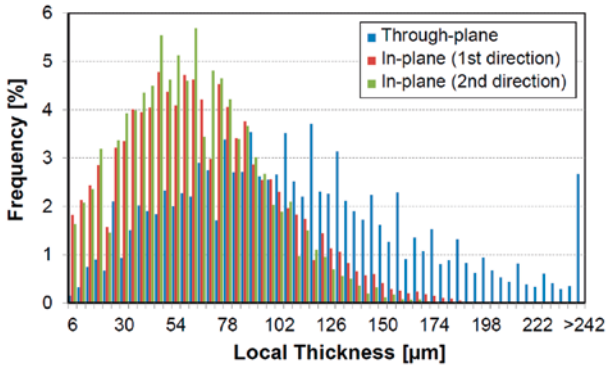

Figure 4: *In- and through plane distributions of the local thickness for SGL 24BA.*

The repeatability of the imbibition process has also been assessed. To do so, water imbibition and withdrawal was performed in a single SGL 24BA and imaging was done for every imbibition at 19 mbar. Very similar water saturation profiles were obtained across the GDL thickness (Figure 5). However, the path taken by water is not completely identical from one imbibition to the next. This may be explained by the residual water at the end of each withdrawal, which can provide new water paths for the following imbibition.

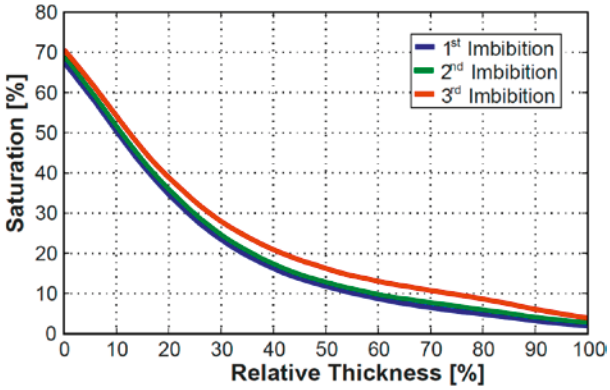

Figure 5: *Local saturation as a function of the position across the GDL thickness during three successive imbibition of an SGL 24BA sample.*

Conclusions

The quantitative characterisation of water imbibition in different GDLs reveals that the void structure of the material plays a significant role for the water transport. A larger pore dimension in through-plane direction favours a water displacement across the GDL thickness. In case a MPL is attached to the GDL, cracks represent the only way for the water to reach the macroporous part of the GDL and the pores at the MPL/GDL interface control the further imbibition into the GDL.

Paths taken by water during successive imbibitions are similar and the differences observed may be the result of the residual water after each withdrawal.

To mimic fuel cell conditions more accurately, further work will focus on the imbibition below a flow field with channels and ribs to take into account the heterogeneous compression of the GDL. In addition, the capillary pressure steps will be reduced to better visualize the path taken by water up to breakthrough.

Acknowledgement

Funding from the European JU-FCH project IMPALA and materials obtained from SGL are gratefully acknowledged.

References

[1] J. Eller, T. Rosén, F. Marone, M. Stampanoni, A. Wokaun, F.N. Büchi, *J. Electrochem. Soc.* **158**, B963 (2011).
[2] J. Roth, J. Eller, F. Marone, F.N. Büchi, *J. Phys. Chem. C* **117**, 25991–25999 (2013).
[3] J.T. Gostick, H.P. Gunterman, B.W. Kienitz, J.S. Newman, A.A. MacDowell, A.Z. Weber, *ECS Trans.* **33** (1), 1407–1412 (2010).
[4] R. Flückiger, F. Marone, M. Stampanoni, A. Wokaun, F.N. Büchi, *Electrochimica Acta* **56**, 2254–2262 (2011).

High pressure polymer electrolyte electrolysis cell test bench

M. Suermann, T.J. Schmidt, F.N. Büchi
phone: +41 56 310 5763, e-mail: michel.suermann@psi.ch

Dynamically operable polymer electrolyte electrolysis cells (PEEC) are used to store fluctuating electric energy from renewable sources in form of chemical energy, i.e., hydrogen and oxygen [1]. The produced hydrogen can be stored and transported in (existing) pipelines and pressurized gas tanks. Therefore pressurization of the gases hydrogen and optionally oxygen is required. Conventionally this is done by mechanical compression which is inefficient, noisy and which may need a number of stages to reach high pressures of 400 or 800 bar required for fuelling vehicles. In contrast, electrochemical compression directly in PEEC or with an electrochemical hydrogen pump after electrolysis offers a possibly more efficient way.

However, research is needed for the understanding of high pressure PEEC operation and for reducing the overall costs to be competitive with existing technologies. Thus a new test bench for PEEC is built up for operation up to 300 bar.

Safety

The safety at 300 bar – no matter what fluids are used – isn't trivial [2]. Therefore, as a first step, the test bench was analysed by a hazard and operability study (HAZOP) on the basis of a piping and instrumentation diagram (PID). Even if such a study isn't a guarantee for a safe operability, it helps to assess the risks (possibility and damage) of possible failures.

The HAZOP was done by a group of persons of PSI with different expertise and a professional moderator from Swissi AG (8304 Wallisellen). Within the systematic study every possible scenario was being analysed. Thus possible hazards were indicated and corresponding risks were estimated and classified in a risk matrix (Figure 1). In case the risk was inacceptable, technical or operational measures were added to reduce the possibility and/or damage. Step by step the test bench was checked and the result of the HAZOP is a revised PID and an instruction manual.

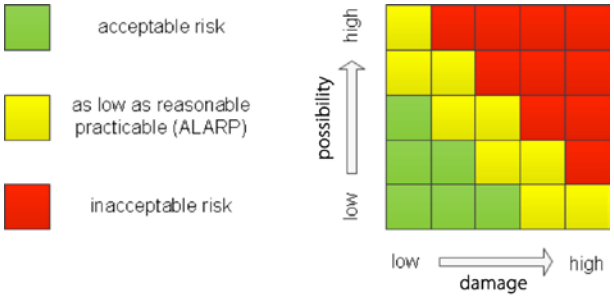

Figure 1: *Example of a risk matrix.*

Test bench

The major task of the test bench is to supply the PEEC with water and to remove the produced gases from the cell to gas/liquid (G/L) separators as well as to pressurize the gases up to 300 bar. The piping and instrumentation diagram is shown in Figure 2 without any safety elements.

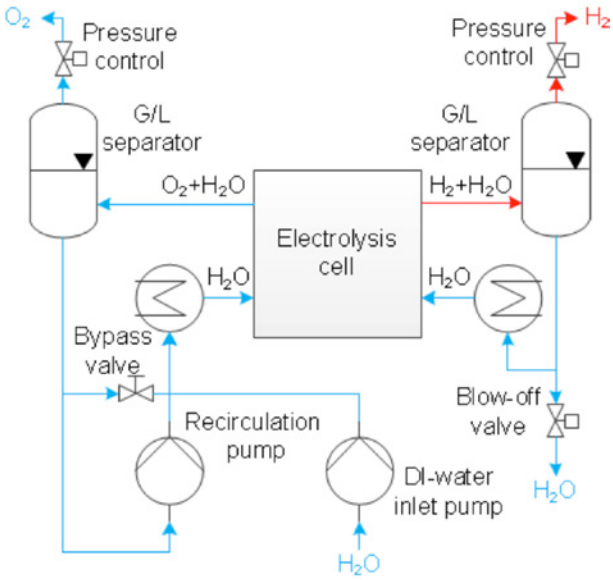

Figure 2: *Schematic set-up of the test bench without safety elements.*

For the sake of safety a number of excess pressure valves and burst disks are implemented. In addition to the pressure, the temperature, the gas concentration due to gas crossover, the water level in the G/L separators and the power control are also monitored and controlled.

Conclusions & outlook

To date, the test bench is tested at low pressure up to 20 bar. When all tests are successful, high pressure operation will gradually be started.

Acknowledgement

Funding by Swiss Federal Office of Energy (SFOE) and Belenos Clean Power is greatly acknowledged.

References

[1] F. Barbir, *Sol. Energy* **78** (5), 661–669 (2005).
[2] S.A. Grigoriev, P. Millet, S.V. Korobtsev, V.I. Porembskiy, M. Pepic, C. Etievant, C. Puyenchet, V.N. Fateev, *Int. J. Hydrogen Energy* **34** (14), 5986–5991 (2009).

Discrimination between ice and water in gas diffusion layers of PEFC

I. Mayrhuber, T.J. Schmidt, F.N. Büchi
phone: +41 56 310 5763, e-mail: felix.buechi@psi.ch

Polymer electrolyte fuel cell (PEFC) start-up at sub-zero temperatures is a challenge, especially for systems used in automotive applications. During start-up at freezing conditions, the product water formed at the cathode is in super-cooled state. Once the super-cooled water undergoes a phase change to ice, the transport of reactant gas in the gas diffusion layer, catalyst layer and gas flow channels is hindered and the system performance drops.

For detailed understanding of the water freezing phenomena, X-ray tomographic microscopy (XTM) is used. This technique allows the observation of the condensed water phase in the opaque porous structure of the fuel cell during freeze starts [1]. To determine the prevailing aggregate state and to understand the influence of freezing kinetics, discrimination between water and ice is necessary [2].

A change in X-ray absorbance comes along with the density difference of water and ice phase and should in principle allow for discrimination between the two aggregate states. XTM images with both water and ice phase in a generic capillary experiment and fuel cell set-up are analyzed and the difference in contrast between the two phases evaluated.

Beamline set-up

Experiments were performed at the TOMCAT beamline of the Swiss Light Source (Paul Scherrer Institute) using:

- Absorption contrast mode with 13.5 keV beam energy,
- 1001 to 2001 projections over 180° of sample rotation,
- 15 ms exposure time.

A cold nitrogen stream, produced with a new Pelltier-element based set-up was utilized for freezing the objects at the beamline.

Results

To show the principal effect of the X-ray absorption difference between ice and water both phases were imaged in a vespel capillary with 0.8 mm bore diameter. The respective images and the grey scale histogram of the water phases are shown in Figure 1.

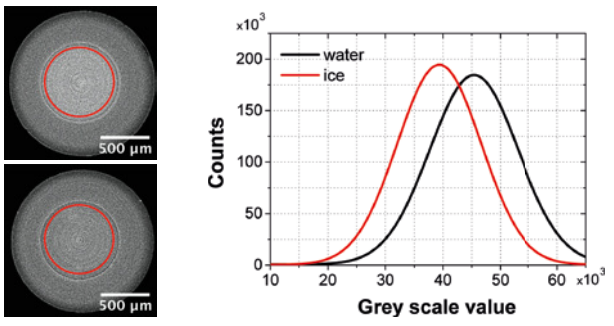

Figure 1: *Grey scale images of water in a vespel capillary of 0.8 mm diameter; top: water at room temperature; bottom: ice at -10°C; right: absorption contrast histogram of water and ice.*

In Figure 2 water in liquid and frozen state in the gas diffusion layer (GDL) of a not-operated PEFC is shown and the area of the red square is analyzed.

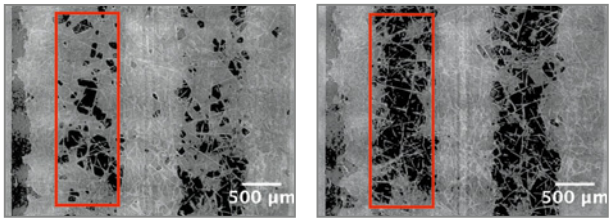

Figure 2: *Grey scale images of an imbibed GDL inside a PEFC. Left: room temperature (dark: void/empty pores; dark grey: water; light grey: carbon fibers). Right: cell at -20°C.*

The grey scale analysis is presented in Table 1. For the capillary experiment, a grey scale value difference of 9.1 % between water and ice is observed, close to the theoretical value of 8.1 %. However in the fuel cell setup only a 2.1 % difference is obtained. The reasons are:

- a highly absorbing platinum catalyst layer in the MEA of the PEFC, which imposes to choose wider scale limits for image reconstruction.
- water/ice volume fraction in the PEFC (incl. carbon flow field body and vespel hull) is only ~5 %, compared to ~50 % in the capillary.

As a result, the signal noise ratio for water and ice inside the PEFC is worse and the image looses contrast, so discrimination between ice and liquid water becomes more challenging.

	Water (+25°C) 8 bit grey scale	*Ice (-20°C) 8 bit grey scale*	*Difference [%]*
Density [g/cm^3]	0.9998	0.9189	8.1
Vespel Capillary	177.4	153.7	9.1
Fuel Cell	104.1	98.8	2.1

Table 1: *Density and grey scale values for water and ice for both capillary and PEFC.*

Conclusions & outlook

Results show that, though difficult, it is possible to discriminate water and ice in the PEFC set-up. Work to identify the moment of phase change will be continued in in-operando cells.

Acknowledgement

Funding by Swiss Federal Office of Energy (SFOE) and Belenos Clean Power is greatly acknowledged.

References

[1] J. Roth, M.R. Zurbrügg, S. Irvine, F. Marone, M. Stampanoni, F.N. Büchi, *ECS Trans.* **58**, 453–462 (2013).
[2] Y. Ishikawa, H. Hamada, M. Uehara, M. Shiozawa, *J. of Power Sources* **179**, 547–552 (2008).

Neutron imaging of polymer electrolyte electrolyzers

J. Seweryn, J. Biesdorf, T.J. Schmidt, P. Boillat
phone: +41 56 310 5034, e-mail: jakub.seweryn@psi.ch

In the past neutron imaging has been successfully implemented to examine the water transport inside operating PEM fuel cells [1] and its impact on cell performance [2]. Now the attempt is made to apply the same technique to the PEM electrolyzers.

Although, in principle, the design of these two device classes is the same, there are still some differences in chosen materials as well as dimensions (Ti as a porous layer, sturdy construction suited for higher pressure and higher amount of water present in flow channels) which can hamper the usage of radiography techniques developed for the fuel cell.

It is worth mentioning, that some work on neutron imaging on PEM electrolyzers had been done already [3]. However, the scope of this work was limited, e.g., it did not investigate the water distribution in the direction across the membrane.

Experimental

Until now one imaging session has been performed at the NEUTRA beamline of the PSI. For this purpose, both a new cell and the new operating conditions control module had been designed and built.

The cell is intended for differential operation [1] allowing both through plane and in plane imaging with 1 cm^2 active area. The control module is able to provide varied conditions in terms of temperature (ambient to 100 °C), pressure (ambient to 5 bar, also differential; with possibility to extend it to 25 bar), anodic water flow (up to 350 mL min^{-1}) and flow of N_2, H_2 and O_2. Voltage and current are limited by the performance of used MEA and porous layer. Resistance measurement is available with constant current operation.

During the session in plane and through plane setups have been investigated. In selected positions the images at varied conditions have been recorded.

Results

The very first results of the performed imaging campaign are presented here, focusing on in plane imaging. Figure 1 shows the image obtained for a cell after drying with N_2 flow on both sides (A) and with flooded anode (B). The latter serves as a reference for the radiograms of cell operation. As can be seen, the Ti porous layer has a very good transparency for neutrons, and even the fully flooded layer remains transparent enough for imaging.

Figure 2 shows the images of the same cell at various currents. These radiograms are referenced to the state with a fully flooded anode and a dry cathode (Figure 2), making visible the gas accumulation in the anode and the water accumulation in the cathode. The visible gradient of the water thickness on the anode side is very little dependent on the current density. Another surprising observation is the absence of rib/channel differences in gas/water accumulation in the GDL (compared to the case of fuel cell, e.g., in reference [2]).

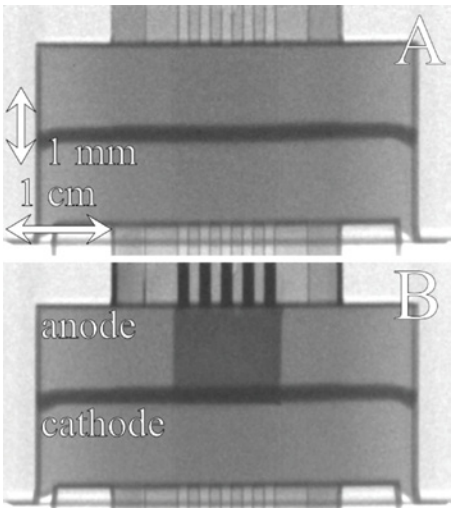

Figure 1: *Image recorded for the dry cell (A) and the cell with flooded anode (B). The difference in horizontal and vertical scales results from the use of a tilted detector setup [1].*

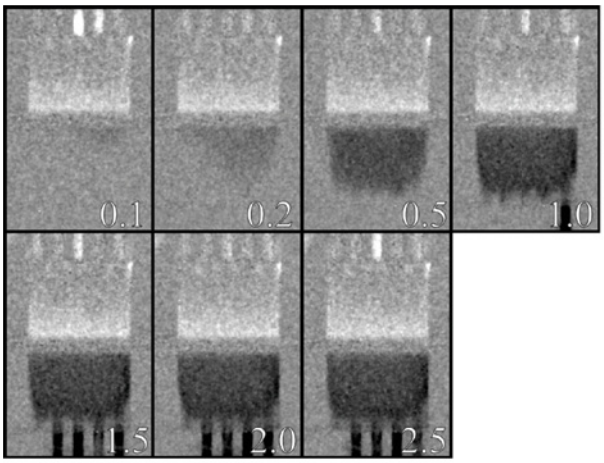

Figure 2: *Images of cell taken at increasing current density (denoted by number in bottom right corner [A cm^{-2}]). The pixel values have been divided by reference values of the cell with flooded anode – white pixels on anode side correspond to gas, while black on the cathode side to water.*

Acknowledgement

The authors are grateful for the financial support received from the Swiss Federal Office of Energy (SFOE).

References

[1] P. Boillat, G. Frei, E.H. Lehmann, G.G. Scherer, A. Wokaun, *Electrochem. Solid-State Lett.* **13** (3), B25–B27 (2010).
[2] P. Boillat, P. Oberholzer, A. Kaestner, R. Siegrist, E.H. Lehmann, G.G. Scherer, A. Wokaun, *J. Electrochem. Soc.* **159**, F210–F218 (2012).
[3] O.F. Selamet, U. Pasaogullari, D. Spernjak, D.S. Hussey, D.L. Jacobson, M.D. Mat, *ECS Trans.* **41** (1), 349–362 (2011).

Influence of operating temperature and pressure on the water management inside gas diffusion layers

J. Biesdorf, A. Forner-Cuenca, T.J. Schmidt, P. Boillat
phone: +41 56 310 5727, e-mail: johannes.biesdorf@psi.ch

In order to maximize the power density of polymer electrolyte fuel cells (PEFC), operation at high current densities (≥ 1 Acm^{-2}) is highly desired. At these operating conditions, the evacuation of product water limits the supply of the reactant gases especially on the cathode, which results in mass transport losses (MTL).

Current PEFC are assembled with a porous layer of carbon fibres (GDL) to optimize the concurrent flow of reactant gases and liquid water. This dynamic equilibrium can be either adjusted by modification of the GDL or by adjustment of the operation conditions. The latter will be discussed in this report.

Experimental

Cell design

The experiments were performed with a cell setup which allows the simultaneous operation of six differential fuel cells [1]. The fuel cells had an active area of 1 cm^2 with a flow field design consisting of 5 parallel channels with a cross section of 0.55 x 1 mm^2. In order to achieve high transparencies for neutron radiography, gold coated aluminum has been used as base material. The experiments have been performed with a commercial catalyst coated membrane (CCM) of type Primea 5710 (Gore Ltd., USA) with Pt-loadings of 0.1 mgPt/cm^2 on the anode side and 0.4 mgPt/cm^2 on the cathode side. Sigracet 24BC (SGL Carbon Group, Germany) have been used as gas diffusion layers (GDL) having 5 wt% of PTFE on both anode and cathode sides. The compression rate was fixed to 25 %.

Pulsed gas analysis

Within these experiments, the pulsed gas analysis published in ref [2] was applied. The method consists in replacing the cathode gas with helox (21 % Helium, 79 % N_2) or pure oxygen. As helium has a higher diffusivity in N_2 (approx. factor 2–3) bulk mass transport losses can be highly reduced. Therefore, the differential voltage between operation under air and helox is an indicator of bulk mass transport losses. However, under operation with pure oxygen, the increased partial pressure of oxygen leads to an elimination of the non-bulk diffusion (Knudsen and thin film diffusion) losses. After correction of the increased Nernst voltage and kinetics under pure oxygen, the difference between the voltage with oxygen and helox gives an estimation about non-bulk diffusion losses. As the membrane tends to dry out and the catalyst coverage of the oxygenated species changes with higher potentials, the gases are supplied as short pulses of 1 s during the continuous operation under air. Further details about the methodology can be found elsewhere [2]. Ohmic losses were analyzed with a high frequency resistance measurement at 5 kHz.

Imaging setup

All experiments presented hereafter were performed at the ICON beamline of the SINQ at the Paul Scherrer Institute. More details about the imaging setup are published in ref [3].

Experimental protocol

The results hereafter are based on nine operation points at a current density of 1 A/cm^2 and a relative humidity of 80 %RH of the inlet gas stream of the anode and cathode. A matrix of three temperatures (30, 50, 70 °C) and three pressures (1.3, 1.6, 2.0 bar$_{abs}$) will be presented. As the dynamic equilibrium of liquid water inside the cells was mostly obtained after 3 minutes, every operation point was held during 15 minutes. The cell voltages and neutron radiographs are averaged over the last 10 minutes of the operation period. As three identical cells have been operated during the experiment, the indicators of performance have been averaged. The cells were operated in a differential mode with stoichiometries of approximately 60 on both sides at constant volume flows during all operation conditions.

Results

Performance

Figure 1 depicts the raw voltage, ohmic, bulk and non-bulk losses as a function of pressure and temperature. The raw voltage (see Figure 1 (a)) shows variations in the order of 100 mV between the different operation points. It can be clearly seen, that an increase in pressure and temperature leads to significant improvements of the cell performance even after correction of the different Nernst potentials.

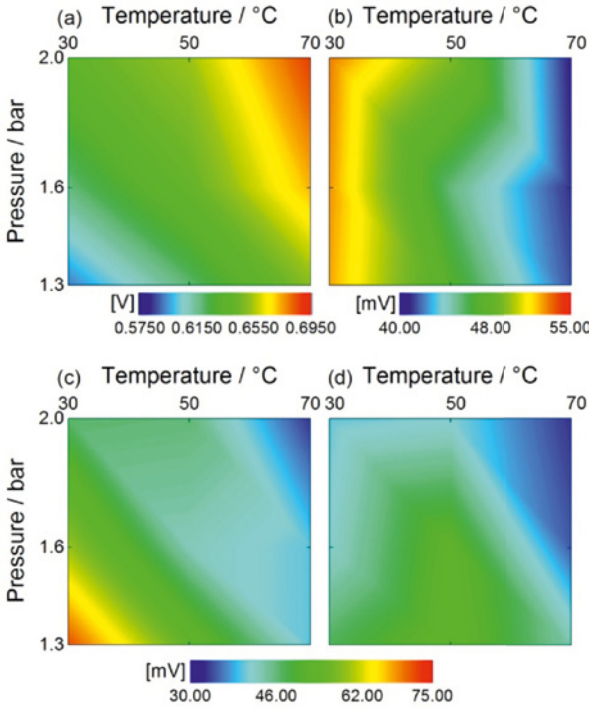

Figure 1: *(a) Raw voltage, (b) ohmic losses, (c) bulk losses and (d) non-bulk losses under operation at 1 A/cm^2 and 80 %RH on anode and cathode side.*

The ohmic losses (see Figure 1 (b)) seem to be independent on the operating pressure, whereas a significant increase can be identified with increasing temperatures.

The indicator of bulk diffusion losses (see Figure 1 (c)) is strongly dependent on its operating temperature. However, only little dependence can be found on its operating pressure.

Non-bulk diffusion losses (see Figure 1 (d)) show a very homogeneous distribution with slightly reduced values at high operation temperatures and pressures.

Neutron radiographs

Figure 2 shows its corresponding in-plane radiographs of the fuel cells at the same operation points. In general, the amount of liquid water in the anode GDL and flow channel is relatively low and is not heavily influenced by the different operation points.

On the cathode side, the amount and distribution of water inside the GDL clearly depends on the operational condition. With increasing temperatures, the integral amount of water in the GDL is decreased, especially under the flow channels. Besides that, with decreasing pressures the patterned water accumulation under the rib compared to the channel is more pronounced and less water can be found under the channel.

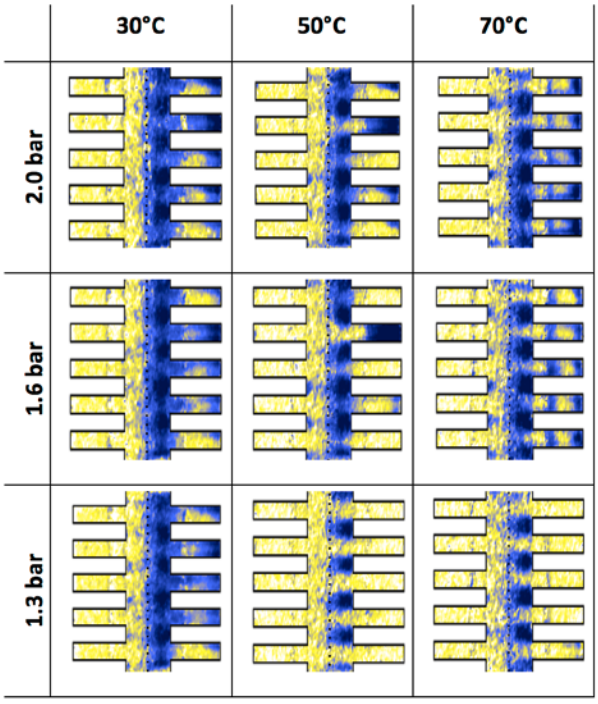

Figure 2: *In-plane radiographs of the fuel cells at the same operation points.*

Discussion

The reduction of the ohmic losses with increasing temperature can be explained with an increased conductivity of the membrane [4]. Regarding the operational pressure, a change in the hydration state could have been expected due to the higher water uptake at lower gas pressures. However, no significant changes could have been identified under different operational pressures which lead to the conclusion that the inlet gas stream is getting saturated while passing through the cell.

The decreased bulk diffusion losses with increasing temperature in Figure 1 (c) can be explained with a lower amount of water inside the GDL (see Figure 2). As has already been reported in ref [5], unfavourable water accumulation under the channels can highly influence the performance of the cell.

As can be clearly seen in Figure 2, water accumulates in particular under the ribs of the flow field, which can be referred to the flow pattern of the reactant gases. However, this pattern between channel-rib is much more patterned with lower operation pressures. This can be explained with the higher water uptake of a gas with lower gas pressure. As expected, these differences in the water distribution are much more pronounced at high temperatures, as the variations in water uptake are much higher.

Non-bulk losses show higher losses at lower pressures, which can be explained with a lower partial pressure of oxygen. A lower partial pressure of oxygen leads to reduced Knudsen and thin-film diffusion.

Conclusions

Based on the combination of neutron radiography with the pulsed gas analysis, performance and water distribution can be correlated. The temperature strongly affects the evaporation rate of water which leads to lower saturation levels and bulk losses in the GDL. Lower operational pressures result in a highly patterned water distribution.

References

[1] P. Oberholzer, P. Boillat, R. Siegrist, A. Kastner, E.H. Lehmann, G.G. Scherer, A. Wokaun, *Electrochem. Commun.* **20**, 67 (2012).
[2] P. Boillat, P. Oberholzer, A. Kaestner, R. Siegrist, E. H. Lehmann, G.G. Scherer, A. Wokaun, *J. Electrochem. Soc.* **159**, F210 (2012).
[3] P. Oberholzer, P. Boillat, A. Kaestner, E.H. Lehmann, G.G. Scherer, T.J. Schmidt, A. Wokaun, *J. Electrochem. Soc.* **160**, F659 (2013).
[4] T.E. Springer, T.A. Zawodzinski, S. Gottesfeld, *J. Electrochem. Soc.* **138**, 2334 (1991).
[5] J. Biesdorf, P. Oberholzer, T.J. Schmidt, P. Boillat, *ECS Trans.* **64**, 467 (2014).

Phosphoric acid redistribution in HT-PEFC under dynamic operation

S.H. Eberhardt, F.N. Büchi, T.J. Schmidt
phone: +41 56 310 2411, e-mail: felix.buechi@psi.ch

Introduction

High temperature polymer electrolyte fuel cells (HT-PEFC) are operating at temperatures up to 200 °C using phosphoric acid (PA) doped polybenzimidazole (PBI) based membranes. PA has a low vapor pressure at these operating temperatures which in principal allows for long term operation without major electrolyte loss. However, only approximately 2 PA molecules per PBI repeating unit (PA/PBI) are directly interacting with the basic pyridinic nitrogen of PBI [1]. It can, therefore, be expected that the bulk of this phosphoric acid is more or less mobile within the molecular pores of the membrane. Hence, movement and redistribution of PA within the porous components (membrane, catalyst layer, microporous and gas diffusion layers) of the cell are expected to play a significant role for fuel cell performance and durability. In this work, synchrotron based X-ray tomographic microscopy will be applied, for the first time, to image in-operando HT-PEFC [2]. The experiments are specifically targeted at imaging the transient phosphoric acid electrolyte redistribution under dynamic load conditions to identify possible fuel cell degradation with respect to electrolyte loss from the electrochemical active area.

Experimental

All experiments were carried out with BASF Celtec® membrane electrode assemblies (MEA). The membrane consists of a polybenzimidazole polymer backbone doped with phosphoric acid of approximately 34–36 $mg_{PA}cm^{-2}$. The symmetric electrodes consist of Pt/Vulcan XC-72 supported platinum catalyst with a loading of 1 $mg_{Pt}cm^{-2}$, coated onto SGL 38 carbon paper gas diffusion layers (GDL) including a microporous layer (MPL).

X-ray tomographic microscopy (XTM) was performed at the TOMCAT beamline of the Swiss Light Source in absorption contrast mode. At a beam energy of 20 keV a total of 2001 projections were acquired during 180° sample rotation with an exposure time of 11 ms per projection. The voxel size in the tomographic images is 2.34 µm.

For electrochemical testing a differential fuel cell design with 0.2 cm^2 active area was used [3]. The experimental protocol consists of a current cycling between 0.2 Acm^{-2} and 0.8 Acm^{-2} approximaetly every 4 hours. The temperature was fixed to 160 °C and the cell was operated with H_2/O_2 ($\lambda > 100$).

Results

Phosphoric acid redistribution is expected to be influenced by a range of parameters, such as temperature, gas dew points and current density. Especially current density is predicted to play a significant role considering the experience gained with phosphoric acid fuel cells (PAFC). In these kind of fuel cells, the migration of phosphoric acid from the cathode to the anode under non-equilibrium conditions can be observed [4-6]. In PBI based HT-PEFC this effect might also be of importance as long as a sufficient amount of PA is able to move freely within the PBI polymer matrix.

In Figure 1 a comparison of the horizontal grayscale slices of the anode gas diffusion layer (GDL) at different time steps is shown while a detailed volumetric quantification of PA is depicted in Figure 2. At start of break-in of a new MEA, initial PA content in the GDLs originates from the membrane. It was transferred there during MEA preparation, which includes mechanical compression for application of the GDL based electrodes. During break-in at 0.2 Acm^{-2} these PA phases are reduced and at the anode only few PA filled pores remain in the GDL while at the cathode no segmented PA phase can be observed anymore. However, an increased grayscale value of the cathode GDL (as compared to pure carbon) indicates that small amounts of PA are still present, possibly accumulating within the micropores of the carbonaceous binder and as thin film wetting the fibers.

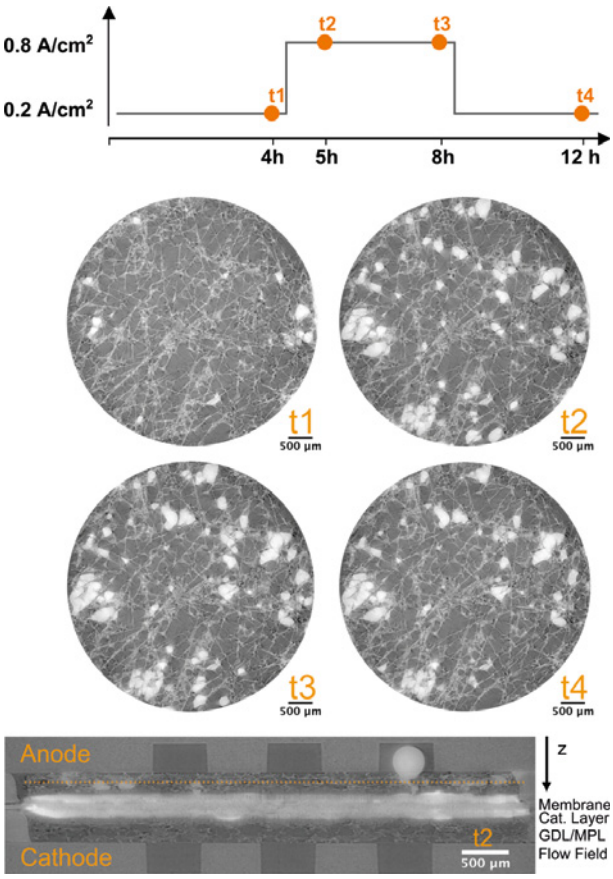

Figure 1: *Horizontal slices of the anode GDL as a function of time (bright gray: PA; light gray: carbon fibers; dark gray: empty pores). Location of the slices is indicated in the vertical cross section of the MEA.*

When the current is increased from 0.2 to 0.8 Acm^{-2}, an almost immediate flow of PA into the anode GDL can be observed as illustrated in Figure 1 and the inset in Figure 2. Within 15 min, a continuous path of PA has formed from the membrane to the anode flow field channels leading to a rise in PA volume in the flow field channels and accumulation under the flow field ribs as shown in Figure 2 and Figure 3. PA saturation in

the GDL increases until it reaches a steady-state after approximately 3 hours at 0.8 Acm^{-2} (Figure 2). After 4 hours at high current density also the PA in the flow field reaches a steady state and the total PA volume in GDL and flow field adds up to 45·10^{-3} mm^{3}mm^{-2} compared to 1.9·10^{-3} mm^{3}mm^{-2} at low current density. At this point one of the three parallel flow field channels is just about filled with electrolyte.

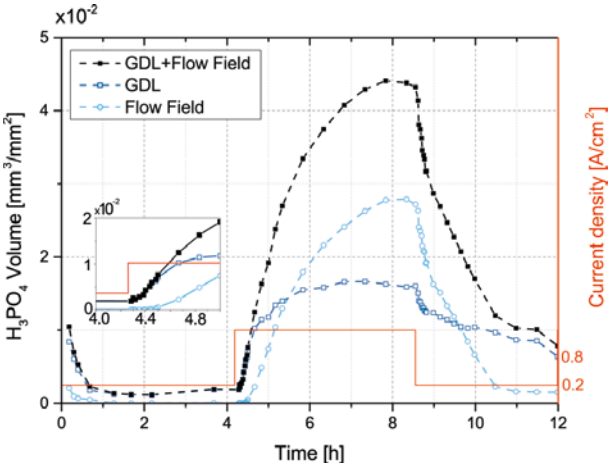

Figure 2: *Volume of PA per active area in GDL, flow field and total as a function of time (dashed lines act as a guide for the eye).*

After 4 hours the current density is decreased back to 0.2 Acm^{-2} and a sudden drop in GDL saturation can be observed concomitant with a decrease of PA volume in the flow field. After 10 min, this sudden drop in PA saturation is followed by a slow and continuous decrease of electrolyte volume in the GDL until the end of the low current cycle after 12 h. The volume of PA in the flow field decreases much faster than in the GDL and reaches a minimum after 3 h at 0.2 Acm^{-2}. Interestingly the condition before the current step is not completely reached. Disconnected PA droplets sticking to the walls remain in the flow field, without continuous path these remainders are unable to diffuse back to the porous layers. These droplets are ultimately lost from the electrolyte reservoir and lead to long term degradation due to electrolyte loss and possibly subsequent membrane and contact resistance increase.

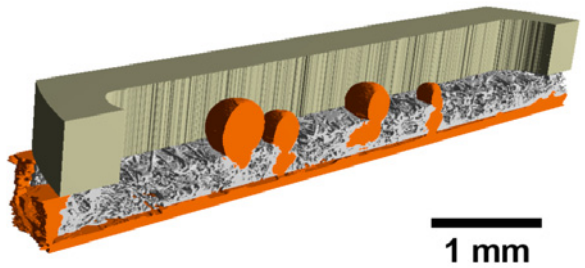

Figure 3: *3D rendering of a vertical along the flow field channel (orange: PA and catalyst layer; olive: flow field; gray: carbon fibers).*

A possible explanation for the observed strong migration of PA to the anode GDL and flow field channels can be given based on results and experience with phosphoric acid fuel cells (PAFC). In these systems phosphoric acid is impregnated in a silicon carbide matrix. It has been described that, when the fuel cell is first started up or the current density is increased, electrochemical pumping is responsible for the migration of electrolyte from the cathode to the anode [3-5]. This is due to the fact that the hydrogen phosphate anion has a finite, non-zero transport number. The transport number determines the fraction of current carried by each ion. When the hydrogen phosphate ion is carrying part of the current, a net movement of hydrogen phosphate from cathode to anode is induced where its charge gets balanced. Eventually a steady state is reached where no net movement of hydrogen phosphate can be observed anymore. At this point back diffusion (and/or hydraulic pressure) of phosphoric acid balances the migration process. In the PBI based systems only 2 PA molecules are bound per repeating unit of PBI, consequently PA also has a large mobility and a majority of the PA electrolyte is able to move freely within the molecular pores of the polymer backbone. A similar behavior as for PAFC can therefore also be expected for PBI based systems.

Conclusion

In this work synchrotron based X-ray tomographic microscopy (XTM) was used to image and quantify the phosphoric acid electrolyte redistribution in in-operando HT-PEFCs. Specifically the processes taking place under dynamic load conditions were investigated in order to identify potential fuel cell degradation mechanisms. It is shown that the examined PBI based membrane systems show extensive electrolyte migration from cathode to anode under high current density operation. This is attributed to the fact that negatively charged hydrogen phosphate anions carry part of the ionic current. This is unlike low temperature polymer electrolyte fuel cells where the anions are covalently bound to the polymer backbone, while in HT-PEFC only a fraction of the phosphoric acid is chemically interacting with the polymer backbone. XTM, for the first time, revealed the current driven electrolyte migration in HT-PEFC.

The intensive phosphoric acid migration has a range of potential consequences, which should be subject of further studies. First of all, long term degradation will occur due to loss of electrolyte with each load cycle due to remaining, unconnected droplets in the GDL and the flow field. Furthermore, with low hydrogen partial pressures in reformate operation the high PA saturation in the GDL could also have an influence on mass transport and consequently fuel cell performance. In case of complete stacks, a migration to adjacent cells might also be possible if the bipolar plates exhibit small defects, allowing PA to crossover.

Acknowledgement

Financial support by BASF SE, precise machining work by M. Hottiger, software and electronic support by T. Gloor and support at the TOMCAT beamline by J. Roth, J. Eller, A. Lamibrac, I. Mayrhuber and T. Lochner are gratefully acknowledged.

References

[1] Q. Li, R. He, R.W. Berg, A.H. Hjuler, N.J. Bjerrum, *Solid State Ionics* **168** (1), 177–185 (2004).
[2] S.H. Eberhardt, M. Toulec, F. Marone, M. Stampanoni, F.N. Büchi, T.J. Schmidt, *J. Electrochem. Soc.* **162** (3), F310–F316 (2015).
[3] J. Roth, J. Eller, F. Marone, F.N. Büchi, *J. Phys. Chem. C* **117** (49), 25991–25999 (2013).
[4] H.R. Kunz, *ECS Trans.* **11** (1), 1447-1460 (2007).
[5] H.R. Kunz, *Electrochem. Soc. Proc.* **99** (14) (2009).
[6] T. Murahashi, *Encyclopedia of Electrochemical Power Sources*, C.K. Dyer, P.T. Moseley, Z. Ogumi, D.A.J. Rand, B. Scrosati, Editors, 564–567 (2009).

Anodic carbon corrosion in high-temperature PEFCs

T. Engl, L. Gubler, T.J. Schmidt
phone: +41 56 310 5237, e-mail: tom.engl@psi.ch

It is winter, it is dark and it is cold. One has to start the fuel cell powered combined heat and power system (CHP). Spring is coming; it is getting brighter and warmer. One has to shut-down the CHP.

This introduction highlights that high temperature polymer electrolyte fuel cells (HT-PEFCs) are not in a continuous operation mode. In fact, they need to change their power output and they may get started-up and shut-down frequently. Unfortunately, changing the fuel electrode gas feed (during start/stop) leads to dramatic carbon oxidation (COR) at the air electrode and therefore irreversible deterioration of the overall fuel cell performance. The corrosion occurs due to the well-known reverse-current decay mechanism described in literature [1, 2] (cf. Figure 1).

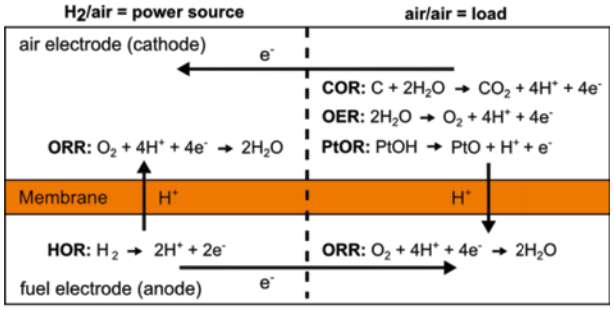

Figure 1: *Simplified start/stop or reverse-current decay mechanism, which highlights carbon corrosion at the air electrode during a gas feed exchange at the fuel electrode (COR, upper right corner). Please note: This sketch specifically cannot explain the carbon corrosion at the fuel electrode which is discussed in this manuscript.*

This very mechanism, however, only describes the carbon oxidation at the air electrode. Corrosion at the fuel electrode is not included in this explanation. Yet, our recent studies reveal that apparently carbon corrosion not only takes place also at the fuel electrode, but it can actually exceed the oxidation rates measured at the air electrode. Therefore, this contribution highlights anodic carbon corrosion.

Experimental

The anodic (fuel electrode) carbon corrosion was investigated during start-up and shut-down at three different flow rates (12, 18 and 24 Nlh^{-1} at both electrodes) and temperatures (80, 120 and 160 °C). A BASF Celtec® based membrane electrode assembly (MEA) was used for the experiments. The MEA exhibits a thickness of approximately 820 µm including a membrane thickness of around 50–75 µm. The MEA consists of a highly H_3PO_4 doped polybenzimidazole (PBI) membrane, electrodes with a symmetrical platinum loading of 1 $mg_{Pt}cm^{-2}$ with an active area of 45.15 cm^2 and a carbon paper gas diffusion layer. During break-in (50 h at 0.2 Acm^{-2} and 160 °C) the fuel cell was operated at stoichiometries of 1.2 for hydrogen and 2.0 for air. The start/stop events were performed by switching the fuel electrode gas feed every 180 seconds (one complete cycle in 360 s) from hydrogen to synthetic air and vice versa. At the air electrode synthetic air is used throughout the experiment. Two three-way magnetic valves (Bürkert Type 0330) are used for switching the fuel electrode gas supply intermittently. During the start/stop cycling the cell was at open circuit voltage. For detecting the carbon corrosion a real-time infrared based CO_2 sensor was used (California Analytical Instruments Model 601) with a detection range up to 10'000 ppm_{CO_2}. The exhaust gas stream from the fuel electrode was fed through a cold trap to condense water before being sent to the CO_2 sensor to avoid interference of the measurement by residual humidity.

The amount of corroded carbon $m_{corroded\ carbon}$, measured via the CO_2 sensor, was calculated according to

$$m_{corroded\,carbon} = \frac{M_C \bullet \dot{n}_{CO_2}}{A_{electrode\,area}}$$

$$m_{corroded\,carbon} = \frac{M_C}{A_{electrode\,area}} \bullet \frac{p\dot{V}}{RT} \bullet A_{CO_2\text{-}peak}$$

where A_{CO_2}-peak is the area of the CO_2 peak (ppm·s) measured by the infrared sensor at the air electrode. R is the universal gas constant, p and T are the ambient pressure and temperature, respectively, M_C is the molar mass of carbon, $\dot{V}$ is the effective volumetric gas flow rate and $A_{electrode\,area}$ is the geometrical electrode area. At least two CO_2 start-up/shut-down peaks were used to average $m_{corroded\,carbon}$.

Results

The fuel electrode CO_2 response and the cell potential is highlighted in Figure 2. One can see a highly pronounced oxidation peak during a shut-down (H_2 is exchanged with synthetic air at the fuel electrode). In comparison, throughout start-up there is only a very small peak recognizable.

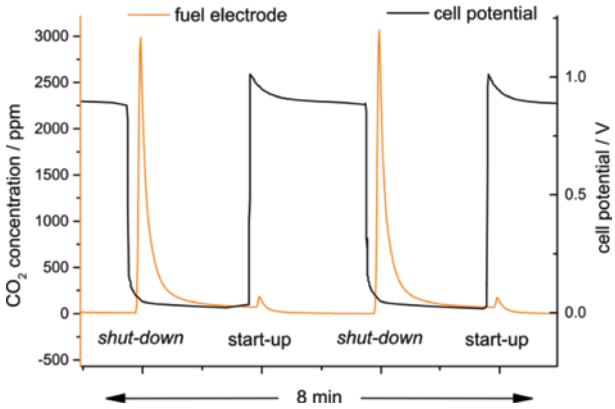

Figure 2: *CO_2 response at the fuel electrode (orange) for HT-PEFC shut-downs and start-ups. Additionally the cell potential is highlighted (black). Measuring conditions: 160 °C, fuel electrode with H_2 @ 12 $L_n h^{-1}$, air electrode with synthetic Air @ 12 $L_n h^{-1}$.*

Subsequently to a shut-down the cell potential is zero because synthetic air is present at both electrodes. The fuel electrode potential though is rather high at around 1 V (only air is present at the fuel electrode). Before the shut-down the electrode potential is quiet low at around 0 V (only H_2 is present at the fuel electrode). Therefore, during a shut-down the fuel electrode potential rapidly increases from approximately 0 to 1 V. During start-up, the rapid potential change is vice versa. These contrary conditions might be a first hint regarding an explanation for anodic carbon corrosion. In order to verify those novel corrosion insights additional experiments were carried out, in which crucial cell parameters were varied.

In Figure 3 the amount of corroded carbon during one start-up and one shut-down per square centimetre is highlighted for the fuel as well as for the air electrode. As seen above, carbon oxidation at the fuel electrode during a start-up is almost negligible compared to a shut-down (between 10 and 20 times smaller). An increased cell temperature leads to higher corrosion rates for both events (about 6 times higher at 160 °C compared to 80 °C). Furthermore, a slower gas flow rate almost consistently leads to higher oxidation values as well. Therefore, anodic carbon corrosion not only occurs at one specific but various parameter constellations. Moreover, the corrosion rate during a shut-down at the fuel electrode is about 3–4 times higher compared to the air electrode depending on the operation conditions.

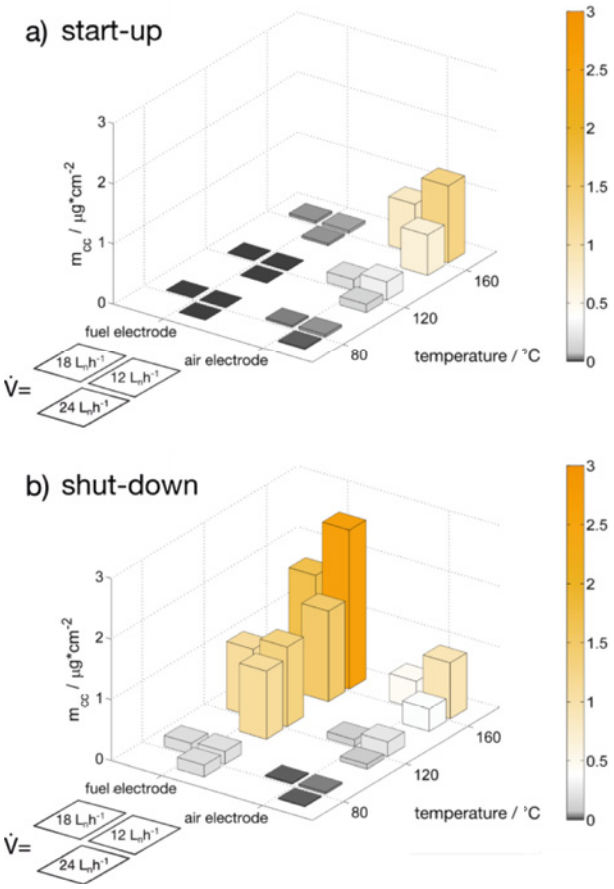

Figure 3: *Carbon corrosion at the fuel and air electrode during a) one start-up and b) one shut-down event at different supply gas flow rates and cell temperatures.*

Conclusion

In this contribution we demonstrated that a fuel cell shut-down, carried out by switching the fuel electrode gas feed from hydrogen to synthetic air, leads to considerable corrosion of the carbon support at the fuel electrode at different conditions (temperature, flow rate). The reverse-current decay mechanism, typically used to explain cathode carbon corrosion, cannot explain this behaviour. We have shown that, at least in our experimental setup, there must be an additional, yet unknown degradation mechanism.

Additional investigations are required and will be performed to improve our understanding of the anodic carbon corrosion mechanism alongside with durability studies. Eventually, the key question is: is anodic carbon corrosion crucial for HT-PEFCs lifetime and performance?

Acknowledgement

Financial support from BASF SE is gratefully acknowledged. We thank our colleagues at the PSI for productive discussions and technical assistance.

References

[1] C.A. Reiser, L. Bregoli, T.W. Patterson, J.S. Yi, J.D. Yang, M.L. Perry, T.D. Jarvi, *Electrochem. Solid-State Lett.* **8**, A273–A276 (2005).
[2] W. Gu, R.N. Carter, P.T. Yu, H.A. Gasteiger, *ECS Trans.* **11**, 963–973 (2007).

SCIENTIFIC ACHIEVEMENTS 2014

Fuel Cells & Electrolysis –

Materials

Engineering and electrochemical characterization of catalyst-coated radiation grafted membranes for use in LT-PEFCs

M. Geormezi, P.A. Patapis, L. Bonorand, T.J. Schmidt, L. Gubler
phone: +41 56 310 5235, e-mail: maria.geormezi@psi.ch

The state-of-the-art membranes for low temperature polymer electrolyte fuel cell (LT-PEFC) membrane-electrode assemblies (MEAs) are PFSA membranes which have found wide-spread use in fuel cells. A promising alternative are radiation grafted membranes, in which we can follow different polymer design strategies [1] in order to introduce a variety of desired functionalities, such as ion-exchange capacity. Our group has synthesized MEAs of radiation grafted membranes [2] that managed to reach the performance of benchmark PFSA based MEAs [3].

Our next logical step was to meet the need of maximized fuel cell efficiency and minimized cost by creating catalyst-coated membranes (CCMs) based on our material. In this attempt aimed at optimizing the «three phase boundary», the point where protons, electrons and gases can meet efficiently, by studying and testing various combinations of ink compositions.

Electrochemical characterization of these CCMs under different operation conditions showed what we expected. Different testing parameters such as relative humidity and stoichiometry of gases require different combinations of ink compositions. In this work, we present results obtained under different operation conditions and the respective performance of the MEAs.

Experimental

PSI Gen2 membranes are based on ETFE film of 25 µm thickness from Saint-Gobain grafted with α methylstyrene (AMS), acrylonitrile (AN), and diisopropenylbenzene (DIPB) as crosslinker. The graft level was 55 ± 1.4 %. Catalyst inks were prepared by mixing a carbon supported platinum (Pt) catalyst (Tanaka K.K., 47 wt% Pt), isopropanol (IPA) / water and a Nafion ionomer solution (Aldrich, EW1100, 5 wt%). The mixtures were sonicated for 45 min. The IPA / water ratio was controlled at 20, 40, 60, 80 wt% of IPA, while the Nafion ionomer content was controlled at 20, 30, and 40 wt% relative to the total solids content of the catalyst inks.

Sample	*Type*	*Isopropanol / Water wt%*	*Nafion wt%*
MEA 1	Membrane/GDE	–	–
MEA 2	Membrane/GDL	20	30
MEA 3	Membrane/GDL	40	30
MEA 4	Membrane/GDL	60	30
MEA 5	Membrane/GDL	80	30
MEA 6	Membrane/GDL	60	20
MEA 7	Membrane/GDL	60	40

Table 1: List of tested MEAs.

Results

Several layers of catalyst ink were sprayed onto the two sides of the PSI Gen2 membranes with an airbrush in a hand-made system, waiting for drying more than 10 min before applicating the next layer. The CCMs were sandwiched between gas diffusion layers (GDLs) (SGL24BC) and were hot-pressed at 140 °C for 1.5 min. Pt loading was 0.4 mg/cm^2. The same procedure was followed for MEA 1, which consists of our PSI Gen2 membrane and JM 0244 gas diffusion electrodes (GDEs). The 29.16 cm^2 MEAs are listed in Table 1.

Each MEA was activated at a constant current density of 0.5 A/cm^2 for 12 h. Humidified H_2 and O_2 were supplied at a stoichiometric ratio of 1.5 and 1.5, respectively. Using bubbler-type humidifiers, the relative humidity of the supplied gases were controlled at 100 % on both sides. After the activation period, we increased the pressure to 2.5 bara. After 1 h, polarization measurements were carried out galvanostatically with an equilibration time of 1 min at each point.

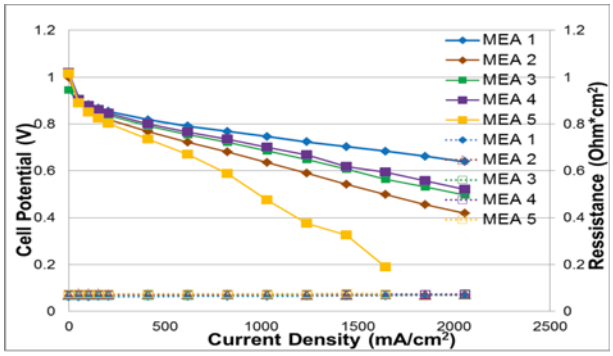

Figure 1: *V-I curves and R_{Ohm} for the MEAs 1–5 at 80 °C with p = 2.5 bara, RH = 100 % and H_2, O_2: 1.5 x stoichiometry.*

The fuel cell tests of the MEAs (Figure 1) showed that the performance peaks as the ratio of the IPA / water in the ink for catalytic layer (CL) preparation is about 60 wt%, while too high (80 wt%) or too low (20 wt%) IPA / water ratio resulted in lower performance. These results suggested that the morphology of the CL and the fuel cell performance of the MEA strongly depend on the composition of the IPA / water solvent of the catalyst ink for CL preparation. Probably, a lower IPA content in the ink results in the formation of aggregated Nafion particles, which block the catalytic sites. On the other hand, a higher IPA content in ink results in bad dispersion of the catalyst and, thus, in a poor performance.

A high-performance MEA requires a combination of effective contact at the three-phase boundary, high Pt catalyst utilization, good proton conduction, and reactants and water product transport to and from Pt active sites. A Nafion ionomer in the CL helps to increase the three-dimensional zone of catalytic activity, serves as the proton conductor in the CLs, facilitates the interaction between the Pt particles, and determines the structure and properties of the CLs.

Each MEA followed the same activation procedure. After the polarization measurements, the single cell was stabilized at 0.5 A/cm^2 for 15 min and electrochemical impedance spectroscopy (EIS) was recorded within the range of 50 kHz

to 10 mHz using an AC amplitude of 200 mA to get reliable values of the ionic and polarization resistance under real fuel cell operation.

Figure 2 and 3 show the polarization curves and ohmic resistances of the MEAs with various ionomer contents in the CLs under O_2 and air operation, respectively. The cell voltages were higher for the MEAs containing 20 and 30 wt% ionomer than for the MEAs with higher ionomer content, such as 40 wt%. Probably, an increased ionomer content in the CLs is hindering the membrane from the absorption of water.

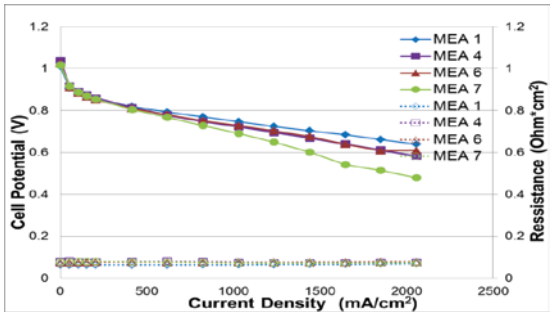

Figure 2: *V-I curves and R_{Ohm} for the MEAs 1,4,6,7 at 80 °C with P = 2.5 bara, RH = 100 % and H_2, O_2: 1.5 x stoichiometry.*

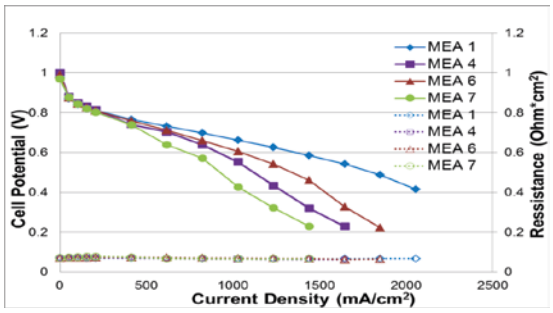

Figure 3: *V-I curves and R_{Ohm} for the MEAs 1,4,6,7 at 80 °C with P = 2.5 bara, RH = 100 % and H_2/Air: 1.5 / 4.0 x stoichiometry.*

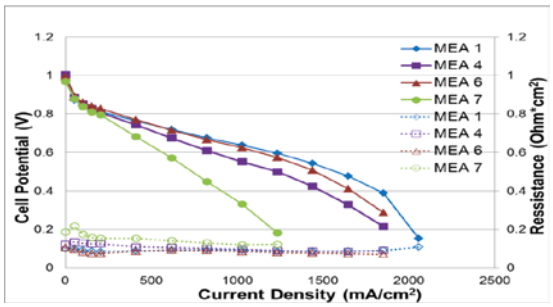

Figure 4: *a) V-I curves and R_{Ohm} for the MEAs 1,4,6,7 at 80 °C with P = 2.5 bara, RH = 50 % and H_2, Air: 1.5 / 4.0 x stoichiometry.*

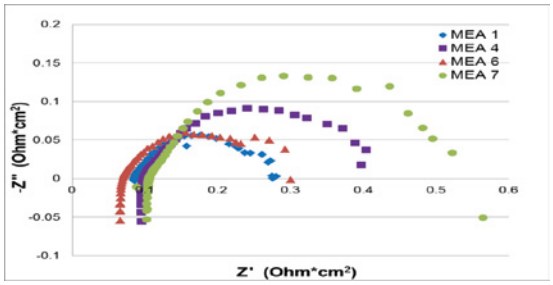

Figure 5: *a) AC impedance at 0.5 A/cm² for the MEAs 1,4,6,7 at 80 °C with P = 2.5 bara, RH = 50 %. H_2, Air: 1.5 / 4.0 x stoichiometry.*

Figure 4 shows the polarization curves and Figure 5 the Nyquist plots of the MEAs with various ionomer contents for operation with air at 50 %. MEA 6 with 20 wt% of Nafion performed better than MEAs 4 and 7 with 30 wt% and 40 wt% of Nafion, respectively. MEA 6 exhibited the highest cell voltage over the entire current density range, which can be attributed to less flooding of the MEA. This obviously results in lower ohmic and polarization resistance of the MEA.

After the cathodic gas was changed to N_2, cyclic voltammetry (CV) was carried out to measure the electrochemically active surface area (ECSA) of the cathodic CL. The curves were recorded with N_2 / 5 % H_2 at the anode at 80 °C using fully humidified gases. In these measurements, the potential was swept from 0.05 V to 1.2 V at a scan rate of 0.1 V/s. The Pt surface area was high enough (57–87 m^2/g) indicating high catalyst utilization.

Surface images were obtained from scanning electron microscopy (SEM) at a magnification x400. Figure 6 shows the SEM images of the CCMs having IPA / water ratios 80 and 20 wt% and Nafion ionomer content 20 and 40 wt% in the catalyst inks. Cracks on the CLs were observed with increasing IPA concentration of the ink while Nafion was found to form aggregated particles with increasing Nafion concentration in the ink.

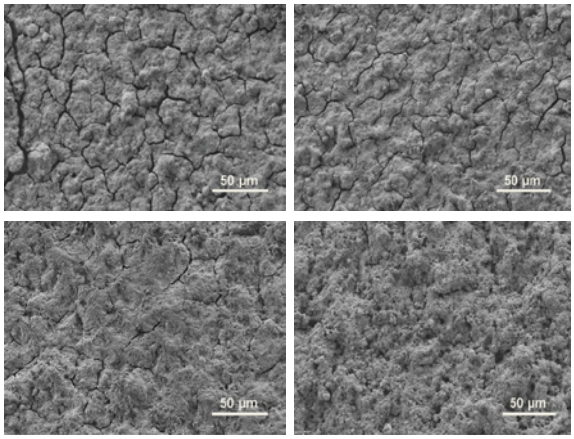

Figure 6: *SEM images at a magnification x400 for the CCMs: with IPA / water ratios 80 wt% (sample 5, upper left) and 20 wt% (sample 2, upper right) and Nafion ionomer content 20 wt% (sample 6, lower left) and 40 wt% (sample 7, lower right).*

Conclusions

Considering that MEA performance is mainly determined by the three-phase boundary, the point where protons, electrons and gases meet, the IPA / water ratio and the Nafion content in the ink was studied for both anode and cathode CLs and MEA 6 (60 wt% IPA / water ratio, 20 wt% Nafion) found to perform close to our reference MEA 1 (MEA with GDEs). In this work, we show that our in-house created MEAs based on CCMs with the PSI Gen2 membrane are performing comparably to the commercial GDEs based MEAs with our membrane as the polymer electrolyte.

References

[1] L. Gubler, *Adv. Energy Mater.* **4**, 1300827 (2014).
[2] L. Gubler, G.G. Scherer, in *Polymer Electrolyte Fuel Cell Durability*, M. Inaba, T.J. Schmidt, F.N. Büchi, Editors, Springer, New York, 133–155 (2009).
[3] L. Gubler, L. Bonorand, *ECS Trans.* **58**, 149–162 (2013).

Stability of radiation grafted proton exchange membranes for water electrolysis cells

A. Albert, T.J. Schmidt, T. Lochner, L. Gubler
phone: +41 56 310 4539, e-mail: albert.albert@psi.ch

The proton conducting membrane is a main component for polymer electrolyte electrolyzers or fuel cells. In the electrolyzer, thick Nafion® membranes, such as Nafion® N115 and N117, are commonly used [1–4]. However, these perfluorinated materials are rather expensive and their gas barrier properties are limited at high pressure [5–7]. Therefore, many alternative membranes are investigated. Radiation grafted membranes are one of these alternatives, since their cost is potentially lower and their properties can be readily modified by varying the composition and architecture of the graft copolymer [8].

Stability of the membrane is an important aspect for a long term application. The stability of radiation grafted membranes can be increased by adding, for example, nitrile containing monomers, crosslinkers or antioxidants [8–10]. In order to investigate the membrane's stability, accelerated stress tests (AST) are often applied. They are based on the known membrane degradation mechanisms.

Radical attack on the membrane is one of the main degradation phenomena observed in fuel cells [11]. It is expected that radical attack also occurs in the electrolyzer. The open circuit voltage (OCV) hold-test is one of the AST protocols in fuel cell research. At OCV, the formation of radicals on the platinum catalyst, which can attack the membrane, is maximised. This AST will be used in this work to assess the stability of the membranes intended for electrolyzers.

The stability of radiation grafted membranes with styrene, acrylonitrile and 1,3 diisopropenylbenzene combinations is investigated (Figure 1). They are synthesised from 50 µm ETFE base films obtained from Saint-Gobain. The five days OCV hold-tests were performed using Nafion® N115, S/AN and S/AN/DiPB grafted membranes. The degradation is investigated by comparing the polarisation curve, area resistance and hydrogen crossover value of the membranes before and after the AST.

Figure 1: *Monomers used for the preparation of radiation grafted membranes.*

Experimental

The pre-treatment of N115, and the detailed synthesis of the S/AN and S/AN/DiPB grafted membranes are described elsewhere [8].

For the OCV hold-test, a fuel cell setup was used. The fully hydrated membrane was hot pressed with two gas diffusion electrodes (JM ELE0162, 0.4 mg Pt/cm^2) at 120 °C and 58 bar for 2 minutes. The active area was 29.2 cm^2. The cell was operated at 80 °C and 2.5 bar absolute reactant gas pressure. The feed gases were pure hydrogen and oxygen with a stoichiometriy of 1.5 each, a flow limit of 200 mL$_n$/min, and 100 % relative humidity. Nitrogen was used instead of oxygen during the hydrogen crossover measurement.

The polarisation curve, area resistance and hydrogen crossover were measured before and after five days OCV hold-test. The experimental details are described elsewhere [12].

Results

The membrane performance can be assessed based on the polarisation curve of the cell. Figure 2 shows the polarization curves and area resistances of the membranes before and after five days of OCV hold-test. At the beginning of test, N115 showed the best performance, followed by the S/AN and S/AN/DiPB grafted membrane. After the test, N115 still showed the best performance, yet the S/AN grafted membrane became worse than the S/AN/DiPB membrane.

The membrane electrode assembly (MEA) based on N115 did not exhibit any significant difference in performance and area resistance after the OCV hold-test. The S/AN grafted membrane underwent a considerable increase of area resistance, which resulted in a much lower performance. Meanwhile, the S/AN/DiPB grafted membrane showed a moderate increase in area resistance and concomitant decrease in performance.

N115 does not seem to degrade according to this result. However, it is known that Nafion membranes also degrade during an OCV hold-test. The fluoride release rate (FRR) measurement is needed to follow the degradation of Nafion® type membranes [13], which was not performed in this work. The result indicates that the S/AN grafted membrane undergoes more significant degradation upon OCV hold testing. The S/AN/DiPB grafted membrane, which contains DiPB crosslinker, degrades less than the S/AN grafted membrane. This proved that the DiPB crosslinker increased the stability of radiation grafted membranes based on styrene and acrylonitrile monomers.

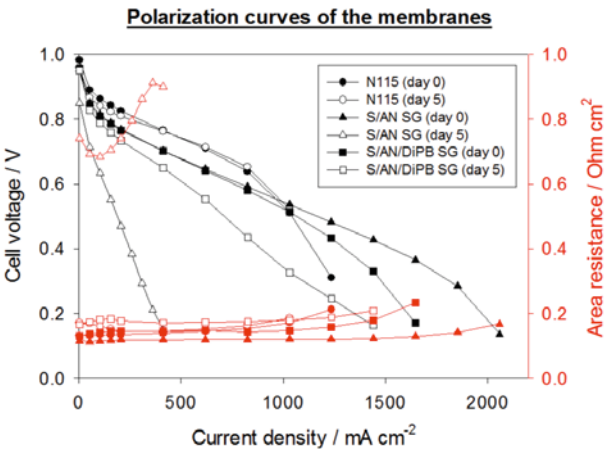

Figure 2: *Polarisation curves of single cells and area resistance values, indicative of membranes resistance.*

Table 1 shows the hydrogen crossover values of the membranes before and after the OCV hold-test. In agreement with the polarisation curves and area resistances, only the S/AN grafted membrane shows a significant increase in the hydrogen crossover, which confirms the degradation of the S/AN grafted membrane. From these results, N115 is the most stable membrane, followed by the S/AN/DiPB and S/AN grafted membrane.

Membrane	*Hydrogen crossover (mA cm^{-2})*
N115 (day 0)	1.61 ± 0.02
N115 (day 5)	1.72 ± 0.01
S/AN SG (day 0)	1.01 ± 0.03
S/AN SG (day 5)	2.27 ± 0.68
S/AN/DiPB SG (day 0)	0.76 ± 0.06
S/AN/DiPB SG (day 5)	0.73 ± 0.05

Table 1: *Hydrogen crossover of the membranes measured before and after the 5 day OCV hold-test.*

Conclusion

OCV hold-tests are a possible accelerated stress protocol for the assessment of the oxidative stability of membranes. Unlike Nafion® 115, the radiation grafted membrane tested here experienced considerable performance loss and increase in resistance upon a 5 days OCV hold-test, in particular the uncrosslinked membrane. In addition, the hydrogen crossover increases, indicating membrane degradation.

The S/AN/DiPB grafted membrane, which is crosslinked, is more stable than the S/AN grafted membrane. Addition of crosslinker improved the stability of radiation grafted membranes. Further work needs to be done to find the right composition of the graft copolymer that will result in a stable radiation grafted membrane.

Despite the apparent stability of Nafion® 115, it is known from literature that polymer degradation does take place, indicated by the fluoride ions found in the effluent water of the cell.

Acknowledgement

The research leading to these results has received funding from the European Union´s Seventh Framework Programme (FP7/2007–2013) for the Fuel Cells and Hydrogen Joint Technology Initiative under grant agreement n°303484 (NOVEL).

References

[1] M. Carmo, D.L. Fritz, J. Mergel, D. Stolten, *Int. J. Hydrogen Energy* **38**, 4901–4934 (2013).
[2] G.G. Scherer, T. Momose, K. Tomiie, *J. Electrochem. Soc.* **135**, 3071–3073 (1988).
[3] P. Millet, F. Andolfatto, R. Durand, *Int. J. Hydrogen Energy* **21**, 7–93 (1996).
[4] A.S. Aricò, S. Siracusano, N. Briguglio, V. Baglio, A. Di Blasi, V. Antonucci, *J. Appl. Electrochem.* **43**, 107–118 (2012).
[5] S.A. Grigoriev, V.I. Porembsky, V.N. Fateev, *Int. J. Hydrogen Energy* **31**, 171–175 (2006).
[6] P.W.T. Lu, S. Srinivasan, *J. Appl. Electrochem.* **9**, 269–283 (1979).
[7] S.A. Grigoriev, V.I. Porembsky, S.V. Korobtsev, V.N. Fateev, F. Aupretre, P. Millet, *Int. J. Hydrogen Energy* **36**, 2721–2728 (2011).
[8] L. Gubler, G.G. Scherer, in: *Handbook of Fuel Cells,* **Vol. 5,** W. Vielstich, H.A. Gasteiger, H. Yokokawa (Editors), John Willey and Sons, Chichester (UK), 313–321 (2009).
[9] K. Jetsrisuparb, H. Ben youcef, A. Wokaun, L. Gubler, *J. Membr. Sci.* **450**, 28–37 (2014).
[10] Y. Buchmüller, A. Wokaun, L. Gubler, *J. Mater. Chem. A* **2**, 5870–5882 (2014).
[11] J.F. Wu, X.Z. Yuan, J.J. Martin, H.J. Wang, J.J. Zhang, J. Shen, S.H. Wu, W. Merida, *J. Power Sources* **184**, 104–119 (2008).
[12] A. Albert, T.J. Schmidt, L. Gubler, *PSI Electrochemistry Annual Report* **2013**, 21–22 (2013), DOI: 10.3929/ethz-a-007047464.
[13] W. Liu, K. Ruth, G. Rusch, *J. New Mater. Electrochem. Syst.* **4**, 227–231 (2001).

Measuring the internal contact angle of gas diffusion layers

A. Forner-Cuenca, P. Gröninger, J. Biesdorf, L. Gubler, T.J. Schmidt, P. Boillat
phone: +41 56 310 5125, e-mail: antoni.forner@psi.ch

Different functions have to be fulfilled by the gas diffusion layers (GDLs) in polymer electrolyte fuel cells (PEFCs), such as providing electrical and thermal conductivity, mechanical stability, and distributing reactant gases while removing liquid water counterflow. The understanding of the transport processes for water is of great importance for the potential optimization and development of advanced water management strategies in fuel cells.

Capillary pressure is the driving force [1] for the liquid water transport and depends on both pore radius and contact angle. Sophisticated characterization techniques exist for pore size distribution measurement such as mercury intrusion porosimetry; however most of the contact angle methods are based on external measurements, such as sessile droplet [2] and Wilhelmy [3]. As previously reported [4], surface dependent measurements lead to misunderstanding (apparent contact angle) since physical forces related to roughness are dominant.

Consequently, information about internal pore walls wettability is required. One possible method is the measurement of the dynamics of liquid imbibition (so called Washburn method), which depend on both pore size and internal contact angle. The parameters are obtained by fitting the experiments to models. Two approaches are possible: either a measurement of the mass gain (experimentally more complex) or the height over time. The internal wettability in GDLs can be seen as a complex phenomenon due to the presence of several media (carbon fibers, coating and binder); however, the estimation of a statistical average internal contact angle is targeted.

The method is easily applicable to hydrophilic samples where the water rises, however it presents practical limitations when hydrophobic materials (like GDLs) are used. To solve this issue different solvents with lower surface tension are used and the value for water is extrapolated.

Synthetically hydrophilic samples are targeted within our project [5] and a method that allows for quantitative comparison is therefore required. Herein, we report the implementation of a new setup for the measurement of 5 samples simultaneously. Limitations were found with respect to previously published work whith hydrophobic GDLs, but the method remains suitable for hydrophilic materials.

Experimental

Procedure

Five samples were sandwiched together between two Plexiglas magnetic plates. Parallelism was assured by using a positioning tool. After that, the support was located in the glass container which was closed with an aluminum lid and sealed with parafilm. A thermocouple and the needle of the syringe for liquid injection were passing through drilled holes into the chamber. Approximately 15 mL of the solvent are initially delivered to the system to allow for saturation of the vapor phase with the solvent (evaporation from GDL can be an important issue). A time of 20 min was found to be enough to saturate the chamber.

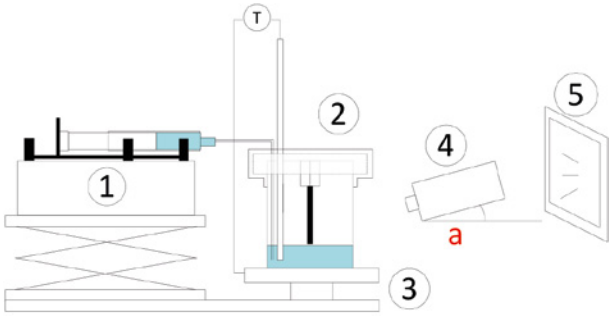

Figure 1: *Schematic of the Washburn setup. 1) Programmable syringe pump; 2) samples container; 3) positioning and heating table; 4) digital microscope camera; 5) white light.*

The solvent was pumped in with a syringe pump (BS-300, Braintree Scientific Inc.) at a rate of 6.0 mL/min and a video was recorded at 15 frames/s (DigiMicro Profi 200.5) and 512 x 468 px. The camera was elevated with respect to the interphase plane between sample and solvent (defining an angle α) in order to avoid the disturbance brought by the meniscus defined between glass container and solvent. After the identification of the inhibition point (clearly visible by the formation of a meniscus GDL-solvent) the pump was stopped.

Solvents

Hexane was used as solvent with full wettability, since pentane solidified on the syringe needle. The following solvents were evaluated: cyclohexane, ethanol, acetone, toluene and water. All solvents were from Sigma Aldrich and had purities greater than 99 %.

Samples

Uncoated GDLs (SGL 24AA and Toray TPGH-060) were used for the validation of the method and equation fitting. Samples with different coating loads (5–70 %FEP) were also tested.

Toray TPGH-060 was coated with 70 %FEP and grafted with N-vinylformamide [5] for the evaluation of water imbibition in a hydrophilic sample.

Image processing

The image processing was performed as follow: first, each image was divided by an average «dry background» image corresponding to the average of 20 images before the start of imbibition, in order to improve the contrast between dry and saturated GDL. Then the solvent height in pixel was extracted automatically for each image and each sample using an in-house software written as ImageJ plugin. Finally, the pixel size was converted to a height in cm taking into account the effect of the camera angle.

Model

A complete energy balance [6] was considered and terms related to inertia and frictions were found to be negligible. Therefore capillary pressure term equals to the viscous forces plus the gravitational effects:

$$\frac{dh}{dt} = \frac{R^2}{8\eta h}\left(\frac{2\gamma_{lv}\cos\theta}{R} - \rho g h\right)$$

Density (ρ), dynamic viscosity (η) and surface tension (γ_{lv}) were implemented in the model as temperature-dependent. Initially, hexane was used as liquid with full wettability ($\cos\theta = 1$) in order to calculate R.

Results

Uncoated materials (SGL and Toray) were used in order to check reproducibility. Relative errors of 1.7 % and 1.5 %, respectively, were obtained when measuring five times the very same sample.

The results obtained with the fitting leaded to no solution ($\cos\theta > 1$) for some materials (uncoated GDLs when hexane was chosen as reference) when using ethanol and acetone as a liquid. This is contradictory with previous literature [4, 6, 7] which reported $\cos\theta < 1$ in every case when measuring with these liquids. Different reasons could contribute to these differences:

- The experimental error implicit in the measurements could explain that, since there is a high sensibility of the parameter R.
- Both parameters R and cosθ compensate each other, therefore the iterative calculation has not a unique solution. Some approaches [5] fitted the equation by iterating both parameters, however nothing was said about the values of R; others [7] estimated the R (or Washburn constant) and then only resolved for the contact angle (this work's approach).
- The assumption that the complex pore structure of the GDL is equivalent to a parallel capillary tube and that the liquid pore volume is saturated may not be accurate enough. The parameter R is not assumed to be consistent with the real pore radius, but rather the hydraulic radius [8]. Depending on the liquid's surface tension, viscosity and density, a liquid could rise up pores that are not accessible for other liquids.
- The concept of «statistical average contact angle» should be handled with care. Possibly the liquid wets only (or preferentially) the GDL component with the higher surface tension which better interacts chemically with the solvent.

Solvent	γ_{lv}*(mN/m)*	$\gamma_{lv(pol)}/\gamma_{lv(disp)}$	θ_I(°)	θ_{II}(°)
Ethanol	22.3	0.59	29±2	44±2
Water	70.1	2.3	85±2	37±2

Table 1: *Measured contact angles (5 repetitions) over two flat surfaces: I. highly oriented pyrolytic graphite; II. N-ninylformamide grafted FEP. Ethanol and water were used as solvents. Values of total surface tension and the ratio between polar and dispersive components are given.*

Table 1 presents the contact angle value measured over flat surfaces. Ethanol wets the graphite much more than water does. However, the trend is reversed when measuring over n-vinylformamide grafted FEP. This result is somehow counterintuitive since solvent with lower surface tension does not wet more of a certain solid surface. This shows the importance of the polar and dispersive components with respect to the solid surface chemical properties, making the solvent choice more challenging.

The method is easily applied to samples that spontaneously imbibe liquid water, avoiding the use of extra solvents. Figure 2 shows the Washburn curves for the synthetic hydrophilic GDL, measured with hexane and liquid water. After fitting the model parameters to the experimental data, an average internal contact angle of 76° is obtained (R obtained from hexane measurement). This value is in good agreement with the measurements performed over flat surfaces and considering mixed wettability (carbon fibers and n-vinylformamide).

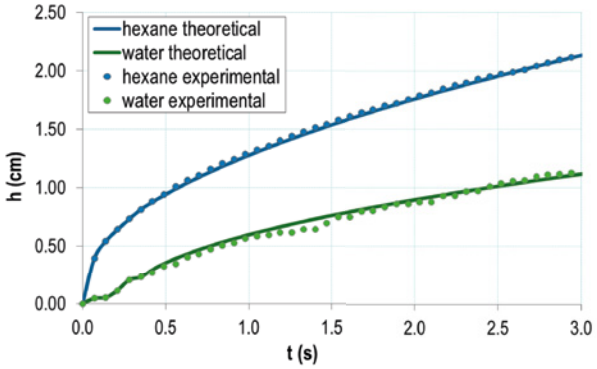

Figure 2: *Washburn curves for the hydrophilized sample measured with hexane (blue) and water (green).*

In conclusion, the Washburn method presents limitations to obtain quantitative results for hydrophobic GDLs. However, it provides a fast and a reliable semi-quantitative characterization technique for hydrophilic samples.

Acknowledgement

Funding by the Swiss National Science Foundation (project no 143432) is gratefully acknowledged.

References

[1] U. Pasaogullari, C.Y. Wang, *J. Electrochem. Soc.* **151** (3), A399–A406 (2004).
[2] S. Park, B.N. Popov, *Fuel* **88**, 2068–2073 (2009).
[3] V. Parry, G. Barthome, J.C. Joud, *Appl. Surf. Sci.* **258** (15), 5619–5627 (2012).
[4] V. Gurau, M.J. Bluemle, E.S. De Casto, Y.-M. Tsou, J.A. Mann Jr., T.A. Zawodzinski Jr., *J. Power Sources* **160**, 1156–1162 (2006).
[5] P. Boillat, A. Forner-Cuenca, L. Gubler, C. Padeste, F.N. Büchi, European Patent Application EP14184065 (2014).
[6] R.K. Phillips, B.R. Friess, A.D. Hicks, J. Bellerive, M. Hoorfar, *Energy Procedia* **29**, 486–495 (2012).
[7] D.L. Wood III, C. Rulison, R.L. Borup, *J. Electrochem. Soc.* **157** (2), B195–B206 (2010).
[8] R. Masoodi, Thesis Dissertation University of Wisconsin-Milwaukee (2010).

Structure-property correlations of ion-containing polymers for fuel cell applications

V. Sproll, G. Nagy, U. Gasser, S. Balog[1], T.J. Schmidt, L. Gubler
phone: +41 56 310 2673, e-mail: lorenz.gubler@psi.ch

Radiation grafted membranes are an alternative to the state-of-the-art perfluorosulfonic acid membranes such as Nafion® (DuPont) in polymer electrolyte fuel cells (PEFCs) [1]. Apart from offering a much cheaper fabrication method, this versatile technique provides a high flexibility in membrane design as a wide range of commercially available monomers and thereby possible functionalizations can be readily combined with various base films. The partially fluorinated ETFE is an excellent candidate for such a base film for fuel cell applications [1]. The microstructure of extruded ETFE is inherently anisotropic (machining direction (MD) vs. transverse direction (TD)) due to its manufacturing process. This anisotropy is partially maintained in the final membranes and is expected to have a strong influence on their performance.

As the relevant properties strongly depend on the structure and orientation of the polymer chains within the proton exchange membrane (PEM), it is crucial to investigate the structure-property relationships in these membranes more closely.

Experimental

The membrane synthesis was conducted similiar to what has been reported in our earlier work (deposited dose 5 kGy, reaction temperature 55 °C) [2]. Pulsed-field-gradient stimulated-echo (PFG-STE) NMR technique was performed [3] on a Bruker Avance II 200 spectrometer (Bruker, Karslruhe, Germany) with a Bruker DIFF-25 gradient probe and a 1H resonance frequency of 200.13 MHz. The gradient pulse was 0.5 ms, the time between the gradients was varied between 20 and 40 ms and the gradient strength was linearly ramped from 0 to 9.6 T/m in 16 steps. The dwell time was 20 µs and the pre-scan delay was 50 µs. NMR data was processed in MatLab (www.mathworks.com). The different relative humidities (r.h.) were adjusted by equilibrating the samples in the tube for 12 days in a sealed container with defined r.h. at 25 °C. The different r.h. were generated using saturated salt solutions ($Mg(NO_3)_2$: 52.8 % r.h.; KNO_3: 93.7 % r.h.) [4]. Afterwards the NMR-tubes were sealed and measured at different temperatures.

A four point-probe conductivity cell from Bekktech BT-112 consisting of four Pt-electrode wires immersed in liquid water was used to measure the in-plane proton conductivity at room temperature. More details can be found in earlier work [5].

Results

Diffusion measurements

Pulsed-field-gradient (PFG) NMR diffusometry is an effective method to gain insight into the mobility of species over an adjustable length and time scale (~100 nm to ~10 µm, ~1 ms to 1 s) thereby providing useful information on coupling of structural heterogeneity with the magnitude of diffusion of the observed species in the studied material [6]. In the present study the dependency of the diffusion coefficient on temperature and r.h. was investigated in a series of polystyrene sulfonic acid grafted membranes (ETFE-g-PSSA) with different grafting levels (GL). Moreover, membranes with a defined GL of 25 % and different contents of crosslinking agent (corresponding to 0, 10 and 20 vol% (wrt. total monomer) of DiPB in the grafting solution) were analyzed. Figure 1a shows only a significant impact of the GL on the diffusion coefficient of water (D_{H_2O}) at 80 °C, whereas the influence at lower temperature is minor (for comparison D_{H_2O} of pure water: $2.2 \cdot 10^{-9}$ m^2 cm^{-1} (21 °C), $6.0 \cdot 10^{-9}$ m^2 cm^{-1} (80 °C))[7].

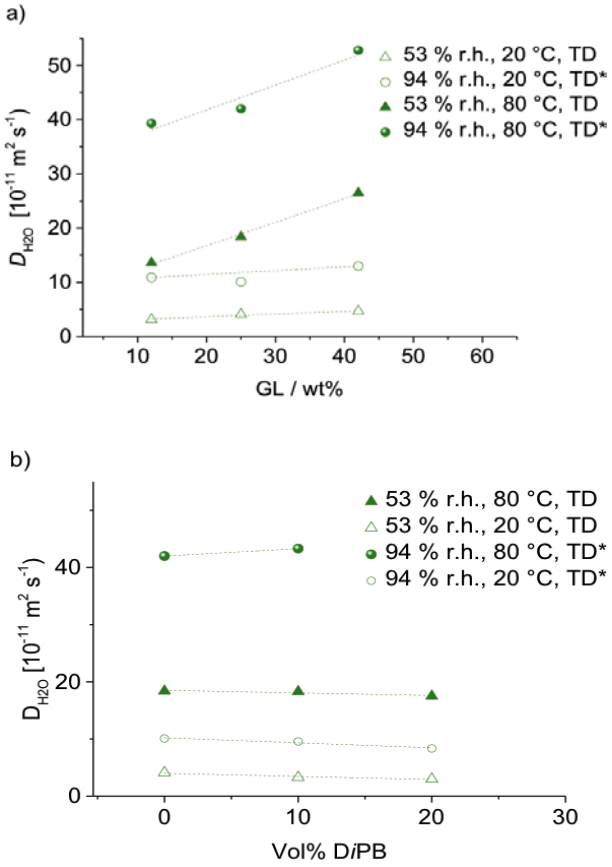

Figure 1: *Diffusion coefficients of H_2O in a) ETFE-g-PSSA membranes for different GL and b) ETFE-g-P(SSA-co-DiPB) membranes with a fixed GL of 25 % and various crosslinking content. *r.h. adjusted at 20 °C, cf experimental section.*

Comparing the influence of the investigated parameter, it is obvious that the other two factors – the r.h. and the temperature – dominate the diffusion, whereas the GL plays only a subordinate role.

An increasing degree of crosslinking agent leads to an unexpected weak decrease of D_{H_2O} as shown in Figure 1b. The influence of the temperature and the r.h., however, lies in a comparable range to the values obtained for the uncrosslinked membrane.

In order to evaluate the impact of the base film anisotropy (MD and TD) on D_{H_2O}, both directions were analyzed for a

[1] Adolphe Merkle Institute, University of Fribourg

crosslinked membrane with a GL of 25 % and a crosslinking content of 10 vol% (wrt. total monomer). The diffusion coefficient in TD appears to be 1.5 times higher than in MD (MD: $1.21 \cdot 10^{-10}$ m^2 s^{-1}; TD: $1.83 \cdot 10^{-10}$ m^2 s^{-1}).

In-plane conductivity measurements

Analysis of the in-plane proton conductivity data corroborates the results of the PFG-NMR measurements showing the impact of the anisotropy of the base film. Both methods show that TD is favored over MD for properties associated with the grafted polymer. A closer look at the data reveals a significant difference of 30 % for MD vs. TD at low GL (Figure 2a). This difference decreases with increasing GL up to 8 % at a GL of 67 % but does not completely vanish indicating that even such a high content of grafted polymer does not lead to completely uniform H^+ transport properties. This observed difference in the two directions is even more pronounced for crosslinked membranes (40 % instead of 20 % difference for an uncrosslinked system with the same GL (Figure 2b).

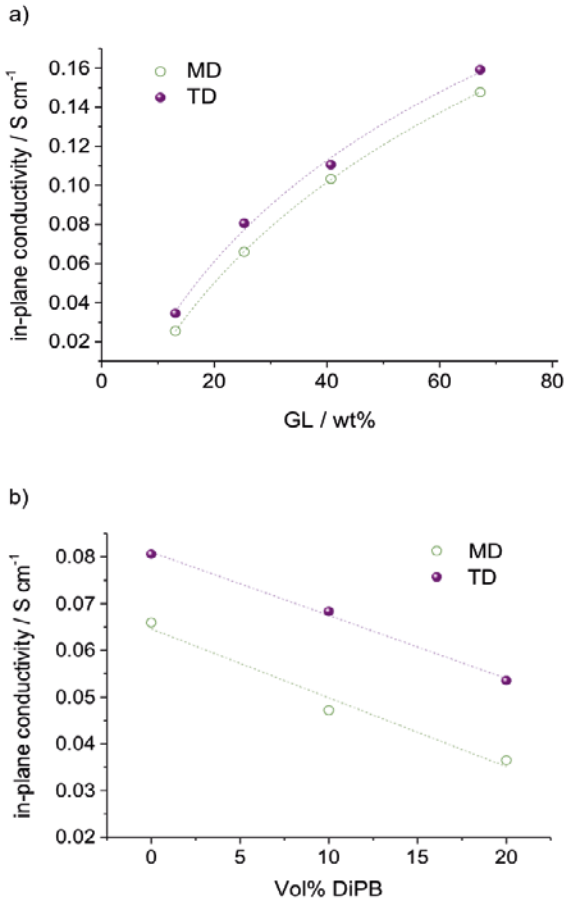

Figure 2: *Conductivity of membranes swollen in liquid water for MD and TD at 25 °C. a) ETFE-g-PSSA membranes with different GL. b) ETFE-g-P(SSA-co-DiPB) membranes with different crosslinking levels at a fixed GL of 25 %.*

Comparing the results of the PFG-NMR and the in-plane conductivity measurements, the impact of a higher GL is much more distinct for the in-plane conductivity whereas the effect seems to be negligible for D_{H_2O} at ambient temperature. This observation can also be extended to the crosslinked system (Figure 2b). Here the conductivity drops significantly for higher crosslinking levels while the diffusion is not much influenced. This behavior can be explained by the different target of both methods. In case of the diffusion, the velocity of the species (water molecule) is important whereas in case of the conductivity the number of the transported charges is the determining factor. By increasing the crosslinking content the width of the hydrophilic channels is narrowed and thereby also the number of transported charges is reduced.

Acknowledgement

Funding by PSI within the framework of the «CROSS Departmental Initiative» is gratefully acknowledged, as well as financial support by the European Soft Matter Infrastructure (ESMI) project (Integrated Infrastructure Initiative Nr. 262348).

References

[1] L. Gubler, *Adv. Energy Mater.* **4** (3), 1300827 (2014).
[2] H. Ben youcef, S. Alkan-Gürsel, A. Buisson, L. Gubler, A. Wokaun, *Fuel Cells* **10** (3), 401–410 (2010).
[3] J.E. Tanner, *J. Chem. Phys.* **52** (5), 2523–2526 (1970).
[4] H. Nyqvist, *J. Pharm. Tech. Prod. Manuf.* **4** (2), 47–48 (1983).
[5] L. Gubler, N. Prost, S. Alkan-Gürsel, G.G. Scherer, *Solid State Ionics* **176** (39), 2849–2860 (2005).
[6] J. Hou, J. Li, D. Mountz, M. Hull, L.A. Madsen, *J. Membrane Sci.* **448**, 292–299 (2013).
[7] T. Dippel, K.D. Kreuer, *Solid State Ionics* **46**, 3–9 (1991).

Ion exchange membranes for the all-vanadium redox flow battery with improved vanadium barrier properties

O. Nibel, T.J. Schmidt, L. Gubler
phone: +41 56 310 2326, e-mail: olga.nibel@psi.ch

Redox flow batteries are considered as one of the options for electricity storage and can be used in applications with energy storage requirements in the range of kilowatt-hours to megawatt-hours [1]. They can be used, for example, for energy storage from renewable sources [1, 2], for remote area power supply [2], for uninterruptable power supply [2], for grid management [2] as well as for electric vehicles charging stations [4].

In particular the all-vanadium redox flow battery (VRB) has received the most attention until today. VRBs use the same element (vanadium) in both half cells, which prevents cross-contamination of the electrolytes and reduces the maintenance costs. Ion exchange membranes are regarded as essential component of all-vanadium redox flow batteries since they largely avoid cross-mixing of electrolytes and at the same time allow the transport of specific ions across the membrane to maintain charge balance during cell operation. An ideal membrane for the VRB should have low vanadium and water crossover, low cost, low area resistance, good stability in strong acidic environment, and good chemical stability in an environment with strongly oxidizing V^{5+}. [1, 2, 3]

The objective of this study is to design partially fluorinated ion exchange membranes for the VRB with low resistance and low vanadium crossover. For this purpose, ETFE-g-poly(S-co-AN) films were successfully prepared by radiation induced graft copolymerization of acrylonitrile (1) and styrene (2) onto ethylene tetrafluoroethylene (ETFE) films of 25 µm thickness. Subsequently, grafted films were functionalized with proton-conducting sulfonic acid groups and vanadium complexing amidoxime groups (Scheme 1).

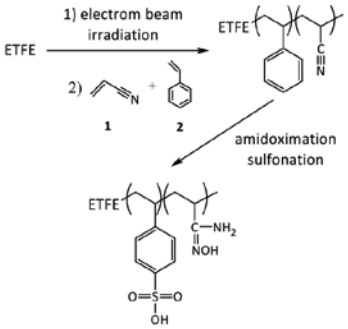

Scheme 1: *Schematic representation of the synthesis of functionalized ETFE-g-poly(S-co-AN) membranes.*

Functionalized membranes were analyzed using FT-IR spectroscopy and energy-dispersive X-ray spectroscopy coupled with scanning electron microscopy (EDX-SEM). Moreover, the key properties of the prepared membranes, such as vanadium ion permeability and area resistance, were studied.

Experimental

Synthesis of grafted films

The ETFE base films (DuPont, 25 µm thickness) were irradiated by an MeV-class electron beam in air and stored at –80 °C. The grafting reaction was performed in glass reactors under nitrogen atmosphere. For that, a grafting solution with the following composition was prepared: 20 % (v/v) monomer solution (S/AN volumetric ratio = 2/3) + 70 % (v/v) iso-propanol + 10 % (v/v) ultra-pure water. Subsequently, the grafting solution containing irradiated films was degassed for 1 h. Then, the reactor was placed in a thermostatic water bath at the desired temperature to initiate the grafting reaction. After the reaction, grafted films were washed with acetone for 18 h and dried under vacuum at 80 °C.

Functionalization of ETFE-g-poly(S-co-AN) films

Sulfonation of the grafted styrene (Scheme 2) was carried out in a 2 L glass reactor using a 3 % solution of chlorosulfonic acid in dichloromethane (DCM). Grafted films were introduced into the solution and after stirring for 6 h at room temperature the sulfonated films were removed from the reaction mixture, washed with ultra-pure water and hydrolyzed at 80 °C in pure water for 16 h.

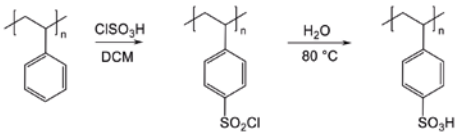

Scheme 2: *Schematic representation of the sulfonation procedure of grafted styrene units.*

Amidoximation of nitrile groups (Scheme 3) was performed in a small glass reactor using 2 M solution of hydroxylamine hydrochloride in H_2O/EtOH (volumetric mixing ratio of H_2O/EtOH = 1:1). The pH value of the solution was adjusted to 7 by adding aqueous NaOH. Subsequently, grafted films were introduced into the prepared solution and placed in a thermostatic water bath at 70 °C for 3 days if the amidoximation was performed after the sulfonation, or for 6 days if the amidoximation was performed prior to sulfonation.

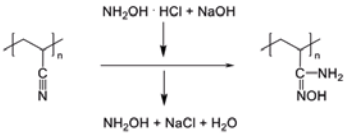

Scheme 3: *Schematic representation of the amidoximation of grafted acrylonitrile units.*

Characterization of functionalized membranes

Vanadium ion permeability: Vanadium ion permeability of membranes was determined using self-made diffusion cells consisting of two round bottom flasks separated by the membrane. The left compartment of the cells was filled with a 1 M

solution of $VOSO_4$ in 2 M H_2SO_4 while the right one was filled with 1 M solution of $MgSO_4$ in 2 M H_2SO_4. At regular time intervals the concentration of diffused VO^{2+} ions in the right compartment was measured using UV-Vis spectroscopy.

Determination of membrane area resistance: The resistance of the membranes was measured in the redox cell test system (Model 857, Scribner Associates) by means of electrochemical-impedance spectroscopy. For this purpose, the redox flow battery containing carbon felt electrodes was fed on both sides with 1 M solution of $VOSO_4$ in 2 M H_2SO_4. The electrolytes were potentiostatically charged until the current density was less than 4 mA/cm^2. All measurements were performed at room temperature.

Results and Discussion

The success of functionalization of ETFE-g-poly(S-co-AN) films was confirmed using FT-IR spectroscopy. Furthermore, it was found that films that were sulfonated in the first step contained not only sulfonic acid and amidoxime groups but also carboxyl groups because of the partial hydrolysis of nitrile groups during the sulfonation. In contrast, films that were amidoximated in the first step contained no carboxyl groups and therefore a higher amount of amidoxime groups.

Elemental distribution in the cross-section of membranes was analyzed by SEM/EDX. As can be seen in Figure 1, membranes with different distribution of grafts in the cross-section could be prepared by changing the temperature of the grafting reaction or using base films that were irradiated with 5 kGy instead of 15 kGy.

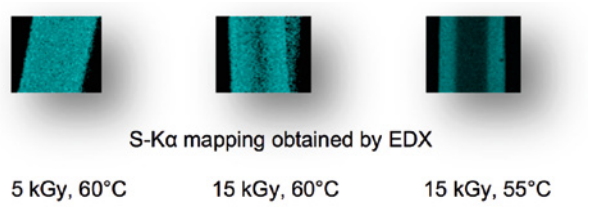

Figure 1: *Influence of grafting temperature and irradiation dose of base films on the distribution of grafts across the membrane thickness.*

In case of membranes with inhomogenous distribution of grafts across the thickness, increase of area resistance and decrease of V^{4+} permeability can be observed with increasing amount of amidoxime groups (Figure 2).

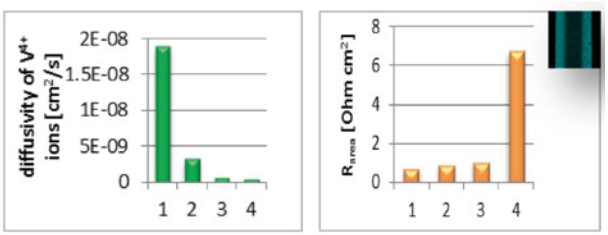

Figure 2: *1 = Nafion 212; 2 = only sulfonated membranes; 3 = sulfonated (1) + amidoximated (2) membranes; 4 = amidoximated (1) + sulfonated (2) membranes.*

As demonstrated in Figure 3, in case of membranes with homogeneous distribution of grafts in the cross-section, an increasing amount of amidoxime groups in the membranes leads to decrease of V^{4+} permeability, while the area resistance is not significantly affected. It is also remarkable that in case of membranes with homogeneous distribution of grafts in the cross-section, only membranes with the highest content of amidoxime groups show lower V^{4+} permeability than Nafion [5].

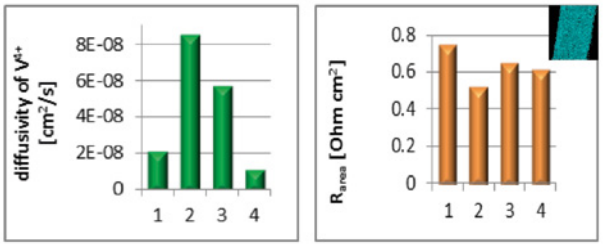

Figure 3: *1 = Nafion 212; 2 = only sulfonated membranes; 3 = sulfonated (1) + amidoximated (2) membranes; 4 = amidoximated (1) + sulfonated (2) membranes*

In addition, based on SEM/EDX results the influence of the inhomogeneous distribution of grafts on membrane properties such as vanadium permeability and resistance was investigated in more detail. It was found that the area resistance increases and vanadium permeability decreases with increasing inhomogeneous distribution of grafts in the cross-section of membranes.

Conclusion

The amount of amidoxime groups in the membrane as well as the distribution of grafts across the membrane thickness allow tuning of vanadium ion permeability and ohmic resistance in targeted manner to design membranes for the VRB.

Acknowledgement

Funding by the Swiss National Science Foundation (Sinergia, project REPCOOL) is gratefully acknowledged.

References

[1] X. Li, H. Zhang, Z. Mai, H. Zhang, I. Vankelecom, *Energ. Environ. Sci.* **4**, 1147 (2011).
[2] G. Kear, A.A. Shah, F.C. Walsh, *Int. J. Energy Res.* **36**, 1105-1120 (2012).
[3] H. Prifti, A. Parasuraman, S. Winardi, T.M. Lim, M. Skyllas-Kazacos, *Membranes* **2**, 275–306 (2012).
[4] H.M. Zhang, *ECS Trans.* **28**, 1–5 (2010).
[5] L. Gubler, O. Nibel, L. Bonorand, European Patent Application EP15154151 (2015).

SCIENTIFIC ACHIEVEMENTS 2014

Batteries –

Materials

Asymmetric porous membrane obtained by plasma-induced graft copolymerization

J. M. Conder, S. Urbonaite, D. Streich, P. Novák, L. Gubler
phone: +41 56 310 2120, e-mail: joanna.conder@psi.ch

Polymer electrolyte membranes have attracted remarkable interest in energy storage applications such as fuel cells, electrolyzers, and supercapacitors, due to their relatively low cost and tunable properties [1]. In batteries they play a role of separator, the primary function of which is to keep the positive and negative electrodes apart to prevent electrical short circuits. At the same time, it is expected to allow the rapid transport of ionic charge carriers, needed to operate the batteries [2]. Apart from being a very good electronic insulator and having the capability of conducting ions, the separator should minimize processes that adversely affect the performance or cycle-life of the battery [3].

One of the main shortfalls of lithium sulfur (Li-S) batteries is an irreversible loss of the active material, sulfur, due to the formation of electrolyte-soluble lithium polysulfides. These polysulfides can diffuse in the electrolyte and eventually be reduced at the negative electrode (lithium metal), leading to the fading of the electrochemical performance. Earlier approaches to retard the diffusion of the polysulfides into the electrolyte have focused either on encapsulation of sulfur inside ultrathin ion conducting nano-membranes [4] or on conducting polymer coating on the surface of carbon-sulfur electrodes [5]. Yang et al. [6] demonstrated that poly(styrene sulfonate)-based electrode coating can effectively trap the polysulfides, thus minimizing the loss of active material. Herein we propose to use styrene sulfonate (SS) for the preparation of Li-ion conducting asymmetric polymer separators with S_n^{2-} (n = 4–8) anion barrier functionality. The modification is done onto surface-near-regions of polypropylene (PP), used here as a base polymer which is plasma-activated and grafted with SS only from one side. The grafting kinetics of the studied system as well as the structural changes of PP are shown and discussed here. Moreover, preliminary results on grafting of SS onto plasma-activated Celgard 2400 are also presented.

Experimental

Asymmetric porous membranes (APM) based on porous polypropylene (TreoPore, branched PP, and Celgard 2400, a monolayer PP film) and SS were prepared by plasma-induced graft copolymerization. The details of APM synthesis are given elsewhere [7]. The graft level (GL) was determined gravimetrically. The modified membranes were characterized with ATR-FTIR spectroscopy to determine chemical changes imparted by copolymerization. The morphology of the pristine porous substrates as well as of the grafted membranes was investigated using a scanning electron microscope (SEM) Ultra 55 (Zeiss Germany) at an acceleration voltage of 3 kV.

Results

The kinetics of plasma-induced graft copolymerization of SS onto TreoPore porous polypropylene has been studied (Figure 1). It can be seen that the GL increases gradually with grafting time from ca. 3 % after 2 h up to ca. 40 % after 24 h. In contrast, when Celgard is used as a base polymer, only 1/3 of the aforementioned value found for TreoPore, can be achieved after 24 h of grafting. However, this discrepancy correlates with the morphology of the base films.

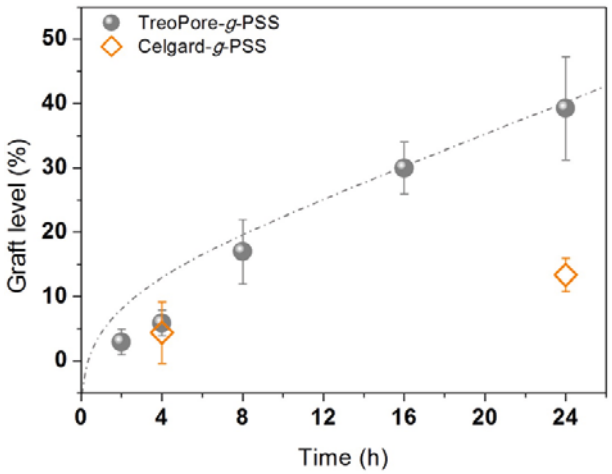

Figure 1: *Grafting kinetics of SS onto porous TreoPore base film (●). Corresponding graft levels of Celgard – based membranes grafted for 4 and 24 h (◇).*

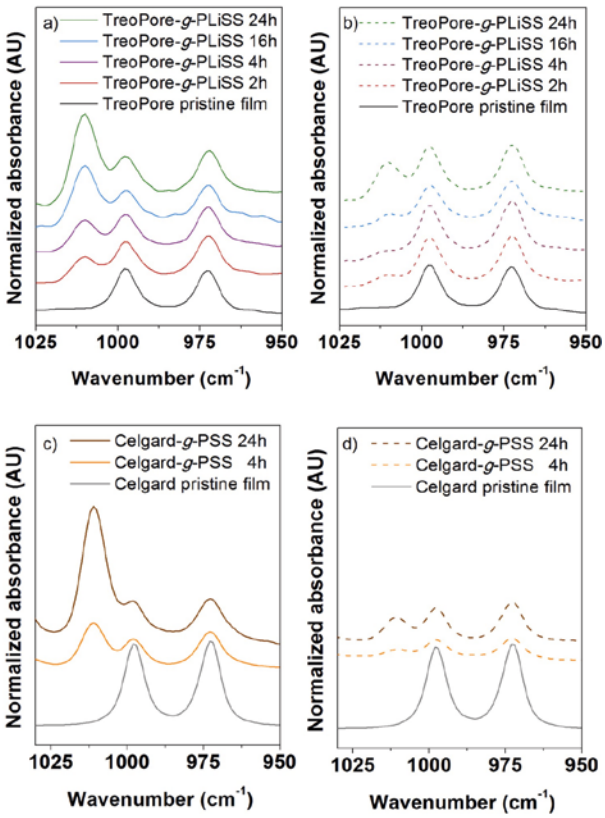

Figure 2: *ATR-FTIR spectra of grafted (a, c) and unmodified side (b, d)) of TreoPore-g-PSS and Celgard-g-PSS, and pristine TreoPore and Celgard, normalized to the PP peak height at 1376 cm^{-1}.*

The presence of the styrene sulfonate groups on the plasma-activated side of the PP films, and thus the asymmetry of obtained membranes, was confirmed by ATR-FTIR spectroscopy. The normalized relevant range of FTIR spectra of TreoPore and Celgard based membranes are shown in Figure 2.The spectral region between 950 and 1030 cm^{-1} contains information about both, the PP base polymers (bands at 973 and 997 cm^{-1}) and the grafted SO_3- groups (band at 1011 cm^{-1}) [8]. The membrane chemistry is changed upon grafting. For both, TreoPore and Celgard, a strong, gradual increase in absorbance with increasing GL is observed on the grafted side at 1011 cm^{-1}. However, in the case of Celgard this peak eventually merges with the PP peak observed at 997 cm^{-1}. This change in the peak shape is not understood so far. On the unmodified side of the PP films, the increase in absorbance at 1011 cm^{-1} is substantially less pronounced, indicating that grafting is indeed highly asymmetric. Nevertheless, after 24 h of grafting the SS monomer signal is visible on both sides of the membrane (TreoPore and Celgard), indicating functionalization throughout the separator. As explained by Yamaguchi et al. [9], one reason for this might be that plasma treatment forms free radicals on the surface of the porous substrate and while the graft copolymerization proceeds, grafted polymer chains grow into the pores of the film. Another interpretation might be that radicals, which are formed on the surface of the substrate, spread through the polypropylene chains. Subsequently, polymer grafts grow from these radicals inside the pores, eventually reaching the unmodified side of the substrate.

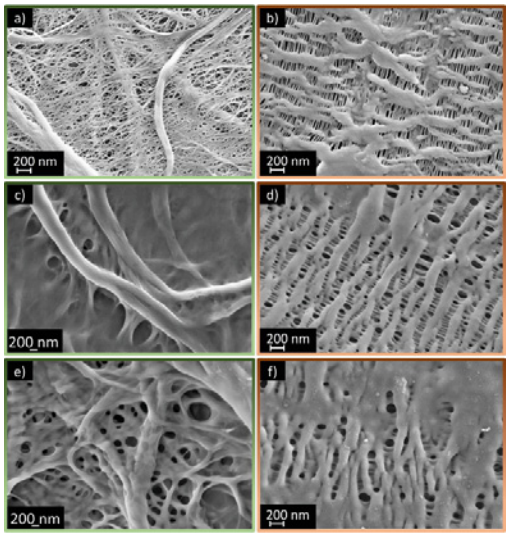

Figure 3: *SEM micrographs of pristine TreoPore (a) and Celgard (b), TreoPore-g-PSS (c, e) and Celgard-g-PSS (d, f) grafted for 24 h. Micrographs c and d show the grafted side of the membrane, whereas its unmodified side is shown in micrographs e and f.*

The tracking of morphological changes induced by grafting was performed by SEM. The PP-g-PSS composites were investigated from both sides (grafted / unmodified side) to assess changes in porosity as a function of the grafting time. A set of PP-g-PSS micrographs is shown in Figure 3 in comparison with the pristine PPs. In the case of the TreoPore, it is clear that as the grafting reaction proceeds, the pores of the films are gradually being closed and the polymer chains («branches») are «knitted» together, creating a random, irregular structure. Eventually, after 24 h of polymerization, the grafted side can be easily identified and distinguished from the unmodified side of the PP film (Figure 3c and e). In the case of Celgard, which is flat and has more regular arrays of pores, there is no clear difference in porosity due to the grafting of SS. Even after 24 h of grafting the morphology of the film does not change significantly (Figure 3d and f). These preliminary results show that the morphology of the substrate may play an important role in the preparation of APM membranes.

Conclusions

SS monomer was successfully grafted onto plasma-activated porous PP, TreoPore and Celgard, with maximum graft yield of ca. 40 % and ca. 13 %, respectively. The asymmetry of the grafted membranes was confirmed by ATR-FTIR and found to be a function of the grafting time and, consequently, graft level. High graft levels of TreoPore result in the loss of the membrane's asymmetry, while Celgard based membranes remain asymmetric even at highest achieved grafting levels.

Acknowledgement

The authors thank the Swiss National Science Foundation (project no 200021_144292) for financial support.

References

[1] M.M. Nasef, R.R. Suppiah, K.Z.M. Dahlan, *Solid State Ionics* **171**, 243–249 (2014).
[2] *Handbook of Battery Materials*, J.O. Besenhard (Ed.), Wiley-VCH, Weinheim, Germany (1999).
[3] A. Pankaj, Z. Zhengming, *Chem. Rev.* **104**, 4419–4462 (2004).
[4] C.B. Bucur, J. Muldoon, A. Lita, J.B. Schlenoff, R.A. Ghostine, S. Dietz, G. Allrede, *Energy Environ. Sci.* **11**, 3286-3290 (2013).
[5] A. Fedorková, R. Orináková, O. Cech, M. Sedlaríková, *Int. J Electrochem. Sci.* **8**, 10308–10319 (2013).
[6] Y. Yang, G. Yu, J.J. Cha, H. Wu, M. Vosgueritchian, Y. Yao, Z. Bao, Y. Cui, *ASC Nano* **5**, 9187–9193 (2011).
[7] J.M. Conder, S. Urbonaite, P. Novák, L. Gubler, *PSI Electrochemistry – Annual Report* **2013**, 39–40, DOI: 10.3929/ethz-a-007047464.
[8] G. Zundel, *Hydration and intermolecular interaction*, Academic Press, New York (1969).
[9] T. Yamaguchi, S. Nakao, S. Kimura, *Macromolecules* **24**, 5522–5527 (1991).

Taming the polysulfide shuttle in the Li-S battery

J. M. Conder, L. Gubler, P. Novák, S. Urbonaite
phone: +41 56 310 2120, e-mail: joanna.conder@psi.ch

The cycle life of the lithium-sulfur (Li-S) battery based on metallic lithium as negative electrode and elemental sulfur as positive electrode is compromised by the dissolution of soluble polysulfide anions (S_n^{2-}, $2 < n < 8$) formed during the cycling of the battery [1]. The reduction of sulfur and thus the formation of S_n^{2-} species proceeds through several steps, each with different intermediate Li_2S_n products (Figure 1). Any of these soluble sulfur-based species in the electrolyte can then diffuse through the separator, reaching the lithium electrode, where they can eventually undergo irreversible reduction to insoluble Li_2S_2 and/or Li_2S [2]. This leads to a permanent loss of the active material and to a severe loss of specific charge with repetitive cycles [1].

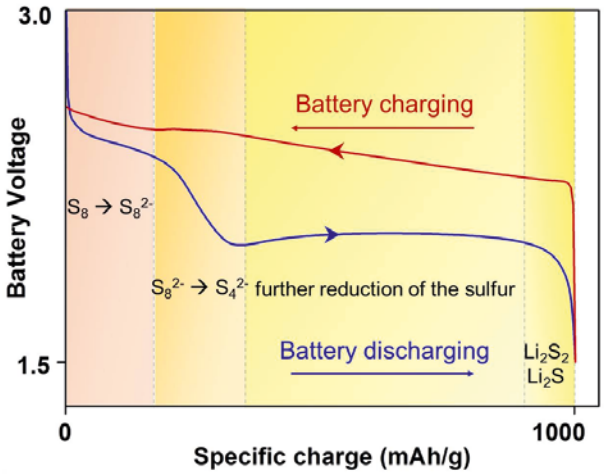

Figure 1: *Typical discharge-charge voltage profile for Li-S battery, adapted from literature [3].*

In an attempt to improve the performance of the Li-S battery, various novel sulfur cathodes and electrolytes have been developed. The influence of the separator however has rarely been considered so far [4]. Therefore, we propose to tackle the limitations of the Li-S battery by designing a Li-ion conducting polymer separator in the form of an asymmetric porous membrane with S_n^{2-} (n = 4–8) anion barrier functionality. The membrane, based on commercial porous polypropylene (PP), consists of two layers. The top, a very thin cation-exchange barrier (polymer skin) suppresses the diffusion of polysulfides and ensures selective Li-ion transport. The bottom porous support layer provides mechanical strength to the polymeric composite. This type of functionalized separator can be obtained by a one-step plasma-induced graft copolymerization of sodium styrene sulfonate (SSS) onto PP film as described elsewhere [5]. Herein we report the polysulfide rejection ability of PP-based membranes, which were tested by exposing samples to a solution of long-chain Li_2S_n ($n \geq 5$) species.

Experimental

Selected PP-based membranes grafted for 4 and 24 h were exchanged to the Li-form by immersion in a saturated aqueous solution of Li_2CO_3 at room temperature for one night. The membranes were subsequently subjected to multi-solvent exchange, evaporation [6], and then vacuum dried. Long-chain lithium polysulfides Li_2S_n ($n \geq 5$) were kindly provided by Bosch GmbH. 1 M LiTFSI in dimethoxyethane (DME) : 1,3-dioxolane (Diox) (2:1 w/w) was used as electrolyte. Nafion 211 and Celgard 2500 were used therein as references for the cation-exchange layer and the porous sublayer, respectively.

The polysulfide-containing solution used in this study was prepared by mixing 0.5 mL of Li_2S_5, Li_2S_6 and Li_2S_7 solutions in tetrahydrofuran (THF) and diluting it (1/10) with the selected electrolyte (1 M LiTFSI in DME : Diox (2:1)). 0.3 mL of this polysulfide mixture was placed inside a glass tube, on top of which the separator was introduced. The glass tube was then turned upside down to wet the separator. This setup was immersed in a vessel filled with the electrolyte (Figure 2). Experiments were performed inside an Ar-filled glove box. To exclude external influences on the diffusion of Li_2S_n species through the separator during the experiment the solutions were maintained without any movement. The resulting color changes were evaluated visually after predefined times.

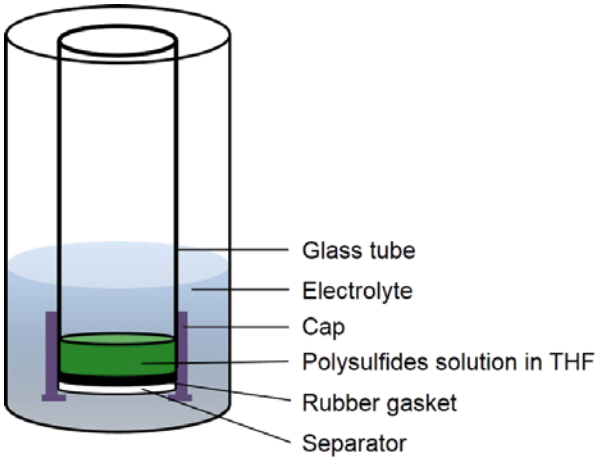

Figure 2: *Experimental setup for polysulfide diffusion tests, adapted from literature [7].*

Results

Figures 3 and 4 show the results of the diffusion experiments for both, the reference materials (Nafion 211 and Celgard 2500) and the selected PP-g-PLiSS polymeric composites. As can be seen in the pictures presented in Figure 3, when a lithiated Nafion 211 is used as a separator, no change in the color of the electrolyte is observed during the course of the experiment. This indicates that the diffusion Li_2S_n through the Nafion is suppressed. However, when Celgard 2500, a monolayer polypropylene separator is introduced, after 30 min of immersion the color of the electrolyte starts to change. It intensifies after further 60 min. Eventually, after 150 min from the beginning of the test, the electrolyte turns to green-brownish solution, all of which indicates that Celgard does not prevent the diffusion of the polysulfides.

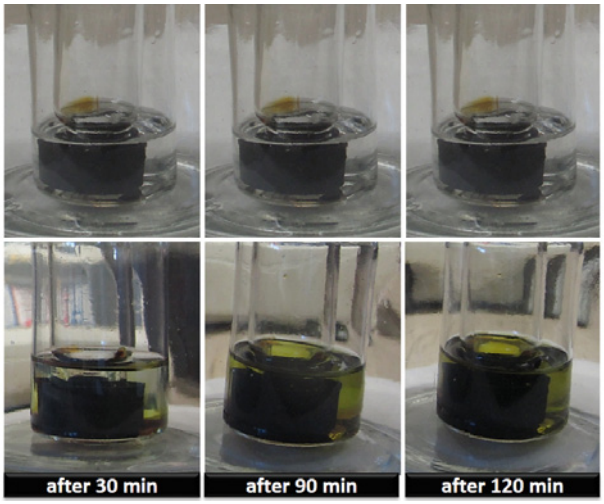

Figure 3: *Polysulfide diffusion test of Li-Nafion 211 (top) and Celgard 2500 (bottom) after various resting times.*

The corresponding results for the selected PP-g-PLiSS samples are shown in Figure 4. Two extreme cases were chosen in order to test their polysulfide rejection ability, namely PP-g-PLiSS grafted for 4 and 24 h, respectively.

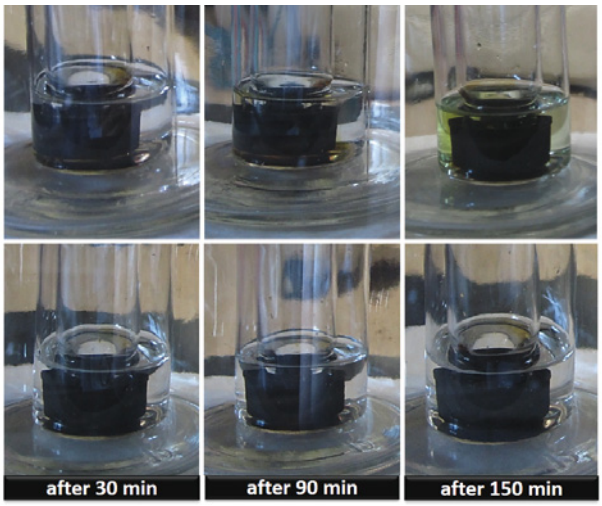

Figure 4: *Polysulfide diffusion tests of PP-g-PLiSS grafted for 4 h (top) and 24 h (bottom) after various resting times.*

With the membrane grafted for only 4 h, no evolution of the color is observed in the electrolyte for 90 min of the test. After that only a faint green coloration arises gradually (Figure 4, top), suggesting that the diffusion of long-chain Li_2S_n species is not completely prevented. This might be attributed to the low GL (~ 6 %) of this membrane and, therefore, to the low concentration of the negative charges (SO_3- groups) in the top layer of the membrane which can reject S_n^{2-} species. With the highly grafted membrane (Figure 4, bottom), no color change is observed even after 150 min from the beginning of the test. Thus, we conclude that a GL » 6 % is required to significantly slow down the polysulfide diffusion through the separator.

Conclusions

The polysulfide rejection ability of the selected PP-g-PLiSS membranes was demonstrated and compared to the reference materials (Nafion 211 and Celgard 2500). It was observed that the modification of the surface-near-regions of the PP separator induces polysulfide rejection ability and thus may have a significant positive influence on the performance of a Li-S battery by mitigating polysulfide reduction at the negative electrode in the Li-S battery.

Acknowledgement

The authors thank the Swiss National Science Foundation (project no 200021_144292) for financial support.

References

[1] M. Barqhamadi, A.S. Best, A.I. Bhatt, A.F. Hollenkamp, M. Musameh, R.J. Rees, T. Rüther, *Energy Environ. Sci.* **7**, 3902–3920 (2014).
[2] G. Xu, B. Ding, J. Pan, P. Nie, L. Shen, X. Zhang, *J. Mater. Chem. A.* **2**, 12662–12676, (2014).
[3] www.gizmag.com/lithium-sulfur-battery-energy-density/29907/.
[4] H. Yao, K. Yan, W. Li, G. Zheng, D. Kong, Z.W. Seh, Y.K. Narasimhan, Z. Liang, Y. Cui, *Energy Environ. Sci.* **7**, 3381–3390 (2014).
[5] J.M. Conder, S. Urbonaite, P. Novak, L. Gubler, *PSI Electrochemistry Laboratory – Annual Report* **2013**, 39–40, DOI: 10.3929/ethz-a-007047464 (2013).
[6] T.E. Davis, D.C. Overmann III, US Patent No 4,430,807, (1984).
[7] I. Bauer, S. Thieme, J. Brückner, H. Althues, S. Kaskel, *J. Power Sources* **251**, 417–422 (2014).

Cycling protocol optimization for low electrolyte-to-sulfur ratio Li-S cells

T. Poux, P. Novák, S. Urbonaite
phone: +41 56 310 3792, e-mail: tiphaine.poux@psi.ch

The lithium-sulfur (Li-S) battery is a promising electro-chemical system for next generation energy applications due to S abundance, its low toxicity, and its high theoretical specific charge (1672 mA/g_{sulfur}). Its commercialization is hampered by several challenges: the so-called polysulfide shuttle leads to a loss of active material and results in a low coulombic efficiency. This effect can be minimized by decreasing the amount of electrolyte in the cell [1, 2]. Low electrolyte amount is also of interest for industrial applications as it increases energy density of the battery. High S loadings are required as well for achieving high energy density, but it results in low cycle life when low electrolyte to sulfur ratio is used [2, 3]. How can high specific charge be obtained with Li-S cells?

Experimental

Electrodes were prepared by mixing 60 wt% sulfur, 30 wt% Super P carbon and 10 wt% polyethylene oxide (PEO) binder by turbo stirring using acetonitrile as a solvent. The resulting slurry was doctor-bladed on a carbon-coated aluminum foil. After drying at room temperature for 24 h, the electrodes were assembled into the cells with Celgard 2400 as separator, metallic Li as counter electrode and 30 µL of electrolyte containing 1 M lithium bis(trifluoromethane sulfone)imide (LiTFSI) in dimethoxyethane : 1,3-dioxolane (2 : 1). The S loading was ~3 mg per electrode (2.3 mg_{sulfur}/cm^2), which corresponds to a ratio of ca. 10 $mL_{electrolyte}/g_{sulfur}$.

Results

Cells with low electrolyte to S ratio are fading very fast, when galvanostatically cycled at a C/5 rate (1C defined as I = 1672 mA/g_{sulfur}) between 1.8 and 2.7 V vs. Li^+/Li. Specific charge of only 200 mAh/g is remaining after the 3rd cycle (Figure 1, green symbols), due to the disappearance of the lower discharge plateau on the galvanostatic profile (not shown).

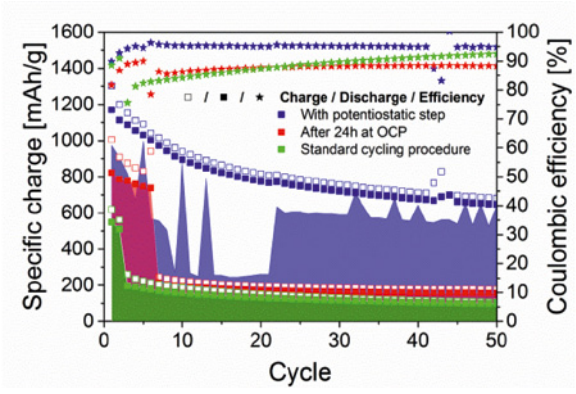

Figure 1: *Total specific charge (squares), coulombic efficiency (stars) and galvanostatic charge (filled area) of Li-S cells with 10 $mL_{electrolyte}/g_{sulfur}$.*

Insufficient wetting of separator and electrode as a possible origin of rapid specific charge fading: In order to wet all the cell components well, some cells were kept at open circuit potential for 24 h before cycling. It was found that failure is not related to poor wetting, as they displayed reasonable specific charge for the very first cycles (Figure 1, red symbols), and then still deteriorated rather quickly.

Incomplete discharge as another possible reason for the specific charge fading: The potential of the Li-S cells was thus kept at 1.8 V for 5 h after each discharge (potentiostatic step). The cell was then charged without potentiostatic step. From the cycling performance (Figure 1, blue symbols), one can see that higher specific charge is reached due to the potentiostatic step, and stays at about 650 mAh/g for 50 cycles. Moreover, the coulombic efficiency is as high as 95 %, showing very little effect of the polysulfide shuttle.

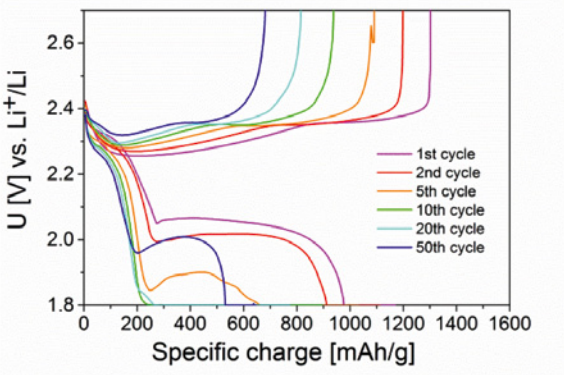

Figure 2: *Galvanostatic profiles of a Li-S cell with 10 $mL_{electrolyte}/g_{sulfur}$ cycled with potentiostatic step.*

The galvanostatic profiles presented in Figure 2 (cell cycled with potentiostatic steps) show that the lower discharge plateau disappears after some cycles due to high overpotential and slow kinetics. Keeping the potential at 1.8 V allows diffusion of the species in the electrode and a better utilization of the S, and therefore to higher specific charge. After ca. 20 cycles, the lower plateau reappears (Figure 2), leading to the higher contribution of the galvanostatic charge to the total specific charge (Figure 1, blue area).

Conclusion

This work demonstrates that the strong fading observed for cells with low electrolyte to S ratio could be minimized using a potentiostatic step at the end of the discharge. Indeed, keeping the potential at 1.8 V helps reaching high specific charge by completing the reaction of the lower plateau. This shows the beneficial effect of complete discharge on the cycle life.

Acknowledgement

BASF SE is acknowledged for financial support.

References

[1] S. Urbonaite, P. Novák, *J. Power Sources* **249**, 497–502 (2014).
[2] J. Zheng, D. Lv, M. Gu, C. Wang, J.G. Zhang, J. Liu, J. Xia, *J. Electrochem. Soc.* **160** (11), A2288–A2292 (2013).
[3] N. Ding, S.W. Chien, T.S.A. Hor, Z. Liu, Y. Zong, *J. Power Sources* **269**, 111–116 (2014).

Silicon, graphite and PVA-based carbon composites for high performance electrodes

T. Poux, J.L. Gómez-Cámer, D. Cericola[1], T. Hucke[1], M. E. Spahr[1], P. Novák
phone: +41 56 310 3792, e-mail: tiphaine.poux@psi.ch

Thanks to its low reaction potential and its impressive performance stability, graphite is the most common negative material for lithium-ion batteries. However, its specific charge of 372 mAh/g is rather low for high energy applications. One promising candidate to partially replace graphite in negative electrodes is silicon which offers a specific charge of 3579 mAh/g and whose reactions occur in a similar potential window than graphite. By simply mixing graphite with a small amount of silicon, high specific charge could already be obtained [1]. However, silicon-based electrodes suffer from strong performance fading upon cycling due to significant volume expansion and shrinkage of silicon during lithiation and delithiation processes. An advanced approach to increase the life time of the silicon-based electrodes is the milling of silicon with a carbon source followed by the carbonization of the carbon source [2]. Indeed, thanks to this route, silicon is well dispersed in a carbon matrix which can buffer the volume changes.

In this work, two composites were prepared via this synthesis route. The Si/graphite/C composite contains a high amount of graphite (94 wt% in the composite) and a small amount of silicon (5 wt%). The Si/C composite contains 50 wt% of silicon and 50 wt% of carbon to allow a sufficient coverage of the silicon by the carbon matrix. It is used as an additive to graphite. The composites were characterized and their performance is compared to the simple mixture of graphite and silicon, and to graphite alone [1].

Experimental

Polyvinyl alcohol (PVA) was chosen as carbon source. Its carbon yield was measured to be ca. 0.1. PVA (Fluka), silicon (30–50 nm, Nanostructured & Amorphous Materials), and graphite (TIMREX® KS6, IMERYS) for Si/graphite/C composites, were placed in stainless steel ballmilling boxes with stainless steel balls of 10 mm diameter (powder : balls, 1 : 10). Tetrahydrofuran (THF, anhydrous ≥ 99.9 %, Sigma-Aldrich) solvent (powder : THF, 1 : 5) was added to avoid high temperature during the ball milling. The ballmilling rotation speed was 450 rpm to allow good dispersion without breaking the graphite flakes. The mixture was ballmilled for 2 h and was then carbonised in a tubular oven in argon flow. The carbonisation procedure was inspired from the synthesis optimization of Guo et al. [3]. It consists of a heating rate at 5 °C/min and a plateau at 800 °C for 2 h. After cooling, the obtained material was ground in a mortar to get a fine powder.

Electrodes were made from these composites. For that, a mixture of carboxymethyl cellulose (CMC, Alfa Aesar) and polyacrylic acid (PAA, 25 wt% sol. in H_2O, average M.W. 240.000, Alfa Aesar) was dissolved in water. Then, Si/C composite and graphite powder were mixed with the binder for the Si/C-based electrodes, while for Si/graphite/C-based electrodes, the Si/graphite/C composite was stirred with the binder without additional components. The slurries were cast onto copper foil and heated at 150 °C under vacuum for 2 h in order to favor the cross-linking reaction between CMC and PAA. The final compositions of the electrodes were: 96 wt% Si/graphite/C, 4 wt% CMC/PAA, and 10 wt% Si/C, 82 wt% graphite, 8 wt% CMC/PAA (higher relative amount of binder was used with the Si/C composite due to expected higher surface area). For comparison, electrodes of simple mixture of Si and graphite (5 wt% Si, 90 wt% graphite, 1 wt% carbon additive (SuperC65, IMERYS), 4 wt% CMC/PAA) and of graphite alone (95 wt% graphite, 1 wt% carbon additive, 4 wt% CMC/PAA) were prepared. After drying at 120 °C under vacuum, the electrodes were assembled into the cells with glass fiber separator, metallic lithium counter electrode and 500 µL of electrolyte (1 M $LiPF_6$ in ethylene carbonate (EC) / dimethyl carbonate (DMC) (1 : 1)). The cycling procedure was a constant current (50 mA/$g_{a.m.}$) constant voltage (5 mV vs. Li^+/Li for lithiation, 1.5 V for delithiation) technique, after a first cycle at 20 mA/g for the solid electrolyte interphase (SEI) formation.

Results

The composition and structure of the composites were studied by X-Ray diffraction (XRD) (Figure 1). The XRD pattern of the Si/C composite presents the typical peaks of silicon and a shoulder at ca. 25° due to the presence of amorphous carbon. No peaks corresponding to graphite can be observed for this composite, as expected. For the Si/graphite/C composite, small peaks of silicon are also present on the pattern together with strong peaks of graphite. The latter peaks are not shifted compared to the pristine graphite, suggesting that the graphite is not modified in the composites. No unexpected phases, such as SiC, could be observed.

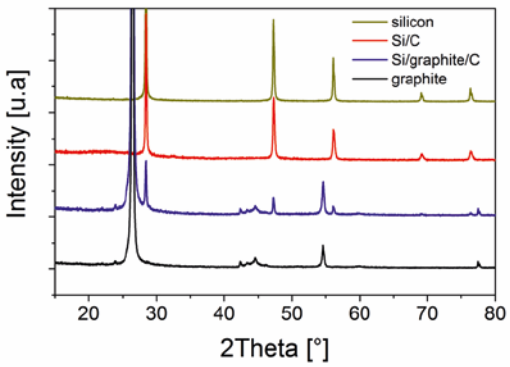

Figure 1: *XRD pattern of Si/graphite/C and Si/C composites compared to pristine material.*

Then, the morphology and dispersion of the composites in the electrodes were analyzed by scanning electron microscopy (SEM). The electrodes made of Si/graphite/C composite show a homogeneous dispersion of silicon nanoparticles and graphite flakes with only some silicon agglomerates (Figure 2 a). However, the Si/C composite (Figure 2 b) is not well dispersed with the graphite flakes in the electrodes made from this composite, but agglomerated in micrometric agglomerates of silicon and amorphous carbon.

[1] IMERYS Graphite & Carbon, Bodio

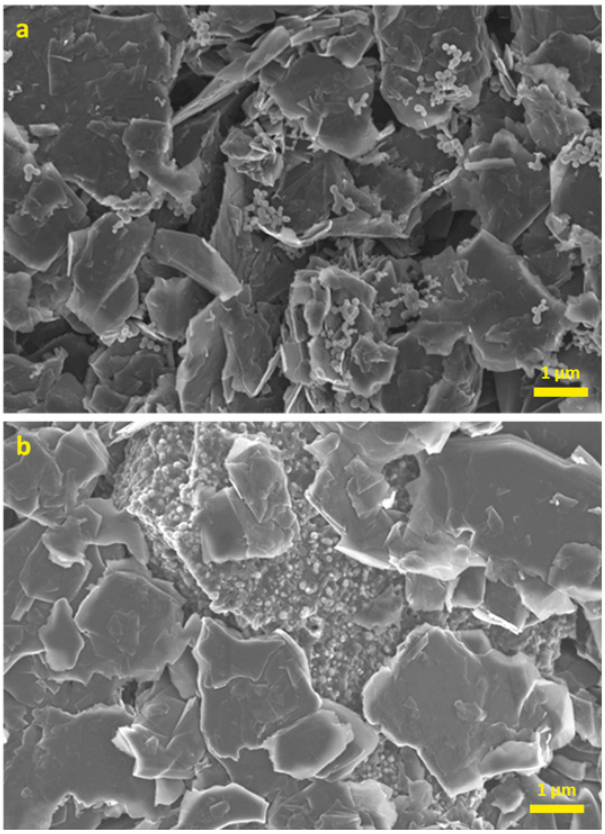

Figure 2: *SEM images of electrodes made of (a) Si/graphite/C and (b) Si/C composites.*

The electrochemical performance of these composites was then studied and compared to simple mixture and graphite electrodes (Figure 3). During the first cycles, the specific charge of the composite electrodes is lower than expected. Indeed, 541 mAh/g can be expected theoretically for Si/graphite/C and 556 mAh/g for Si/C composites. This might result from overestimation of the active material content or poor silicon utilization in the composite. The latter is probably true for the Si/C composite which is very badly dispersed into the graphite electrode (Figure 2 b). Nevertheless, the specific charge with only 5 wt% of silicon is ca. 40 % higher than that of graphite electrodes.

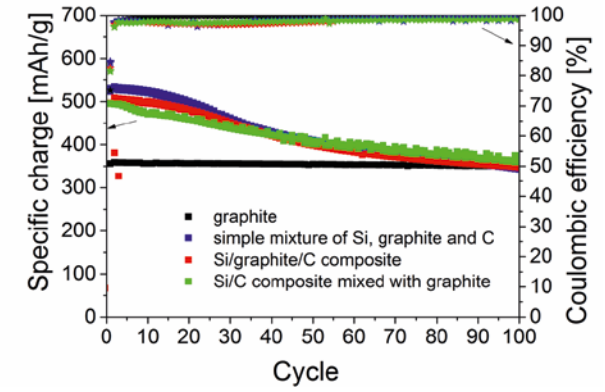

Figure 3: *Cycle dependence of the specific charge (squares) and coulombic efficiency (stars) of electrodes made from Si/graphite/C and Si/C composites compared to simple mixture and graphite electrodes.*

The coulombic efficiency of the first cycle is lower for the composite (ca. 79 %) than for simple mixture electrodes (ca. 84 %). This may be due to an increase of the exposed surface area due to ballmilling, which leads to more SEI formation. During the following cycles, high efficiency is reached and the loss of specific charge per cycle seems to be lower for composite than for simple mixture electrodes. Despite its inhomogeneous dispersion (Figure 2 b), the Si/C-based electrodes have a loss between the 2nd and the 50th cycle of ca. 18 % while simple mixture electrodes present a loss of 24 %.

Conclusions and outlook

Silicon composites were obtained by ballmilling of the silicon with a carbon source, followed by its carbonisation. The expected phases were obtained with this synthesis. It was observed by SEM that Si/graphite/C composites are well dispersed in the electrodes while Si/C composites are locally agglomerated and not well mixed with the additional graphite. The low specific charge obtained during the first cycles of the composite electrodes suggests a poor utilization of the silicon. Despite this, the composite electrodes display promising performance stability.

Further optimization of the composite electrodes will be performed. To increase the silicon utilization, carbon additive can be added to the slurry preparation. Also, a ballmilling step after the carbonisation can be useful to reduce the agglomerate size. Other carbon sources and other carbonization procedures will also be investigated to tune the silicon composite properties.

Acknowledgement

IMERYS Graphite & Carbon is acknowledged for financial support.

References

[1] C. Bünzli, D. Cericola, T. Hucke, M.E. Spahr, P. Novák, J.L. Gómez-Cámer, *PSI Electrochemistry Laboratory – Annual Report* **2013**, 35–36 (2013).

[2] B.C. Kim, H. Uono, T. Sato, T. Fuse, T. Ishiara, M. Senna, *Solid State Ionics* **172**, 33–37 (2004).

[3] Z.P. Guo, D.Z. Jia, L. Yuan, H.K. Liu, *J. Power Sources* **159**, 332–335 (2006).

Lithium iron methylene diphosphonate, a new organic-inorganic hybrid active material for Li-ion batteries

S. Schmidt, C. Villevieille, P. Novák, S. Sallard
phone: +41 56 310 5762, e-mail: sebastian.schmidt@psi.ch

Li-ion batteries are nowadays one of the most important applied electrochemical energy storage systems, especially for portable consumer electronics.

In the last decades, numerous materials have been investigated to improve Li-ion batteries in terms of energy density or to overcome safety issues [1]. For the positive electrode, the research focus lies mainly on inorganic substances such as transition metal oxides and metal phosphates [2]. Purely organic materials such as benzoquinones have been proven to cycle Li^+ reversibly yielding a high specific charge at a reasonable potential, however with low stability [3].

A combination of organic-inorganic hybrid materials could therefore lead to a new class of electrodes combining the stability of inorganic materials with the high specific charge of organic materials. A quasi-infinite number of synthetic possibilities can arise due to an interchangeable organic component R. Very few examples of organic-inorganic hybrid positive electrode materials have been reported in the literature so far [4].

We investigate diphosphonates as they carry two phosphonic acid groups on the organic component, which can act as ligands to the metal ions. Additionally, the structural proximity allows a comparison to the fully inorganic pyrophosphates (Figure 1). As a first reference material, lithium iron methylene diphosphonate was chosen for electrochemical characterization.

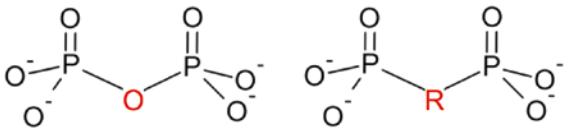

Figure 1: *Comparison of a pyrophosphate anion (left) and a diphosphonate anion (right). R describes any organic component.*

Experimental

Lithium iron methylene diphosphonate was synthesized by a hydrothermal route.

X-ray powder diffraction (XRD) was measured at the MS-powder beamline at SLS using a wavelength of 0.7082 Å. Scanning electron microscopy (SEM) was performed on a Zeiss Ultra55 SmartSEM electron microscope. The Fourier transform infrared (FTIR) spectra were measured on a Perkin Elmer 2000 infrared spectrometer. Galvanostatic cycling was performed in in-house built electrochemical cells in a half-cell system, using LP30 as electrolyte in a potential window of 1.5 V – 4.5 V vs. Li^+/Li. The working electrodes were prepared by doctor-blading a slurry based on 50 wt% active material, 40 wt% Super C65 carbon black and 10 wt% PVdF binder on aluminum foil.

Results

Powder X-ray diffraction indicated that lithium iron methylene diphosphonate crystallizes in a new, monoclinic phase never described in the literature so far. The presence of the O=P-C functionalities in the product originating from the diphosphonate was confirmed by FTIR (Figure 2).

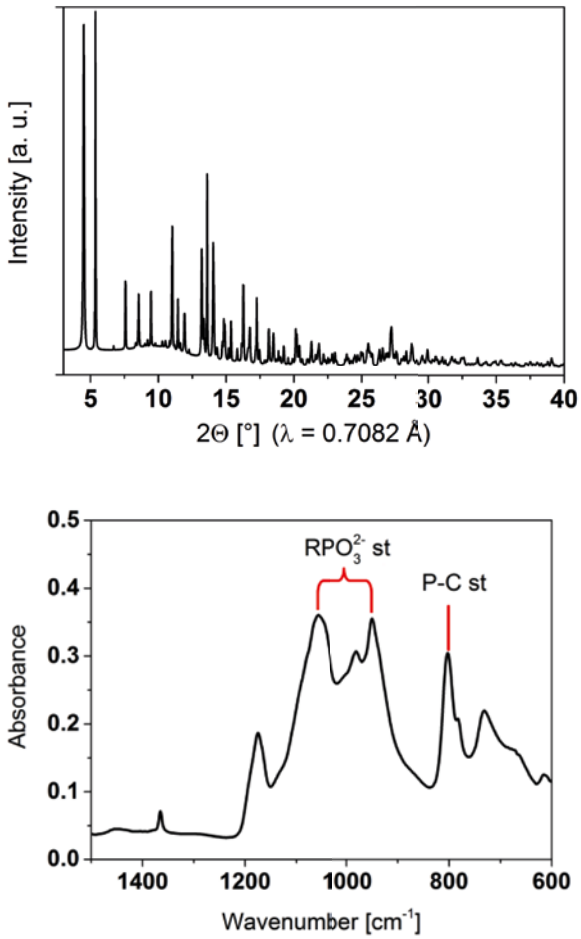

Figure 2: *Top: XRD powder pattern of lithium iron methylene diphosphonate. Bottom: FTIR spectrum of lithium iron methylene diphosphonate.*

Investigations by scanning electron microscopy showed thin platelets, which aggregate in larger clusters. A small amount of spherical impurities could also be observed. They consist mainly of carbon, according to energy-dispersive X-ray spectroscopy (Figure 3).

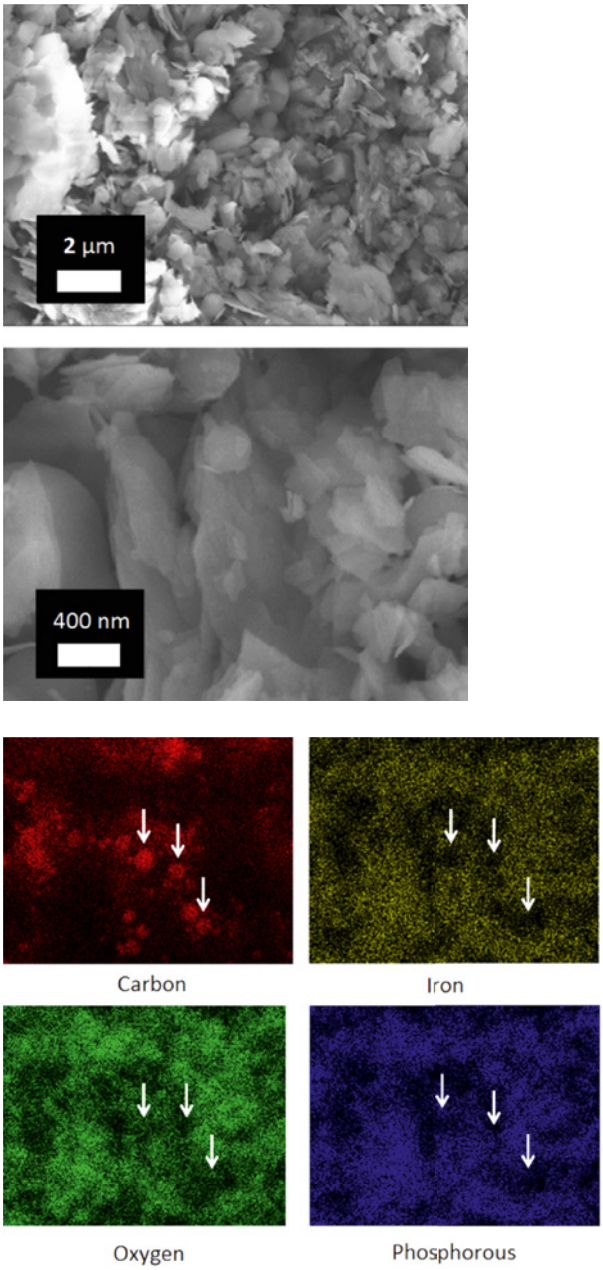

Figure 3: *Top: SEM images of lithium iron methylene diphosphonate. Bottom: EDX elemental mapping of lithium iron methylene diphosphonate showing the agglomeration of C and depletion of the other elements in the spherical impurities indicated by the white arrows.*

Galvanostatic cycling performed at a C/20 rate showed some evolution in the potential which stabilized after 20 cycles, yielding a stable specific charge of 90 mAh/g during 100 cycles. This is close to the theoretical specific charge (110 mAh/g). The potential profile however exhibits a large overpotential, which is slightly lower after the first 20 cycles. During the first delithiation, a large irreversible specific charge is obtained, which can come from

- the electrolyte decomposition,
- an activation step, and/or
- the decomposition of the carbon-based impurities (Figure 4).

Ex situ FTIR investigations performed on an electrode cycled for 40 cycles showed the presence of the O=P-C functionalities, providing a first hint that the organic component is stable during cycling (Figure 5).

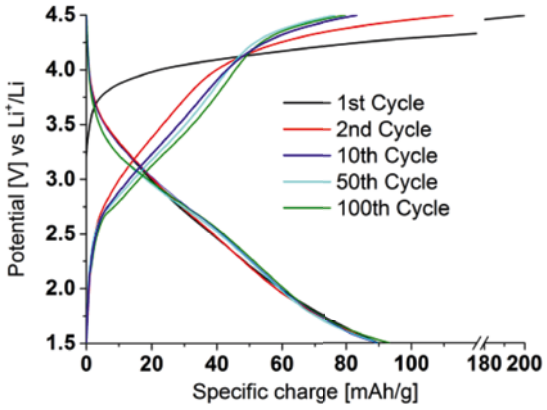

Figure 4: *Galvanostatic cycling curves of lithium iron methylene diphosphonate at C/20 rate.*

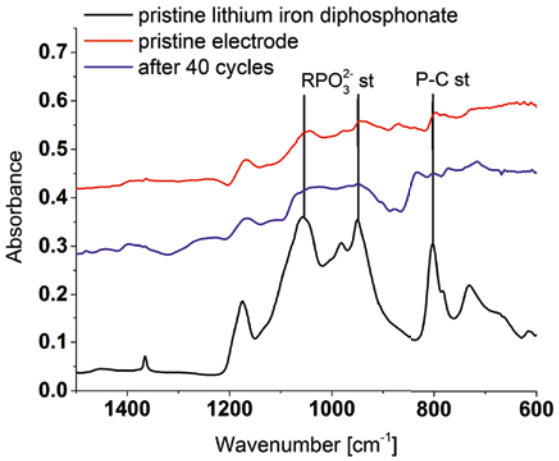

Figure 5: *Ex situ FTIR spectrum of lithium iron methylene diphosphonate after 40 cycles compared to the powder and a pristine electrode.*

Conclusions

Lithium iron diphosphonate was successfully synthesized and electrochemically tested yielding a specific charge close to the theoretical value. The stability of the organic P-C bonds was verified by *ex situ* FTIR.

Acknowledgement

The authors would like to express their gratitude to SNF for funding (project 200021_146224) and to Dr. Nicola Casati from the MS-powder beamline at SLS for experimental support.

References

[1] V. Etacheri, R. Marom, R. Elazari, G. Salitra, D. Aurbach, *Energy Environ. Sci.* **4**, 3243–3262 (2011).
[2] J.W. Fergus, *J. Power Sources* **195**, 939–954 (2010).
[3] H. Chen, M. Armand, G. Demailly, F. Dolhem, P. Poizot, J.M. Tarascon, *ChemSusChem* **1**, 348–355 (2008).
[4] G. Férey, F. Millange, M. Morcrette, C. Serre, M.L. Doublet, J.M. Grenèche, J.M. Tarascon, *Angew. Chem. Int. Ed.* **46**, 3259–3263 (2007).

$LiCrP_2O_7$/C as new insertion material for Li-ion batteries

M. Reichardt, C. Villevieille, P. Novák, S. Sallard
phone: +41 56 310 5850, e-mail: martin.reichardt@psi.ch

Li-ion batteries are nowadays massively used for mobile electronic devices like smartphones or notebooks. However, higher energy density of the batteries is required especially for the development of the electrical mobility.

Most of the cathode materials, e.g., $LiFePO_4$ and $LiCoO_2$, used in commercial Li-ion batteries involve only one electron exchange reaction (and consequently one Li^+) per metal atom, for example Fe^{3+}/Fe^{2+} or Co^{4+}/Co^{3+}. This results in a relatively low specific charge which has a direct influence on the energy density of the battery.

Chromium compounds present stable oxidation states from +2 to +6. It is then possible, in theory, to overcome the one-electron limitation and to obtain high specific charge with Cr-based polyanion materials Li_yCrX (X as anionic part) [1]; but only a few electrochemical investigations have been reported so far [2, 3].

The lithium chromium pyrophosphate $LiCrP_2O_7$ was chosen for a proof of concept of Cr-based polyanions used as insertion materials in Li-ion batteries, since its structure is known and preliminary studies proved that $LiCrP_2O_7$ possesses an electrochemical activity [3].

Experimental

$LiCrP_2O_7$ was first synthesized by a solid state route [4]. A second synthesis route based on the sol-gel chemistry was used to produce an *in situ* carbon coated $LiCrP_2O_7$/C [3] (approx. 6 wt% carbon – measured by weight loss with O_2-TGA).

The precursors for the sol-gel synthesis were $Li(CH_3COO)_2H_2O$ (Alfa Aesar), $Cr_3(CH_3COO)_7(OH)_2$ (Sigma-Aldrich), $NH_4H_2PO_4$ (Alfa Aesar) acrylamide (Fluka) and citric acid (Sigma-Aldrich) in molar ratio 3 : 1 : 6 in demineralized water. The solution was degassed with argon and heated to 80 °C for 6 h. The gel was dried at 160 °C for 12 h and calcined in 2 steps, at 300 °C for 6 h under air and then under argon at 800 °C for 5 h. After each step, the material was ground carefully to homogenize the powder. Before the electrode preparation, the material was ball milled.

Scanning electron microscopy (SEM) measurements were done on a Carl Zeiss Ultra 55 microscope. X-Ray diffraction (XRD) experiments were performed with a PANalytical Empyrean diffractometer using Cu-Kα radiation. Operando measurements were performed using an *in situ* XRD cell.

Electrodes for cyclic voltammetry have been prepared by mixing the components with following ratio: 50 wt% $LiCrP_2O_7$/C: 50 wt% SuperC65 (TIMCAL), the total electrode mass was 40 mg in a test cell.

Galvanostatic cycling: Composite electrode consisting of 50 wt% $LiCrP_2O_7$/C, 40 wt% SuperC65 (TIMCAL) and 10 wt% PVDF (Kynar Polymer, Solvay) plus using NMP for mixing the components forming a slurry. Self-standing electrode for operando XRD measurements consist of 70 wt% $LiCrP_2O_7$/C 20 wt% PVDF (Kynar Flex, Solvay) and 10 wt% SuperC65 (TIMCAL).

All measurements were done using 1 M $LiPF_6$ in EC:DMC 1:1 wt. as electrolyte.

Results

The XRD pattern of the material obtained by the sol-gel synthesis (Figure 1) corresponds to the one of the $LiCrP_2O_7$ reference. As can be seen the material is rather amorphous with broad peaks; however the peaks can be indexed in the reference pattern.

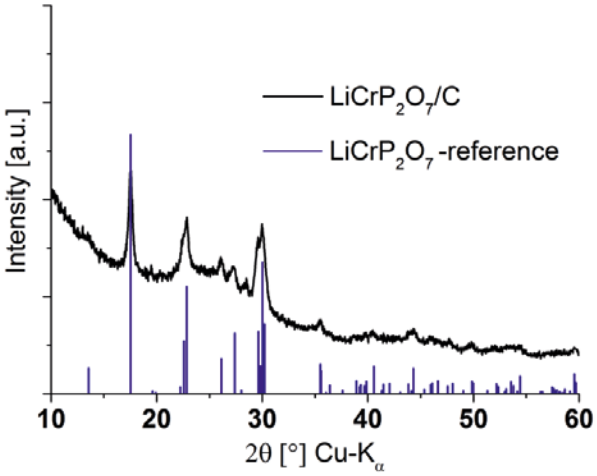

Figure 1: *XRD of $LiCrP_2O_7$/C after calcination under Ar-atmosphere at 800°C; reference no. 01-076-9862.*

The SEM images of the freshly synthesized $LiCrP_2O_7$/C show a particle size distribution exceeding 10 µm. After ball milling the average size decreases to around 1–3 µm. The influence of the particle morphology of the $LiCrP_2O_7$/C is important as the practical specific charge of the material can be doubled after ball milling (data not shown). This phenomenon is probably caused by low conductivity of the polyanion materials, which is planned to be verified by 4-probes conductivity measurements.

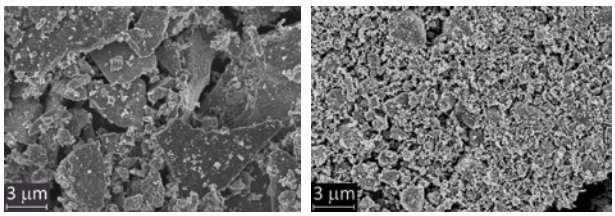

Figure 2: *SEM images of the $LiCrP_2O_7$/C material before and after ball milling.*

Note that the $LiCrP_2O_7$ synthesized by solid state route presents a well-defined crystallinity. However, its specific charge is even lower (< 20 mAh/g) even after ball milling. It is attributed to the absence of carbon coating and average particle size > 10 µm.

The $LiCrP_2O_7$/C shows a reversible electrochemical activity at 1.8 and 2.25 V vs. Li^+/Li for reduction and oxidation, respectively. This activity is assumed as the Cr^{3+}/Cr^{2+} redox couple (Figure 3) in agreement with DFT calculation [1]. The second redox couple, Cr^{4+}/Cr^{3+}, is expected to be at a potential above 5.0 V vs. Li^+/Li, however it cannot be observed with the present cell set-up due to the electrolyte decomposition at such high potentials.

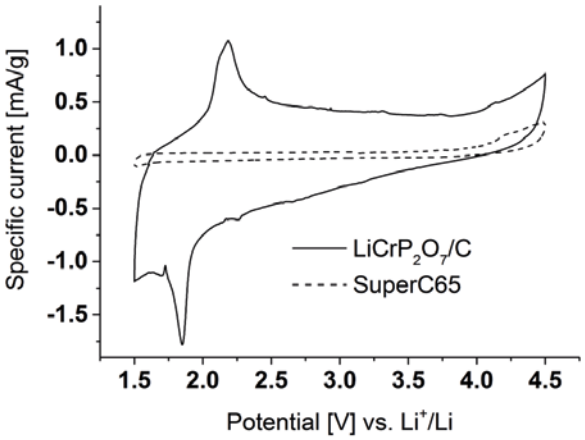

Figure 3: *Cyclic voltammetry of ball-milled $LiCrP_2O_7$/C in the potential range of 1.5–4.5 V vs. Li^+/Li; scan rate 5 µV/s.*

Long term cycling in galvanostatic mode (Figure 4) shows an initial specific charge of 70–80 mAh/g. During cycling the specific charge is increasing to reach ≈ 105 mAh/g after 100 cycles with a coulombic efficiency of 96 %.

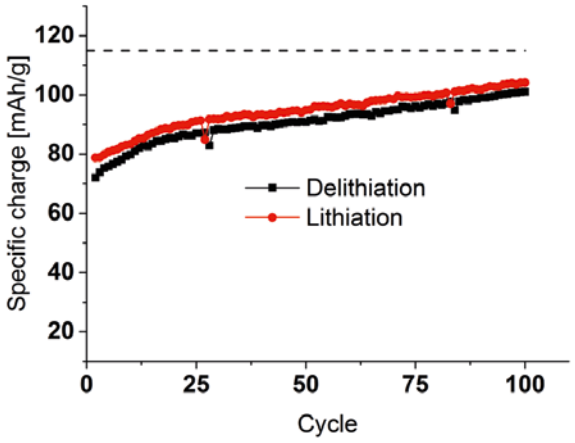

Figure 4: *Galvanostatic cycling of $LiCrP_2O_7$/C between 1.5–4.5 V vs. Li^+/Li at C/5 rate – 23 mA/g. The dash line at 115 mAh/g represents the theoretical specific charge for 1 electron exchange per formula unit.*

In order to investigate the electrochemical mechanism of the $LiCrP_2O_7$/C reduction/oxidation, *ex situ* XRD measurements at different charge states of lithiation/delithiation were performed. Unfortunately, probably due to relaxation of the material, no significant changes in the structure could be observed compared to the pristine material. Consequently, an operando XRD measurement was performed (Figure 5).

During the lithiation step, the main peaks of the phase are slightly shifted to lower angles until the potential reaches 1.8 V vs. Li^+/Li. When reaching the assumed Cr^{3+} reduction potential at 1.8 V vs. Li^+/Li (reduction peak, see Figure 3) [1], the diffraction peaks almost vanish. During the delithiation step, when reaching 2.25 V vs. Li^+/Li (oxidation peak, see Figure 3), the intensity of the XRD pattern is back to the pristine one. Note that the reflex of the Al-window stays constant.

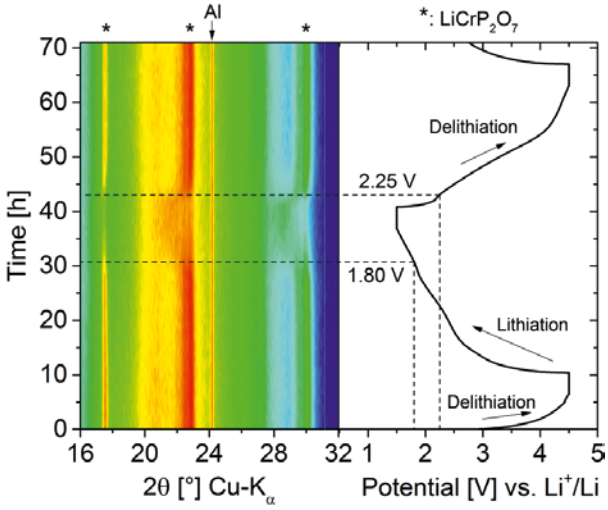

Figure 5: *Operando XRD of $LiCrP_2O_7$/C in the potential range of 1.5–4.5 V vs. Li^+/Li at a cycling rate of C/30. XRD pattern was recorded within 1 h; 2θ 16°–32°.*

These results are a proof for reversible structural changes in the $LiCrP_2O_7$/C during the lithiation and delithiation process. Unfortunately, XRD is not really sensitive for the light elements like Li and limits the accuracy of the data refinement. Due to the reversible change of the structure, in agreement with the electrochemistry and in accordance with theoretical calculations, these results seem to proof the concept of an insertion mechanism for the Cr^{3+}/Cr^{2+} redox couple.

Conclusion

We synthesized $LiCrP_2O_7$/C material by sol-gel chemistry. After reducing the particle's size by ball milling below 10 µm, the specific charge of the $LiCrP_2O_7$/C can reach a stable value of 105 mAh/g close to the theoretical one. The Cr^{3+}/Cr^{2+} redox couple activity is assumed to be between 1.8 and 2.25 V vs. Li^+/Li. Operando XRD measurements show a reversible structural change during litihation and delithiation in the same potential range and agree with a Li-ion insertion mechanism.

References

[1] G. Hautier, A. Jain, T. Mueller, C. Moore, S. Ping Ong, G. Ceder, *Chem. Mater.* **25** (10), 2064–2074 (2013).
[2] M. Herklotz, F. Scheiba, R. Glaum, E. Mosymow, S. Oswald, J. Eckert, H. Ehrenberg, *Electrochim. Acta* **139**, 356–364 (2014).
[3] G. Babu, D. Bhuvaneswari, N. Kalaiselvi, N. Jayaprakash, P. Periasamy, *J. Sol-Gel Sci. Technol.* **49**, 137–144 (2009).
[4] L.S. Ivashkevich, K.A. Selevich, A.I. Lesnikovich, A.F. Selevich, *Acta Crystallogr. Sect. E* **63**, 70–72 (2007).

Cycling-related factors influencing electrolyte (de-)composition in an EC/EMC binary solvent based battery system

H.-J. Peng, C. Villevieille, S. Urbonaite, H. Wolf[1], K. Leitner[1], P. Novák
phone: +41 56 310 5737, e-mail: hai-jung.peng@psi.ch

In order to improve the performance of battery systems, it is essential to understand the origin of degradation that impedes its advance. One of the key issues which rule the cycle life and capacity retention of a battery is electrolyte stability against both positive and negative electrodes. It plays an important role in particular when electrode materials, which are operated at high potential (> 4.5 V vs. Li^+/Li) such as lithium-rich nickel cobalt manganese oxide (called hereafter HE-NCM) and lithium manganese nickel oxide, are used to gain higher specific energy [1]. Ethylene carbonate (EC) / ethyl methyl carbonate (EMC) is one of the most commonly used binary solvent systems for lithium ion battery electrolyte. It has been reported in the literature [2, 3] that EMC undergoes transesterification reaction during cycling to form diethyl carbonate (DEC) and dimethyl carbonate (DMC) as shown in the following equation:

$$2\ CH_3OCO_2C_2H_5\ (EMC) \leftrightarrow CH_3OCO_2CH_3\ (DMC) + C_2H_5OCO_2C_2H_5\ (DEC)$$

It has also been demonstrated that by using electrolyte additive (e.g., vinylene carbonate (VC) [4]) such reactions are suppressed. However, the link between transesterification reaction and electrochemical performance degradation is still obscure. Aiming at shedding some light on this, it is therefore necessary to understand the parameters that influence electrolyte composition during cycling.

Experimental

NCM111 ($Li_{1.05}(Ni_{0.33}Co_{0.33}Mn_{0.33})_{0.95}O_2$),
NCM523 ($Li_{1.03}(Ni_{0.50}Co_{0.20}Mn_{0.30})_{0.97}O_2$), and
HE-NCM ($Li_{1.17}(Ni_{0.22}Co_{0.12}Mn_{0.66})_{0.83}O_2$) electrodes containing 93 wt%, 93 wt%, and 88 wt% of active material, respectively, were cycled either against lithium or graphite anode with LP57 (1 M $LiPF_6$ in EC:EMC=3:7 wt%) electrolyte and glass fibre separator. Typical cycling conditions are summarized in Table 1. After 100 cycles, the cells were disassembled and the electrolyte remaining in the cathode and the separator were retrieved by leaching it with 1 mL of propylene carbonate. The composition of the cycled electrolyte was analysed by gas chromatography (GC).

Active Material	*Potential Window (V vs. Li^+/Li)*	*Cycle Rate*
NCM111	2.5–4.3	1st 2 cycles: C/10 3rd and the following cycles: C/2 1 C = 2.22 mA/cm² Only constant current step
NCM523	2.5–4.3	1st 2 cycles: C/10 3rd and the following cycles: C/2 1 C = 2.37 mA/cm² Only constant current step
HE-NCM	2.5–4.8	1st 2 cycles: C/10 3rd and the following cycles: C/2 1 C = 1.49 mA/cm² Only constant current step

Table 1: *Summary of the typical cycling conditions for NCM111, NCM523, and HE-NCM.*

The experiments were carried out with Agilent 7890A gas chromatograph with DB-1 capillary (60 m x 0.32 mm i.d., 5 µm) and built-in flame ionization detector from Agilent Technologies. A constant flow of N_2 at 1 mL/min was used as carrier gas. 1 µL of the sample solution was transferred from the injector, which was maintained at 240 °C, to the capillary column. The temperature of the column was ramped from 80 °C to 260 °C with a rate of 6 K/min and held for 25 minutes at 260 °C. The duration of each measurement was 47.5 min.

Results

By comparing the electrolyte composition of LP57 from NCM111 or NCM523 full cells after 100 cycles with the composition of the pristine electrolyte (Figure 1abc), it can be seen that small amounts of DMC and DEC are detected after cycling. This indicates the presence of transesterification reaction during electrochemical cycling, as also observed elsewhere [2, 3].

Takeuchi et al. [2] have proposed that transesterification reaction is initiated by reactive alkoxide intermediates, which are generated by the reduction of carbonate solvents. Furthermore, the extent of this reaction is closely associated to anode passivation.

When the SEI on the graphite electrode gradually becomes stable during the first cycles, further production of reactive intermediates is prevented and the existing radicals can be quenched at the higher potential at the cathode side. Consequently, the transformation of EMC into DMC and DEC is ceased. Therefore, by replacing graphite with lithium, one would expect more transesterification reaction to take place, and thus more DEC and DMC to be detected. Indeed, this is what is observed in the electrolyte composition of NCM111/NCM523 half cells (Figure 1de). In this case, EMC content reduces drastically from 80 to less than 40 relative peak area percent (RPA%) while the signals for DEC and DMC increase accordingly. The reason is that, due to lithium redeposition, high-surface and mossy SEI is formed when the cells are cycled against metallic lithium. This enhances the electrode/electrolyte interface reactions, resulting in the continuous change of EMC, DEC, and DMC concentrations until equilibrium is reached.

The dependence of esterification on the applied potential window was examined through HE-NCM-based half cells, cycled between 2.5 and 4.8 V vs. Li^+/Li, after 100 cycles. Constant voltage step was applied at the end of the charging process to better visualize the voltage effect.

It can be seen in Figure 2a that the content of EMC in such a cell is around ~ 50 RPA%, and clearly less DEC/DMC transformation is observed. However, due to the difference in active material loading between NCM111/NCM523 and HE-NCM electrodes, it is ambiguous whether the differences in electrolyte composition between NCM111/NCM523 and HE-NCM-based half cells are current-density or potential-window related. To understand the importance of these two param-

[1] BASF SE, Ludwigshafen, Germany

eters, HE-NCM-based half cells were cycled with the potential windows and current densiteis which are typically applied for the NCM523 material (Table 1).

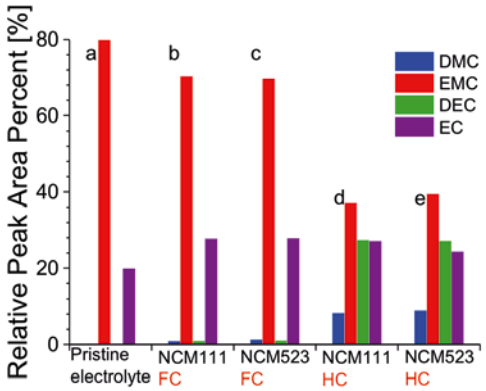

Figure 1: *Comparison of the relative peak area percent (RPA%) of different electrolyte components in pristine LP57 electrolyte (a) and LP57-containing NCM111 (b) and NCM523 (c) full cells (FC) with the respective half cells (HC) after 100 cycles (d, e).*

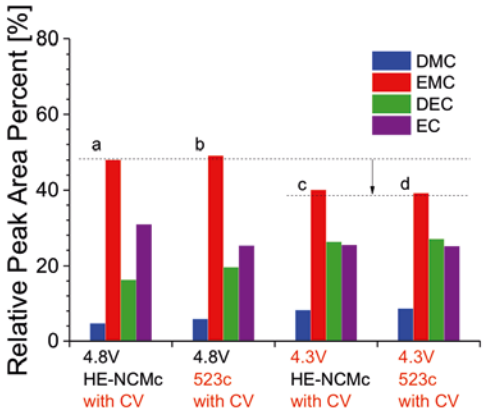

Figure 2: *Comparison of the RPA% of different electrolyte constituents in LP57-containing HE-NCM half cells after 100 cycles with different upper cut-off potential or current. (HE-NCMc and 523c correspond to the current density typically used for HE-NCM and NCM523 materials, respectively. CV refers to constant voltage step.)*

By comparing Figure 2 (a) and Figure 2 (b), one can conclude that, although the current applied to HE-NCM is indeed lower than the current applied to NCM523 electrode, the difference is not large enough for HE-NCM cells to benefit from lesser extent of transesterification reaction. On the other hand, when a lower potential is applied to HE-NCM half cells (Figure 2 (c, d)), EMC drops roughly from 50 to 40 RPA%. Furthermore, if we compare the electrolyte composition in the HE-NCM cell cycled only to 4.3 V vs. Li^+/Li with the ones of NCM111/NCM523 cells (Figure 3), one would notice that the extent of transesterification reaction is similar. (To provide a common basis for the comparison, the NCM111/NCM523-based half cells used in Figure 3 are subjected to constant voltage step at the end of charging at 4.3 V vs. Li^+/Li as well.) Therefore, it can be concluded that, in addition to the negative electrode passivation, the applied potential window is the other important parameter, which dominates the composition in cycled LP57 electrolyte.

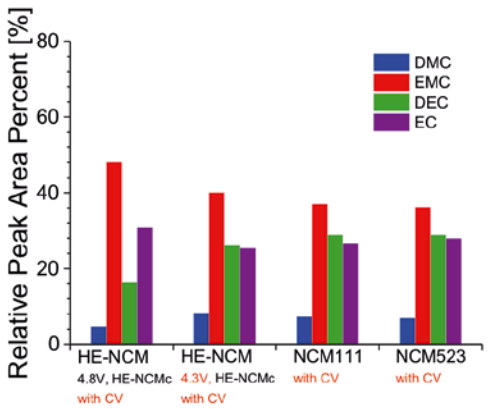

Figure 3: *Comparison of the RPA% of different electrolyte constituents in LP57-containing HE-NCM half cells after 100 cycles with NCM111 and NCM523-based half cells.*

Conclusion

LP57 electrolyte undergoes transesterification where methyl and ethyl groups of EMC molecules exchange to form DMC and DEC during electrochemical cycling. By comparing the results of full-cell with the ones of half-cell, it is apparent that anode passivation (or, to generalize, the nature of negative electrode) plays a crucial role in the extent of transesterification. In addition to that, the applied potential window was also identified to be an important parameter, where higher potential seems to suppress this type of reactions.

Acknowledgment

The authors are grateful for financial support from BASF SE as well as Mr. Dietze Robert, Mr. Schmitt Volker, and Ms. Kimmel Michaela for the experimental supports and Ms. Laschak Vibeke for the gas chromatography measurements.

References

[1] J.B. Goodenough, Y. Kim, *Chem. Mater.* **22**, 587–603 (2010).
[2] E.S. Takeuchi, H. Gan, M. Palazzo, R.A. Leising, S.M. Davis, *J. Electrochem. Soc.* **144**, 1944–1948 (1997).
[3] H. Yoshida, T. Fukunaga, T. Hazama, M. Terasaki, M. Yamachi, *J. Power Sources* **68**, 311–315 (1997).
[4] R. Petibon, L. Rotermund, K.J. Nelson, A.S. Gozdz, J. Xia, J.R. Dahn, *J. Electrochem. Soc.* **161**, A1167–A1172 (2014).

Bulk analysis of Sn-electrodes in sodium-ion batteries

L.O. Vogt, R. Caputo[1], C. Villevieille
phone: +41 56 310 5738, e-mail: leonie.vogt@psi.ch

The high demand for advanced energy storage systems has resulted in increased research into novel battery systems. Na-ion batteries are a promising candidate for large-scale energy storage due to the abundance and low cost of Na. As Na is also an alkali metal, the electrochemistry and basic principles of Na-ion batteries are analogous to the well-known Li-ion batteries. It was recently reported that commercially available elements such as P, Sb and Sn react electrochemically with three or more Na ions per formula unit through conversion reactions [1–3]. For anode materials specific charge of above 500 mAh/g for over 100 cycles has been demonstrated [4].

Sn, in particular, is a promising anode material with a specific charge of above 800 mAh/g upon full sodiation, resulting in the formation of $Na_{15}Sn_4$. Understanding the reaction mechanism of sodiation/desodiation processes is crucial for further development of Sn and related composites as high energy density anode materials in Na-ion batteries. In the present work we investigated the bulk reaction mechanism of the sodiation of a Sn anode by using *in situ* X-ray Diffraction (XRD) and first-principles crystal structure prediction methodologies.

Experimental

XRD measurements were performed at room temperature with a PANalytical Empyrean diffractometer using Cu Kα radiation. *In situ* measurements were performed in a homemade cell with a beryllium window in the Bragg-Brentano geometry. One spectrum was recorded every hour. A self-standing electrode was used in the setup composed of 70 wt% Sn (Sigma Aldrich, 325 mesh), 20 wt% PVDF binder (Arkema Inc.) and 10 wt% Super P® carbon (Imerys). The electrode was cast from an acetone suspension onto Teflon film and then dried in air. It was cycled against sodium metal at a C/30 rate in the electrolyte $NaClO_4$ in PC + 5 % FEC; 250 µL of electrolyte were used to soak the glass fibre separator in the cell.

Computational methodology

We employed the cluster expansion approach interfaced with Quantum ESPRESSO calculations for the structure modelling of Na_xSn compounds at different compositions for $0 < x < 3.75$, following a similar approach reported elsewhere [5]. In addition and in parallel to that, we used the AIRSS method to generate possible model structures coupled with CASTEP calculations. In Quantum ESPRESSO and in CASTEP we used the generalized gradient form (GGA) of the exchange–correlation functional and in particular the Perdew-Burke-Ernzerhof96 (PBE) for one and norm-conserving pseudo-potential for both Na and Sn atoms, which valence shells contain 9 and 4 electrons, respectively.

Results

The phase diagram of Na-Sn reports nine possible binary phases, of which one, NaSn can be found in two different polymorphs. The composition range of Na_xSn is for for $0 < x < 3.75$. The sodiation and desodiation processes in the electrochemical cell can visit not only the thermodynamic states of the phase space of the Na-Sn system but also pass through local minima and accordingly show the formation of unknown phases.

Therefore, the first-principles crystal structure prediction can serve as a complementary and important tool for predicting possible structures and understanding the structure-composition relationships.

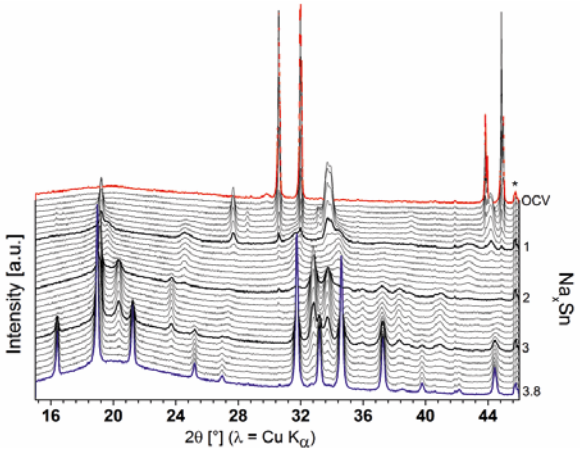

Figure 1: *In situ XRD of the first sodiation of Sn electrodes cycled in $NaClO_4$ in PC + 5 % FEC at a rate of C/30.*

The *in situ* XRD patterns of the sodiation process are shown in Figure 1. One scan was taken every hour, which means that one spectrum is taken while 0.125 Na is transferred to the anode (given the C/30 rate applied). The crystalline phase of the tetragonal Sn is clearly visible at open circuit voltage (OCV). As the sodiation proceeds, new phases are formed.

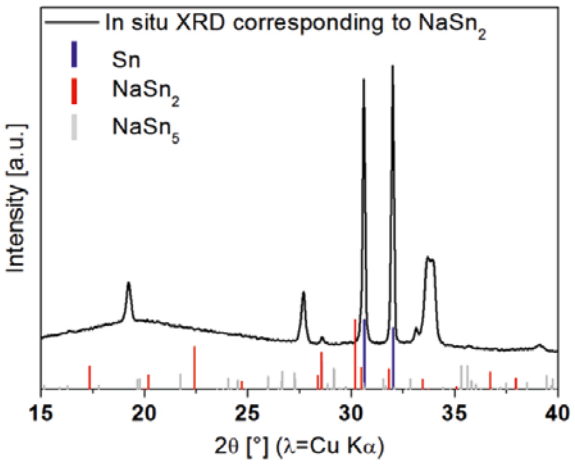

Figure 2: *In situ XRD corresponding to $NaSn_2$ with three references from the ICSD.*

In the Sn-rich region, for $x < 1$, none of the phases reported in the Inorganic Crystallographic Structure Database (ICSD),

[1] ETH Zürich

$NaSn_5$ and $NaSn_2$, match the scanned diffraction patterns (see Figure 2), thus an unknown phase is seen.

As the regime is changed from the tin rich to the sodium rich phases ($x > 1$ Na per Sn atom) the unknown phase disappeares and is replaced by NaSn phase in the range of $1.125 < x < 1.250$. This extra 0.25 sodium can be attributed to the SEI formation identified around 0.55 V.

The NaSn phase rapidly shows amorphization as the sodiation proceeds (i.e., $Na_1 \rightarrow Na_{2.5}$) and new peaks appear. As with the first intermediate phase formed these new peaks belong to an unknown phase. They could not be matched to the reported phase Na_9Sn_4 (Figure 3).

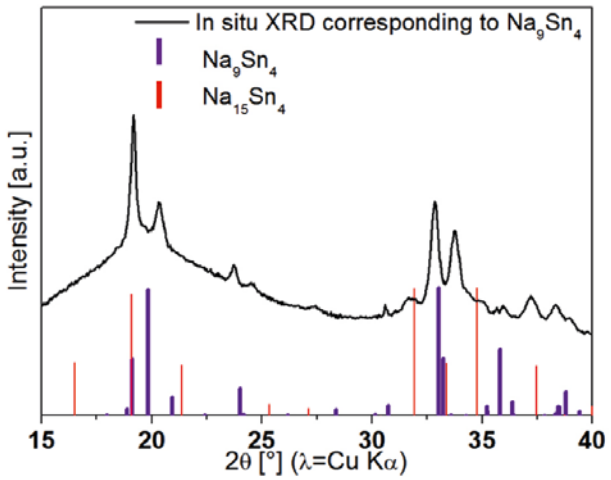

Figure 3: *In situ XRD corresponding to Na_9Sn_4 with two references from the ICSD.*

As sodiation progresses an interesting feature becomes visible during the second and third sodiation steps (Figure 1). Careful examination of the peak at 19.07° reveals an increasing intensity around $x = 2$, a maximum around $x = 2.5$, and then a decreasing intensity and shift to lower angles at $x = 3$, where the final phase $Na_{15}Sn_4$ is formed. In literature an additional phase $Na_{29.58}Sn_8$, which crystallizes in an orthorhombic system, has been mentioned, however we didn't identify this phase in our experiments.

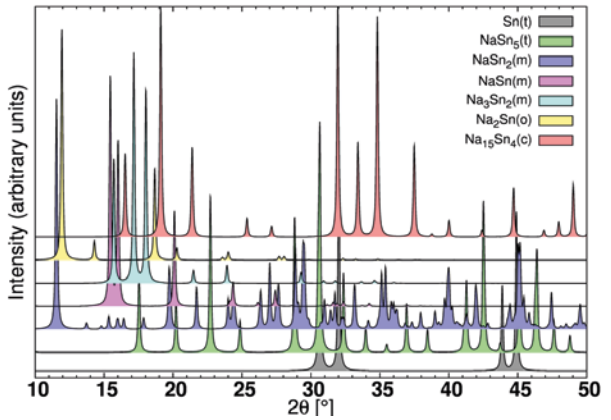

Figure 4: *The theoretical XRD patterns of selected structures at different compositions compared to pristine Sn. The letters in brackets stand for tetragonal (t), monoclinic (m), orthorhombic (o) and cubic (c).*

The theoretical XRD patterns of selected structures are shown in Figure 4. Although a numerical match between the *in situ* XRD patterns and the calculated XRD patterns of the modelled structures could not be achieved, the comparison suggested that for $x < 1$ concomitant reactions consuming Na occurred, most likely the formation of a solid electrolyte interphase (SEI) leading to a difficult evaluation of the Na content in the structure. For $x \geq 1$ the Na-Sn bulk reaction dominates as found by a better match between the nominal Na:Sn atomic ratio given by the electrochemistry and the bulk composition.

In terms of enthalpy of absorption of Na in Sn(t), the calculations indicated that the first steps of sodiation, for $x \leq 0.063$, are endothermic processes. The enthalpy of reaction exhibited a plateau-like feature for $1 < x < 2$ followed by a step down to the final state for $x = 3.750$ in $Na_{15}Sn_4$ (Figure 5).

The calculated potential of the discharge reaction is about 0.25 V for $1 < x < 2$ and 0.143 V for $x = 3.750$.

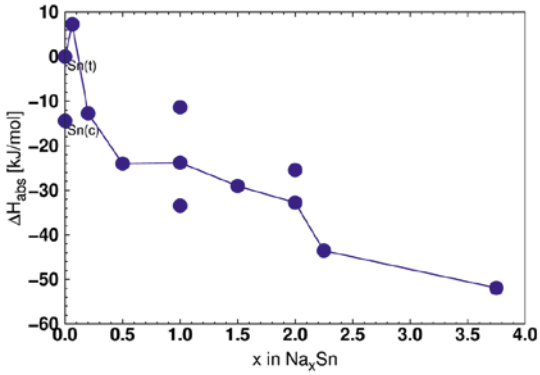

Figure 5: *Calculated enthalpy of absorption (kJ/mol of Sn) of the sodiation reaction. The blue line connects the low energy structure at each composition. For $x = 1$ the tetragonal structure, optimized starting with the reference structure, is lower in energy than other modelled structures.*

Conclusion and Outlook

The Na-Sn system has been studied via *in situ* XRD measurements during the cycling of high energy density Sn electrodes in sodium ion batteries. The material undergoes a range of phase transitions. Three known phases as well as two unknown phases have been observed. First theoretical studies of the Na-Sn system via first-principle crystal structure prediction, suggested that the NaSn monoclinic structure and Na_2Sn orthorhombic structure are possible candidates for the unknown phases. The determination of the reaction mechanism of Sn with Na is a crucial step to be able to understand and further develop this promising anode material and its derivatives.

References

[1] Y. Kim, Y. Park, A. Choi, N.S. Choi, J. Kim, J. Lee, J.H. Ryu, SM. Oh, K.T. Lee, *J. Adv. Mater.* **25** (22), 3045–3049 (2013).
[2] J.F. Qian, Y. Chen, L. Wu, Y. Cao, X. Ai, H. Yang, *Chem. Commun.* **48** (56), 7070–7072 (2012).
[3] Y. Xu, Y. Zhu, Y. Liu, C. Wang, *Adv. Energy Mater.* **3** (1), 128–133 (2013).
[4] A. Darwiche, C. Marino, M.T. Sougrati, B. Fraisse, L. Stievano, L. Monconduit, *J. Am. Chem. Soc.* **134** (51), 20805–20811 (2012).
[5] R. Caputo, *RSC Adv.* **3** (26), 10230 (2013).

Mg-doped high-energy lithium nickel-cobalt-manganese-oxides (HE-NCM) as cathode materials for Li-ion batteries

S. Sallard, P. Novák, C. Villevieille
phone: +41 56 310 5746, e-mail: sebastien.sallard@psi.ch, claire.villevieille@psi.ch

The lithiated nickel cobalt manganese oxide material (NCM) $LiNi_{1-x-y}CoyMnxO_2$ was first introduced in 2001 by Ohzuku et al. [1]. The NCM materials can cycle at high voltage, superior to 4 V vs. Li^+/Li, and deliver a specific charge between 160–180 mAh/g, corresponding to an energy density superior to the one of $LiCoO_2$. In 2007, high energy NCM (HE-NCM) with the chemical formula a (Li_2MnO_3) • b ($LiNi_{1-x-y}Co_yMn_xO_2$) was introduced by Thackeray et al. [2]. The main advantages of HE-NCM are

- a specific charge between 250–290 mAh/g and
- an average voltage window close to 4.5 V vs. Li^+/Li.

HE NCM contains 2 phases, a monoclinic Li_2MnO_3 (space group C2/m), so called Li_2MnO_3-domains, and a rhombohedral $LiMO_2$ (space group R-3m). During the first charge, the HE-NCM is activated, i.e., the Li_2MnO_3 domains release oxygen irreversibly, leading to the activation of the manganese. However during cycling HE-NCM suffers from further structural changes due to the Mn activation, leading to a voltage fading [3]. The reason for this voltage drop is the mobility of the Mn between slabs and interslabs. To overcome this problem of voltage drop and metal leaching occurring at potentials positive to 4.5 V vs. Li^+/Li, coatings have been considered by some researchers [4]. The capacity retention for the bare NCM and the coated NCM after 300 cycles can be at room temperature 93 % and 98 % and at 60 °C 70 % and 85 %, respectively. However the gain is only temporary, the time for the coating to be leached by the HF present in the electrolyte. Moreover, the effectiveness of the coating method is highly dependent of the thickness and the uniformity of the coating.

Another method to stabilize this material is to substitute Li and/or transition metal by an inert element in order to fix the position of the Mn and to avoid its mobility inside the structure. This new concept, so far not described in the literature, was tested using Mg^{2+} as partial substituent of Li^+. Mg^{2+} possesses an ionic radius of 66 pm, slightly smaller than the one of Li^+, 68 pm. The Mg ions present in the Li^+ interlayer should be quasi-non-mobile due to high columbic interaction with the oxygen anions O^{2-} present in the metal-oxygen layers [5].

Experimental

Lithium nitrate, nickel nitrate hexahydrate, magnesium nitrate hexahydrate, cobalt nitrate hexahydrate, manganese nitrate tetrahydrate, and citric acid monohydrate are dissolved in water at room temperature. The solution is heated up to 100 °C under stirring until a dried powder is obtained. The powder is calcined in two steps at 450 °C and finally at 850 °C.

The synthesized powders labelled $Li_{100-x}Mg_{x/2}$-NCM (called hereafter $Mg_{x/2}$-NCM) were characterized by X-ray diffraction (XRD). Slurries were done by mixing $Mg_{x/2}$-NCM powder with black carbon Super-C and Kynar Flex in a 80/10/10 weight ratio in n-methyl-2-pyrrolidone. The slurries were doctor-bladed on an aluminum foil and dried. Coin-like test cells were built with lithium metal as counter electrode, glass fibers as separator, and $LiPF_6$ 1 M in ethylene carbonate/dimethylcarbonate (1:1 in weight ratio) as electrolyte solution. The galvanostatic measurements were performed between 2.5 to 4.8 V vs. Li^+/Li with a specific current of 25.6 mA/g (C/10 for a theoretical capacity of 1 Li^+ extraction per metallic atom).

Results

The Rietveld refinement of the XRD pattern of the $Li_{98}Mg_1$-NCM (Figure 1) confirms the presence of the 2 phases in the pristine material with the Mg^{2+} located in the lithium slabs. As can be seen in Table 1, the presence of the Mg influences the microstructure of the material. The size of the lithium slabs and metal slabs are getting significantly smaller and bigger, respectively, in comparison to HE-NCM. It could be attributed to the high columbic interaction of the Mg^{2+} from the Li-slabs with the O^{2-} present in the M-slabs.

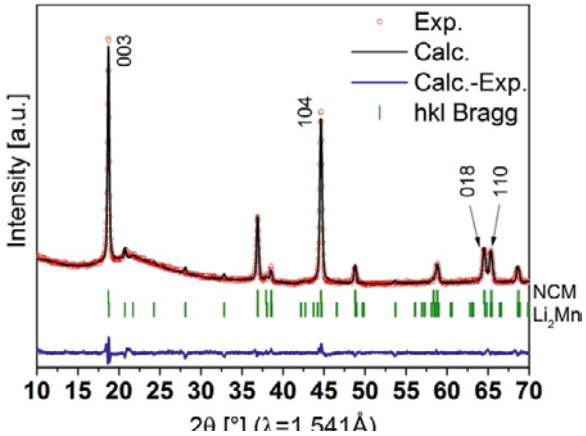

Figure 1: *Rietveld refinement of the Mg_1-NCM.*

Sample	*Li-slab (Å)*	*M-slab (Å)*	*Li/Ni exchange (%)*	*Ratio NCM/ Li_2MnO_3*
HE-NCM	2.453	2.293	9.7	44/56
Mg_1-NCM	2.206	2.547	5	55/45

Table 1: *Microstructural parameters of the reference HE-NCM and Mg_1-NCM materials.*

All synthesized materials $Mg_{x/2}$-NCM with x = 2, 5, 10, and 20 show a layered structure close to HE-NCM. However, the higher the Mg content, the higher the changes are in the XRD pattern regarding the reference (data not shown).

As expected, the lower the amount of lithium in the pristine Mg_x-NCM materials, the lower the specific charge is (Figure 2). Surprisingly, during cycling the specific charge of the Mg_x-NCM is increasing, leading us to conclude that there is a possible activation process or a possible restructuring of the layers. Another important point is that the higher the amount of Mg, the higher the specific charge increase is and the sooner it starts.

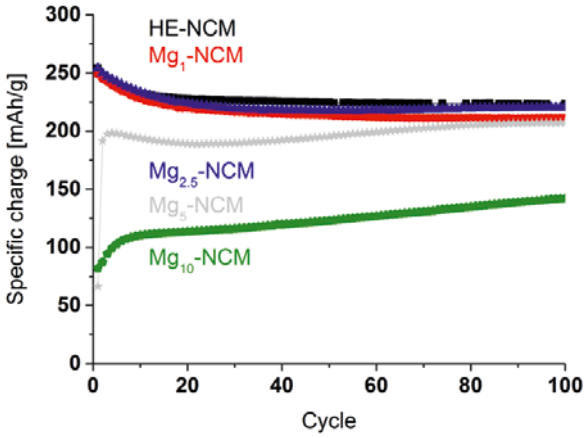

Figure 2: *Specific charge of different samples.*

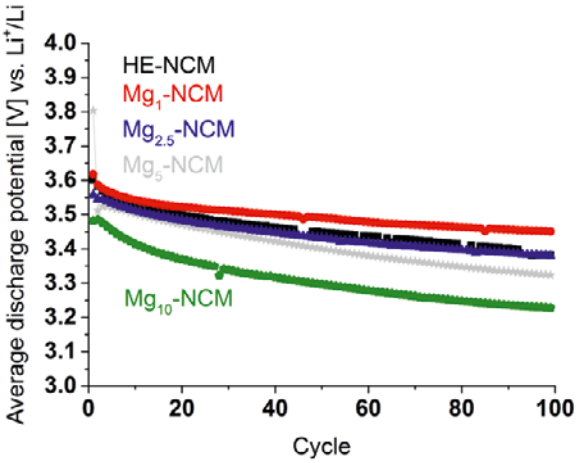

Figure 3: *Average discharge potential evolution of different samples.*

Further observations allow to separate the $Mg_{x/2}$-NCM samples into two classes:

- When $x \leq 5$, the specific charge evolution of $Mg_{x/2}$-NCM is similar to the reference HE-NCM for the first 50 cycles.
- When $x \geq 10$, the specific charge evolution of $Mg_{x/2}$-NCM is increasing with the cycle number. In the case of $x = 20$, the specific charge is increasing from 80 mAh/g (1st cycle) to 140 mAh/g (100th cycle).

The evolution of the average potential in discharge emphasizes even more this difference between low and high values of x (Figure 3). For $x \geq 10$, the initial average potential of the $Mg_{x/2}$-NCM is inferior to the one of HE-NCM. Moreover the average potential is decreasing faster for the $Mg_{x/2}$-NCM than HE-NCM, excluding them as potential candidates for insertion material in Li-ion batteries. The most interesting sample is $x = 2$ where the average potential is slightly increased and slightly stabilized in comparison to HE-NCM.

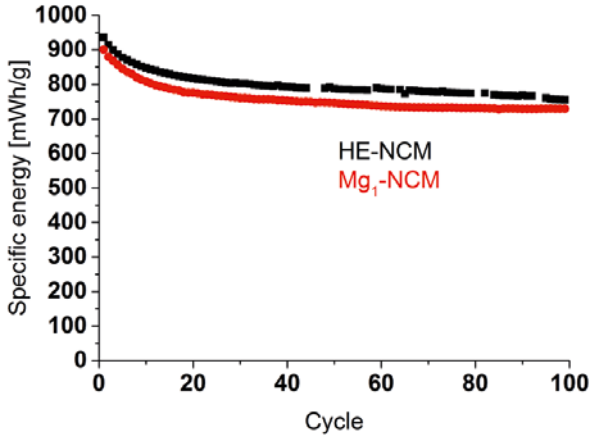

Figure 4: *Evolution of the specific energy of different samples.*

The evolution of the specific energy (Figure 4) shows that $Mg_{x/2}$-NCM with $x = 2$, after 100 cycles exhibits a specific energy fading lower than the one of HE-NCM and a specific energy almost identical.

Conclusion

We demonstrate a new way to stabilize the voltage fading of HE-NCM materials by a partial substitution of the lithium. The preliminary results showed that the concept is working with a low level of substitution.

References

[1] T. Ohzuku, Y. Makiumura, *Chem. Lett.* **30**, 642-643 (2001).
[2] S.H. Kang, P. Kempengs, S. Greenbaum, A. Kropf, K. Amine, M.M. Thackeray, *J. Mater. Chem.* **17**, 2069–2077 (2007).
[3] Y. Li, M. Bettge, B. Polzin, Y. Zhu, M. Balasubramanian, D.P. Abraham, *J. Electrochem. Soc.* **160**, A3006–A3019, (2013).
[4] S.T. Myung, K. Izumi, S. Komaba, Y.K. Sun, H. Yashiro, N. Kumagai, *J. Chem. Mater.* **17**, 3695–3704 (2005).
[5] E. Levi, M.D. Levi, O. Chasid, D. Aurbach, *J. Electroceram.* **22**, 13–19 (2009).

Operando neutron powder diffraction of $LiNi_{0.5}Mn_{1.5}O_4$ vs. graphite performed in a cylindrical cell

L. Boulet-Roblin, P. Borel[1], D. Sheptiakov, C. Tessier[1], P. Novák, C. Villevieille
phone: +41 56 310 2115, e-mail: lucien.boulet@psi.ch

To answer the question about the needs of today's mobile society, Li-ion technology is one of the most promising solutions for storage applications [1]. It is widely used in nomads tools such as smartphones, laptops, cameras etc. – but improvements are needed to fulfil the requirements for electric mobility. $LiNi_{0.5}Mn_{1.5}O_4$ spinel (named hereafter LNMO), was selected as cathode material thanks to its high energy density in batteries with an average potential of 4.7 V vs. Li^+/Li [2]. Furthermore, LNMO is known for its structural stability [3]. Neutron powder diffraction (NPD) is a technique of choice to investigate structural changes, especially for light elements like lithium. The challenge of operando neutron powder diffraction is to develop a cell able to cycle an important quantity of active materials and obtain

- a good electrochemistry, and,
- patterns quality allowing Rietveld refinement analyses.

For this purpose, we developed a cylindrical cell based on industrial cylindrical cells design (18650). We selected a full cell configuration based on LNMO vs. graphite system.

Experimental

The positive electrode was prepared by casting a mixture of 92 wt.% LNMO (provided by SAFT), 4 wt.% Super-P carbon and 4 wt.% PVDF binder suspended in N-methyl-2-pyrrolidinone onto an aluminum foil as current collector. The casted slurry was dried at 80 °C under vacuum overnight. The negative electrode based on a mixture of graphite and Na-CMC binder was casted onto a copper foil used as current collector. The cell made of iron is filled with the two electrodes separated by a polymeric separator PE/PP polyolefin soaked with LP30 electrolyte (ethylene carbonate (EC) : dimethyl carbonate (DMC) (1 : 1 w/w) and 1 M $LiPF_6$). The design of the cell is depicted in Figure 1.

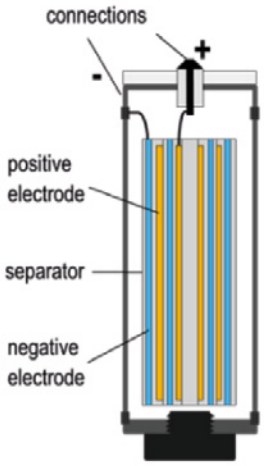

Figure 1: *Scheme of the cylindrical cell used for the operando NPD.*

The cycling of the cells was carried out galvanostatically between 3.5 V and ~4.8 V at different C-rates, assuming experimental specific charges of 135 mAh/g for LNMO and 340 mAh/g for graphite. For the operando NPD, the cell was filled with a deuterated LP30 (no hydrogen content). The patterns were acquired during cycling at the SINQ High-Resolution Powder Diffractometer for Thermal Neutrons (HRPT) beamline, with a wavelength of 1.494 Å. To improve the quality and resolution of the patterns, they were acquired using high intensity settings and each scan corresponds to 40 min of measurement.

Results

Figure 2 represents the galvanostatic profile at C/10 rate of the cylindrical cell. The specific charge has been normalized due to different loading of the electrodes. The galvanostatic profile of the cell shows the graphite and LNMO electrochemical activities via the different plateaus during (de)lithiation at different voltages.

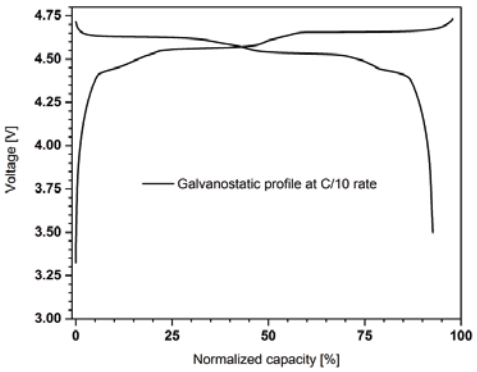

Figure 2: *Galvanostatic profile of the cylindrical cell at C/10 rate.*

Figure 3 represents the refinement of NPD pattern obtained at OCV. Despite few contributions from cell parts (nickel, iron, copper and aluminum) and slightly high background due to incoherent scattering of hydrogen (polymer separator), the phases of interest can be refined. LNMO (Fd-3m) and the graphite (P63/mmc) structures are refined with the following lattice parameters of a = b = c = 8.145 Å, and a = b = 2.457 Å and c = 6.700 Å, respectively.

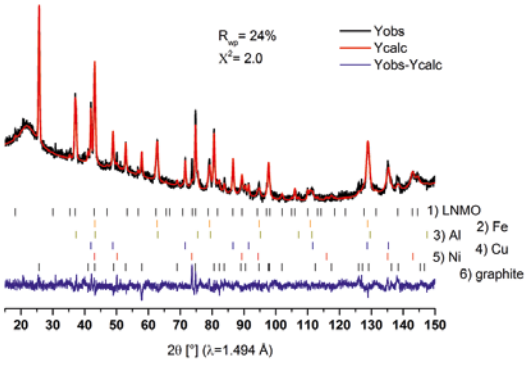

Figure 3: *NPD refinement at OCV state of the cylindrical cell.*

[1] SAFT, Bordeaux, France

For the operando measurements, the cell was (dis)charged at C/25 rate. The main peaks of the two electroactive materials ((002) reflection for graphite, (222) reflection for LNMO) were monitored and their structural evolutions are represented in Figures 4 and 5 (intensity of the contour plot rises from blue to red). The different stages of graphite lithiation can be observed ($Li_0C \rightarrow LiC_{24} \rightarrow LiC_{12} \rightarrow LiC_6$) with an expansion of the unit cell parameters of around 8 %. During discharge, the processes are reversible and the unit cell parameters are coming back to their starting values.

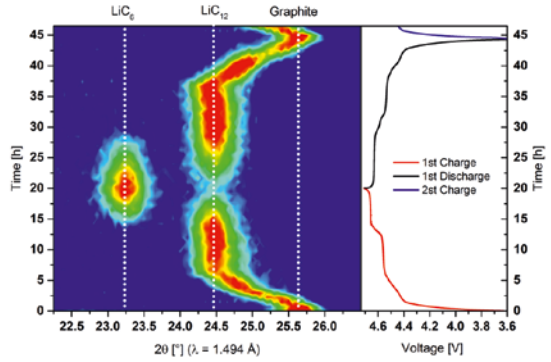

Figure 4: *NPD patterns of the (200) graphite reflection.*

Simultaneously, we followed the evolution of the lattice parameters of LNMO during its delithiation (Figure 5) which leads to a shrinkage of its unit cell. We observed a shift of the peaks to higher angles in two steps i) a solid-solution reaction (involving $Ni2^+/Ni3^+$ redox couple) fol-lowed by ii) a two-phase reaction (involving $Ni3^+/Ni4^+$ redox couple). As for graphite, the processes are re-versible.

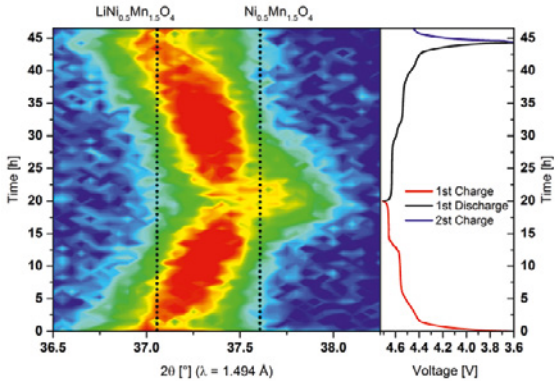

Figure 5: *NPD patterns of the (222) LNMO reflection.*

In order to study the structural stability of the active materials, operando NPD of a cell cycled 50 times at 1-C rate with a non-deuterated LP30 electrolyte was measured. Figures 6 and 7 show the NPD measurements, graphite and LNMO reflections, respectively. During the operando measurement, the cell was charged at C/5 rate. The cycling had to be paused for few minutes at different times due to beam problems and as consequence the active materials were relaxing during that time, provoking the spikes in the galvanostatic profile.

Even with a lower resolution of the peaks, due to the short measurement time and the use of a non-deuterated electrolyte (higher hydrogen content), shifts and new phases are detected while charging. Indeed the different stages of the graphite lithiation are observed at the same plateaus (Figure 6) than with the first operando NPD measurement, confirming that even after 50 cycles the graphite behavior is similar to the first cycle.

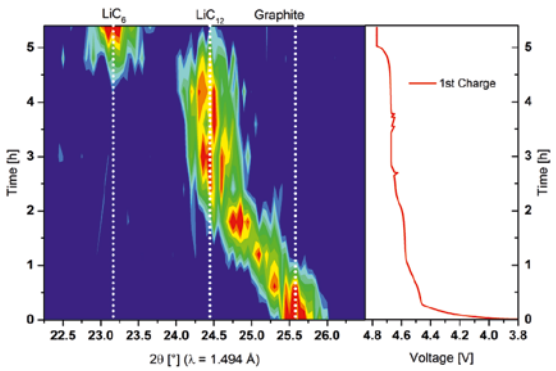

Figure 6: *NPD patterns of the (200) graphite reflection after 50 cycles at 1-C rate.*

For the LNMO delithiation (Figure 7), the two processes (solid-solution and two-phase reactions) are also detected, and again, the results show the good structural stability of this electroactive material after 50 cycles versus graphite.

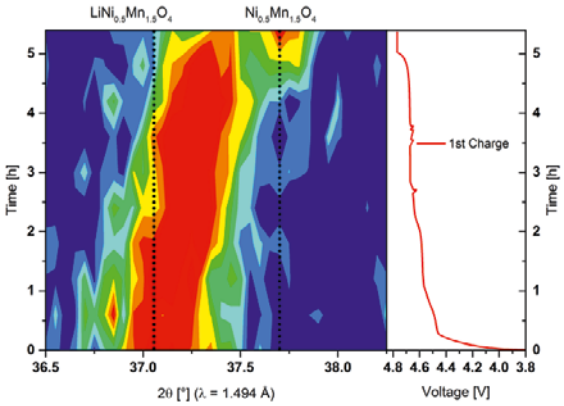

Figure 7: *NPD patterns during cycling of the (222) LNMO reflection at C/5 rate and after 50 cycles at 1-C rate.*

This last measurement proves the feasibility of operando NPD at relatively fast rate and the monitoring of the cell parameter evolution. Moreover the use of a deuterated electrolyte should lower the background intensity roughly to its half and might allow good NPD pattern refinement.

Conclusion

We developed a new cylindrical Li-ion cell suitable for operando NPD measurement at the SINQ source. We were able to follow and study the structural changes of the system LNMO vs. graphite during lithiation/delithiation.

Acknowledgement

The authors are grateful to SAFT for the financial support. This work is (partly) based on experiments performed at the Swiss spallation neutron source SINQ at Paul Scherrer Institute, Villigen, Switzerland.

References

[1] J.M. Tarascon, M. Armand, *Nature* **414**, 359 (2001).
[2] A. Manthiram, K. Chemelewski, E.-S. Lee, *Energy Environ. Sci.* **7**, 1339 (2014).
[3] R. Santhanam, B. Rambabu, *J. Power Sources* **195**, 5442 (2010).

SCIENTIFIC ACHIEVEMENTS 2014

Batteries –

Diagnostics

Interface study of HE-NCM electrodes during cycling using OEMS

A. Guéguen, E. Jämstorp Berg, P. Novák
phone: +41 56 310 2176, e-mail: aurelie.gueguen@psi.ch

The demand for large-scale rechargeable batteries requires materials with higher rechargeable capacities than materials currently used in commercial batteries. Among the positive electrode materials reported so far, Li-rich manganese layered oxides represented by the chemical formula

$$xLi_2MnO_3 \cdot (1\text{-}x)LiMO_2 \quad (M = Ni, Co, Mn)$$

and hereafter called HE-NCM deliver high specific charge (~250 mAh g^{-1}) at high potential (~4.5 V), but suffer from capacity fading. The extra capacity of the material compared to the stoichiometric NCM compound arises from the presence of the Li_2MnO_3 component, which is activated during the 1st charge. During activation, lithium and oxygen are removed from the structure, whereby the latter further reacts with the carbonate-based electrolyte. Such side-reactions can strongly influence the electrochemical performances of the cell.

One approach to better understand the reactions taking place during the 1st charge is to analyze the gaseous products evolving during this period and the following discharges and charges using Online Electrochemical Mass Spectrometry (OEMS). Previous OEMS studies by our group reported the evolution of O_2 and CO_2 gases for HE-NCM electrodes cycled vs. graphite or Li metal [1–3]. By improving the OEMS experimental setup, we are now, in addition, able to follow the evolution of other gases such as H_2 and POF_3. The aim of the present work is to investigate the possible mechanisms leading to the gas evolutions observed by OEMS.

Experimental

The electrodes were prepared by coating thin glass-fiber sheets (Sigma Aldrich) with a mixture of 93 wt% HE-NCM (BASF SE), 3 wt% PVdF (polyvinylidene fluoride) and 4 wt % conductive carbon (Imerys) dispersed in N-methylpyrrolidone (NMP, Sigma-Aldrich). The NMP was evaporated under vacuum at 80 °C for 8 hours. Electrodes were subsequently punched (18 mm diameter) and dried overnight at 120 °C before being introduced into an Ar-filled glove-box.

The OEMS cells were assembled in a home-designed electrochemical cell (Annual Report 2012, p. 47). The HE-NCM electrodes were cycled vs Li metal (i.e., all potentials in the report are given vs. Li^+/Li) between 2 and 4.7 V. The 1st charge was carried out at a C/15 rate while the rest of the cycling at a faster rate (C/10). Two different electrolytes were tested:
1 M $LiPF_6$ in EC:DEC (3:7) and 1 M $LiClO_4$ in EC:DEC (3:7).
Separators were made of the glass-fiber sheets used for the electrode preparation.

Results and discussion

Figure 1 shows the OEMS results collected during the two first galvanostatic cycles for HE-NCM electrodes cycled vs. Li metal with 1 M $LiPF_6$ in EC:DEC (3:7). During the 1st charge, CO_2 starts evolving before O_2 ~ 4.15 V. At the end of the activation plateau, both O_2 and CO_2 evolution increase strongly, reaching their maximum at the end of charge. This agrees well with previous reports [3]. At the same time, fragments with m/z = 77, 85 and 104 start evolving. It is not clear so far to which species the fragment m/z = 77 can be attributed. The two other fragments 85 and 104 indicate presence of POF_3 gas. POF_3 formation most probably involves the $LiPF_6$ salt.

In order to verify the hypothesis, a similar experiment was done with electrolyte containing $LiClO_4$ salt instead of $LiPF_6$ (Figure 2). No evolution was observed for the fragments 77 and 85 (the fragment 104 was not recorded for that experiment). A possible reaction mechanism, which can lead to the formation of POF_3 is:

(1) $LiPF_6 \rightarrow LiF + PF_5$
$PF_5 + H_2O \rightarrow POF_3 + 2HF$ [4]

The H_2O, which is required for the mechanism (1) may have several sources. However, considering the electrochemical activation of POF_3 evolution, H_2O is most probably formed during oxygen removal from the active material, thus initiating reaction (I). Interestingly, further information is given by the evolution of hydrogen. When using $LiPF_6$ salt, H_2 evolution is observed at the end of discharge (Figure 1). At such potential, H_2 results from H_2O reduction. Hence we assume H_2O is present in the cell during the 1st cycle when the $LiPF_6$ salt is employed.

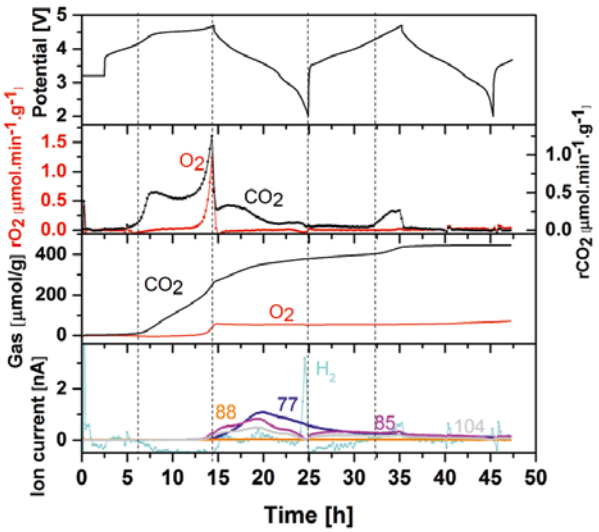

Figure 1: *Plots of the CO_2 and O_2 evolution rate and gas amounts, ion current evolution for fragments with m/z = 2, 77, 85, 88 and 104 for HE-NCM electrodes cycled vs. Li with 1 M $LiPF_6$ in EC:DEC (3:7).*

During the 2nd cycle, much lower amounts of POF_3 gas was observed when using the $LiPF_6$ salt, which confirms the assumption of H_2O formation in the first cycle and its role of triggering reaction (1), as most of H_2O formed during the 1st cycle is reduced at the end of the 1st discharge. If no more H_2O is further produced during the 2nd charge, no POF_3 gas can be formed during the 2nd cycle.

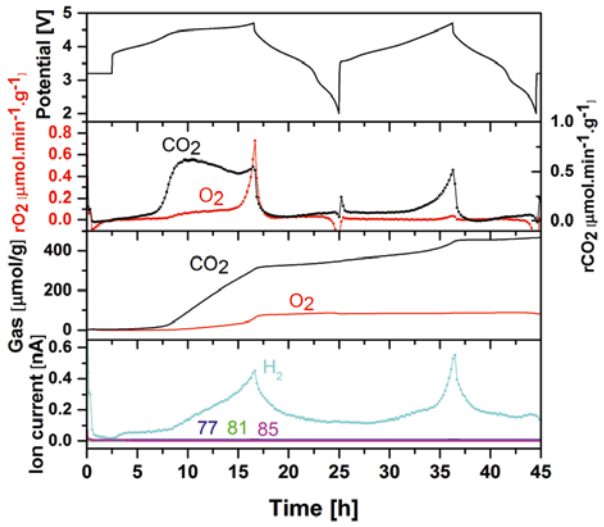

Figure 2: *Plots of the CO_2 and O_2 evolution rate and gas amounts, ion current evolution for fragments with m/z = 2, 77, 81 and 85 for HE-NCM electrodes cycled vs. Li with 1 M $LiClO_4$ in EC:DEC (3:7).*

Figure 3 shows the potential and gas evolution profiles for a similar cell containing delithiated $LiFePO_4$ instead of Li metal as a counter electrode. The gas evolution rates are comparable (see Figure 1), although the evolution rate of the fragment m/z = 85 is higher during the 2nd cycle than during the 1st cycle. Presumably, compared to delithiated $LiFePO_4$, the lithium counter electrode plays an active role in removing H_2O from the electrolyte. As a consequence, when using the delithiated $LiFePO_4$ counter electrode, enough H_2O is still present during the 2nd cycle to drive reaction (1) and the formation of POF_3.

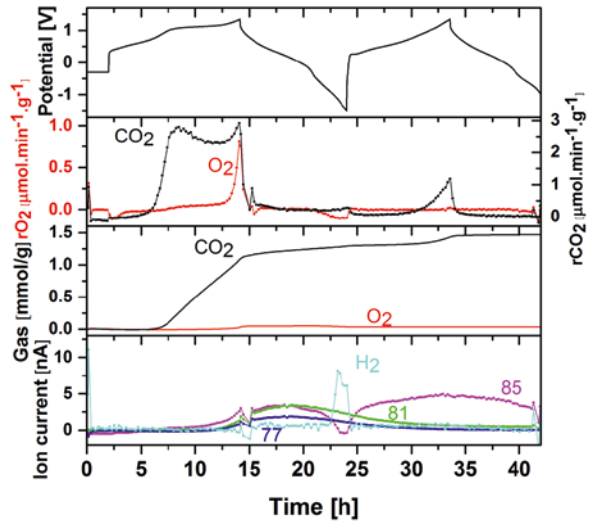

Figure 3: *Plots of the CO_2 and O_2 evolution rate and gas amounts, ion current evolution for fragments with m/z = 2, 77, 81 and 85 for HE-NCM electrodes cycled vs. delithiated $LiFePO_4$ with 1 M LiPF6 in EC:DEC (3:7).*

Conclusions

The OEMS technique demonstrates the formation of volatile species, such as O_2, CO_2, H_2, and POF_3, *in situ* during galvanostatic cycling of HE-NCM electrodes vs. Li metal and delithiated $LiFePO_4$ in an electrolyte based on 1 M $LiPF_6$ EC;DEC (3:7). The removal of radical oxygen species from the lattice of HE-NCM during the activation of its Li_2MnO_3 domains in the 1st cycle most probably results in the formation of H_2O. The H_2O subsequently hydrolyses the $LiPF_6$ salt, thus explaining the formation of POF_3.

Furthermore, the Li metal counter electrode probably partially comsumes H_2O during cycling, thus explaining the considerably lower evolution rate of POF_3 present in the 2nd cycle compared to when the delithiated $LiFePO_4$ is employed. The latter consequence might also explain the significantly improved cycling stability of HE-NCM, which has been reported in literature for cells cycled vs. metallic Li compared to other counter electrodes. The metallic Li may play an active role in «cleaning» the electrolyte of contaminants, such as H_2O, during cycling, which improves the stability of the $LiPF_6$ salt.

Acknowledgement

The authors thank BASF SE for financial support.

References

[1] F. La Mantia, F. Rosciano, N. Tran, P. Novák, *J. Appl. Electrochem.* **38**, 893 (2008).
[2] P. Lanz, H. Sommer, M. Schulz-Dobrick, P. Novák, *Electrochim. Acta* **93**, 114 (2013).
[3] E. Castel, E.J. Berg, M. El Kazzi, P. Novák, C. Villevieille, *Chem. Mater.* **26**, 5051 (2014).
[4] Y. Okamoto, *J. Electrochem. Soc.* **160**, A404 (2013).

In situ gas analysis during oxidation of pre-filled Li_2O_2 electrodes

E. Jämstorp Berg, P. Novák
Phone: +41 56 310 5736, e-mail: erik.jaemstorp-berg@psi.ch

Li-O_2 batteries have received considerable attention during past years due to their promising higher specific charge compared to most other battery systems [1]. On discharge of the Li-O_2 cell, gaseous O_2 is reduced at the cathode surface and combines with Li^+ from the negative metallic lithium electrode to form lithium peroxide, while on charge the process is reversed according to the overall chemical reaction $2\,Li + O_2 \leftrightarrows Li_2O_2$. Despite significant research efforts, there are several critical bottlenecks to be addressed before a viable Li-O_2 energy storage device can be developed. For instance, the Li-O_2 system displays a limited rate capability, low round trip efficiency and electrode/electrolyte instabilities lead to poor rechargeability. Reduced O_2 has been observed [1] to readily react with most cell components such as the electrode carbon substrate, the binder, the electrolyte solvent and salt, which causes the formation of a variety of decomposition products. The latter side-reaction processes are detrimental to both cell impedance as well as cycle life, and finally lead to the failure of the cell. Online Electrochemical Mass Spectrometry (OEMS) permits the *in situ* analysis of volatile chemical species in an electrochemical cell during cycling. The technique thus offers unique possibilities to determine Li-O_2 cell rechargeability (i.e., the molar ratio of O_2 consumed during discharge to O_2 evolved during charge) as well as to monitor any volatile side-reactions products. In order to avoid effects associated with the Li-O_2 discharge, model pre-filled Li_2O_2 electrodes have been developed to study the charge reaction separately [2]. The aim of the present study is to monitor the gas evolution of a pre-filled Li_2O_2 electrode *in situ* during charge with a novel OEMS setup developed in our labs [3].

Experimental

Pre-filled powder electrodes were prepared in an Ar-filled glovebox (O_2, H_2O < 3 ppm) by grinding 80 wt% of technical grade Li_2O_2 (~ 90 %, Sigma-Aldrich, Germany) with 20 wt% conductive carbon (Super C65, Imerys Graphite and Carbon, Switzerland) for 10 min with a mortar and pestle. The grinded Li_2O_2/C powder (~ 2 mg) was carefully dispersed as a thin layer on a glass fibre separator (Ø24 mm, Grade GF/C, Whatmann Inc., UK), then covered and pressed in a fine stainless steel mesh (Ø 20 mm, 20 µm mesh-size) before carefully inserted into the OEMS cell [3] on top of a piece of metallic lithium (Ø 20 mm, Sigma-Aldrich, Germany). The electrode was soaked with 120 µL of electrolyte (0.2 M LiTFSI in Diglyme, Sigma-Aldrich, Germany). The sealed cell was mounted on the OEMS setup [3], connected to the galvanostat (CCCC, Astrol, Switzerland), which applied a current of 0.15 mA over the cell until a cut-off potential of 4.8 V vs. Li/Li^+ is reached. The partial pressures of the cell headspace on masses m/z = 2 (H_2), 18 (H_2O), 28 (CO), 32 (O_2), 44 (CO_2), 45 (DME) were recorded in 10 min intervals.

Results

Figure 1 shows the potential and gas evolution profiles of the galvanostatically charged pre-filled electrode. On charge, E increases from open circuit potential of 2.6 V to 4.5 V before it drops to the potential plateau at 4.07 V. The initial potential peak has previously [2] been associated with the oxidation of the ether electrolyte to form H_2O and other organic species, which indeed can be confirmed by our OEMS. The latter species are suggested [2] to enable the oxidation of the electronically insulating µm-sized Li_2O_2 electrode particles, either by increasing their solubility or acting as redox shuttles.

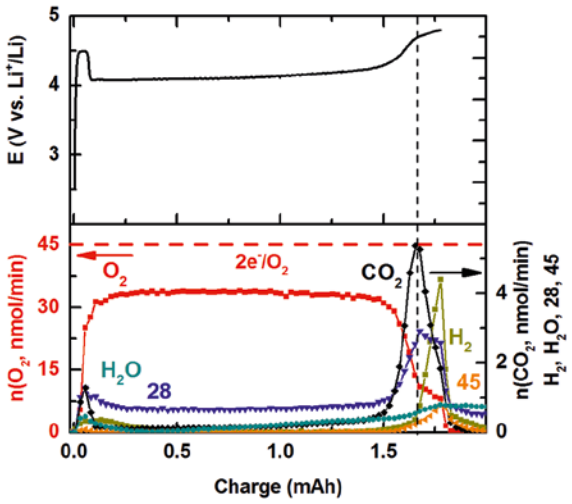

Figure 1: *Potential and gas evolution profiles during the galvanostatic charge of the pre-filled Li_2O_2 electrode.*

Interestingly, nearly all Li_2O_2 available in the electrode is oxidized (dashed line in Figure 1 denotes estimated charge available). However, judging from the total O_2 yield (~ 79 %) and the variety of volatile side-reaction products registered (e.g., H_2O, CO, CO_2, H_2), the parasitic reactions are extensive during the whole charge process. The oxidation process at the potential plateau indicates a single process, generating a constant evolution rate of O_2, CO and possibly non-volatile products (e.g., Li_2CO_3) as the CO_2 evolves at higher E in the end of charge. Unlike dimethyl ether (m/z = 45), CO_2 is not a direct product of the anodically decomposed electrolyte [1].

Conclusion

OEMS provides valuable insights into the oxidation of pre-filled Li_2O_2 electrodes. The initial potential peak and the accompanying formation of H_2O is likely a prerequisite for Li_2O_2 oxidation, which thereafter results in a constant evolution of O_2, CO and possibly non-volatile decomposition products until all Li_2O_2 is depleted.

Acknowledgment

The authors acknowledge BASF for financial support.

References

[1] A.C. Luntz, B.D. McCloskey, *Chem. Rev.* **114**, 11721–11750 (2014).
[2] S. Meini, S. Solchenbach, M. Piana, H.A. Gasteiger, *J. Electrochem. Soc.* **161**, A1306–A1314 (2014).
[3] E. Berg, P. Novák, *ECL – Annual Report* **2012**, 47–48 (2012).

Investigation of the early stages of surface layer formation on cycled HE-NCM vs. LTO electrodes using XPS

A.J. Gillen, C. Villevieille, E. Jämstorp Berg, P. Novák, M. El Kazzi
Phone: +41 56 310 5149, e-mail: mario.el-kazzi@psi.ch

Nowadays, it is well known that the surface layer developed on positive and negative electrodes during cycling directly affects the batteries performance. The mechanisms behind the formation of the surface layer and its chemical composition have a direct impact on its physical and chemical properties. Moreover, parameters like the applied potential, electrolyte, temperature, cycle number and cycle rate are considered important elements leading to drastic modification of the surface of the electrodes.

In this context, the aim of this work is to investigate the surface layers developed on top of HE-NCM and LTO when cycled together in a full cell configuration at room temperature using carbonate-based electrolyte. Thanks to the appropriate balancing of the electrodes, it is possible to cycle HE-NCM within 2.4 V – 5.1 V vs. Li/Li^+ cutoff limits, while LTO remains on the plateau of 1.55 V vs. Li/Li^+ (see Figure 1). For this purpose, post mortem scanning electron microscopy (SEM) will be performed after long cycling in order to elucidate the evolution of the surface morphology and to clarify the impact of the washing.

These measurements will be correlated with post mortem X-ray photoelectron spectroscopy (XPS) carried out during the early stages of cycling (first charge) (see Figure 1) to monitor the impact of the applied potentials on the chemical composition.

Experimental

Negative and positive electrodes were prepared by casting a mixture of 90 % active material LTO (Clarient) or HE-NCM (BASF) with 6 % PVDF (binder) and 4 % Super-C carbon which was used as a conductive additive (TIMCAL), all suspended in N-methyl-2-pyrrolidone (Fluka) and then spread onto an aluminum foil current collector. After drying at 120 °C overnight, the electrodes were punched out and assembled in an argon-filled glove box. Two carbonate based electrolytes were employed for this study:

- LP30 (from BASF) which is a mixture of 1 M $LiPF_6$ with ethylene carbonate and dimethyl carbonate (EC:DMC, 1:1), and
- LC30, which is a mixture of 1 M $LiClO_4$ again with a 1:1 ratio of EC:DMC.

The measurements were carried out on both unwashed and washed (with DMC) electrodes, which were transferred from the glovebox to the XPS/SEM using an Ar-filled atmosphere chamber or vacuum transfer chamber, respectively.

Electrochemical properties

Figure 1 shows the first one and a half cycles of a galvanostatic (GS) curve performed in a three electrodes arrangement cell. HE-NCM is cycled vs. LTO at room temperature (RT) at a C/5 rate using LP30 as electrolyte. Metallic lithium is used as a reference electrode enabling the exact measurement of the potential across the LTO and HE-NCM.

During the first delithiation in LP30 two main plateaus are visible. The first plateau is attributable to the oxidation of Ni^{2+} to Ni^{3+} while the second plateau is associated with Li_2MnO_3 activation with the irreversible removal of Li_2O. Once the material is activated by releasing oxygen, we can clearly see that this peak disappears during the following cycle.

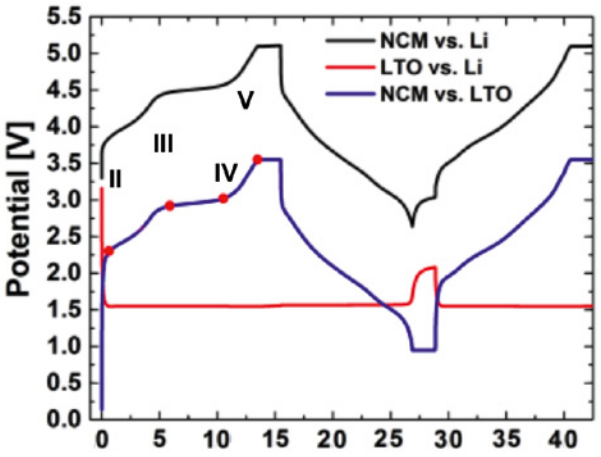

Figure 1: *Galvanostatic curve for the first full cycle and the second charge performed in 3 electrodes arrangement cell. HE-NMC is cycled vs. LTO with LP30 electrolyte at room temperature and using metallic Li as a reference electrode. Potentiostatic steps examined using XPS are marked in red.*

Post mortem SEM

Figure 2 shows the SEM images of HE-NCM and LTO electrodes (Figure 2 A and B) soaked for over 3 weeks in LP30 which are compared with the unwashed samples (Figure 2 C and D) cycled at C/5 rate in LP30 for ~125 cycles. A thick surface layer was detected on top of LTO covering completely the LTO particles and Super C, while a much thinner layer was seen on the HE-NCM supported by the fact that it's still possible to distinguish individual particles. This observation is contrary to what was expected, as the LTO was cycled on the plateau at 1.55 V (Figure 1) above the reduction potential (~0.8 V) of the EC and DMC. Thus, there should have been no reduction of the electrolyte, meaning no surface layer formation as claimed by the battery community.

The SEM measurements performed on the electrodes soaked in LP30, show no surface layer on LTO, excluding the impact of the EC and DMC drying process. On the other hand Figure 2. E and F, performed on washed electrodes cycled with LP30, show that the surface layer is removed and LTO and Super C particles are visible again. This observation confirms there is a risk of destroying precious information from the surface by washing the electrodes with DMC before performing measurements.

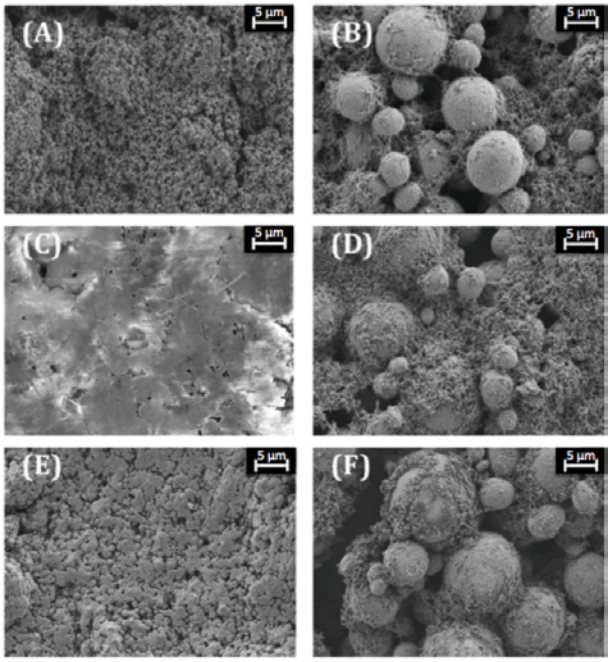

Figure 2: *SEM images of (A) LTO and (B) HE-NCM electrodes soaked 3.5 weeks in LP30; unwashed (C) LTO and (D) HE-NCM after ~125 cycles in LP30 at C/5 rate; (E) LTO and (F) HE-NCM after washing with DMC.*

Post mortem XPS

The XPS measurements presented in the following paragraphs were performed on unwashed electrodes in order to preserve the integrity of the species. It was decided that LC30, a fluorine free electrolyte, rather than LP30 would be used for these experiments. This electrolyte enabled the evolution of the fluorine from the PVdF to be followed without the need to consider any contribution from the ionic salts within the electrolyte.

All the measured cycled electrodes are compared to pristine LTO and HE-NCM which are used as reference electrodes.

(A) LTO electrodes

The C1s, F1s and Ti2p$_{3/2\text{-}1/2}$ core levels spectra acquired on the LTO electrodes at the various potentiostatic steps shown in Figure 1 are presented in Figure 3.

On the LTO pristine electrode, the most intense component in the C1s peak is at 284.01 eV binding energy (BE) attributed to the C-C bond of the Super C (shown in green). The peaks related to the two carbon species of the PVdF binder, (-CH_2-) and (-CF_2-), are also detected at 286.72 eV and 291.25 eV, respectively, (green). Additional components are observed, linked to hydrocarbons at 285.5 eV, carbon in the environment of C=O at 287.35 eV and of O-C=O at 288.8 eV (all in orange), and carbonate species Li_2CO_3/CO_3 at 290.1 eV (in blue). On the other hand the Ti2p$_{3/2\text{-}1/2}$ peak shows one single component associated with Ti^{4+} originating from the LTO. However, the F1s peak presents two components at 688.3 eV (red) and 685.6 eV (blue) related to the two species CF2 (PVdF) and LiF (reacted Li with the binder).

The increase of the potential on HE-NMC from open circuit until 5.1 V vs. Li/Li^+ leads to noticeable modification on the LTO surface. The C1s peak shows attenuation of the super C peak (C-C bond) until complete disappearance at 4.5 V, which is due to the continuing formation of a surface layer. Simultaneously, additional peaks show up at 285.7 eV, 287.6 eV, 290.1 eV and 291.5 eV associated with C-H hydrocarbon (orange), C=O (orange), Li_2CO_3 (blue) and either CF_2 or more complex species (in purple), respectively. The two components at 285.7 eV and 287.6 eV can be attributed to EC and DMC decomposition leading to the formation of linear polymers [3, 4].

As previously mentioned, the component at 291.5 eV cannot be completely attributed to the PVdF (CF_2) as from analysing the relative composition of this component and the F1s peak related to the PVdF, the implied ratio is close to C_5F_2. Therefore, we believe that the component at 291.5 eV is an overlap of two components, CF_2 from the binder and also dicarbonate generated from the EC/DMC decomposition [3].

The attenuation of the intensity of the Ti2p spectra supports the C1s behavior regarding the continuous increase of the surface layer during the first charge. At 5.1 V, the signal from the Ti2p remains detectible confirming that the surface layer thickness is approximatively below 8 nm (max. depth analysis of the XPS). The appearance of the Ti^{3+} peak, in addition to the presence of the Ti^{4+}, corresponds to the insertion of the Li^+ ions, as predicted by the equation [5]:

$$Li_4Ti_5^{IV}O_{12} + 3e^- + 3Li^+ \rightarrow Li_7\left(Ti_3^{III}Ti_2^{IV}\right)O_{12}$$

On the other hand the presence of the Ti^{2+} peak was unexpected, and its origin is still under consideration requiring further studies.

The additional peak detected in the F1s spectra at a potential of 3.85 V is due to the presence of LiF species. The only source of fluorine in the system is from the binder, PVdF, as the electrolyte was deliberately chosen to be fluorine free. As a result, the presence of the LiF peak implies that Lithium ions are reacting with the binder as the electrodes are being cycled.

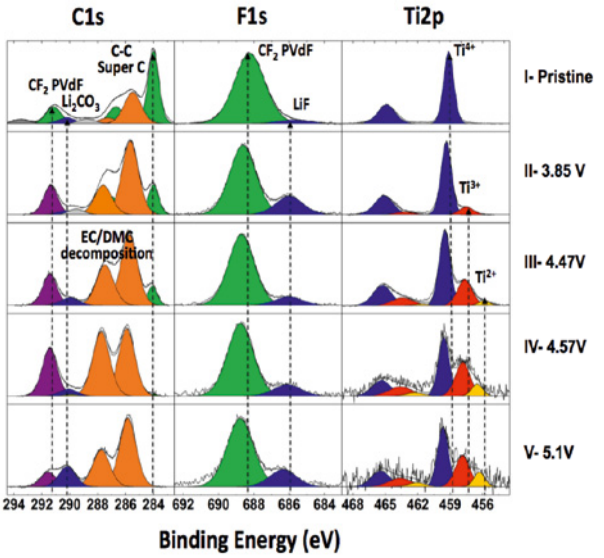

Figure 3: *C1s, F1s and Ti2p$_{3/2\text{-}1/2}$ XPS core levels acquired on pristine and unwashed LTO electrodes cycled to various potentiostatic points in LC30.*

No signals indicating the dissolution or migration of the transition metals (by measuring the Mn2p or Co2p core levels) were detected in the first cycle (not shown). However, trace amounts of Mn were detected after the second charge indicating that the migration of the transition metals occurred even in the early stages of cycling.

(B) HE-NCM electrodes

C1s, F1s and O1s spectra were recorded on the HE-NCM electrodes. On the pristine electrode, we are able to distinguish in the C1s and F1s peaks signals originating from Super C and PVdF (green). However, for the O1s peak the main component is related to oxygen metal bonds from HE-NCM.

For the electrodes measured after the potentiostatic steps, we observed an obvious shift of the PVdF component in the C1s and F1s peaks toward lower binding energy. The origin of the shift is still under investigation, but we believe it is related to the presence of negative charge trapped on the binder due to bad conductivity between the different particles within the electrode. This shift makes the tracking of the Li_2CO_3 species quit difficult due to the overlapping of the CO_3 component with CF_2 at ~ 290 eV in the C1s peak.

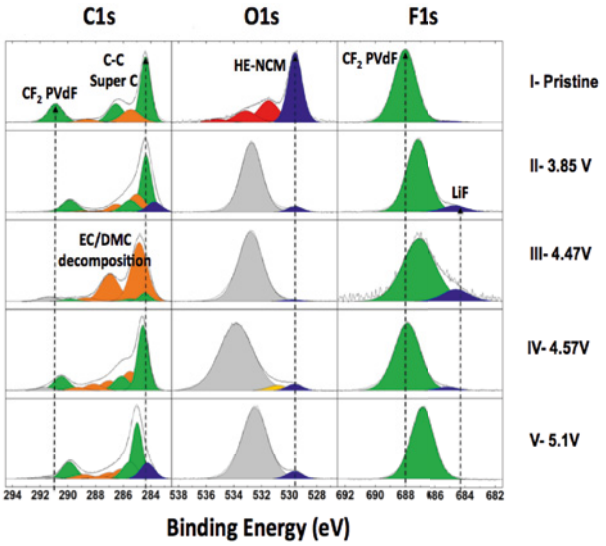

Figure 4: *C1s, F1s and O1s XPS core levels acquired on pristine and unwashed HE-NCM electrodes cycled to various potentiostatic points in LC30.*

Even though we have the shift on the PVdF, we were able to track the thickness evolution of the surface layer by following the super C and the M-O signals. At a first glance, we can notice that the intensity of these two components decreases slightly at 3.85 V and considerably at 4.47 V with a complete disappearance of the M-O signal. This behavior is followed by an increase of the C1s components associated to EC/DMC decomposition (in orange). However, the opposite phenomenon occurs for the further potentials 4.57 V and 5.1 V. The intensities of the Super C and M-O peaks increase continuously, followed by a diminution of the decomposed EC/DMC components (in orange). This behavior confirms that the surface on HE-NCM is thinner than on LTO due to the decomposition phenomena occurring at high potentials.

The decomposition of the binder in the HE-NCM electrodes is also significantly reduced compared to the LTO, indicated by the reduction in the intensity of the LiF peak in the F1s spectra.

Conclusion

It is clear from the information obtained using both XPS and SEM that there is an appreciable difference in the thickness and composition of the surface layer on the LTO compared to the HE-NCM.

The post mortem XPS acquired on both negative and positive electrodes after the early stages of cycling provided precious information regarding the electrolyte stability and the stages of surface layer formation and composition.

On HE-NCM, the surface layer seems to be much thinner than on LTO with a breathing dynamic mechanism around 4.47 V, corresponding to the beginning of the second plateau in the galvanostatic curve which is associated to the oxygen release. We observe a thickness increase during the charge up to 4.47 V which is then followed by a decrease at higher potentials. This behavior confirms:

- that the oxygen released from the surface contributes in the formation of species rich in oxygen like C-O and C=O, which are unstable at higher potential, and
- on the positive electrode the oxidation of the electrolyte is directly dissolved without being deposited as a thick solid layer on the surface.

On the other hand, the LiF species associated to the Li reaction with the PVdF appear at 3.85 V and 4.47 V, however again these species are not stable at higher potential and thus the decomposition phenomenon occurs.

Regarding the LTO electrode, the decomposition products of EC/DMC are more pronounced, and the thickness of the surface layer is continuously increasing with the applied potential. Moreover, unlike the HE-NCM electrode the LiF species are present along the full charge process, indicating an absence of the decomposition phenomenon. The origin of the surface layer developed on the 1.55 V plateau is still not completely elucidated, however we suggest two possibilities. The surface layer may either be related to

- the reduction of the electrolyte or
- to the diffusion of organic species formed at the positive electrode toward the negative.

Acknowledgment

The authors are very grateful for the financial support from BASF SE.

References

[1] J. Christensen, V. Srinivasan, J. Newmana, *J. Electrochem. Soc.* **153** (3), A560–A565 (2006).
[2] H. Yu, H. Kim, Y. Wang, P. He, D. Asakura, Y. Nakamura, H. Zhou, *Phys. Chem. Chem. Phys.* **14**, 6584–6595 (2012).
[3] I.A. Shkrob, Y. Zhu, T.W. Marin, D. Abraham, *J. Phys. Chem.* **117**, 19270–19279 (2013).
[4] I.A. Shkrob, Y. Zhu, T.W. Marin, D. Abraham, *J. Phys. Chem.* **117**, 19255–19269 (2013).
[5] D.R. Simon, *Characterization of $Li_4Ti_5O_{12}$ and $LiMn_2O_4$ spinel materials treated with aqueous acidic solutions*, PhD Thesis, University of Cincinnati (2007).

Gas evolution reactions on carbon additives in lithium-ion batteries

M. He, P. Novák, E.J. Berg
phone: +41 56 310 5032, e-mail: minglong.he@psi.ch

Lithium-ion batteries are expected to become the power supply in future electrical and hybrid vehicles.

However, lithium-ion batteries still face several issues related to performance and safety, which consequently act as a barrier for the commercial application. For instance, it has been widely reported that electrolyte decomposition occurs on the carbon electrode surface with gas generation and irreversible capacity loss when a solid electrolyte interphase (SEI) layer is formed [1–3]. The gas evolution increases the internal pressure of lithium-ion batteries gradually, which may lead to the deformation of electrodes and expansion of the sealed cell body, and in the end, both safety and performance is compromised.

The electrolyte decomposition reaction rate and mechanism depend not only on the electrolyte composition but also on the electrode components and the surface chemistry/structure of the electrodes. The influence of various electrode additives on electrolyte stability needs to be defined separately. Due to the high sensitivity and specificity of the mass spectrometers, online electrochemical mass spectrometry (OEMS) offers an approach for analysing gaseous and volatile species evolved at the electrode surface [4]. During the cycling, electrolyte decomposition products, e.g., H_2, CO_2 and C_2H_4, can be detected continually. The goal of the present study is to investigate the gas evolution reactions on most commonly used carbon additives by OEMS technique.

Experimental

Carbon working electrodes were prepared by adding Super C65 carbon (Imerys Graphite & Carbon, Switzerland) to polytetrafluoroethylene (PTFE) dispersion (PTFE:water = 6:4 by weight ratio, Sigma Aldrich, Switzerland) under stirring at 100 °C until complete solvent evaporation. Then the obtained dry paste (carbon:PTFE = 9:1 by weight ratio) was rolled to the desired thickness of 200 µm. The electrodes were heated at 80 °C under dynamic vacuum overnight before introducing them into an argon-filled glove box where both oxygen and water content was less than 0.1 ppm. LP30 (1 M $LiPF_6$ in EC:DMC = 1:1 by weight ratio, BASF, Germany), was used as the electrolyte. The water content of LP30 was measured by Karl Fischer titration to be less than 15 ppm.

The OEMS cell [5] was assembled with metallic lithium (Ø 18 mm) as counter electrode, Celgard 2400 separator (Ø 28 mm), carbon electrode as working electrode (Ø 18 mm) and 200 µL LP30 electrolyte. The working principle of OEMS has been introduced in the literature [4]. Cyclic voltammetry (CCCC, Astrol Electronics, Switzerland) was performed at a scan rate of 0.25 mV/s in potential windows of 5 mV – 3 V and 3-5 V vs. Li^+/Li. For OEMS experiments, 3 hours of equilibration time at 3 V vs. Li^+/Li was added before starting the cyclic voltammetry.

Results

Figure 1 shows the potential and CO_2 gas evolution profiles of a Super C65 carbon based electrode during potentiodynamic cycling in the positive potential window. Three peaks of CO_2 evolution are observed at 3.8–4.6 V, 4.6–5 V and 3.6–3 V vs. Li^+/Li, respectively. The first CO_2 evolution onset located at 3.8 V vs. Li^+/Li probably origins from the oxidation of carbon surface groups, while the second CO_2 evolution peak starting at 4.6 V vs. Li^+/Li typically comes from the direct oxidation of organic carbonate based electrolytes, e.g., ethylene carbonate (EC) and dimethyl carbonate (DMC) [6]. Detailed suggested mechanisms of EC oxidation are illustrated in Scheme 1. CO_2, CO, acetaldehyde, ethylene oxide and the other active radicals are believed to be the main products of oxidation reactions. However, only the volatile species, e.g., CO_2 and CO, can be detected by mass spectrometry.

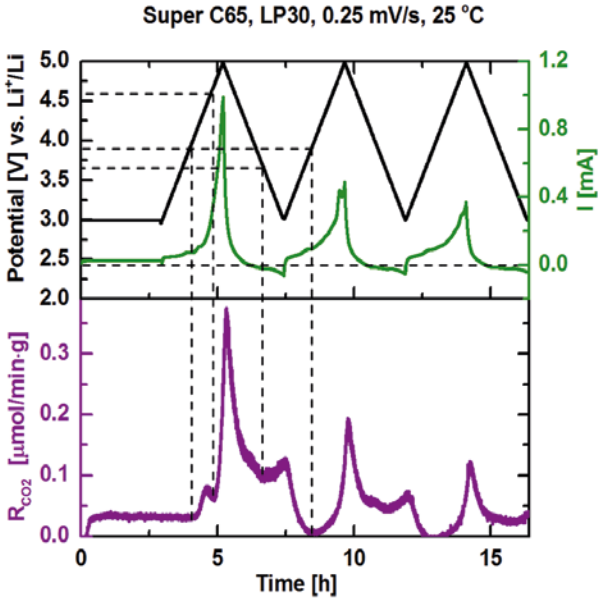

Figure 1: *Potential and gas evolution profiles of CO_2 in the half-cell with Super C65 in LP30 electrolyte.*

The third CO_2 evolution peak onset appears when the potential sweeps back to 3.6 V–3 V vs. Li^+/Li. This gas evolution peak may be explained by two possible mechanisms: Firstly CO_2 gases which evolve during two oxidation processes are trapped in the micro/meso-pores and/or passivation layers in the carbon matrix and they are released with a delay. Secondly, the oxidation products formed during the anodic sweep and residing at the electrode may be reduced on the reverse sweep, leading to additional gas evolution.

The amount of CO_2 can be quantified by integrating the area of the curve of the CO_2 evolution rate as a function of time. In the initial cycle, the oxidation of functional groups contributes 1.2 µmol/g CO_2, which is one order of magnitude less than the amount of CO_2 (15 µmol/g) from electrolyte oxidation. The peak of CO_2 evolution caused by oxidation of surface groups

disappears in the later cycles. On the contrary, CO_2 induced by electrolyte decomposition continues to evolve, though the quantity decreases gradually indicating the formation of a passivation layer on the electrode, which retards further electrolyte oxidation.

Figure 2 shows the potential and CO_2 gas evolution profiles of Super C65 carbon based electrodes during potentiodynamic cycling in the reductive potential window. C_2H_4 and H_2 start to evolve simultaneously when the potential approaches 0.75 V vs. Li^+/Li. This potential agrees with the formation of a SEI layer on graphite electrodes at a potential around 0.8 V vs. Li^+/Li [7] followed by the reductive decomposition of EC and DMC [8]. The suggested reductive reaction routes of EC are shown in Scheme 1.

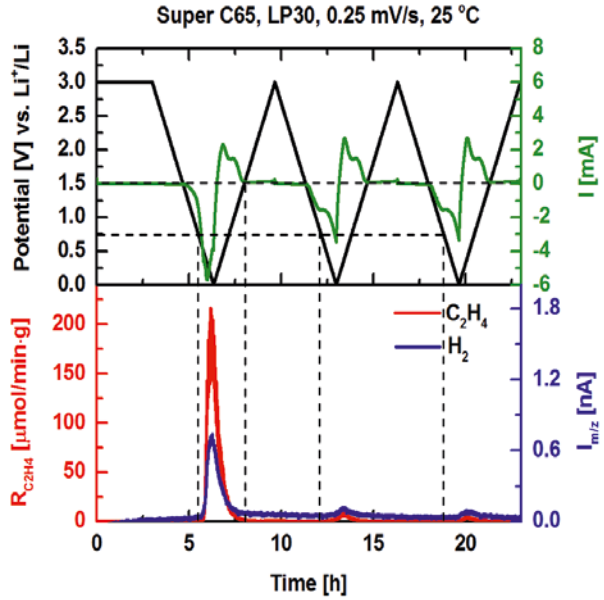

Figure 2: *Potential and gas evolution profiles of C_2H_4 and H_2 in the half-cell with Super C65 in LP30 electrolyte.*

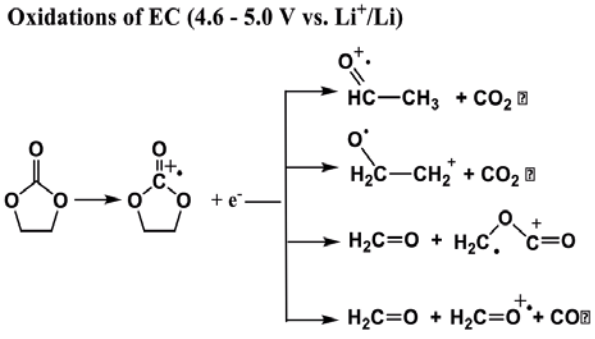

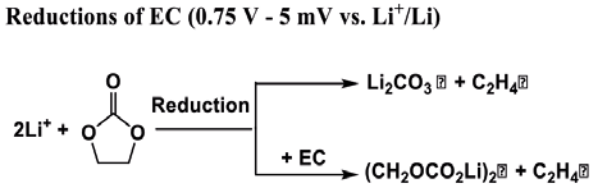

Scheme 1: *Oxidative and reductive decomposition reactions of ethylene carbonate [6, 8].*

C_2H_4 and H_2 are typical by-products of EC reduction [4, 9]. The maximum C_2H_4 and H_2 evolution rates are observed at the potential of 0.15 V vs. Li^+/Li and gas evolution vanishes at the potential of 1.5 V vs. Li^+/Li during the positive CV sweep. In later cycles, gas evolution onsets remain unchanged, while the maximum value of C_2H_4 evolution rate drops down dramatically from 216 µmol/g·min to 4.3 µmol/g·min during the first 3 cycles. A SEI like passivation layer is believed to form on the surface of carbon additives, which effectively protects electrolyte from further decomposition.

Conclusions

In this work, onsets, the type and the extent of side reactions on the conductive carbon have been quantified by *in situ* OEMS technique. When the potential sweeps to a more positive potential range (> 3 V vs. Li^+/Li), surface groups on the carbon surface are oxidized first in the potential window of 3.8 – 4.6 V vs. Li^+/Li. Then CO_2 gas continues to evolve at 4.6 – 5.0 V vs. Li^+/Li due to the electrolyte oxidation. In the potential window of 5 mV – 1.5 V vs. Li^+/Li, C_2H_4 and H_2 are detected as a result of electrolytes reduction. A SEI like passivation layer on the carbon is also formed on the surface of carbon additives. According to the quantitative analysis of gas evolution, side reactions on conductive carbons in lithium-ion batteries are often disregarded, but are considerable.

Acknowledgement

The authors are grateful to the Polish-Swiss Research Programme for the financial support.

References

[1] R. Fong, U. von Sacken, J.R. Dahn, *J. Electrochem. Soc.* **137**, 2009–2013 (1990).
[2] H. Yoshida, T. Fukunaga, T. Hazama, M. Terasaki, M. Mizutani, M. Yamachi, *J. Power Sources* **68**, 311–315 (1997).
[3] M. Winter, J.O. Besenhard, M.E. Spahr, P. Novák, *Adv. Mater.* **10**, 725–763 (1998).
[4] R. Imhof, P. Novák, *J. Electrochem. Soc.* **145**, 1081–1087 (1998).
[5] E.J. Berg, P. Novak, *PSI – Annual Report* **2012**, 47 (2012).
[6] L. Xing, W. Li, C. Wang, F. Gu, M. Xu, C. Tan, J. Yi, *J. Phys. Chem. B* **113**, 16596–16602 (2009).
[7] P. Verma, P. Maire, P. Novák, *Electrochim. Acta* **55**, 6332–6341 (2010).
[8] K. Xu, *Chem. Rev.* **104**, 4303–4418 (2004).
[9] P. Novák, F. Joho, R. Imhof, J.C. Panitz, O. Haas, *J. Power Sources* **81-82**, 212–216 (1999).

Surface electrochemical and DEMS studies of the 4 V cathode material $LiNi_{0.80}Co_{0.15}Al_{0.05}O_2$ for Li-ion batteries

R. Robert, C. Bünzli, E. J. Berg, P. Novák
phone: +41 56 310 5426, e-mail: rosa.robert@psi.ch

The layered oxides cathode materials have been and are still under intense investigations for Li-ion batteries. The layered $LiNi_{0.80}Co_{0.15}Al_{0.05}O_2$, also known as NCA, is a promising high-voltage Li-ion cathode material where Al doping provides an improved thermal stability at high potentials. In the NCA electrode, the first charge oxidation process is characterized by an activation of the electrode and a large irreversible specific charge loss with respect to the second charge cycle. These effects have been attributed to surface reactions [1, 2], and/or to structural changes [3]. Despite much work done on this material, there still is no detailed understanding of the contribution of surface reactions to the activation of the material and how these reactions affect the (de)lithiation potential of the NCA electrode when the electrodes are cycled at different scan rates.

In this work, we carried out operando differential electrochemical mass spectrometry (DEMS), electrochemical cyclic voltammetry, and electrochemical impedance spectroscopy to identify how the surface changed after the first three charge/discharge cycles and its effects on electrochemical response.

Experimental

The positive NCA electrode was prepared as in [4]. Cyclic voltammograms were carried out at rate of 20 µV/s. Structural investigations were performed at the Materials Science Beamline of the Swiss Light Source (SLS) at PSI Villigen. DEMS experiments were performed in an electrochemical half-cell as described elsewhere [5]. Electrochemical impedance spectroscopy (EIS) of the NCA electrodes was measured in the LP30 electrolyte in a 3-electrode setup [6] with a $Li_4Ti_5O_{12}$-based counter electrode and lithium metal as the reference electrode. The data was recorded with a VMP3 potentiostat (BioLogic Science Instruments) in a temperature controlled chamber at 25 °C.

Results

Results of operando DEMS experiments, performed during cell operation in cyclic voltammetry mode in the potential range of 3.0 V to 4.9 V vs. Li^+/Li at 50 µV/s, are shown in Figure 1. DEMS results reveal that CO_2 gas ($I_{m/z} = 44$) is constantly released during oxidation, starting at ~ 4 V in the first and at ~ 3.6 V in the second cycle. CO_2 evolution is observed to be promoted by both higher potentials and cell currents (dashed lines, Figure 1b) as charge transfer at the interface occurs.

Synchrotron X-ray powder diffraction experiments reveal the existence of a minor Li_2CO_3 phase in the diffraction pattern of the pristine material (Figure 2). Lithium carbonate is formed as a result of a surface reaction of the NCA electrode with atmospheric CO_2 as follows:
$Li(Ni,Co,Al)O_2 + ½\ CO_2 + ¼\ O_2 \rightarrow Li_{1-x}(Ni,Co,Al)O_2 + ½\ Li_2CO_3$ [7].

Thus, the largest contribution to the CO_2 signal until overcharge condition is attributed to the decomposition of the Li_2CO_3 surface film. Above the potential at which the carbonate electrolyte is stable, CO_2 gas evolution is expected from its oxidative decomposition [8].

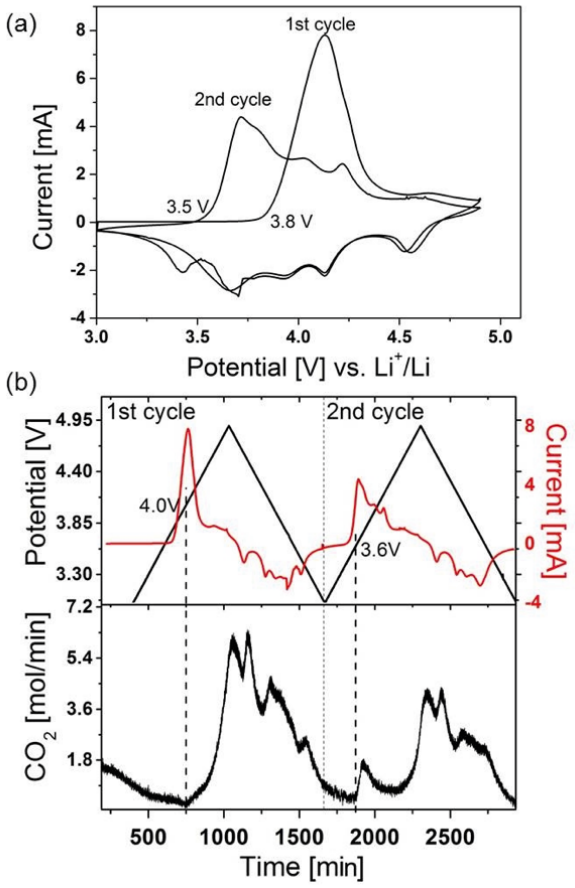

Figure 1: *a) Cyclic voltammogram of $LiNi_{0.80}Co_{0.15}Al_{0.05}O_2$ in the potential range of 3.0 V to 4.9 V vs. Li^+/Li at 50 µV/s in LP30, and b) DEMS data vs. time with the current, potential, and plot of the most relevant mass signal intensity CO_2 ($I_{m/z} = 44$).*

Figure 2 displays the X-ray patterns of powders charged to several potential values, on the first charge at 4.3 V, 4.6 V, 4.9 V, and on second charge at 4.3 V, 4.9 V, respectively. The Li_2CO_3 phase, existing already in the pristine powder, persists under electrochemical conditions until 4.6 V, above this potential, i.e., at 4.9 V, the Bragg peaks of the lithium carbonate phase disappear. After electrochemical reduction to 3.0 V and subsequent oxidation to 4.3 V, Li_2CO_3 phase is again present which indicates that the Li_2CO_3 phase is reformed during reduction with a possibly associated consumption of gaseous CO_2.

EIS measurements were used to evaluate the effect of Li_2CO_3 dissolution and reformation on the resistance of the NCA electrode before cycling at OCV and at the end of charge and discharge for 3 cycles when cycling between 3.0 and 4.3 V vs. Li^+/Li. The EIS spectra were fitted based on the equivalent circuit

$[R_S([R_1Q]C_1)]$ at 3.0 V and $[R_O(R_1C_1)([R_2W]C_2)]$ at 4.3 V, where R_O is the ohmic resistance (mainly solution resistance contribution), R_1 and C_1 are the resistance and capacitance of the high frequency semicircle, respectively, while R_2 and C_2 correspond to the resistance and capacitance of the low frequency arc, Q is a constant phase element, and W is a Warburg impedance.

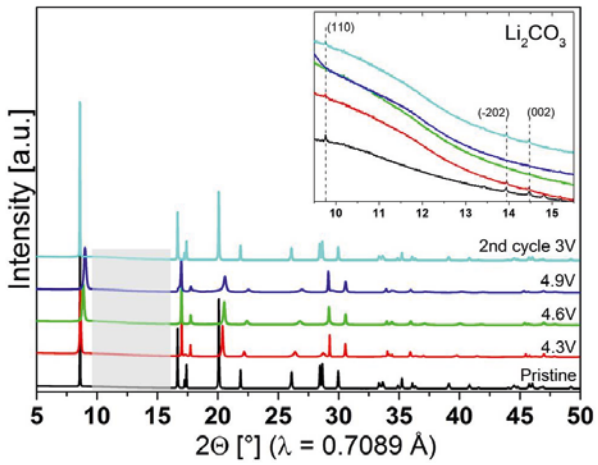

Figure 2: *Synchrotron ex situ X-ray diffraction pattern for pristine $LiNi_{0.80}Co_{0.15}Al_{0.05}O_2$ and powders cycled to different upper cut-off potentials during the first and second charge and discharged to 3 V at room temperature. Bragg peaks are assigned to the Li_2CO_3 phase C12/c1 (S.G. 15). Inset: enlarged patterns of NCA electrodes in the 2 θ range between 9.5° and 15.5°.*

Figure 3 represents the evolution of the corresponding R_1 and C_1 with cycle number, at the end of charge and discharge. After the first charge to 4.3 V, R_1 initially increases with respect to the OCV value, however, in the following cycles, the resistance R_1 decreases during delithiation to 4.3 V and increases upon lithiation to 3.0 V.

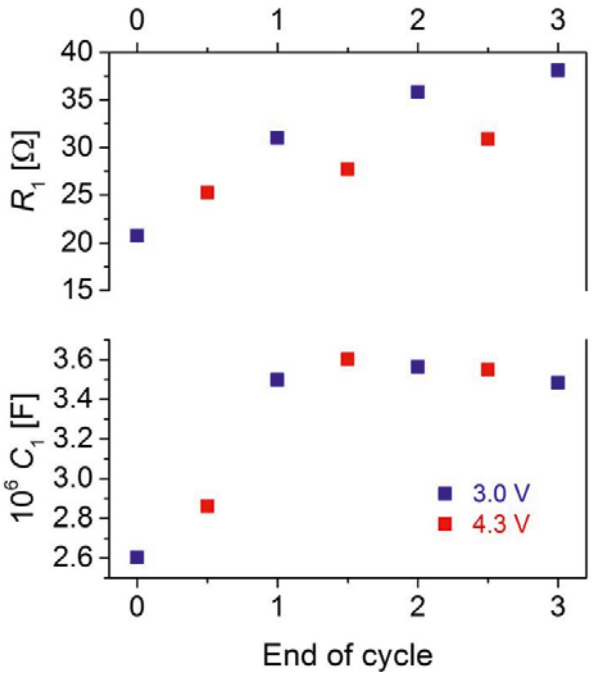

Figure 3: *The resistance (R_1) and the capacitance (C_1) values corresponding to the high frequency arc obtained from fitting the spectra (see text for equivalent circuit model).*

The observed alternating resistance is most likely caused by the lithium carbonate evolution during cycling. After the first charge cycle, both R_1 and R_2 increase with every cycle due to the microstructural degradation at the surface of the NCA particles [9] and to the accumulation of an insulating surface film and loss of particle contact(s).

On the basis of these studies, we can conclude that the Li_2CO_3 surface film on the NCA electrode degrades on oxidation and reforms on reduction having an effect on the lithium (de)-insertion reaction's kinetics.

References

[1] S.S. Zhang, K. Xu, T.R. Jow, *Electrochem. Solid-State Lett.* **5**, A92–A94 (2002).
[2] J. Choi, A. Manthiram, *Electrochem. Solid-State Lett.* **8**, C102–C105 (2005).
[3] H. Arai, S. Okada, Y. Sakurai, J.-I. Yamaki, *Solid State Ionics* **95**, 275–282 (1997).
[4] R. Robert, C. Bünzli, E.J. Berg, P. Novák, *Chem. Mater.* **27** (2), 526–536 (2015).
[5] P. Novák, D. Goers, L. Hardwick, M. Holzapfel, W. Scheifele, J. Ufheil, A. Würsig, *J. Power Sources* **146**, 15–20 (2005).
[6] C. Bünzli, H. Kaiser, P. Novák, *J. Electrochem. Soc.* **162** (1), A218–A222 (2014).
[7] K. Matsumoto, R. Kuzuo, K. Takeya, A. Yamanaka, *J. Power Sources* **81-82**, 558–561 (1999).
[8] E. Castel, E.J. Berg, M. El Kazzi, P. Novák, C. Villevieille, *Chem. Mater.* **26**, 5051–5057 (2014).
[9] S. Muto, K. Tatsumi, Y. Kojima, H. Oka, H. Kondo, K. Horibuchi, Y. Ukyo, *J. Power Sources* **205**, 449–455 (2012).

Complementary operando XPS and Raman spectroscopy of graphite cycled in ionic liquids

D. Streich, E. Jämstorp Berg, P. Novák, M. El Kazzi
phone: +41 56 310 5149, e-mail: mario.el-kazzi@psi.ch

Graphite is the most common negative electrode material in Li-ion batteries today and has been extensively studied, in particular in carbonate electrolytes [1]. In contrast, comparatively little is known about the electrochemistry of graphite in ionic liquid electrolytes which are considered to be an alternative for next generation high energy density Li-ion batteries owing to their low vapor pressure and high thermal as well as electrochemical stability [2].

While positive electrode materials have been shown to reversibly cycle in ionic liquid electrolytes [3], similar attempts using graphite as negative electrode have so far been less successful [4]. However, it was demonstrated recently that the reversibility of graphite cycling is significantly improved in presence of bis(fluorosulfonyl) imide ($[FSI]^-$, Scheme 1) [5]. To understand the origin of this beneficial effect, structural and chemical information is needed at the level of the electrode, the electrode/electrolyte interface and the electrolyte. The aim of the work presented here is to acquire this kind of information for graphite electrochemically cycled in 1-ethyl-3-methylimidazolium / bis(trifluorome-thanesulfonyl) imide ([EMIM][TFSI], Scheme 1) ionic liquid electrolyte (IL). The impact of the employed Li salt (LiTFSI or LiFSI, Scheme 1) was investigated using two complementary operando characterization techniques. Structural changes on the level of the electrode were studied by operando Raman spectroscopy. Ionic liquid electrolyte stability at the electrode/electrolyte interface during electrochemical cycling was monitored by operando X-ray photoelectron spectroscopy (XPS).

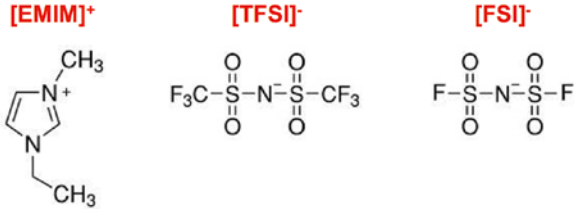

Scheme 1: *Ionic species comprising the ionic liquid electrolytes employed for electrochemical graphite cycling.*

Operando Raman study of T1000-8000 graphite particles

Raman spectroscopy is a convenient tool for monitoring ion intercalation and de-intercalation processes in graphitic carbon. Graphite has a characteristic g-band absorption located at 1585 cm^{-1}. During the different stages of Li^+ intercalation into graphite (e.g., during cycling of graphite against Li metal in LP30 electrolyte) this g-band initially shifts a few cm^{-1} towards higher energy and eventually splits into two bands located at 1580 and 1600 cm^{-1}, respectively. In ionic liquid electrolytes interesting deviations from this behavior were observed. When a polished Timrex T1000-8000 graphite particle (Imerys) is cycled against a Li metal counter electrode in 1 M LiTFSI / [EMIM][TFSI], one new band located at 1605 cm^{-1} grows in at the expense of the original g-band when the potential is decreased stepwise (Figure 1, top). The spectral changes are partially reversed when the potential is increased back to values positive of 1 V vs. Li^+/Li and also observed with Li^+-free [EMIM][TFSI] electrolyte (data not shown). In contrast, a striking difference in cycling behavior is obtained when the electrolyte salt LiTFSI is replaced by LiFSI (Figure 1, bottom). Under these conditions the formation of the 1605 cm^{-1} band is still observed but in addition there is also clear evidence for reversible Li^+ intercalation into graphite. Our current interpretation of these findings is that $[EMIM]^+$ and Li^+ compete for intercalation sites in graphite. In the absence of Li^+ and when LiTFSI is used as electrolyte salt, only $[EMIM]^+$ intercalation takes place. The presence of $[FSI]^-$, in contrast, appears to facilitate Li^+ intercalation.

The most obvious hypotheses for why this happens are that $[FSI]^-$ has a beneficial influence on the formation of the solid electrolyte interphase (SEI) and/or on Li^+ de-solvation. Since SEI formation and Li^+ de-solvation are processes that cannot be monitored by operando Raman spectroscopy, further studies employing X-ray photoelectron spectroscopy (XPS) were carried out. For reasons of practicability highly ordered pyrolytic graphite (HOPG) electrodes were used in this context.

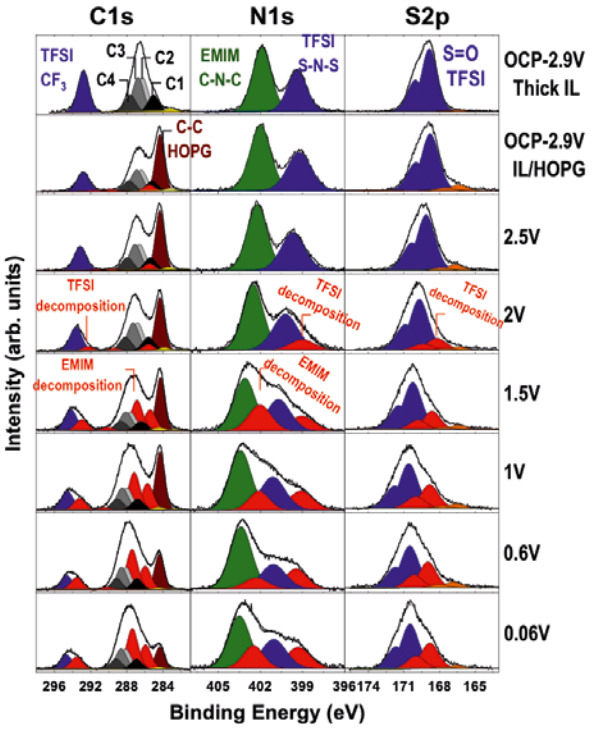

Figure 1: *Operando Raman characterization of T1000-8000 graphite particles cycled in discrete potential steps against Li metal in 1 M LiTFSI / [EMIM][TFSI] (top) and 1 M LiFSI / [EMIM][TFSI] (bottom). Solid vertical lines highlight the positions of the original g-band and the new band growing in at potentials ≤ 770 mV vs. Li^+/Li. The bent arrows indicate the g-band shift and split associated with Li^+ intercalation. Dashed vertical lines refer to the positions of the split g-band components characteristic for the later stages of Li^+ intercalation.*

Operando XPS study of HOPG

Operando XPS measurements were performed at the electrode/electrolyte interface and at a spot representative of the bulk electrolyte in an electrochemical cell comprising 1 M LiTFSI / [EMIM][TFSI] ionic liquid electrolyte, a highly ordered pyrolytic graphite (HOPG) working electrode and a Li metal counter electrode (Figure 2).

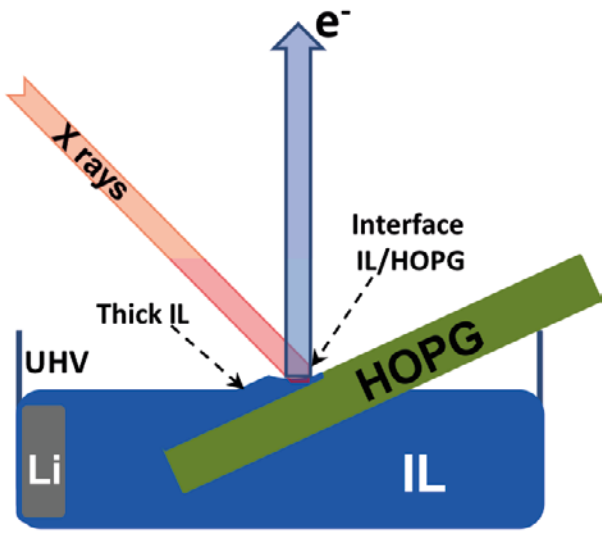

Figure 2: *Sketch of the operando XPS electrochemical cell. Dashed arrows indicate the spots probed to characterize bulk ionic liquid («Thick IL») and the ionic liquid / HOPG interface («Interface IL/HOPG»).*

In the bulk electrolyte («Thick IL»), signals originating from $[EMIM]^+$ and $[TFSI]^-$ are observed in the C1s, N1s and S2p core level spectra (Figure 3, top row). The C1s spectrum allows to distinguish between $[TFSI]^-$ CF_3 carbon on the one hand and the different $[EMIM]^+$ carbon atoms on the other hand (black: aliphatic carbon {C1}, light grey: C-N carbons {C2}, grey: imidazolium ring C=C*-N carbon {C3}, dark grey: imidazolium ring N-C-N carbon {C4}). In the N1s spectrum the $[EMIM]^+$ C-N-C (green) and [TFSI] S-N-S (dark blue) nitrogen atoms can be observed and distinguished. The $[TFSI]^-$ S=O sulphur atoms are the only species contributing to the S2p spectrum. At the electrode/electrolyte interface all of the bulk electrolyte signals are observed (Figure 3, second row). The only difference with respect to bulk electrolyte is an additional signal in the C1s spectrum that originates from HOPG C-C carbon atoms (wine). When the potential is stepped from OCP to 2.5 V vs. Li^+/Li no changes in any of the monitored XPS core levels are observed, suggesting that the ionic liquid is stable (Figure 3, third row). At 2.0 V vs. Li^+/Li, additional components (red) start to appear in the C1s, N1s and S2p spectra (Figure 3, fourth row). These components correspond to CF_3, S-N-S and S=O signals shifted towards lower binding energy compared to $[TFSI]^-$, and are therefore tentatively assigned to $[TFSI]^-$ decomposition products. Interestingly, there is no evidence for $[EMIM]^+$ decomposition until the potential is stepped further down to 1.5 V vs. Li^+/Li when new, low binding energy $[EMIM]^+$ C1s as well as N1s signals are observed (Figure 3, fifth row). All $[TFSI]^-$ and $[EMIM]^+$ de-composition product signals remain visible down to 0.06 V vs. Li^+/Li (Figure 3, sixth through bottom row). However, no new HOPG C-C C1s species are observed even at potentials as low as 0.06 V vs. Li^+/Li suggesting that Li^+ intercalation into HOPG is severely impeded or not occurring at all under these experimental conditions.

Conclusion

Complementary information about the changes occurring at the electrode/electrolyte interface of graphite negative electrodes electrochemically cycled in [EMIM][TFSI] ionic liquid electrolyte was successfully obtained by a combination of operando Raman and X-ray photoelectron spectroscopy. The Raman results show that $[EMIM]^+$ competes strongly with Li^+ for intercalation sites in graphite. Li^+ intercalation only takes place at a detectable level in presence of $[FSI]^-$. The operando XPS results indicate that both $[TFSI]^-$ and $[EMIM]^+$ undergo reductive decomposition reactions during cycling. Interestingly, $[TFSI]^-$ decomposition starts already at 2.0 V whereas $[EMIM]^+$ decomposition requires potentials ≤ 1.5 V vs. Li^+/Li.

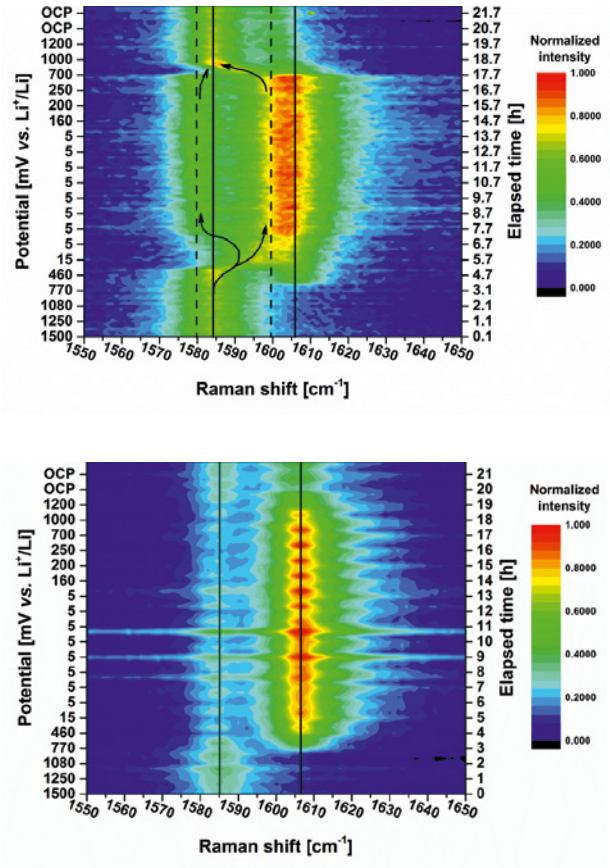

Figure 3: *Operando XPS spectra during first reduction of HOPG against Li metal in 1 M LiTFSI / [EMIM][TFSI]. The C1s, N1s and S2p spectra at the surface of bulk ionic liquid (1 M LiTFSI / [EMIM][TFSI]) at 2.9 V open circuit potential (top row) are compared to the spectra acquired at the electrode/electrolyte interface at potentials ranging from 2.9 V (open circuit potential, second row) down to 0.06 V (bottom row).*

References

[1] M. Winter, J.O. Besenhard, M.E. Spahr, P. Novák, *Adv. Mater.* **10**, 725–763 (1998).
[2] M. Armand, F. Endres, D.R. MacFarlane, H. Ohno, B. Scrosati, *Nat. Mater.* **8**, 621–629 (2009).
[3] V. Borgel, E. Markevich, D. Aurbach, G. Semrau, M. Schmidt, *J. Power Sources* **189**, 331–336 (2009).
[4] H.H. Zheng, K. Jiang, T. Abe, Z. Ogumi, *Carbon* **44**, 203–210 (2006).
[5] M. Ishikawa, T. Sugimoto, M. Kikuta, E. Ishiko, M. Kono, *J. Power Sources* **162**, 658–662 (2006).

Role of carbon in Li–S battery performance

S. Urbonaite, P. Novàk
phone: +41 56 310 5775, e-mail: sigita.urbonaite@psi.ch

In extensive research over the past few years, Li–S batteries have been established as strong candidates for practical next-generation post-Li-ion systems. The prospect of a readily available, low-cost, environmentally friendly battery with high specific charge (1672 mAh/g) outweighs the challenges encountered on the way to full-scale commercialization. These challenges include in particular the insulating nature of sulphur and the so-called polysulphide-shuttle. Whereas the former issue can be alleviated by using conductive additives (typically carbons [1]), a general and practical method for protecting Li–S systems from detrimental polysulphide-shuttle effects is yet to be developed. Several strategies have been explored, from using various solid electrolytes, new liquid electrolytes, electrolyte additives and coatings on impregnated materials or electrodes, to inserting single-ion-conducting membranes, which prevent polysulphides from reaching the Li counter electrode, where they can be reduced and rendered inactive [2].

An alternative approach with significantly lower complexity is to contain the polysulphides within the carbonaceous matrix by tailoring its pore-size structure. In the work reported here, two high-surface-area carbons were studied (MM2046; Imerys, Switzerland and YP; Maxwell Technologies, USA) and compared with the electrode of our standard Li–S battery [3] based on Super P (Imerys, Switzerland). The aim of this work is to identify a relationship between the carbon properties, especially pore-size distribution, and its performance as a host for sulphur in the positive electrodes of Li–S batteries.

Experimental

Sulphur–carbon composite electrodes were prepared by simple physical mixture of 60 % of S (refined), 30 % of C (Super P, MM2046, YP), and 10 % of binder (PEO, M = 4.000.000 mol/g). The slurry was prepared by turbostirring, followed by doctor blading onto carbon-pre-coated Al-foil. After drying at RT for at least 24 h, electrodes were punched out and assembled in an Ar-filled glove box into coin-type cells, using Celgard 2400 as a separator, metallic Li foil as a counter electrode and 30 µL of electrolyte containing 1 M LiTFSI in DME:Diox (2:1). Electrodes were galvanostatically cycled at a C/5 rate (1C is defined as I = 1672 mA/g_S) between 1.8 and 2.7 V vs Li^+/Li. For morphology comparison, carbon micrographs were obtained by scanning electron microscopy (SEM) operated at an accelerating voltage of 5 kV. Gas-adsorption measurements were performed at 77 K; full N_2 isotherms (adsorption and desorption) were recorded. For pore size distribution (PSD) analysis, the non-local density functional theory (NLDFT) module was used.

Results

The morphologies of the two carbons were distinctly different (Figures 1 and 2). In YP carbon, a wide range of particle sizes was observed and all particles had a monolithic appearance and smooth walls. In contrast, MM2046 consists of very small, randomly arranged particles, giving it a ‹fluffy› appearance.

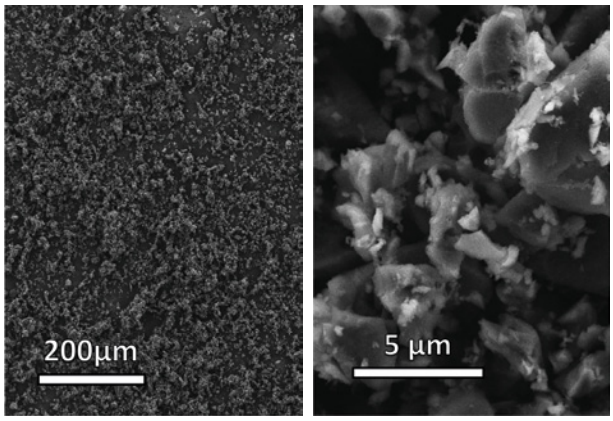

Figure 1: *SEM micrographs of YP carbon at different magnifications.*

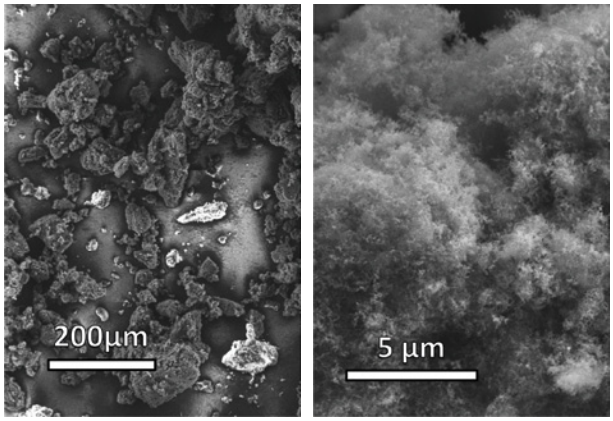

Figure 2: *SEM micrographs of MM2046 carbon at different magnifications.*

Despite these clearly different morphologies, both carbons have very similar and high specific surface areas, S_{Bet} ~ 1500–1600 m^2/g, as compared to Super P with a specific surface area of only ~65 m^2/g.

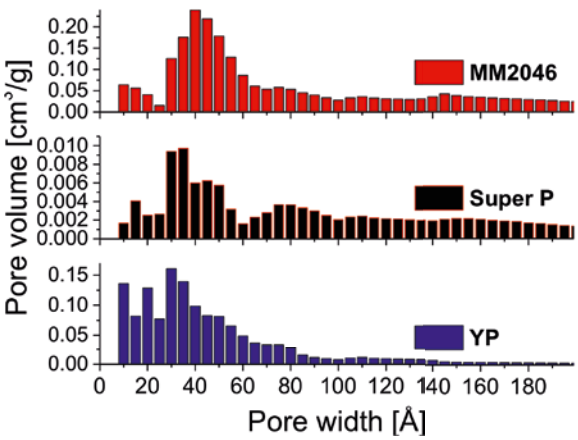

Figure 3: *Pore size distribution of both tested carbons in comparison with standard Super P.*

The pore-volume histograms (Figure 3) show that the main difference in PSD between YP and MM2046 is in the microporous region (< 20 Å), where MM2046 has only 20–30 % of the pore volume of YP carbon. The PSD of MM2046 is dominated by narrow mesopores. For comparison, the PSD of Super P (see Figure 3) has similarities to both high-surface carbons, MM2046 and YP. The microporosity of Super P is proportionally lower relative to MM20146, but at the same time the pore volume in the ~ 30 Å pore-size region is similar to that of YP carbon. However, in Super P the relative amount of pore volume is higher for wider pores and of course total pore volume is much smaller as compared to any of the other two studied carbons.

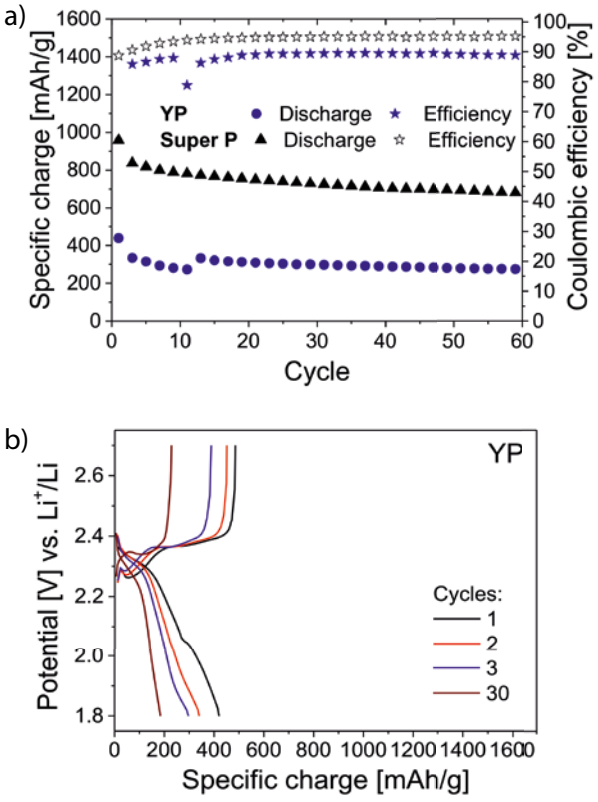

Figure 4: *Galvanostatic cycling performance of C-S composite electrode based on microporous YP carbon in comparison to the standard, Super P based, one (a) and corresponding voltage profiles (b).*

Figure 4 shows the results of galvanostatic cycling experiments using composite electrodes based on YP carbon. These are clearly inferior in performance compared to standard Super-P-based electrodes. Dominant pore volumes at pore sizes below 20 Å might therefore be disadvantageous for Li–S electrodes.

On the other hand, when using MM2046 (Figure 5), the specific charge is 200 mAh/g higher than for standard Super-P-based electrodes, indicating that the optimal pore size for Li–S systems is in the region of narrow mesopores. Comparing the galvanostatic profiles of YP and MM2046 carbons (see lower panels of Figures 4 and 5), it is evident that for YP carbons the overpotentials are considerably higher, which – in accord with the distinctly different morphologies of these carbons – suggests that despite their similar specific surface areas, the accessible pore volume of YP is much smaller than that of MM2046.

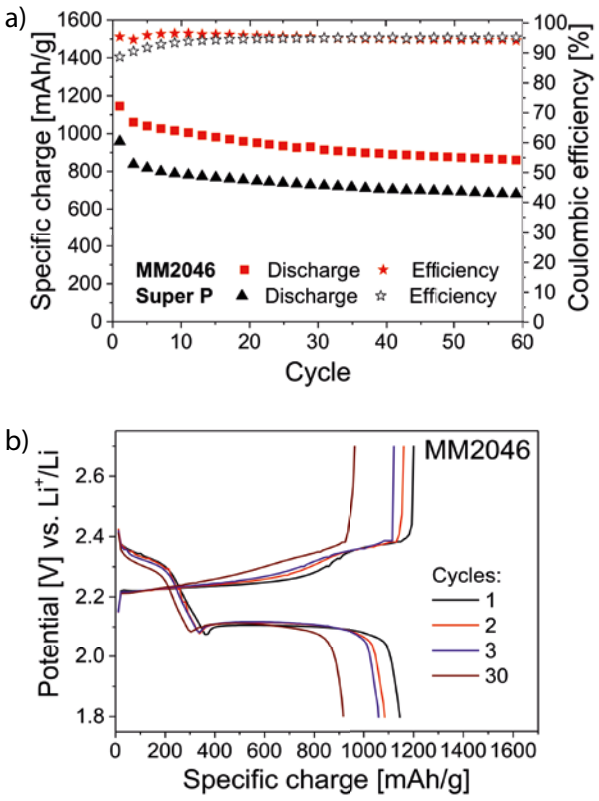

Figure 5: *Galvanostatic cycling performance of C-S composite electrode based on mesoporous MM2046 carbon in comparison to the standard, Super P based, one (a) and corresponding voltage profiles (b).*

Conclusions

This study unambiguously shows the importance of the pore structure of the carbon used as a host for sulphur in the positive electrodes in Li–S batteries. Clearly, not only the overall surface area and pore-size distribution are of importance. The openness of the structure cannot be neglected: a dominance of microporosity does not lead to better Li–S performance, but more narrow mesopores do.

Acknowledgement

BASF SE is acknowledged for financial support within the «BASF Scientific Network for Electrochemistry and Batteries».

References

[1] X. Ji, L.F. Nazar, *J. Mater. Chem.* **20**, 9821–9826 (2010).
[2] L. Chen, L.L. Shaw, *J. Power Sources* **267**, 770–783 (2014).
[3] S. Urbonaite, P. Novák, *J. Power Sources* **249**, 497–502 (2014).

High resolution operando X-ray tomography imaging and diffraction of lithium-ion battery electrodes revealing core-shell lithiation of Sb electrodes

C. Villevieille, M. Ebner[1], J. L. Gómez-Cámer, F. Marone, V. Wood[1], P. Novák
phone: +41 56 310 2410, e-mail: claire.villevieille@psi.ch

Thanks to their high energy and power densities, lithium-ion batteries are highly promising for many growing technology markets, including electric mobility. In order to achieve the necessary performance targets for these markets, extensive research has been devoted to the development of new active materials. Among these are conversion materials such as tin [1], antimony [2], and silicon [3] that undergo alloying reactions with lithium. They offer enhanced specific charge of at least 600 mAh/g and volumetric charge capacities of over 5000 Ah/L in comparison with graphite (372 mAh/g, 800 Ah/L), which is used in most commercial cells to date. However, conversion materials suffer from poor cyclability due to particle fracture during cell operation.

At the ensemble level, the cycling behavior of conversion materials has been studied *in situ* using X-ray diffraction, Mössbauer spectroscopy, X-ray absorption, acoustic emission, and X-ray transmission. Microscopic investigations of lithium-ion battery electrodes include optical microscopy, scanning electron microscopy, transmission electron microscopy, and AFM. As a bulk characterization technique capable of resolving single particles, transmission X-ray microscopy has been used to observe volume change of conversion materials. However, this 2D technique does not allow direct quantification of volume change. As a 3D technique, synchrotron X-ray tomographic microscopy (SXRTM) enables the quantification of the microstructure of lithium-ion battery electrodes and allows the study of phase evolution and quantification of the volume change at both the single particle and the electrode scale during battery operation.

Here we link structural phase information determined from operando X-ray diffraction (XRD) to time-resolved 3D phase evolution visualized operando at the single particle level using large volume and high resolution SXRTM. We choose to study a conversion material composed of Ti-containing Sb particles (called Sb_Ti in the following text) that exhibits multi-step phase evolution during the first electrochemical lithiation (reduction).

In situ X-ray diffraction

First, we performe high resolution operando X-ray synchrotron diffraction (XRD) (Figure 1a) in order to quantify the phase evolution (Figure 1b) and calculate attenuation coefficient and volume change (Figure 1c). Figure 1a shows 14 XRD scans taken at regular intervals during the first electrochemical reduction (Figure 1d). Scan 0 corresponds to an OCV step. As expected, scan 0 shows mainly rhombohedral (R-3m) Sb (6.69 g/cm^3), tetragonal (I4/mcm) $TiSb_2$ (7.53 g/cm^3), as well as minor contributions from the cell housing. To facilitate discussion of the phase evolution, we identify four distinct steps (I-IV).

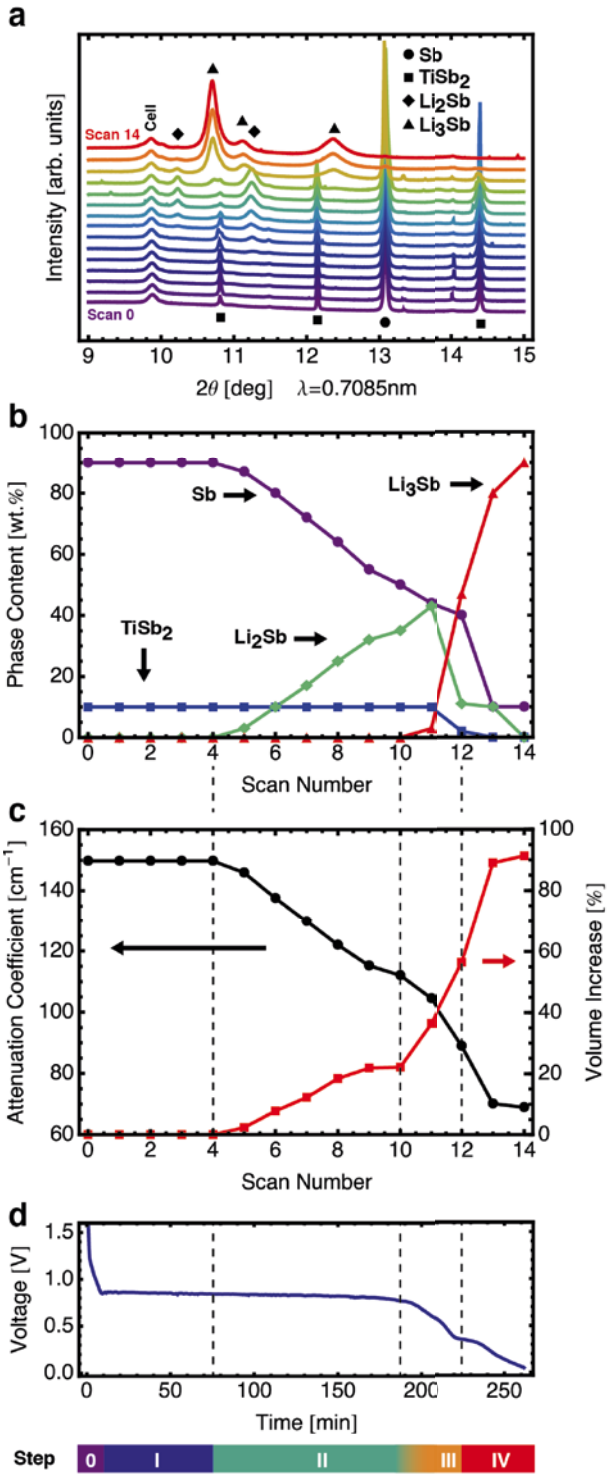

Figure 1: *(a) Operando XRD scans recorded during constant current electrochemical reduction, (b) the corresponding phase indexation, (c) attenuation coefficient, and volume change. The voltage of the in situ cell is plotted in (d) and relates scan number to time and voltage.*

[1] ETH Zürich

At the beginning of the constant current reduction step, no perceptible peak evolution takes place (scans 1–4). Accordingly, the calculated attenuation coefficient and volume stay constant. This reaction takes place at a constant potential of about 0.85 V vs. Li^+/Li. These observations are consistent with reduction of the electrolyte and SEI formation on the surface of the Sb_Ti particles (step I). From scans 5 to 10, reduction of the particles takes place as the potential slowly decays to approximately 0.80 V vs. Li^+/Li. In this step (step II), the hexagonal (P-62m) Li_2Sb (3.79 g/cm^3) phase appears and continuously increases while the amount of the rhombohedral Sb phase decreases (Figure 1b). The attenuation coefficient decreases and the volume increases due to the significantly lower density of Li_2Sb compared to Sb (Figure 1c). In a transitional step (step III), the potential drops further as the cubic (Fm-3m) Li_3Sb phase (3.36 g/cm^3) begins to form (scans 10–12). The tetragonal (I4/mcm) $TiSb_2$ phase also disappears, and it is assumed that Ti (4.506 g/cm^3) is ejected from the particles in the form of metallic nanoparticles. During step IV (scans 12–14), the phase content of the rhombohedral Sb phase decreases rapidly in favor of the Li_3Sb phase. At the end of the reduction step (scan 14), the sample consisted of 90 % Li_3Sb and 10 % remaining Sb.

Based on the structural information obtained via operando XRD analysis, it is possible to predict when fracture is likely to occur. The Sb particles start as a rhombohedral phase with a density of 6.69 g/cm^3. In step II, this phase is converted into the Li_2Sb phase, which crystallizes in a hexagonal lattice with a density of 3.79 g/cm^3. Because the rhombohedral cell is a primitive cell of the hexagonal cell, a change from rhombohedral to hexagonal systems can be considered ‹soft› and the change in structure is probably not strong enough to induce particle facture. However, in step III, the rhombohedral Sb and hexagonal Li_2Sb phases are both converted to cubic Li_3Sb. Because symmetry breaking is high during the transition from a rhombohedral/hexagonal to a cubic crystal structure (breaking of the mirror planes and rotation in order to increase the symmetry level), the particles are likely to crack.

In situ X-Ray tomography

We now examine the multi-step phase evolution process with operando X-ray tomography. Figures 2b and 2c represent a two-dimensional cross-sections (i.e., tomograms) of the particles during cycling. The colours correspond to the X-ray attenuation coefficient, which is linked to mass density and elemental composition. The color red can be associated with the high-density phases (mainly Sb), whereas yellow-green corresponds to low-density phases (i.e., Li_2Sb and Li_3Sb). The blue regions relate to weakly absorbing components of the electrode, i.e., carbon black, polymeric binder, and electrolyte. We visually inspect the particle cross-sections in Figures 2b and 2c and correlate the observed color and morphology changes to the steps outlined in Figure 2a. We then label each particle with a Roman numeral corresponding to the appropriate step.

The particle in Figure 2b shows no apparent change 144 min into reduction. This is consistent with the growth of the SEI surface layer (step I), which we do not expect to be observable with X-ray tomography due to the low X-ray absorption coefficient of the SEI. Between 168 min and 192 min, the tomograms show inward growth of a low-absorption front (yellow) consuming a high-absorption region (red) in a core-shell process. We identify this as step II in the phase evolution where the low-density Li_2Sb phase consumes the high-density Sb phase. In the tomogram taken at 216 min, the onset of particle fracture is observed. This is consistent with step III, where the phase transition-induced strain initiates crack formation.

In the two remaining tomograms, crack propagation and complete particle fracture are observed. This behavior is consistent with step IV. However, the particle in Figure 2b appears to consist entirely of a weakly absorbing material (i.e., it is completely yellow). This implies that the particle has completely transformed from the high-density Sb or $TiSb_2$ phases to a low-density (Li_2Sb or Li_3Sb) phase. To reconcile this seemingly complete transition to a low density phase with operando XRD data, this indicates that 10 % of the Sb phase remains at the end of the lithiation. We find that, while some particles exhibit no remaining high-density phase, others show a high-density phase remaining in the centre of the particle. This is highlighted in Figure 2c, which shows two neighboring particles of different sizes. In the smaller particle, a complete transition to a low density phase is observed after 240 min (Step IV), while the larger particle is still exhibiting reduction through a core-shell process (Step II). We conclude that during constant current reduction, particles within an electrode show different phase evolution depending on their size. Because this 10 % phase is observed for both the slow C/10 rate for XRD and fast C/1 rate for tomography, we hypothesize that the remaining 10 % of the Sb phase do not result from kinetic effects, but rather from the core-shell process where the core of the particles is electronically decoupled.

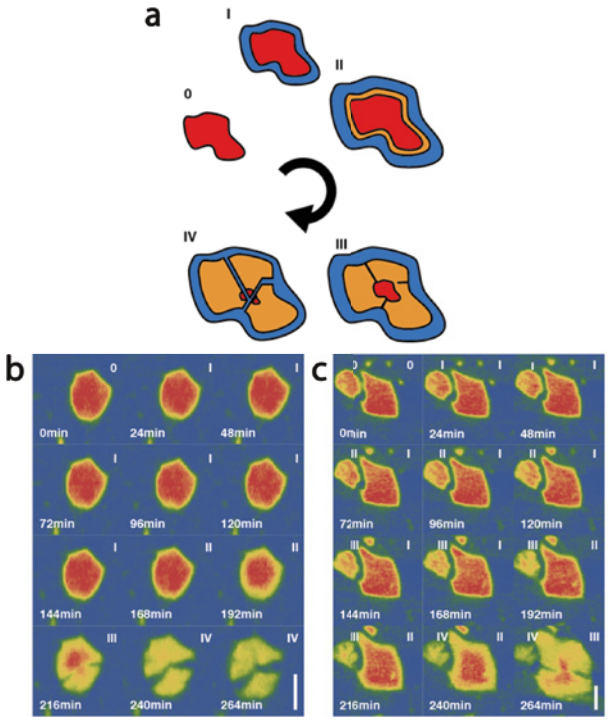

Figure 2:
a) Proposed steps during electrochemical reduction showing a pristine Sb_Ti particle (step 0). The next step is ascribable to the SEI layer growth (step I), then lithiation of Sb begins through a core-shell process (step II), undergoes a phase transition, which induces particle fracture and ejection of Ti (step III), and continues in fracture and volume expansion (step IV).
b) and c) X-ray tomograms of selected particles presenting experimental evidence for a core-shell phase-evolution process and for unequal reduction kinetics in different particles. The white scale bar in the lower right of panels b and c is 20 µm.

Conclusion

In conclusion, we present the first study that links operando X-ray diffraction measurements of the ensemble phase evolution during reduction to operando X-ray tomography, which provides a spatially resolved map of the phase evolution for a large number of single particles operating in a realistic lithium-ion battery porous electrode. Previously, variations in phase evolution at a single particle level have been inaccessible using ensemble techniques. By confirming that the spatial evolution of the phase during reduction of our intermetallic system is a core-shell process and resolving differences in the dynamics of this core-shell process as a function of particle size and morphology, we can offer guidelines for the development of such conversion materials. In particular, we observe kinetically limited reduction in large (> 5 μm), dense particles, while smaller particles or large particles with a high inner porosity exhibit a more uniform phase evolution with time and complete phase transformation during constant-current reduction. The spatial resolution provided via operando X-ray tomography also enables us to examine particle fractures and to conclude that, while smaller particles and larger «porous» particles have similar kinetics, the larger «porous» particles are mechanically more stable and do not exhibit fractures.

References

[1] J.O. Besenhard, J. Yang, M. Winter, Will advanced lithium-alloy anodes have a chance in lithium-ion batteries? *J. Power Sources* **68**, 87–90 (1997).

[2] J.M. Tarascon, S. Grugeon, M. Morcrette, S. Laruelle, P. Rozier, P. Poizot, New concepts for the search of better electrode materials for rechargeable lithium batteries. *Comptes Rendus Chimie* **8** (1), 9–15 (2005).

[3] R.A. Huggins, Lithium alloy anodes. *Handbook of Battery Materials*, 359–381 (1999).

SCIENTIFIC ACHIEVEMENTS 2014

Electrocatalysis & Interfaces

Nanostructured NiO as a new concept for an oxygen evolution catalyst in alkaline environment

E. Fabbri, G.R. Meseck[1], S. Seeger[1], T.J. Schmidt
phone: +41 56 310 2795, e-mail: emiliana.fabbri@psi.ch

As a consequence of the future fossil fuel depletion and the energy policies of several countries to abandon nuclear energy, the renewable energy implementation is becoming one of the most important priorities of this century.

Therefore, the future electric power supply will rely on a larger extent than today on fluctuating primary solar and wind energy. In fact, although primary renewable energy sources have the advantages of being sustainable and relatively benign in terms of impact on the environment and human health, most of them are intermittent on daily, seasonal and also regional scales with considerable variability in supply. This uncertainty in energy supply can be eliminated by connecting a local energy storage system to an electricity producing unit. In this context, water electrolyzers can play a fundamental role in the development of a sustainable energy system.[1]

Water electrolyzers are electrochemical energy conversion devices that can produce hydrogen and oxygen from intermittent energy sources. Stored hydrogen and oxygen can be consequently reconverted in electricity by a fuel cell, representing overall an electricity storage system alternative to batteries. The main advantage of electrolyzers compared to batteries is that the energy vector, i.e., the hydrogen, can be stored outside the electrochemical device allowing independent scaling of the electrolyzer size and stored energy [1].

Both for electrolyzers based on an acidic or an alkaline electrolyte, one of the main challenges towards their widespread commercialization is the development of oxygen electrodes

- showing a high catalytic activity towards the oxygen evolution reaction (OER),
- showing good stability under electrolyzer operative condition, and
- being low cost using abundant materials.

While only few materials, mostly noble metals, present adequate chemical stability in contact with an acidic electrolyte, several transition metals possess good chemical stability in alkaline environment. Among the stable materials in alkaline environment, nickel oxide is one of the most active towards the OER, especially when doped with Fe or Co. Generally, nickel-based catalysts for the OER have been investigated in form of thin films [1]. However, being the OER a pure surface reaction, only high surface area catalysts allow reaching high performance per mass of catalysts.

In this work, a novel concept of nickel-based catalysts has been developed by supporting NiO on silicone nanofilaments (SNFs) [1]. SNFs-supported NiO represents a novel catalyst structure concept since it is free-standing, i.e., it does not require the use of a binder, and it provides large surface area for the OER to occur. SNFs are one-dimensional nanostructures which can be grown as thin carpets on a variety of surfaces via chemical vapor deposition [2] and they can serve as a nanosized support to disperse an electrochemically active phase, such as TiO_2 [3] or NiO as in the present case.

Experimental

Glass coated fluorine doped tin oxide (FTO) (Sigma Aldrich) was used as SNF substrate and also as the current collector for the electrochemical characterization. Cleaned FTO coated glass was placed in a sealed desiccator (relative humidity of 40 %) and ethyltrichlorosilane (500 µl) was injected through a septum. The growth of the SNFs proceeded for 4 h at room temperature. Afterwards, the samples were rinsed with deionized water to remove HCl residues from the hydrolyzation of the silane, and activated by 60 s treatment in oxygen plasma at 100 W (Femto, Diener Electronic, Ebhausen, Germany). A home-made reactor for the decoration of the SNF with NiO was developed. The reactor was filled with deionized water and under cooling on an ice bath and magnetic stirring, urea and nickel nitrate hexahydrate were added in small portions. After homogenization for 5 min the reactor was transferred into an oil bath where the reaction proceeded for 6 h at 80 °C. The samples were then rinsed with deionized water and left to dry under ambient conditions prior to calcination at 400 °C for 5 h [4].

For the electrochemical characterization, the NiO electrodes were tested in a home-made Teflon cell. The NiO electrodes were immersed under potential control (1.2 V RHE) in 0.1 M KOH (Sigma Aldrich, 99.99 %) electrolyte saturated with synthetic air (99.999) at room temperature. The measurements were performed using a hydrogen reference electrode (RHE) and a gold counter electrode in a 3-electrode configuration. Cyclic voltammetry (CV) measurements were carried out between 0.6 and 1.8 V (RHE) with a scan rate of 10 mV s^{-1}. The Tafel plot for the NiO electrodes was determined by performing a series of chronoamperometry measurements: The potential was increased by steps of 50 and 20 mV in the potential range of 1.2–1.45 V (RHE) and 1.45–1.8 V (RHE), respectively, holding the potential for 1 h at each potential step. Such long potential holding was performed in order to obtain almost steady state currents. The ohmic drop was evaluated by impedance spectroscopy at potential intervals of 300 mV [4].

Results

Figure 1 shows a scanning electron microscopy (SEM) image of the SNFs coated with NiO, revealing a network-like superstructure with pores in the micrometer range and filaments with diameters in the range from ca. 40–60 nm with a mean of 47 ± 6 nm [4].

Before the determination of the activity of the SNF-supported NiO catalysts towards the OER, an electrochemical activation step was performed. Particularly, the samples were potentially cycled between 0.6 and 1.8 V (RHE) with a scan rate of 10 mV s^{-1}. The series of the 30 cyclic voltammograms (CVs) is shown in Figure 2. Potential cycling induces the growth of the peaks related to the Ni(II/III), i.e., $Ni(OH)_2$/NiOOH, redox couple [4].

[1] Department of Chemistry, University of Zurich

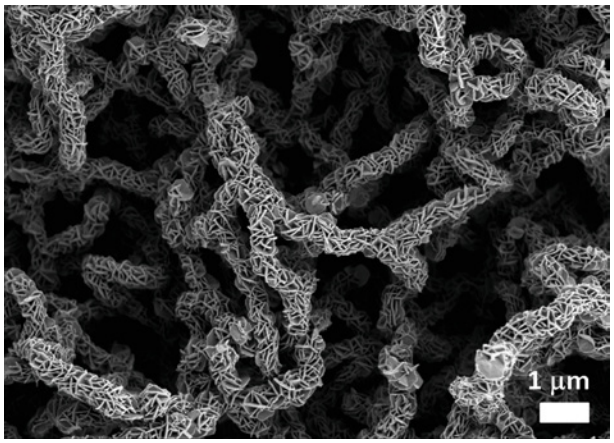

Figure 1: *SEM image of the SNF-supported NiO after calcination at 400 °C for 5 h.*

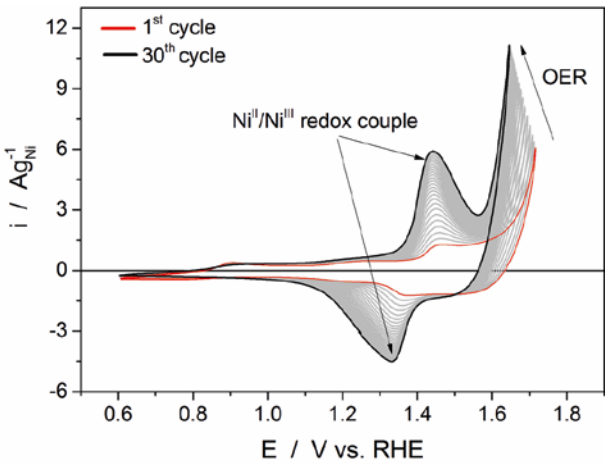

Figure 2: *CVs (ohmic drop corrected) of a SNF-supported NiO electrode recorded in Air-saturated 0.1 M KOH, at 10 mV s^{-1}.*

It is widely reported in the literature that NiO electrodes immersed in an aqueous solution instantaneously form a $Ni(OH)_2$ layer on their surface [1]. The $Ni(OH)_2$ layer grows upon potential cycling across the Ni(II/III) redox couple [5]. The change in the CV of the SNF-supported NiO catalyst upon potential cycling (Figure 2) indicates the growth of a hydrous oxide layer on the nickel oxide surface, and therefore an increase in the surface roughness and/or in the amount of the electrochemically active surface sites [4]. Furthermore, the potential cycling also induced a shift of the anodic Ni(II/III) peak to more anodic potentials, which is indicative of material conversion from α-$Ni(OH)_2$ to β-$Ni(OH)_2$ phase [5].

It has been proposed by several studies that an initially formed α-$Ni(OH)_2$ phase can gradually change into a more crystalline β-$Ni(OH)_2$ phase due to potential cycling in a strong base. It has been also suggested that the β-$Ni(OH)_2$ phase is the «right type» of oxide to catalyze the OER [1]. Indeed, the CVs shown in Figure 2 also indicate an increase in the OER activity upon potential cycling. The increase in the OER activity upon potential cycling might be the result of synergistic effects, i.e., an increase in the exposed surface area / active sites and the development of a more catalytically active $Ni(OH)_2$ surface layer.

To determine the activity parameters, i.e., Tafel slope and mass activity at 10 Ag^{-1} [1], a series of chronoamperometry measurements after the potential cycling experiment was performed. Varying the applied potential in the OER regime (holding time of 1 h for each potential), steady state currents could be achieved. The Tafel plots showed a Tafel slope of 50 ± 2 mV dec^{-1} and a steady state potential of 1.59 ± 0.012 V (RHE) at the mass current density of 10 A/g_{Ni}.

So far, a large variety of Tafel slope and activity parameters / values have been reported for nickel-based electrodes; indeed, the Ni OER activity has been found strongly depended in the processing and measuring parameters [1]. Tafel slopes in the literature vary from about 40 to 130 mV dec^{-1}, while generally mass activity is not reported [1].

EDX analysis of the measured samples was performed after the electrochemical measurements in order to determine possible metal contamination. Particularly, contamination with Fe leads to significant change in the Tafel slope and OER activity. No evidence of Fe or other metal contamination could be detected.

Conclusions

So far, most of the Ni-based electrodes developed for water electrolysis applications consist of physically or electrochemically deposited Ni thin films. Thin films are suitable model electrodes to study fundamental electrochemical reactions. However they cannot provide high mass activity. High mass activity can be generally achieved increasing the catalytic active surface area per mass of catalysts as in the case of 3D structure or dispersed nanoparticles. To the best of our knowledge, only few 3D, high surface area NiO electrodes have been developed for water electrolysis applications so far. In this contribution we have demonstrated the feasibility of developing a free-standing, high surface area NiO catalyst structure showing reasonable catalytic activity towards the OER. The oxygen evolution activity for the present catalyst system can be definitively increased by doping the NiO catalyst with Fe or Co.

It should be also mentioned that besides maximizing the mass activity, nanostructured materials with an optimized microstructure can allow reducing the gas bubble formation on the electrode surface during the oxygen evolution. Gas bubble can temporary block the electron transfer and therefore reduce the efficiency of the devices. Stability studies of the SNF-supported NiO are currently under development.

Acknowledgement

Funding was provided by the Swiss National Foundation (Ambizione project 148041/1 and grant 20-146421) and CTI within the SCCER Heat & Electricity Storage.

References

[1] E. Fabbri, A. Habereder, K. Waltar, R. Kötz, T.J. Schmidt, *Catal. Sci. Technol.* **4**, 3800–3821 (2014).
[2] G.R.J. Artus, S. Jung, J. Zimmermann, H.P. Gautschi, K. Marquardt, S. Seeger, *Adv. Mater.* **18**, 2758–2762 (2006).
[3] G.R. Meseck, R. Kontic, G.R. Patzke, S. Seeger, *Adv. Funct. Mater.* **22**, 4433–4438 (2012).
[4] G.R. Meseck, E. Fabbri, T.J. Schmidt, S. Seeger, *Adv. Mater. Interfaces*, submitted, (2015).
[5] M.E.G. Lyons, M.P. Brandon, *Int. J. Electrochem. Sci.* **3**, 1386–1424 (2008).

Study of the oxygen evolution mechanism and activity of perovskite – $La_{1-x}Sr_xCoO_{3-\delta}$-based electrodes in alkaline media by thin film rotating disk electrode measurements

X. Cheng, E. Fabbri, T.J. Schmidt
phone: +41 56 310 5937, e-mail: xi.cheng@psi.ch

Fuel cell and electrolyzers can represent a mid-term solution to the present need for a sustainable energy economy; they can be combined with renewable energy resources to build up a novel and sustainable energy based on power grids. One of the main drawbacks which hinders low temperature fuel cells and electrolyzers commercialization is the high costs of these devices. A considerable decrease in their cost can be achieved by developing non-noble metal electrocatalysts which are able to provide high catalytic activity towards the oxygen reduction and evolution reaction (fuel cell and electrolyzer mode, respectively). Particularly, perovskite oxides have recently shown the potentials of high electrocatalytic activity towards oxygen evolution reaction (OER) [1] in alkaline media. The basic perovskite oxide structure can be represented as ABO_3, where A is the larger cation, such as a lanthanide or an alkaline earth element, and B is the smaller cation, generally a transition metal.

The ABO_3 structure can accommodate cation substitution in a wide range by partial substitution of either the A and the B cation with another element giving $(A_xA`_{1-x})(B_yB`_{1-y})O_3$ compositions. Even though the A-site ion does not really contribute to the electronic conduction, its size and valence were found to be important factors controlling the perovskite crystal structure and as a consequence also the electronic properties. A particular interesting case is $La_{1-x}Sr_xCoO_{3-\delta}$. At low values of x these oxides are p-type semiconductors while x > 0.2 the conductivity can become semi-metallic or metallic type [2]. In the present work we have investigated the OER mechanism and activity of single electrodes based on $La_{1-x}Sr_xCoO_{3-\delta}$ (x = 0, 0.2, 0.4, 0.8, 1) perovskite by thin film rotating disk electrode (RDE) technique.

Experimental

$La_{1-x}Sr_xCoO_{3-\delta}$ powder was synthesized using a modified sol gel process. In brief, stoichiometric quantities of commercial La_2O_3 (Aldrich, 99.9 %), $Sr(NO_3)_2$ (Aldrich, 99 %), $Co(NO_3)_2{\cdot}6H_2O$ (Aldrich, 99 %) precursors were dissolved in an aqueous solution of 0.2 M nitric acid. Citric acid (Aldrich, 99.5 %) was used as a chelating agent in a 2:1 ratio with respect to the total metal cations. After obtaining a transparent solution, the pH was adjusted between 9 and 10 by NH_4OH additions. The solution was then heated under stirring to evaporate water until it changed into a viscous gel and finally ignited to flame, resulting in a black ash. To obtain single phase oxide material, the $LaCoO_{3-\delta}$ powder was calcined at 1000 °C for 4 h in air. The $SrCoO_{3-\delta}$ powder was calcined at 900 °C for 8 h in air, while other $La_{1-x}Sr_xCoO_{3-\delta}$ (x = 0.2, 0.4, 0.8) powders were calcined at 1050 °C for 4 h in air. The single phase material was confirmed by X-ray diffraction analysis. The microstructure of the powder was observed using a scanning electron microscope (SEM, Gemini Ultra 55). The specific surface area of the powder was determined by Brunauer-Emmett-Teller (BET) analysis. To measure the *ex situ* conductivity for each material, impedance spectroscopy measurements have been performed. The pure oxide powders were kept under a constant pressure of 0.6 MPa for 5 minutes and the electrical resistivity was evaluated by 4-wire impedance spectroscopy measurements at room temperature applying a bias of 100 mV in the frequency range between 1 MHz and 1 Hz.

The oxygen evolution reaction (OER) was investigated by thin-film RDE measurements using a home-made Teflon cell with a Biologic VMP-300 potentiostat system. The working electrodes were immersed under potential control (1.0 V vs. RHE) in 0.1 M KOH electrolyte at room temperature and the measurements were performed using a hydrogen reference electrode (RHE) separated by a salt bridge with diffusion barrier and a gold counter electrode in a three electrode configuration. After 30 reverse scan sweeps between 1–1.7 V (RHE) at 10 mVs^{-1} and 1600 rpm in synthetic air-saturated electrolyte, chronoamperometry measurements holding each potential for 30 sec (synthetic air-saturated and 1600 rpm) were performed. The chronoamperometry measurements allow obtaining an almost steady-state current with no capacitive contribution. Current densities were normalized by the BET surface area of the perovskite oxide in each of the electrode compositions and all the potentials were corrected for the ohmic-drop measured by impedance spectroscopy. Figure 1 shows an exam-ple of the cyclic voltammetry and chronoamperometry measurements for $SrCoO_{3-\delta}$.

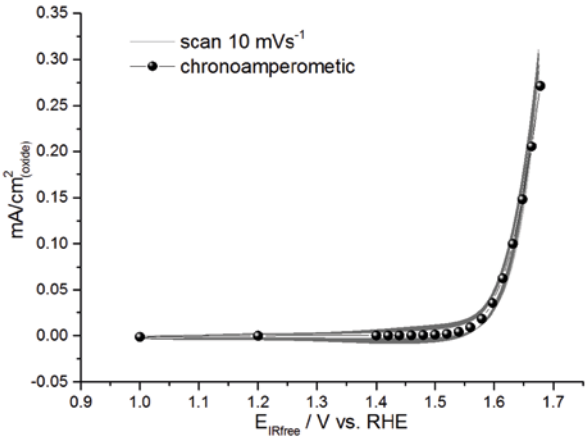

Figure 1: *Cyclic voltammetry (30 cycles at 10 mVs^{-1}) and chronoamperometry (holding for each potential for 30 sec) measurements for $SrCoO_{3-\delta}$ electrode in synthetic air-saturated 0.1 M KOH electrolyte at 1600 rpm.*

Results

The X-ray diffraction (XRD) pattern of the $La_{1-x}Sr_xCoO_{3-\delta}$ powders shown in Figure 2 confirmed that single phase materials were achieved. Among the patterns of the $La_{1-x}Sr_xCoO_{3-\delta}$ series, the perovskite-type structure was obtained for x = 0, 0.2, 0.4 and 0.8. In particular, the composition with x = 0 and 0.2 show a rhombohedral structure; while for x = 0.4 and 0.8 cubic structure was obtained. The $SrCoO_{3-\delta}$ oxide presents a hexagonal system which may exist as $SrCoO_{2.5}$ in composition. These results are in agreement with the previous study of Matsumoto et al. on the $La_{1-x}Sr_xCoO_{3-\delta}$ series [3].

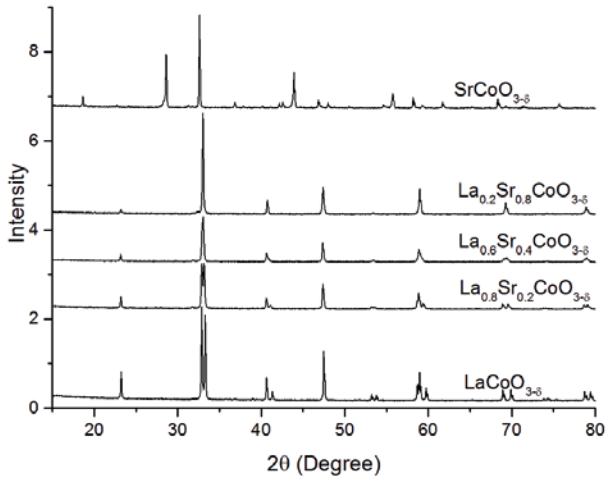

Figure 2: *XRD spectra of $La_{1-x}Sr_xCoO_{3-\delta}$ powders as synthesized.*

Table 1 shows the specific surface area of $La_{1-x}Sr_xCoO_{3-\delta}$ powders obtained by BET analysis. All the oxides present a relatively low BET surface area, typical of perovskite oxides [4].

Sample	SBET($m^2.g^{-1}$)	Sample	SBET($m^2.g^{-1}$)
$LaCoO_{3-\delta}$	3.77	$La_{0.2}Sr_{0.8}CoO_{3-\delta}$	1.54
$La_{0.8}Sr_{0.2}CoO_{3-\delta}$	4.18	$SrCoO_{3-\delta}$	2.50
$La_{0.6}Sr_{0.4}CoO_{3-\delta}$	3.74		

Table 1: *BET surface area of $La_{1-x}Sr_xCoO_{3-\delta}$ powders.*

With the SEM analysis, we noticed that the $La_{0.8}Sr_{0.2}CoO_{3-\delta}$ oxide with the highest BET surface area presented relative small grain size and high porosity (Figure 3, left). In the case of $La_{0.8}Sr_{0.2}CoO_{3-\delta}$ oxide which has the lowest BET surface area, larger aggregation and lower porosity was achieved (Figure 3, right).

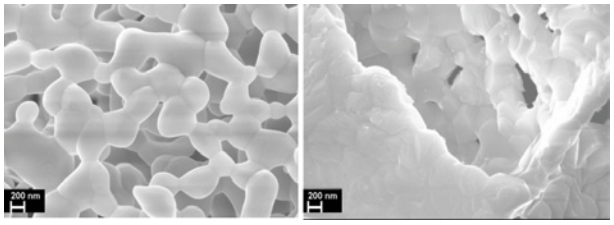

Figure 3: *SEM image of $La_{0.8}Sr_{0.2}CoO_{3-\delta}$ (left) and $La_{0.2}Sr_{0.8}CoO_{3-\delta}$ (right) as synthesized.*

Figure 4 shows the current density for the OER and the *ex situ* conductivity of $La_{1-x}Sr_xCoO_{3-\delta}$ powders as a function of x. The conductivity significantly increases from $LaCoO_3$ to $La_{0.8}Sr_{0.2}CoO_{3-\delta}$ by a factor of 300. When La^{3+} is replaced with Sr^{2+}, the excess charge induced by Sr-doping could be compensated by the transformation of Co^{3+} to Co^{4+} (equation 1), or by the creation of oxygen vacancies (equation 2). When x = 0.2, the oxidation of Co is predominant, increasing the electronic bandwidth of Co cation and enhancing its interaction with O^{2-} ion in the lattice, thus improving the conductivity [5]. Meanwhile, from x = 0.4 to x = 0.8, the increase of the *ex situ* conductivity is much less pronounced (only by a factor of 3). This finding may be explained considering that for $x \geq 0.4$, the creation of oxygen vacancies becomes predominant, and this would vanish the interaction between Co cation and O^{2-} ion in the lattice, thus putting a brake on the increase of the conductivity. The relatively high resistance of $SrCoO_{3-\delta}$ is assigned to its non-perovskite-type structure, as also reported in reference [3].

$$LaCoO_3 \xrightarrow{Sr} La'_{Sr} + Co^{\cdot}_{Co} \qquad (1)$$

$$LaCoO_3 \xrightarrow{Sr} La'_{Sr} + \tfrac{1}{2}V_o^{\cdot\cdot} + \tfrac{1}{2}O_2 \qquad (2)$$

Figure 4 also shows the steady-state current normalized by the BET surface area of the oxides at a potential of 1.6 V vs. RHE, taken as a parameter for the OER activity. The OER activity shows a smilar trend of the *ex situ* conductivity values for the $La_{1-x}Sr_xCoO_{3-\delta}$ series. Therefore, the presents result seems to indicate that the higher the perovskite conductivity the higher the OER activity. Previous investigation [3] reports that $SrCoO_{3-\delta}$ with a cubic perovskite structure should display the highest conductivity (metal-like) among the $La_{1-x}Sr_xCoO_{3-\delta}$ series. Thus, the present OER activity vs. conductivity trend suggests that being able to further increase the conductivity from $La_{0.8}Sr_{0.2}CoO_{3-\delta}$ to $SrCoO_{3-\delta}$ (i.e., synthesizing the material with cubic structure) would lead to a further enhancement of the OER activity. This point requires additional investigations. However, also the previous study of Matsumoto et al. [3] led to the conclusion that $SrCoO_{3-\delta}$ oxide with a stoichiometric composition and perovskite-type structure should possess the highest *ex situ* conductivity and the highest OER activity within the investigated oxide series.

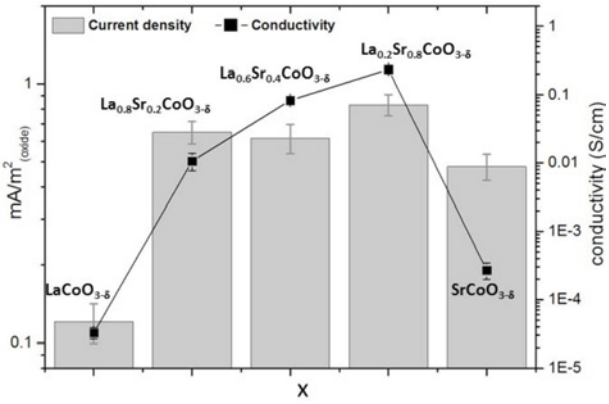

Figure 4: *Current density (at 1.6 V vs. RHE) normalized by the BET surface area and ex situ conductivity of $La_{0.8}Sr_{0.2}CoO_{3-\delta}$ powders as a function of x.*

Acknowledgement

The authors gratefully acknowledge the Ambizione Program of the Swiss National Science Foundation, the commission for Technology & Innovation and the Swiss Competence Center for Energy Research (SCCER) Heat & Electricity Storage for financial contributions to this work.

References

[1] J. Suntivich, K.J. May, H.A. Gasteiger, J.B. Goodenough, Y. Shao-Horn, *Science* **334**, 1383–1385 (2011).
[2] E.J.M. O'Sullivan, E.J. Calvo, in *Reactions at Metal Oxide Electrodes Comprehensive Chemical Kinetics*, Elsevier Science Publishing Company Inc., New York (1987).
[3] Y. Matsumoto, S. Yamada, T. Nishida, E. Sato, *J. Electrochem. Soc.* **127** (11), 2360–2364 (1980).
[4] A. Lan, A.S. Mukasyan, *J. Phys. Chem. C* **111**, 9573–9582 (2007).
[5] A. Mineshige, M. Inaba, T. Yao, Z. Ogumi, *J. Solid State Chem.* **121**, 432–429 (1996).

Electrocatalysis of perovskites: The influence of carbon on the oxygen evolution activity

R. Mohamed[1], X. Cheng, E. Fabbri, P. Levecque[1], R. Kötz, O. Conrad[1], T.J. Schmidt
phone: +41 56 310 2795, e-mail: emiliana.fabbri@psi.ch

The oxygen evolution reaction, occurring at the anode of water splitting devices is said to be central to the development of the clean, reliable and emissions-free hydrogen economy. This reaction is primarily governed by slow kinetics and significant overpotential losses which even with state-of-the-art materials such as RuO_2 and IrO_2 remains a hurdle [1]. The design, synthesis and characterization of cost effective, robust and highly active anode materials for the OER therefore yield a great challenge and have been a focus of much research attention. Towards this end, efforts have been directed on a myriad of low-cost transition metal oxides [1] as alternatives to precious-metal-based materials. Among these, the perovskite oxides have been of interest for a number of years [2] and have again re-emerged as promising candidates. In particular, it was shown that the perovskite $Ba_{0.5}Sr_{0.5}Co_{0.8}Fe_{0.2}O_{3-\delta}$ (BSCF) showed an intrinsic activity at least an order of magnitude higher than that of the state-of-the-art iridium oxide catalyst in alkaline electrolyte [3].

The electronic conductivity of this class of materials is known to vary significantly and as such, carbon is often added to the electrode composition in order to provide a conductive pathway and increase the electrocatalyst utilization of the oxide for electrochemical studies. One of the major problems with carbon, however, is that it undergoes electrochemical oxidation forming CO_2 at high potentials (standard potential of 0.207 V vs. NHE) pointing to the need to exclude carbon as an electrocatalyst component [4]. Alternatively, as was shown for the oxygen reduction reaction in alkaline electrolyte, carbon may not only act to enhance the electronic conductive pathway but can also affect the electrocatalytic process in various ways [5]. Although attention has been paid to the role of carbon in composite electrodes for the ORR, not much work has been done to identify the role of carbon in these electrodes for the OER, and therefore it is yet to be fully understood.

In this study we evaluate the effect of using functionalized acetylene black carbon (ABf) as an electrode additive for thin-film rotating disk electrode (RDE) measurements of the OER activity of the perovskite oxide BSCF. New insights towards the study of this material with and without the addition of carbon for the OER have been achieved by performing thin-film RDE measurements in alkaline media. This study provides some important insight into the considerations that need to be taken into account by the addition of carbon into the electrode for thin-film RDE measurements of perovskite oxide materials for the OER.

Experimental

As-prepared $Ba_{0.5}Sr_{0.5}Co_{0.8}Fe_{0.2}O_{3-\delta}$ (BSCF) powder was synthesized by a modified sol gel process as previously described [6]. To obtain single phase oxide material, the as-prepared BSCF powder was calcined at 1000 °C for 2 h in air and confirmed by XRD [6].

For the electrochemical characterization, porous thin-film rotating disk electrodes were prepared from a catalyst ink suspension consisting of 15 mg catalyst, 20 µL Na^+-exchanged Nafion solution (Nafion 1100 solution, Alfa Aesar) and 5 mL isopropanol. The catalyst ink was sonicated for 30 minutes and a known aliquot was drop-coated on a rotating mirror polished glassy carbon electrode (0.196 cm^2) and dried prior to use. To evaluate any limitations as a result of the oxide resistivity the OER current at 1.6 V vs. RHE of the pure BSCF oxide electrode was studied as a function of the oxide loading used in the thin-film rotating disk electrode (RDE) measurements. The optimal catalyst loading was then selected for subsequent OER activity measurements and comprised of either the oxide only or a combination of the oxide and AB_f in a 5:1 wt. ratio [7].

The OER activity was investigated by thin-film RDE measurements using a home-made Teflon cell with a Biologic VMP-300 potentiostat system. Cyclic voltammetry (CV) at a scan rate of 10 mV s^{-1} in the oxygen evolution reaction potential regime (1.0–1.7 V vs. RHE) at a rotation rate of 1600 rpm was used.The working electrodes were immersed under potential control (1.0 V vs. RHE) in O_2-saturated 0.1 M KOH electrolyte at room temperature and the measurements were performed using a hydrogen reference electrode (RHE) separated by a salt bridge with diffusion barrier and a gold counter electrode in a three electrode configuration.

The 0.1 M KOH electrolyte was prepared from Milli-Q water and KOH pellets (Sigma Aldrich, 99.99 %). Respective cathodic and anodic scans of the disk electrode were performed with a scan rate of 10 mV s^{-1} at a rotation rate of 1600 rpm. Current densities were normalized by the mass of the perovskite metals (cations) present in each of the electrode compositions and all the potentials were corrected for the ohmic-drop measured by electrochemical impedance spectroscopy.

Results

Cyclic voltammetry (CV) was used to evaluate the electrochemical activity towards the OER for pure BSCF electrodes and BSCF/AB_f composite electrodes in alkaline electrolyte. Figure 1 shows the current obtained at 1.6 V vs. RHE plotted as a function of the BSCF electrode loading, giving an indication of the RDE electrode film thickness. The OER current increased in proportion to the increase of loading up to ~ 460 mg_{BSCF} cm^{-2}, indicating no major conductivity limitation for the pure BSCF electrodes. For a higher loading, however, there was no longer a proportional increase in current observed, indicating that electronic limitations became significant. A loading of ~ 460 mg_{BSCF} cm^{-2}, also corresponding to the same total catalyst loading for the BSCF/AB_f composite electrodes, was therefore used in the subsequent measurements respectively.

Figure 2 shows the ohmic-drop corrected anodic CV scans for AB_f, BSCF and BSCF/AB_f electrodes. It can be seen that pure BSCF (i.e., without carbon) and AB_f itself do not achieve high OER mass current densities. The current density was also fairly constant for the 30 cycles performed for BSCF and decreased for AB_f upon potential cycling (not shown) [8].

[1] HySA/Catalysis, Department of Chemical Engineering, University of Cape Town, Rondebosch, 7701, South Africa

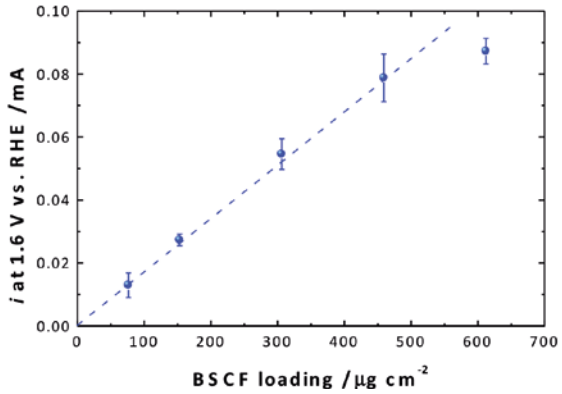

Figure 1: *Comparison of the OER current as a function of the BSCF oxide loading 1.6 V vs. RHE.*

The composite BSCF/AB_f on the other hand showed a higher initial OER current density, higher than the sum of the current densities of the individual components and a further significant increase in the OER current density upon potential cycling which was either not observed or not as pronounced for BSCF of AB_f individually. This substantial increase in current density for BSCF/AB_f translated to a 10-fold increase in the OER mass activity or a lowering of the overpotential by more than 90 mV at 10 A g^{-1}_{metals} for the composite BSCF/AB_f. Considering carbon degradation upon cycling of the composite BSCF/AB_f electrode in this study, the observed increase in the current density of the BSCF/AB_f composite electrode appears to be the result of a significant OER mass activity increase when the BSCF catalyst is combined with AB_f. This indicates some synergetic effect between BSCF and AB_f carbon in the BSCF/AB_f composite electrode leading to enhanced OER activity.

Our results show a significant increase in current density upon cycling occurring for the BSCF/AB_f composite electrode while a continuous increase in the current with consecutive cycles was not observed for the pure BSCF electrode material. The observed increase in the current density was attributed to be a result of some corrosion phenomena upon cycling in the OER region leading to a loss of crystallinity on the surface due to metal dissolution/re-deposition processes previously reported as surface amorphization [8]. This suggests that higher the OER catalytic activity, the less stable the oxide is.

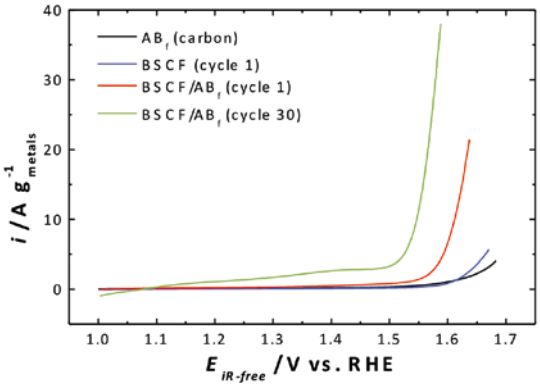

Figure 2: *Anodic OER currents for ABf, BSCF and BSCF/AB_f (5:1) electrodes measured by at 10 mV s^{-1} and 1600 rpm in O_2-saturated 0.1 M KOH.*

Summary and Conclusions

Thin-film rotating disk electrode analysis was used to show an enhanced OER activity when carbon is present for the perovskite BSCF. The increase in the OER activity was not found to be correlated to the oxide electrical resistivity as no electronic limitations were observed for the oxide on its own up to the catalyst loading used for the OER measurements. The results point to a synergetic effect between carbon and the selected perovskite oxide leading to enhanced OER activity.

Based on this study several important conclusions are drawn. The nature of the interaction between perovskite oxides and carbon in perovskite/carbon composite electrodes, that can lead to improved OER activity, needs to be clearly understood. This will enable the further development of better catalytic systems based on perovskite/carbon composite electrodes for the OER. However, as a consequence of its significant corrosion at high potentials, the inclusion of carbon may also be detrimental to the performance of such catalyst systems in the long term. One important focus would therefore be to develop alternative electrocatalysts with high OER activity without the need for carbon in the electrode composition. In order to achieve this by improving the rational design of new perovskite oxides for the OER, it is important to understand the intrinsic properties of the perovskite oxides under OER conditions. For this, carbon should be excluded from the electrode composition as it may significantly affect the OER behavior of selected oxides and lead to a misinterpretation of the intrinsic oxide activity.

Acknowledgement

We thank the South African Department of Science and Technology for financial support in the form of HySA/Catalysis Centre of Competence programme funding and a HySA/Catalysis student bursary. The financial assistance of the National Research Foundation (DAAD-NRF) towards this research is hereby acknowledged. Opinions expressed and conclusions arrived at, are those of the authors and are not necessarily to be attributed to the DAAD-NRF. We wish to also gratefully acknowledge the Swiss National Foundation (SNF) within the Ambizione Program (contract PZOOP2_148041/1) and the Swiss Competence Center for Energy Research (SCCER) Heat & Electricity Storage for financial support.

References

[1] E. Fabbri, A. Habereder, K. Waltar, R. Kötz, T.J. Schmidt, *Catal. Sci. Technol.* **4**, 3800 (2014).
[2] J.O.M. Bockris, T. Otagawa, *J. Electrochem. Soc.* **131**, 290– 302 (1984).
[3] J. Suntivich, K.J. May, H.A. Gasteiger, J.B. Goodenough, Y. Shao-Horn, *Science* **334**, 1383–1385 (2011).
[4] K. Kinoshita, *Carbon: Electrochemical and Physicochemical Properties*, Wiley: New York (1988).
[5] E. Fabbri, R. Mohamed, P. Levecque, O. Conrad, R. Kötz, T.J. Schmidt, *ACS Catalysis* **4**, 1061 (2014).
[6] E. Fabbri, R. Mohamed, P. Levecque, O. Conrad, R. Kötz, T.J. Schmidt, *ChemElectroChem* **1** (2), 338–342 (2014).
[7] R. Mohamed, E. Fabbri, P. Levecque, R. Kötz, T.J. Schmidt, O. Conrad, *ECS Trans.* **58**, 9 (2014).
[8] K.J. May, C.E. Carlton, K.A. Stoerzinger, M. Risch, J. Suntivich, Y.-L. Lee, A. Grimaud, Y. Shao-Horn, *J. Phys. Chem. Lett.* **3**, 3264 (2012).

Differential electrochemical mass spectrometry study of CO_2-electroreduction on model metal surfaces

Y. Paratcha, J. Herranz, J. Durst, J. Araújo, M. Özaslan, T.J. Schmidt
phone: +41 56 310 4189, e-mail: yohan.paratcha@psi.ch

Carbon dioxide is a major contributor to global warming and the possibility of recycling this greenhouse gas is becoming increasingly attractive. The electrochemical reduction of CO_2 is an interesting pathway since a broad range of useful products can be formed [1]. Nevertheless, on top of the high overpotential required to drive this reaction, the electrochemical reduction of CO_2 suffers from a poor yield/selectivity towards hydrocarbons [2, 3]. Improvements in this respect require a better understanding of the reaction yield on various metal surfaces, along with the development of analytical tools that allow for the quantification of the reaction products. Differential Electrochemical Mass Spectrometry (DEMS) appears as an excellent choice for the in-operando quantification of the volatile species produced upon CO_2 reduction [4]. With this motivation, we have designed and built an electrochemical flow cell coupled to a DEMS setup for the study of CO_2-reduction selectivity on surfaces. As an example of the possibilities offered by this setup, herein we present our results upon studying the reduction of CO_2 on polycrystalline Cu.

Experimental

The measurement setup, schematized in Figure 1, consists of an electrochemical flow cell separated from the DEMS' first vacuum chamber by a PTFE porous membrane of 0.02 µm pores that allow the crossing of volatile products. An aperture of 0.2 mm diameter results in a differential pressure between the DEMS' first and second vacuum chambers (at $\approx 10^{-2}$ and $\approx 10^{-5}$ mbar, respectively), whereby the latter holds the ion source and quadrupole mass analyzer.

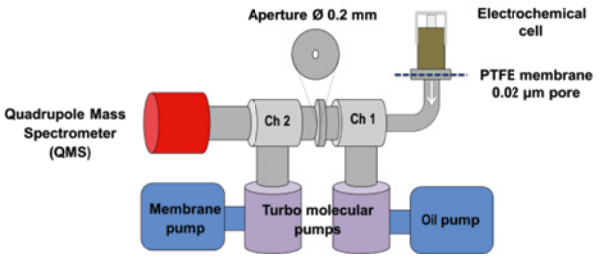

Figure 1: *Scheme of the DEMS setup.*

A polycrystalline Cu disk of 10 mm diameter was mechanically polished on a microcloth. The disk was sonicated three times for five minutes in ultrapure water and assembled onto the electrochemical cell connected to the DEMS. 100 mL of 0.1 M $KHCO_3$ saturated with CO_2 were used as electrolyte. A flame-annealed Pt mesh was used as counter electrode, along with a $Hg/HgSO_4$ reference electrode. Potential steps were applied to the system, starting from -0.5 V vs. RHE and decreasing by 50 mV in each step. Every step was 5 min long and between two steps, the potential was held for 5 min at -0.5 V vs. RHE. Different mass fractions were recorded by the MS during the reaction.

Results

Figure 2 shows the time evolution of the potential profile and the mass fragment signals m/z = 2 (H^{2+}) and m/z = 15 (CH^{3+}). Despite H_2 production, hydrocarbon production such as methane is observed in this study. Nevertheless, the yield of the hydrocarbon production is not as high as specified in literature, meaning that some parameters need to be adjusted. Oxygen was detected in the system and some leakages need to be fixed.

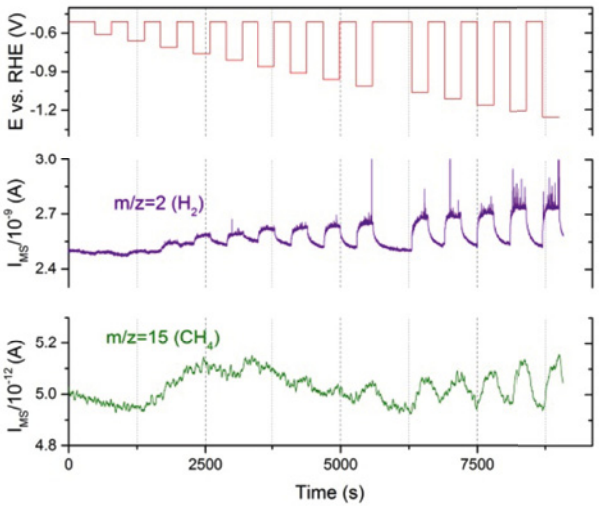

Figure 2: *(a) Potential steps in cathodic region of Cu. Ion current recorded by MS for mass fraction (b) m/z = 2 and (c) m/z = 15.*

Conclusion

Our preliminary experiments with this novel DEMS-system successfully confirmed the production of hydrocarbon via CO_2 electroreduction. However, the system suffers from sealing issues that have been tackled by improving the designs of the cell and the electrodes. Once these changes will be successfully implemented, we will apply this technique on Cu single crystals.

References

[1] K.P. Kuhl, E.R. Cave, D.N. Abram, T.F. Jaramillo, *Energy Environ. Sci.* **5**, 7050–7059 (2012).
[2] M. Watanabe, M. Shibata, A. Kato, *J. Electrochem. Soc.* **138**, 3382–3389 (1991).
[3] Y. Hori, H. Wakebe, T. Tsukamoto, O. Koga, *Electrochim. Acta,* **39**, 1833–1839 (1994).
[4] K.J.P. Schouten, E.P. Gallent, M.T.M. Koper, *J. Electrochem. Soc.* **716**, 53–57 (2014).

Oxygen reduction on Pt/SnO_2 catalysts: A model electrode study

A. Rabis, E. Fabbri, T.J. Schmidt
phone: +41 56 310 5172, e-mail: annett.rabis@psi.ch

Metal oxides are gaining growing interest as support materials for Pt catalysts in polymer electrolyte fuel cells (PEFCs) because they are expected to have higher stability in the oxidative electrochemical environment of a PEFC cathode compared to carbon supports of standard Pt/C catalysts [1]. One of the most promising candidates is SnO_2. Single cell and rotating disc electrode (RDE) measurements on the durability of Pt catalysts supported on SnO_2 showed an increased stability while keeping the same activity compared to Pt/C. An increase in oxygen reduction reaction (ORR) activity was found for Pt supported on Sb or Nb doped SnO_2 [2]. So far this effect is attributed to the increased conductivity of the doped SnO_2 supports. To unravel if the conductivity of the support is the only limiting factor influencing the activity of the Pt based catalyst we have prepared un-doped as well as Ta and Nb doped SnO_2 thin film electrodes by reactive magnetron sputtering. Doping SnO_2 with Nb or Ta results in an increase in the tin oxide con-ductivity, and therefore it allows investigating the influence of the dopant and of the support conductivity on the ORR activity of Pt based electrocatalysts.

Experimental

Pt/SnO_2 thin film model electrodes have been prepared by magnetron sputtering as described in reference [3]. Doping of SnO_2 thin films was achieved by modifying the Sn target with Nb or Ta chips. Doped SnO_2 supports were characterized by X-ray photoelectron spectroscopy (XPS) and four-point probe analysis. Electrochemical characterizations were carried out in a conventional three-electrode setup, with a $Hg/HgSO_4$ reference electrode and a platinum mesh counter electrode in 0.1 M $HClO_4$. An advance H_{upd} method [4] has been applied for the determination of the electrochemical active surface area (ECSA) of the oxide supported Pt catalysts. The ORR activity of the prepared catalysts was analyzed by performing slow scan voltammetry in oxygen-saturated electrolyte. More details on the catalyst characterization can be found in reference [5].

Results

XPS measurements were performed to evaluate the surface composition of the doped SnO_2 thin films. The binding energies of Sn $3d_{5/2}$, Nb $3d_{5/2}$ and Ta $4d_{5/2}$ are 487.0, 207.0 and 229.8 eV, respectively, These binding energies correspond to SnO_2, Nb_2O_5 and Ta_2O_5 showing that the dopants are present in the pentavalent oxidation state which is supposed to increase the conductivity of SnO_2. The concentration of the dopant before and after annealing did not show a change. Therefore, we expect no dopant segregating during sample preparation.

Electrical properties of the doped thin films were analyzed by four-point probe measurements. The conductivity of the Nb doped SnO_2 (NTO) was increased from $3{\cdot}10^2$ to $7.6{\cdot}10^3$ Scm^{-1} by increasing the dopant concentration from 0.5 to 2.0 at%. The highest conductivity of the Ta doped SnO_2 (TTO) is $6.5{\cdot}10^3$ Scm^{-1} at a dopant concentration of 1.1 at%. The increase of the conductivity by 2–3 orders of magnitude compared to the undoped SnO_2 prepared under the same conditions is a reliable indication for the homogeneous distribution of the dopant in the SnO_2 lattice.

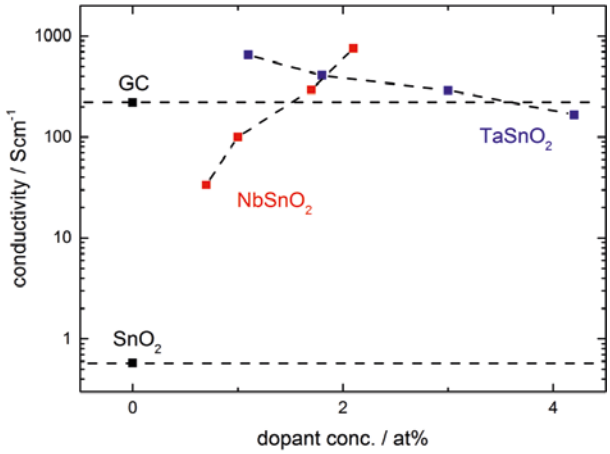

Figure 1: *Conductivity of TTO and NTO depending on the dopant concentration. GC and SnO_2 are given as a reference.*

To evaluate the ORR activity depending on the SnO_2 support 2 μgcm^{-2} Pt were deposited on NTO with 1.7 and 2.1 at% and on TTO having 1.1 and 1.8 at% dopant in the SnO_2 lattice. The CVs of the resulting catalysts are shown in Figure 2. In general, the characteristic Pt features as hydrogen adsorption/desorption (H_{upd}) and Pt-O formation/reduction can be observed. The H_{upd} region is less pronounced as standardly seen for Pt in perchloric acid [6]. This is mainly due to the large capacitive currents coming from the SnO_2 support.

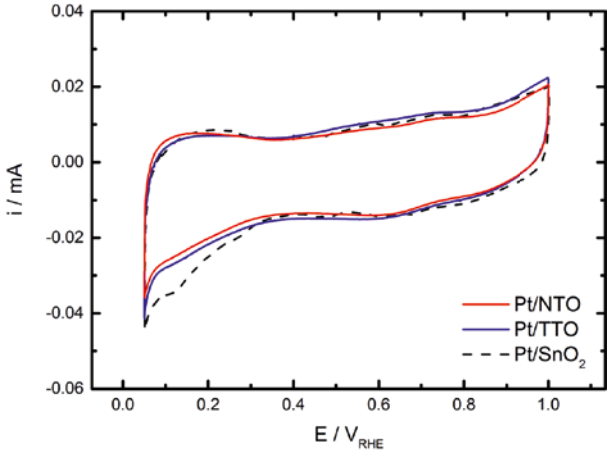

Figure 2: *CVs of 2 μgcm^{-2} Pt deposited on SnO_2, TTO and NTO thin film electrodes in 0.1 M $HClO_4$; scan rate 50 mVs^{-1}.*

Therefore, net currents of the Pt H_{upd} have been calculated by subtracting capacitive currents coming from the SnO_2 support. Using this method reproducible ECSA values of 30 ± 1 m^2/g were found for all catalysts.

The Pt oxide formation and reduction peaks are quite small for Pt on TTO and NTO. This can be related to PtSn alloy formation resulting from the deposition of Pt nanoparticles by magnetron sputtering which we already observed by XPS for Pt on undoped SnO_2 [5].

The ORR activity of Pt on undoped and doped SnO_2 was evaluated using RDE measurements. Figure 3 shows the polarization curves obtained from 2 μgcm^{-2} Pt deposited on either SnO_2, TTO and NTO. All curves show regions of mixed diffusion-kinetic control at high potentials and a pure diffusion controlled region at lower potentials. For the Pt on SnO_2 the diffusion limiting current was reached at a potential below 0.4 V. This might be caused by the relatively low conductivity of the SnO_2 film.

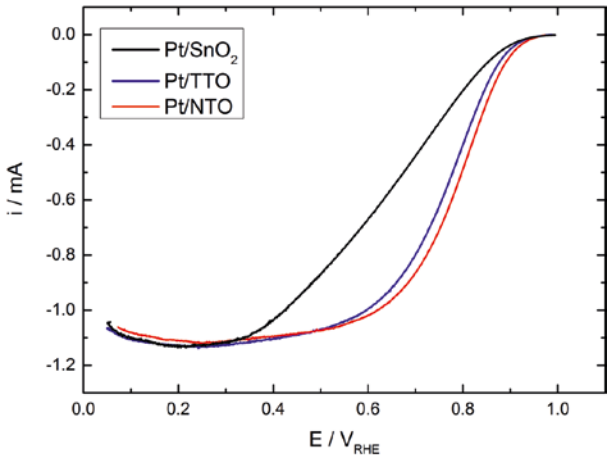

Figure 3: *Polarization curves of Pt/SnO_2, Pt/NTO and Pt/TTO in O_2-saturated electrolyte at 1600 rpm, cathodic sweeps are shown.*

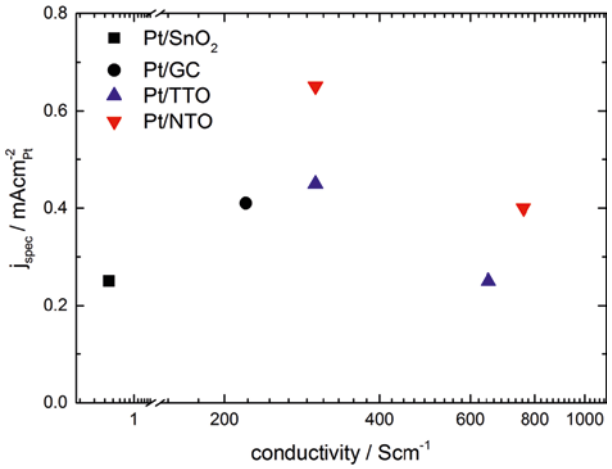

Figure 4: *Comparison of specific activities at 0.9 V for Pt/GC, Pt/SnO_2, Pt/NTO and Pt/TTO versus the conductivity of the support.*

To compare the ORR activity of the Pt/SnO_2 catalysts the polarization curves were corrected for mass transport limitations and normalized to the specific surface area. Values at 0.9 V were taken and plotted against the conductivity of the supports, as shown in Figure 4. The lowest ORR activities were found for Pt on pure SnO_2 and for TTO with 1.1 at% of dopant. The low activity of Pt/SnO_2 might be limited by the low conductivity of this support. Already the slope of the polarization curve (Figure 3) shows a high resistance which reduces the electronic contact to the Pt particles and therefore its activity. This is not the case for Pt on TTO with 1.1 at% of Ta. It has a conductivity which is three times higher than GC but the ORR activity is similar to the Pt/SnO_2 catalyst. This leads to the assumption that the ORR activity of Pt on TTO is not related to its conductivity. The same trend exists for Pt/NTO since the highest catalytic activity was found for Pt/NTO with 1.7 at% Nb. Even though this support is not showing the highest conductivity. To understand which characteristics are governing the ORR activity of Pt catalysts on SnO_2 supports the impact of the dopant onto the physical properties of SnO_2 needs to be analyzed in depth. Dopants as Nb and Ta do not only modify the conductivity but also influence crystal growth and density of SnO_2. Preliminary X-ray diffraction analysis indicated strain and differences in the crystal orientation depending on the nature and the concentration of the dopant. Both investigated dopants seem to introduce strain and, depending on the dopant concentration, a preferential 200 orientation of the SnO_2 lattice. These aspects might influence the surface of the support and therefore the electronic properties of the deposited Pt.

This study clearly demonstrates that the conductivity of the support is limiting the ORR of the catalysts if it is below a certain value. For supports having conductivities above this threshold material properties like crystal orientation, crystallite size and strain become important factors to tune the electronic properties of the supported catalyst.

Acknowledgement

The authors thank Umicore AG & Co. KG and the Competence Center for Energy and Mobility (CCEM) of Switzerland for their financial support within the project DuraCat.

References

[1] A. Rabis, P. Rodriguez, T.J. Schmidt, *ACS Catal.* **2**, 864 (2012).
[2] F. Takasaki, S. Matsuiea, Y. Takabatakea, Z. Nodab, A. Hayashib, Y. Shiratoria, K. Itoa, K. Sasakia, *J. Electrochem. Soc.* **158** (10), B1270 (2011).
[3] A. Rabis, E. Fabbri, A. Foelske, M. Horisberger, R. Kötz, T.J. Schmidt, *ECS Trans.* **50**, 9 (2013).
[4] T. Binninger, E. Fabbri, R. Kötz, T.J. Schmidt, *J. Electrochem. Soc.* **161**, H121 (2014).
[5] A. Rabis, D. Kramer, E. Fabbri, M. Worsdale, R. Kötz, T.J. Schmidt, *J. Phys. Chem. C* **118**, 11292 (2014).
[6] U.A. Paulus, A. Wokaun, T.J. Schmidt, V. Stamenkovic, N.M. Markovic, P.N. Ross, *Electrochim. Acta* **47**, 3787 (2002).

MEA with $Ir_xTi_{1-x}O_2$ supported Pt prepared by spray coating – influence of the ionomer content

A. Pătru, R. Kötz, T.J. Schmidt

phone: +41 56 310 2318, e-mail: alexandra.patru@psi.ch

Among the various areas of research on PEFC catalysts, alternative support development with improved stability and conductivity is one of the most important. The actual studies in this field are focused on conductive metal oxides, as they can exhibit a high electrochemical stability and a high conductivity when used in their higher oxidation states [1]. Additionally, these materials can be tailored with a high specific surface area, compatible with the targeted PEFC catalyst support application. The electrode design process is a crucial step in the introduction of this new type of catalyst support in real PEFC systems. Introduction of this catalyst support type in real PEFC electrode requires reviewing the entire electrode design process.

Due to its crucial role in formation of the three phase boundary, the influence of the ionomer content was investigated. An optimal content was determined for Nafion® with $Pt/Ir_xTi_{1-x}O_2$ (Umicore) as model catalyst.

Experimental

A 80/20 wt% water/isopropanol mixture was additioned with a commercial Nafion® solution and ultrasonicated for 10 minutes. The catalyst powder was dispersed in the as-prepared solution by sonication for at least 30 minutes. The solvent and co-solvent ratio has been optimized by Ngo et al. [2] with respect to the Nafion® morphology. When Pt/C was used, the Nafion® loading was fixed at 30 wt% with respect to the catalyst weight. For $Pt/Ir_xTi_{1-x}O_2$ the Nafion® loading was ranging from 5 to 20 wt%. A total of 4 catalyst ink solutions were prepared for $Pt/Ir_xTi_{1-x}O_2$.

The prepared catalytic ink was sprayed on each side of a Nafion® XL 100 membrane by using an airbrush with 20 mm diameter nozzle. The membrane was fixed on a vacuum plate and no additional heating was used for drying. Each layer of the sprayed catalyst ink was dried in an air flow. The membranes were sprayed until a quantity of ~0.4 $mg_{Pt}cm^{-2}$ was found on each side of the membrane. The catalyst coated membrane has been fixed between two gas diffusion layers by hot pressing at 1 ton m^{-2} and 120 °C for 1 minute. The laminated MEA was assembled into the single cell fixtures using PTFE gaskets of 0.8 mm thickness on both sides.

MEAs obtained from different inks were characterized in a single test cell with 29.16 cm^2 geometrical surface area. Pure oxygen and air were used alternatively as cathode reactants and pure hydrogen as anode reactant. A stoechiometric flow rate of $\lambda = 2$ was used for anode. Stoichiometric flow rates of $\lambda = 9.5$ for O_2 and $\lambda = 2$ for air were used for cathode. Reactant humidification was achieved by passing the gas through water at the respective dew point. Cell resistances as a function of current density were determined by using an AC perturbation at 1 KHz (Tsuruga milliohm meter).

The cell was started up and operated for about 12 hours at a temperature of 80 °C ($i = 0.5$ A cm^{-2}, ambient pressure, fully humidified H_2 and O_2 for Pt/C MEAs and 50 % RH for $Pt/Ir_xTi_{1-x}O_2$ MEAs). After the cell conditioning the cell back pressure was fixed at 1.5 bar_{abs}. The polarization curves were measured in a galvanostatic way. For each data point, the cell current was stabilized for 5 minutes and data were averaged from the last 3 minutes.

Results

The performances of $Pt/Ir_xTi_{1-x}O_2$ MEAs with different Nafion® loadings are shown in Figure 1. The performances in terms of power densities, increase when the ionomer loading in the CL is reduced from 20 wt% to 10 wt%. When the ionomer loading is reduced to 5 wt% in the CL, the performances decrease again. This trend is observed independently of the oxidant used (Figure 1 A, B).

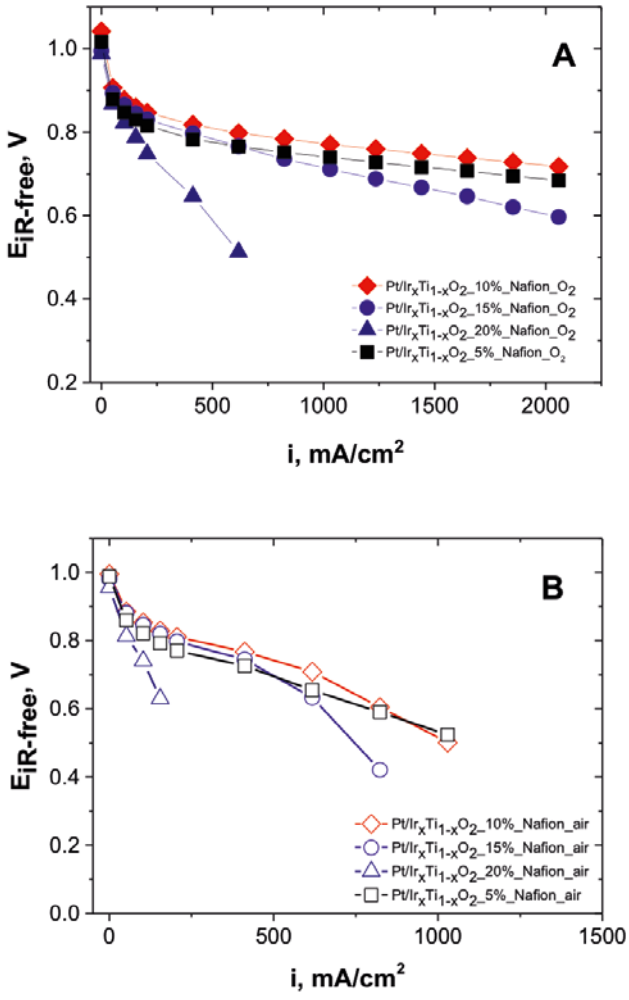

Figure 1: *Resistance corrected 29.16 cm^2 performance of the CCM based on $Pt/Ir_xTi_{1-x}O_2$ with different ionomer content. Performances obtained using oxygen (A) and air (B) as oxidant.*

At high ionomer content in the CL, some of the platinum particles are most likely embedded within ionomer and the reactants cannot access the catalyst surface. At low ionomer content (< 5 wt%), the protonic percolation network between the platinum catalyst is not fully ensured and the overall protonic conductivity is poor.

The SEM images represented in Figure 2 also support this interpretation. When 20 and 15 wt% Nafion® loading are used, the ionomer can be observed in the images (Figure 2 A, B). When 10 wt% Nafion® is used, the ionomer agglomeration is not visible on the SEM images (Figure 2 C). Moreover, the SEM images show a uniform catalyst layer without significant particle agglomeration.

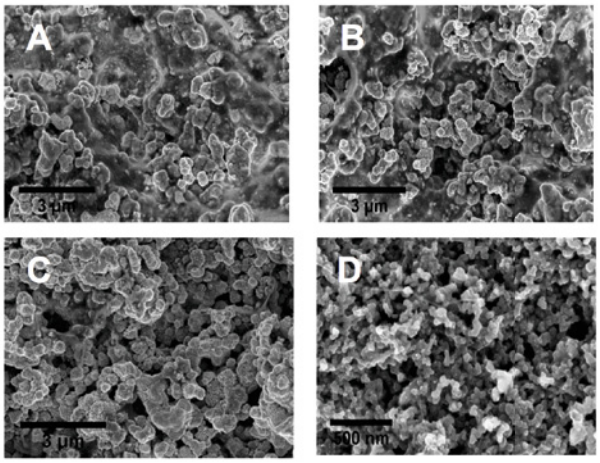

Figure 2: *Scanning electron microscopy images of Nafion® membrane coated with Pt/$Ir_xTi_{1-x}O_2$ (A, B, C) and Pt/C (D). Different ionomer contain are used for Pt/$Ir_xTi_{1-x}O_2$: 20 wt% (A), 15 wt% (B) and 10 wt% (C).*

The performances of optimised MEAs based on Pt/$Ir_xTi_{1-x}O_2$ were compared with the home-made MEAs based on a standard Pt/C catalyst (Tanaka 47 wt% Pt). In the case of Pt/C catalyst the optimal Nafion® content is above 30 wt% [3]. Figure 3 shows the polarisation curves of MEAs based on Pt/C catalyst and Pt/$Ir_xTi_{1-x}O_2$ (10 wt% Nafion® content). MEAs based on Pt/$Ir_xTi_{1-x}O_2$ cathode catalyst show similar performances when compared to the Pt/C catalyst.

MEA	Ionomer, wt %	Power density @ 0.65V, W/cm²	Specific power density @ 0.65V, g_{Pt}/kW
Pt/$Ir_xTi_{1-x}O_2$	5	0.400	1.25
Pt/$Ir_xTi_{1-x}O_2$	10	0.475	1.12
Pt/$Ir_xTi_{1-x}O_2$	15	0.377	1.34
Pt/$Ir_xTi_{1-x}O_2$	20	0.094	5.68
Pt/C	30	0.510	1.10

* @ 80°C, 150 kPa_{abs}, H_2/air reactants (λ =2/2)

Table 1: *Performance of MEAs after iR corrections based on Pt/$Ir_xTi_{1-x}O_2$ with different ionomer content and Pt/C.*

Table 1 summarises the MEAs performances expressed as power densities (Wcm^{-2}) and specific power densities ($g_{Pt}kW^{-1}$) at 0.65 V, 80 °C, 150 KPa_{abs} using H_2/air reactants (λ = 2/2) [4]. The specific power density obtained for a 10 wt% ionomer Pt/$Ir_xTi_{1-x}O_2$ is close to the value obtained for the Pt/C system, 1.12 $g_{Pt}kW^{-1}$ vs 1.1 $g_{Pt}kW^{-1}$. This suggests that the new type of oxide catalyst support can be used in a fuel cell without drastically reducing the performances.

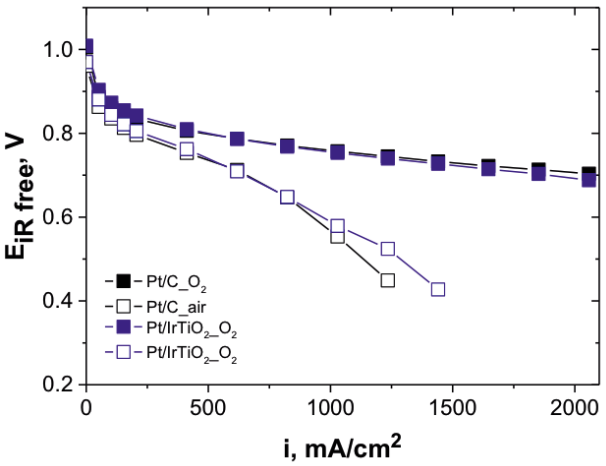

Figure 3: *i-E polarization curves comparing the performances of Pt/C and Pt/$Ir_xTi_{1-x}O_2$ MEAs registered using both oxygen and air as oxidant.*

Conclusions

MEAs based on Pt/$Ir_xTi_{1-x}O_2$ cathode catalyst have been optimised. Due to the catalyst morphological differences (BET surface area, texture), the ionomer content in the catalytic layer is different in the CCM based on Pt/oxide. An optimum was found at 10 wt% ionomer.

Optimised MEAs based on Pt/$Ir_xTi_{1-x}O_2$ cathode catalyst show similar performances compared to Pt/C catalyst.

As the feasibility and the reproducibility of the deposition process was successfully demonstrated, the next research phase will focus on the evaluation of the stability of the manufactured MEAs. For this purpose, start-stop cycling tests and/or other accelerated stress tests will be performed.

Acknowledgement

The authors thank Umicore AG&Co. KG and the Competence Center for Energy and Mobility (CCEM) of Switzerland for their financial support within the project DuraCat.

References

[1] E. Fabbri, A. Rabis, R. Kötz, T.J. Schmidt, *Phys. Chem. Chem. Phys.* **16**, 13672–13681 (2014).
[2] T.T. Ngo, T. Leon Yu, H-L. Lin, *J. Power Sources* **225**, 293–303 (2013).
[3] G. Sasikumar, J.W. Ihm, H. Ryu, *Electrochim. Acta* **50**, 601–605 (2004).
[4] H.A. Gasteiger, S.S. Kocha, B. Sompalli, F.T. Wagner, *Appl. Catal., B* **56**, 9–35 (2005).

Influence of spatial particle-support correlations on small-angle X-ray scattering spectra from supported catalyst materials

T. Binninger, M. Garganourakis, J. Han, A. Pătru, E. Fabbri, O. Sereda, R. Kötz, A. Menzel, T.J. Schmidt

phone: +41 56 310 5728, e-mail: tobias.binninger@psi.ch

The structure of catalyst particles at the nanoscale plays an important role in both heterogeneous catalysis and electrocatalysis. It determines the active surface area and therefore the efficiency of catalyst utilization. Catalyst degradation generally occurs due to a loss of active surface area originating from various mechanisms that affect the nanostructure of the catalyst. Therefore, for a detailed investigation of catalyst corrosion, structure-resolving techniques must be applied. Ideally, such techniques can be used *in situ* to monitor the dynamic changes of the catalyst structure in an experimental environment that is equal or at least simulating the conditions in a real application.

The most commonly used technique for structural characterization at the nanoscale is transmission electron microscopy (TEM). The clear advantages of this technique are the visual pictures that appear like «photographs» of the nanostructure. However, there are several limitations to this technique: Firstly, the information is only obtained on a very small part of the sample. Thus, conclusions about average properties of the entire catalyst sample must be taken with care. Secondly, the contrast between support and supported catalyst nanoparticles can be very weak for certain systems like Pt nanoparticles on a high-Z metal oxide support. This can make it difficult to distinguish the catalyst nanoparticles from individual support crystallites. In extreme cases, the absorption from the support can be so high that the supported catalyst particles become effectively invisible for TEM. Finally, due to the very short electron absorption length in condensed matter, TEM investigations cannot be performed *in situ* during operation.

These limitations of TEM can be overcome by small-angle X-ray scattering (SAXS): Firstly, even for very small beam diameters of a couple of hundred micrometers, the scattering curve contains information of hundreds of millions of catalyst nanoparticles. Secondly, the support contribution to the scattering curve can be subtracted with high precision by anomalous SAXS (ASAXS). This technique uses the anomalous changes of the scattering cross section close to elemental absorption edges which arise from the resonant excitation of electrons from low-energy core levels. In this way, the scattering contribution of a specific element can be varied by several ten percent by slightly varying the X-ray energy close to a respective absorption edge whereas the contribution of all other elements present in the sample remains approximately constant. After subtracting the SAXS curves recorded at two different X-ray energies the energy-independent contributions are eliminated and the subtracted signal generally is interpreted in terms of the sole catalyst nanoparticle scattering. This net scattering curve is commonly fitted with the model of scattering from an ensemble of spherical particles. However, a careful examination of the relevant scattering terms reveals that this procedure implicitly neglects the scattering interference between catalyst particles and support particles. Even for a completely random distribution of the catalyst particles on the support surface, the spatial correlations between catalyst particles and support do not average to zero: Each catalyst particle will be in direct contact with the support surface resulting in a strong spatial correlation and consequently in a strong scattering interference contribution.

We proved the existence and the strong influence of this particle-support interference both experimentally and theoretically [1]. The ASAXS experiments were performed at the cSAXS beamline X12SA at the Swiss Light Source (SLS) synchrotron at Paul Scherrer Institut on a iridium-titanium oxide supported platinum catalyst (Pt/IrO_2-TiO_2) which serves as a model for the search for stable metal oxide supported platinum catalysts for the oxygen reduction reaction (ORR) at the cathode side of polymer electrolyte fuel cells. The SAXS curves were recorded at several energies close to the Pt LIII absorption edge ($E_{Pt,LIII}$ = 11.56 keV).

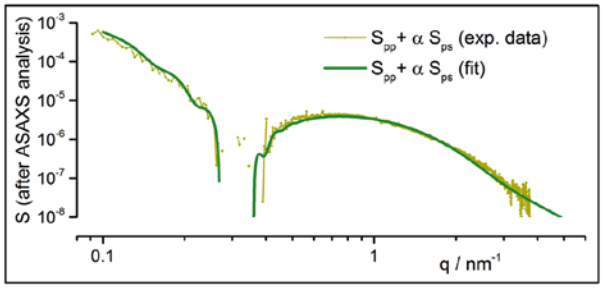

Figure 1: *Experimental Pt signal after ASAXS analysis (light). Also shown is a fit with the extended spherical particle model incorporating the particle-support interference (dark).*

Figure 1 plots the net Pt signal extracted by ASAXS analysis. The region of negative values (gap at intermediate q) is a clear signature of the particle-support interference, because the sole Pt structure factor must always be positive. We have extended the conventional model of spherical catalyst particles to incorporate this interference effect. A fit of the resulting function is also shown in Figure 1 and it agrees very well with the experimental data. This proves that the particle-support interference not only has a strong influence on the SAXS pattern of supported catalyst nanoparticles, but it can also be taken into account in the data analysis with high precision.

Acknowledgement

This work was supported by CCEM Switzerland and Umicore AG & Co KG within the project DuraCat. We acknowledge the Paul Scherrer Institut, Villigen, Switzerland, for provision of synchrotron radiation beamtime at the cSAXS beamline of the SLS.

References

[1] T. Binninger, M. Garganourakis, J. Han, A. Pătru, E. Fabbri, O. Sereda, R. Kötz, A. Menzel, T.J. Schmidt, *Phys. Rev. Applied* **3**, 024012 (2015).

New approach to Pt electrocatalysts by means of pulsed laser deposition

S.E. Temmel, D. Pergolesi, E. Fabbri, T. Lippert, T.J. Schmidt
phone: +41 56 310 2128, e-mail: sandra.temmel@psi.ch

One of the main obstacles towards a broad commercialization of polymer electrolyte fuel cells (PEFCs) is the potential loss at the cathode side caused by the sluggish kinetics of the oxygen reduction reaction (ORR). To improve the PEFC performance, a lot of attempts have been made to improve the electrocatalytic activity of Pt, state-of-the-art catalyst for the ORR [1]. For instance, Strasser et al. [2] showed that the Pt rich shell of dealloyed Pt-Co nanoparticles (NPs) exhibits lattice parameters smaller than bulk Pt and the NPs were, thus, of higher catalytic activity compared to relaxed NPs. However, in this work, Co contaminations or contribution of the underlying alloy to the electrocatalytic activity cannot be completely excluded.

We present, therefore, a new approach for tailoring strained Pt model electrocatalysts. Thin, epitaxial, strained pure Pt films were prepared using pulsed laser deposition (PLD) avoiding any alloy contaminations. By tuning the deposition parameters and varying the substrate, Pt films of different interatomic spacing and crystalline orientation can be prepared (Figure 1).

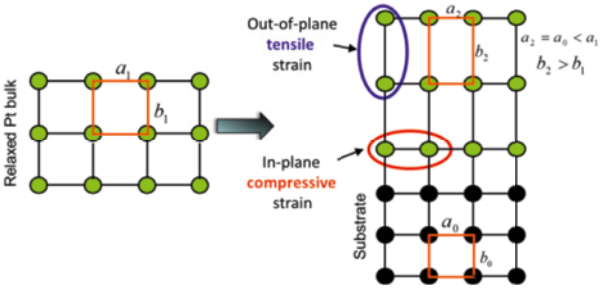

Figure 1: *Illustration of epitaxially strained Pt film grown on a single crystalline substrate with smaller lattice parameter.*

Strain refers to the change in the lattice constant due to forced matching to the substrate's lattice and is given by

$$\varepsilon = \frac{\Delta d}{d_{bulk}} \quad and \quad \Delta d = d_{bulk} - d_{Strain}$$

with d_{bulk} and d_{Strain} being the lattice constant of the bulk and the strained Pt film, respectively. In an epitaxial film growth, the Pt film lattice adapts to the lattice constant of the substrate and the crystallographic orientation of the substrate surface determines that of the film. The cubic perovskite structure of $SrTiO_3$ (STO) single crystal substrates allows the epitaxyally oriented cube-on-cube growth of Pt films. Due to the smaller lattice parameter of STO (3.905 Å) as compared to Pt (3.92 Å), the Pt film will grow compressively strained in-plane, whereas tensile strain is expected along the out-of-plane direction to preserve the unit cell volume. The overall aim of the project is to study the influence of the strain-induced variations of Pt interatomic distances and/or surface crystallographic orientation on its electrocatalytic activity towards ORR. Results on as-deposited (111) Pt films (12 nm) produced at varying temperatures concerning the crystalline orientation, the surface morphology, and the surface properties for electrocatalytic reactions are presented.

Experimental

Thin Pt films were grown on (111) oriented STO substrates (CrysTec, thickness of 0.5 mm, one-sided epipolished, miscut angle < 0.5°,10 x 10 mm^2) in O_2 atmosphere ($1{,}5 \cdot 10^{-2}$ mbar) by PLD using a KrF excimer laser (248 nm, 10 Hz, 26 kV). The target (positioned at 5 cm normal to the substrate surface) was rastered by the laser beam (spot size = $1 \cdot 10^{-2}$ cm^2, Fluence F = 1.8 J/cm^2) under a 45° angle for a total number of 20000 pulses. The substrate temperature was varied between 250 and 550 °C. Prior to deposition, the substrates were ultrasonically cleaned in ethanol, acetone and isopropanol for 10 min each. The Pt target was preablated for 10 min to smoothen and clean its surface. All deposition parameters are summarized in Table 1.

Substrate	(111) STO
Laser repetition rate	10 Hz
No. Of pulses	20000
Spotsize	0.1 cm^2
Fluence	1.8 J cm^{-2}
Substrate-Target-Distance	5 cm
Background gas	O_2
Pressure	$1x10^{-2}$mbar
Temperature	400°C

Table 1: *Deposition parameters for the fabrication of thin Pt films on (111) STO using PLD.*

θ–2θ X-ray scans were carried out with a D500 diffractometer (Bruker, Germany) using Cu-Kα radiation to examine the crystal structure and the out-of-plane strain of the Pt films. All measurements were performed at room temperature in the Bragg-Brentano diffraction geometry varying 2θ from 35° to 50°. The film thickness was determined via X-ray reflectometry (XRR) in a θ–2θ scan. The morphology of the film was investigated with scanning electron microscopy (SEM-Zeiss Supra) and atomic force microscopy (AFM-Nanoscope).

Physical characterization	Crystallographic orientation	**XRD**
	Film thickness	**XRR**
	Morphoology	**SEM**
	Surface roughness	**AFM**

Table 2: *Measurement techniques applied to characterize as-produced Pt films.*

An in-house designed flow cell using a three-electrode setup was used to test the catalytic activity of the as-produced Pt-films. Oxygen reduction reaction curves (ORRs) were recorded at room temperature in oxygen-saturated 0.5 M sulfuric acid at a sweep rate of 10 mV sec^{-1} (cathodic scan).

Results

One major challenge when producing thin Pt films is that 3D island growth is favoured over 2D layer-by-layer growth. However, a homogenous, continuous film is crucial for

- the conductivity throughout the whole Pt film,
- a well-determined electrochemically active area of inter-

est and
- a homogenous strain distribution.

Therefore, the effect of varying deposition temperatures on the Pt film morphology was investigated. SEM images (Figure 2) reveal that at 550 °C the Pt film clearly consists of separated islands whereas at 400 °C a homogenous film nearly fully covering the substrate was obtained. At 250 °C indistinct features,typically in the case of non-textured samples with low crystalline quality, were observed.

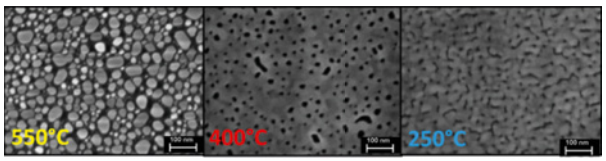

Figure 2: *SEM images of (111) Pt films deposited at varying temperatures.*

The XRD pattern clearly shows that all Pt films were (111) oriented, independent of the deposition temperature. However, the smaller relative intensity and broadening of (111) peak for the Pt film deposited at 250 °C strongly suggests that this film is not of good crystallinity. In contrast, the Pt film prepared at 400 °C exhibits Kiessig fringes, indicating a good crystalline quality. This is confirmed by the relatively small FWHM (full width at half maximum) of about 0.08° of the rocking curve of the (111) Pt peak. Further evaluation of the XRD pattern gives a tensile out-of-plane strain about 1 %, in turn proving the presence of compressive in-plane strain.

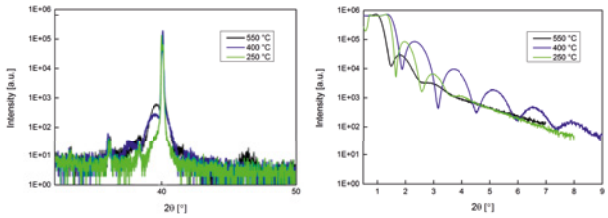

Figure 3: *XRD (left) and XRR (right) pattern of (111) Pt films grown by PLD in O_2 atmosphere on (111) STO at 10 Hz, 20000 pulses, 1.8 J cm^{-2} and varying temperatures.*

A thickness of 12 nm was calculated from the XRR patterns (Figure 3b). The well-defined oscillations and their slow decay for the Pt film produced at 400 °C are a good sign for a homogenous and smooth surface. Those findings are corrobated by AFM images showing a flat surface with RMS (root-mean-square) and Ra (average roughness) values of 0.4 and 0.18 nm, respectively.

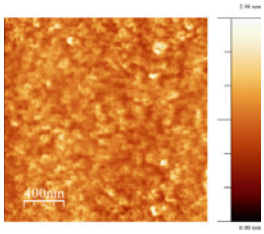

Figure 4: *AFM images (2x2 µm, Δz = 3 nm) of the surface of the (111) Pt film deposited at 400 °C.*

Due to its homogenous surface, the Pt films deposited at 400 °C were chosen for the electrochemical investigation. ORR curves were recorded at different flow rates (Figure 5) to evaluate the performance of the as-produced Pt (111) films. The dependence of the diffusion-limited current on the flow rate demonstrates the appropriateness of the flow cell design in addition to the good sample conductivity.

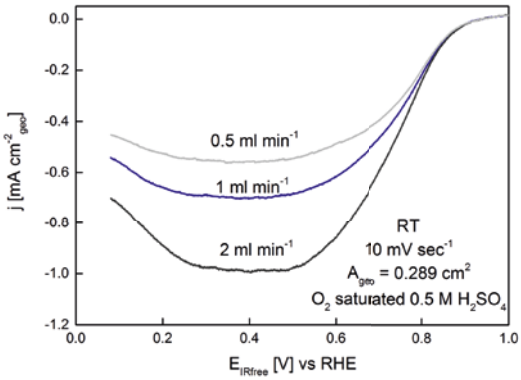

Figure 5: *ORR curves of the (111) Pt film deposited at 400 °C recorded at 3 different flow rates at 10 mV sec^{-1}.*

Assuming a negligible influence of mass transport on the current at 0.9 V (seen by the current independence on the flow rate at this potential), the kinetic current can be directly be extracted from Figure 5 and compared to kinetic data of (relaxed) Pt (111) single crystals from the literature [3]. Table 3 shows that the activity of the strained Pt (111) film is clearly improved as compared to a Pt (111) surface.

Flow cell	Setup	RDE [*]
0.5 M H_2SO_4	Electrolyte	0.05 M H_2SO_4
Strained (111)-Pt thin film	Electrode	Single crystalline (111)-Pt
10	Sweep rate [mV sec^{-1}]	20
23 @ RT	I [µA cm^{-2}] @ 0.9 V vs RHE	No activity @ RT

Table 3: *Comparison of kinetic current at 0.9 V vs RHE (reference hydrogen electrode) between strained Pt films and literature values of Pt bulk single crystals.*

Conclusion and Summary

A new approach to Pt electrocatalysts by PLD was shown. By optimizing the deposition temperature, (111) thin strained, epitaxial (111) Pt films were produced. Electrochemical characterization using a flow cell showed that the Pt films were active towards ORR. In comparison to Pt (111) bulk single crystals, their performance was significantly better, demonstrating the positive influence of the compressive strain on the ORR kinetics. This is a very promising result for further investigations of the impact of strain on the ORR activity of Pt electrocatalysts.

Acknowledgement

Kindly acknowledged is financial support from Kabelwerke Brugg AG, FH Nordwestschweiz and PSI.

References

[1] A. Rabis, P. Rodriguez, T.J. Schmidt, *ACS Catal.* **2**, 864–890 (2012).
[2] P. Strasser, S. Koh, T. Anniyev, J. Greeley, K. More, C.F. Yu, Z.C. Liu, S. Kaya, D. Nordlund, H. Ogasawara, *Nat. Chem.* **2** (6), 454 (2010).
[3] B.N. Grgur, N.M. Marković, P.N. Ross, *Can. J. Chem.* **75**, 1465–1471 (1997).

Process parameter study for plasma etching of platinum with an HSQ mask

S.A. Tschupp, W. Karim, Y. Ekinci, T.J. Schmidt
phone: +41 56 310 2127, e-mail: simon.tschupp@psi.ch

In order to study catalyst size and distance effects for fundamental electrocatalytic reactions, we are using top-down nanofabrication methods to obtain a narrow distribution of these parameters in contrast to chemical synthesis. Particle sizes in the sub-20 nm range have attracted considerable interest as they lie most closely to real systems [1]; for compatibility with common analytical tools areas in the range of cm^2 need to be patterned uniformly limiting the choice of suitable nanofabrication tools.

We adopted achromatic Talbot lithography (ATL) at the XIL-II beamline of the Swiss Light Source (SLS) fulfilling both requirements [2, 3]. For the pattern transfer to platinum – chosen as a reference catalyst metal – a process based on etching was used offering the possibility to further decrease the size of the metal structures below the size of the mask by overetching with an etch stop or applying isotropic chemical etching leading to an undercut.

Reactive ion etching (RIE), where material is removed at a solid-plasma interface, has the advantage that a broad range of process gases and energies can be used to achieve both physical sputtering and chemical etching. Using an inorganic resist as directly patternable hard mask the need for an extra layer of etch-resistant material is mitigated. Hydrogen silsesquioxane (HSQ) – a high resolution negative tone resist – is a promising material due to its chemical composition of SiO_{2-x}, as it has been shown that silica can be used as a hard mask material for platinum etching in high-density O_2/Ar plasmas [4, 5].

It has been proposed that oxygen ions passivate the oxide mask whereas the etch rate of platinum, mostly related to physical sputtering by high-energy argon ions, is largely unaffected by the oxygen concentration. A high etch selectivity for platinum to mask material is desirable to use thin masks which is a requirement for patterning small feature sizes.

Our aim is to optimize this process using HSQ – which can be directly patterned at the XIL-II beamline – instead of silica as hard mask material for the high-density plasma systems available at the Laboratory for Micro and Nanotechnology (LMN).

Experimental

RIE experiments were carried out using an Oxford Plasmalab System 100 fitted with a helical inductively coupled plasma (ICP) head for independent control of ion energy and plasma density. Samples were placed on a 4" silicon wafer which was mechanically clamped on a 240 mm diameter electrode, the temperature of which was kept constant at 30 °C during etching. Helium was injected at the backside of the supporting wafer for increased thermal contact. Prior to etching, the chamber was cleaned by a SF_6/O_2 plasma for 30 min, followed by preconditioning with an O_2/Ar plasma for 15 min. The plasma was generated by an ICP source (PICP = 500 W unless otherwise mentioned) operating at 13.56 MHz and the sample was biased through the application of RF power (PRF = 50 W unless otherwise mentioned). The chamber pressure, controlled by a butterfly valve, was kept at 10 mTorr with a total gas flow rate of 20 sccm unless otherwise mentioned. Samples were cleaned in an oxygen plasma for 60 s, followed by etching at the specified parameters for 30 s. The cleaning step was repeated every 30 s of the 4 min etching process.

Etch rates were determined by measuring step heights by atomic force microscopy (AFM) before and after RIE as well as after removal of the HSQ hard mask by buffered oxide etch (BOE), as outlined in Figure 1.

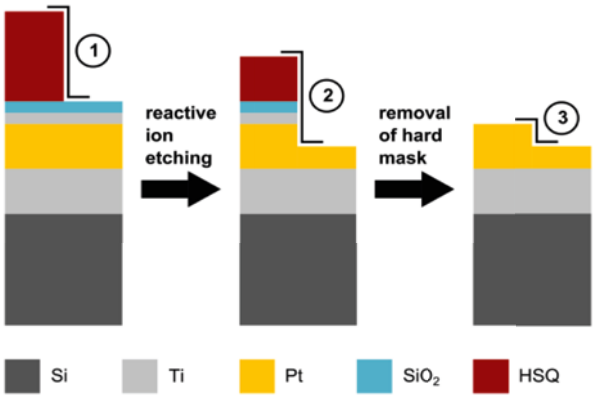

Figure 1: *Process flow for the determination of etch rates by AFM (step heights ①, ② and ③) before and after RIE and mask removal, respectively. Etch rates of HSQ were determined by division of ①+③–② by the etch time; etch rates of platinum by division of ③ by time.*

Samples for etching were prepared by coating a 4" silicon wafer with an e-beam evaporated Ti/Pt/Ti/SiO_2 multilayer of 20/20/2/2 nm thickness, respectively. HSQ (FOX XR1541, Dow Corning) was spin-coated at 2000 rpm for 60 s resulting in a 40 nm thick resist layer and squares of 1.7 mm side length were exposed at the XIL-II beamline with a mask-sample gap of 0.5 mm and a dose-on-mask of 250 mJ cm^{-2}. After the exposure the wafer was developed in a 25 % aqueous solution of Developer 351 (Microposit, Shipley) for 30 s and cleaved into 7x7 mm^2 dies each containing a single HSQ square.

Results

Figures 2 (a) and (b) show the etch rates of HSQ and platinum as a function of RF power at PICP = 500 W and as a function of ICP power at PRF = 50 W, respectively. For both, increasing ion energy (RF power) and increasing plasma density (ICP power), etch rates increase up to approximately 10 nm min^{-1} and 1.2 nm min^{-1} for HSQ and platinum, respectively. It should be noted that higher etch rates for HSQ result from the etching of the 4 nm Ti/SiO_2 adhesion layer or the titanium underlayer, as the total etch time was 4 min for a 40 nm thick HSQ mask.

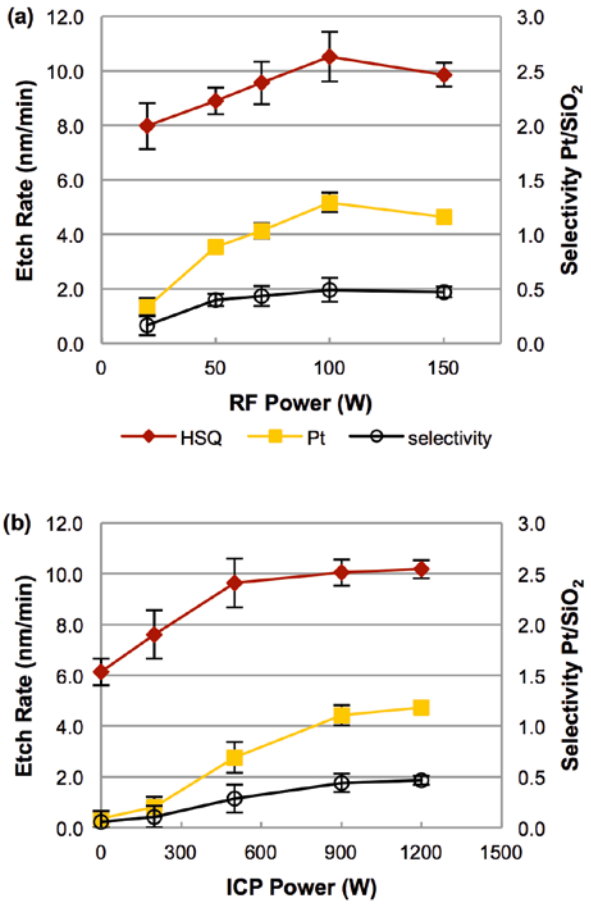

Figure 2: *Etch rates of HSQ and platinum (a) as function of RF power at PICP = 200 W and (b) as function of ICP power at PRF = 50 W. Chamber pressure was 10 mTorr at a total gas flow rate of 20 sccm for both experiments. Plasma composition was 16.7% O_2 in O_2/Ar. The lines serve as guide to the eye.*

Figures 3 (a) and (b) show the etch rates of HSQ and platinum as a function of pressure at 16.7 % O_2 in O_2/Ar and as a function of gas composition at 10 mTorr, respectively. For the parameters RF power, ICP power and pressure we obtained expected trends relating the mechanism of material removal for both HSQ and platinum predominantly to physical sputtering.

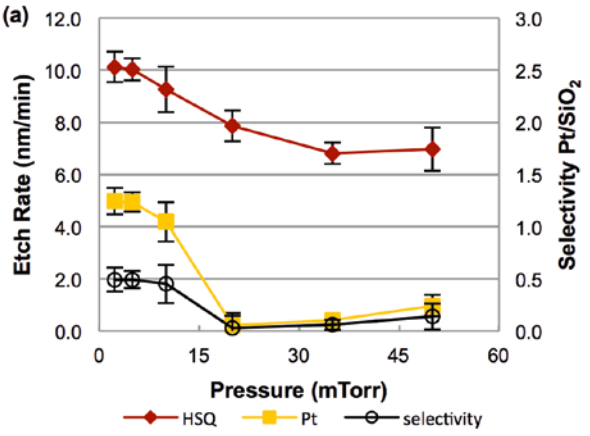

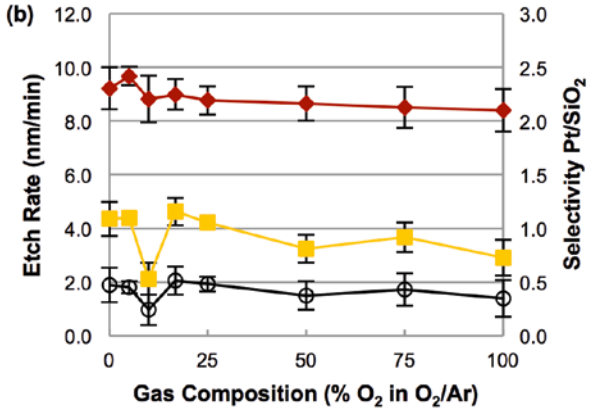

Figure 3: *Etch rates of HSQ and platinum (a) as function of pressure and total gas flow rate (not shown) at 16.7 % O_2 in O_2/Ar and (b) as function of gas composition at 10 mTorr. RF power was 50 W and ICP power was 500 W for both experiments. The lines serve as guide to the eye.*

Conclusions

We have not observed an increase in selectivity upon variation of the plasma composition as expected which could be attributed to small amounts of fluorine ions in the plasma chemically etching HSQ. Another possibility is the different densities of HSQ and silica resulting in different behavior with respect to physical sputtering.

In the next steps, we will extend this study to vary the electrode temperature as a mean of control over chemical etching processes and change the hard mask density via annealing. Furthermore, we aim to apply this knowledge to etch feature sizes in the nm range as a mean of pattern transfer to fabricate platinum model catalysts.

Other activities include the fabrication of carbon hard masks for argon ion milling, electrochemical (isotropic) etching of platinum and construction and testing of an electrochemical flow cell for the characterization of model catalysts on thin substrate wafers.

Acknowledgement

Part of this work was carried out at the XIL-II beamline of the SLS and in the Scanning Probe Microscopy Laboratory (SPM-Lab) of LMN. The authors would like to thank Michaela Vockenhuber and Markus Kropf for technical and PSI Research Commission for financial support.

References

[1] M. Shao, A. Peles, K. Shoemaker, *Nano Lett.* **11**, 3714–3719 (2011).
[2] L. Wang, B. Terhalle, M. Hojeij, V.A. Guzenko, Y. Ekinci, *J. Vac. Sci. Technol., B* **30**, 375302 (2011).
[3] K. Waiz, S.A. Tschupp. M. Özaslan, T.J. Schmidt, J. Gobrecht, J.A. van Bokhoven, Y. Ekinci, *Nanoscale*, (2015).
[4] T. Shibano, K. Nakamura, T. Oomori, *J. Vac. Sci. Technol., A* **16**, 502–508 (1998).
[5] K. Nakamura, T. Kitagawa, K. Ozari, K. Takahashi, K. Ono, *Vacuum* **80**, 761–767 (2006).

Study of the Ce(IV)/Ce(III) redox couple on different catalysts for redox flow cell application – reaction reversibility and catalyst performance

S.M. Taylor, A. Pătru, T.J. Schmidt
phone: +41 563104340, e-mail: susan.taylor@psi.ch

Redox flow cell technology has received significant attention in the application for renewable energy conversion systems over the past few decades [1]. The overall cell performance in terms of power density can be improved by several approaches:

- increasing the redox species solubility and stability in the electrolyte solution,
- maximising the potential difference between the two redox couples and
- using an active electrode material in order to obtain high current densities.

Today, the all-vanadium systems belong to the best researched technologies in this field. The main advantage of using vanadium redox couples V(II)/V(III) and V(V)/V(IV) in the anolyte and catholyte, respectively, is that cross mixing of electrolyte between the positive and negative side of the cell basically does not affect the overall cell performance [2, 3]. However, the maximum achievable power density of this particular system is limited by the standard redox potential of the positive electrolyte redox couple V(V)/V(IV) of 1.02 V vs. SHE.

The Ce(IV)/Ce(III) redox couple is an attractive positive electrolyte system for use in a redox flow cell, owing to its high positive standard redox potential of 1.44 V vs. SHE in H_2SO_4, and even higher 1.72 V vs. SHE in $HClO_4$ [4]. This could potentially result in a higher cell voltage and hence greater power density of the overall system. The reversibility of the selected redox couple plays a crucial role in the overall cell efficiency and durability.

In this study the reversibility and kinetics of the Ce(IV)/Ce(III) redox couple in H_2SO_4 were investigated on different catalyst surfaces.

Experimental

A 0.426 $molL^{-1}$ Ce(IV) solution was prepared by dissolving the corresponding amount of cerium (IV) sulphate (Sigma Aldrich, 99%) in a 1 $molL^{-1}$ solution of H_2SO_4 (Merk, Ultra Pure, 96%) giving a solution with the maximum Ce(IV) solubility in 1 $molL^{-1}$ H_2SO_4 [5]. All measurements were carried out at 298 K under an argon atmosphere in a conventional three-electrode setup, with a $Hg/HgSO_4$ reference electrode and a platinum mesh counter electrode. The Ce(IV) reduction reaction was studied on four different carbon surfaces, namely: glassy carbon, activated glassy carbon, VulcanXC72® and an onion-like carbon. The reaction was also carried out on a polycrystalline gold electrode. The glassy carbon electrode was activated by potential cycling in 1 $molL^{-1}$ H_2SO_4 between 1.9 and 0.5 V vs. RHE for 50 cycles.

Results

Figure 1 shows the cyclic voltammograms obtained for the Ce(IV) reduction reaction in 1 $molL^{-1}$ H_2SO_4 on four different carbon catalysts.

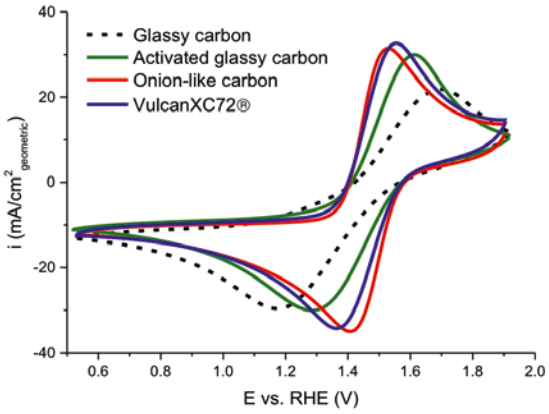

Figure 1: *Cyclic voltammograms of 0.426 $molL^{-1}$ Ce(IV) in 1 $molL^{-1}$ H_2SO_4 at 298 K, scan rate 50 mV/s, on different carbon catalysts.*

The reversibility of this system was assessed in terms of the separation of peak potentials between the anodic and cathodic peaks, ideally equal to 59 mV, and in terms of the ratio of the cathodic to anodic peak current densities, ideally equal to unity [6]. From Table 1 it can be seen that the peak separation is not equal to 59 mV for the Ce(IV)/Ce(III) redox couple on any of the catalysts investigated. The system can be described as quasi-reversible in this case [6]. The redox reaction of Ce(IV)/Ce(III) on the onion-like carbon catalyst showed the best reversibility, indicated by the smallest value for the peak separation measured at 5 mV/s. Moreover, the kinetics of the Ce(IV) reduction reaction appear to be very active on this type of carbon, as shown by the high kinetic rate constant (k_0).

Table 1 summarises the reversibility parameters and the kinetic rate constants determined using the Nicholson method for the Ce(IV)/Ce(III) redox couple on the different catalyst surfaces [7].

Catalyst	ΔE_p (mV) @5 mV/s	$i_{p,c}/i_{p,a}$	$^{a}k_0$ $x10^4$ (cm/s)	$^{b}k_0$ $x10^4$ (cm/s)
Onion-like carbon	98	1.06	8.7	3.4
Gold	140	1.20	5.3	5.3
VulcanXC72®	117	1.01	5.1	1.8
Activated glassy carbon	191	1.00	0.98	0.93
Glassy carbon	314	1.30	0.27	0.27

a k_0 calculated using current densities normalised by the geometric surface area of a 5 mm diameter glassy carbon disk electrode and **b** k_0 calculated using the normalised carbon surface area.

Table 1: *Summary of reversibility and kinetic parameters for Ce(IV) reduction on different catalysts at 298 K.*

Figure 2 shows the cyclic voltammograms obtained on polycrystalline gold compared to the best carbon catalyst, onion–like carbon. In terms of the kinetic rate constant k_0, the polycrystalline gold also appears to be active towards Ce(IV) reduction reaction.

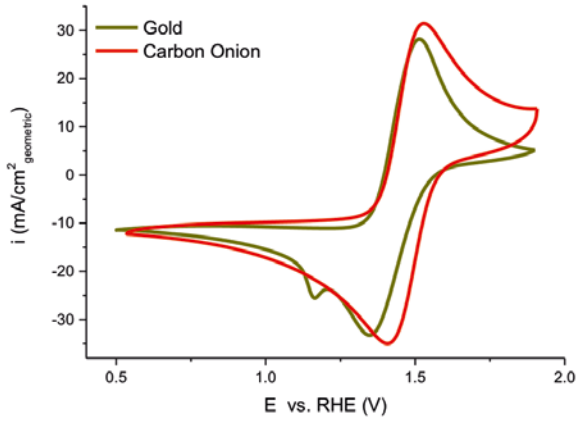

Figure 2: *Cyclic voltammograms for 0.426 molL^{-1} Ce(IV) in 1 molL^{-1} H_2SO_4 at 298 K, scan rate 50 mV/s for polycrystalline gold and onion-like carbon catalysts.*

The kinetics and reversibility study of Ce(IV) reduction on the different carbon catalysts and on gold indicate that this reaction is not strongly dependent on the catalyst surface material itself. This behavior suggests that Ce(IV) reduction occurs via an outer-sphere reaction mechanism, with the coordination sphere remaining intact during the electron-transfer process. This could be a possible advantage of the Ce(IV)/Ce(III) system over the V(V)/V(IV) system which has been found to have a more complex reaction mechanism and a greater dependence on the catalyst surface material [8].

This study has been carried out primarily for the understanding of the system reversibility and kinetic parameters on different catalyst surfaces. The system performance itself in terms of current density could be improved by increasing the species solubility in the supporting electrolyte as well as optimising the catalyst active surface area for the reaction. Studies focusing on increasing Ce(IV) solubility by the use of methane sulphonic acid (MSA) are part of ongoing research on this topic [9].

Conclusions

This study serves as a preliminary indication of the reversibility of the Ce(IV)/Ce(III) redox couple on various catalyst materials. The Ce(IV)/Ce(III) redox couple is termed quasi-reversible on all the catalyst materials investigated here. The onion-like carbon catalyst showed the best results with respect to reversibility and kinetics of the redox system. However, it is notable that there seems to be little dependence of reversibility on the catalyst surface itself, which is an indication of an outer-sphere reaction mechanism for Ce(IV) reduction. This is of great interest as it is a possible advantage of this redox system and would allow a greater flexibility in choice of electrode material. The promising results for the gold catalyst could also be advantageous for this type of system owing to the stability of gold under high potential conditions. In the next research phase, different electrode morphologies based on gold will be studied.

Acknowledgement

The authors thank The Swiss National Science Foundation (SNF) for their financial support within the REPCOOL Project (Grant No. 147 661). The authors also thank Dr. Daniel Weingarth and Dr. Volker Presser (INM – Leibnitz-Institut für Neue Materialien GmbH) for providing the onion-like carbon catalyst.

References

[1] C. Ponce de Léon, A. Frias-Ferrer, J. Gonzalez-Garcia, D.A. Szanto, F.C. Walsh, *J. Power Sources* **160**, 716–732 (2006).
[2] F. Rahman, M. Skyllas-Kazacos, *J. Power Sources* **189**, 1212–1219 (2009).
[3] G. Oriji, Y. Katayama, T. Miura, *J. Power Sources* **139**, 321–324 (2005).
[4] G.H. Aylward, T. Findlay, *SI Chemical Data* (2007).
[5] A. Paulenova, S.E. Creager, J.D. Navratil, Y. Wei, *J. Power Sources* **109**, 431–438 (2002).
[6] J. Bard, L.R. Faulkner, *Electrochemical Methods Fundamentals and Applications*, 2nd Ed. (2001).
[7] R.S. Nicholson, *J. Anal. Chem.* **37** 1351–1355 (1965).
[8] M. Gattrell, J. Park, B. MacDougall, J. Apte, S. McCarthy, C.W. Wu, *J. Electrochem. Soc.* **151**, A123–A130 (2004).
[9] P.K. Leung, C. Ponce de Léon, C.T.J. Low, F.C. Walsh, *Electrochim. Acta* **56**, 2145–2153 (2011).

High surface area oxygen evolution catalysts

K. Waltar, D. Lebedev[1], E. Fabbri, A. Fedorov[1], C. Coperet[1], T.J. Schmidt
phone: +41 56 310 4131, e-mail: kay.waltar@psi.ch

Within the development of a green hydrogen economy Polymer Electrolyte Membrane (PEM) Electrolyzers are projected to play a key role [1]. They provide the opportunity of energy conversion from intermittently produced electrical excess energy, generated as green solar or wind energy, into chemical energy carriers, particularly hydrogen. The underlying process of water electrolysis includes the generation of hydrogen at the electrolyzers' cathode and the evolution of oxygen at its anode. While the generation of hydrogen proceeds with fast electrochemical kinetics on Pt containing catalysts, the concomitant oxygen evolution reaction (OER) faces sluggish kinetics and high overpotentials. In addition, the corrosive environment at the anode due to an acidic environment, high interfacial potentials and high temperature, forms a limiting factor of the electrodes lifetime. The pool of possible OER catalysts is therefore limited to a few noble metal (mixed-)oxides among which the state-of-the-art materials showing a sufficient compromise between stability [2] and activity are IrO_2 and $Ir_xRu_{1-x}O_2$. A cost-effective implementation of PEM electrolyzers on a large scale is based on the reduction of the anodes noble metal content. To fulfill these objectives there are 3 main pathways as summarized in Figure 1.

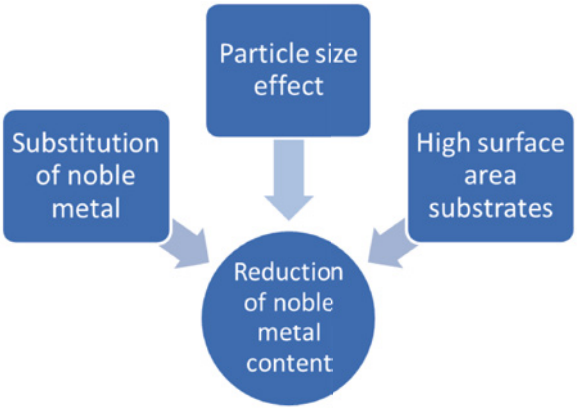

Figure 1: *The three main strategies to decrease the catalysts noble metal content.*

The present research work is focused on capitalizing the particle size effect. A reduction of the catalyst particle diameter enhances its surface to volume ratio and is thereby expected to increase the electrochemically active surface area per unit of mass.

Experimental

In collaboration with the Surface and Interfacial Chemistry (SIC) group at ETH Zürich different IrO_2 catalyst samples of high surface area were synthesized via a modified Adams fusion method, namely the formation of oxide nanoparticles from molten sodium nitrate. Nanoparticles obtained through this synthesis method were characterized by powder X-ray diffraction (XRD), transmission electron microscopy (TEM), nitrogen adsorption/desorption measurements and by electrochemical methods amongst which are Cyclic Voltammetry, Chronopotentiometry and Electrochemical Impedance Spectroscopy. Furthermore, the rotating-ring disk electrode (RRDE) technique was investigated in consideration of determining faradaic current efficiencies during the OER on different catalyst materials. As an important parameter, the collection efficiency of the RRDE setup was determined by employing hydrogen peroxide as the electroactive species. Compared to the commonly used ferrocyanide/ferricyanide redox couple it has the advantage of mimicking the OER as a gas evolving reaction in a potential regime in which the electrolyte is still stable. A potential limit of oxygen generation due to oxygen saturation of the electrolyte can therefore be determined. For three different catalysts the trend of the faradaic current efficiency with potential during OER has been determined.

Results

The synthesized IrO_2 nanoparticles were smaller than 5 nm thereby developing surface areas higher than 200 m^2/g according to N_2 adsorption/desorption measurements. Despite the small size, they crystallized in rutile structure.

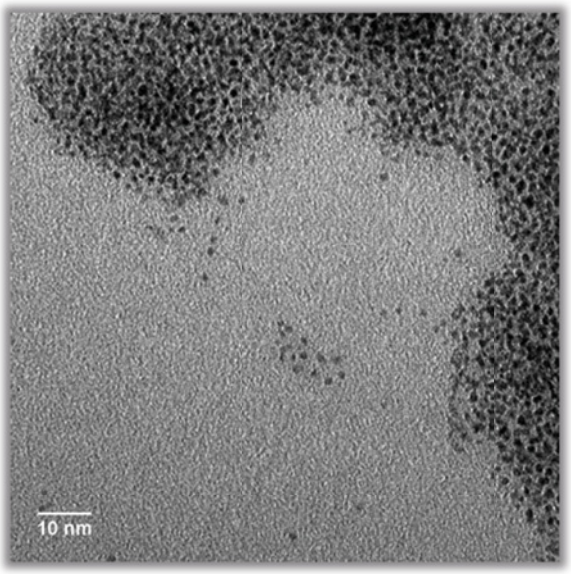

Figure 2: *TEM picture emphasizing the size and distribution of IrO_2 nanoparticles synthesized by a modified Adams fusion method.*

In order to compare different catalysts electrochemically, a comparable quantity had to be defined first. Different to the situation on Pt catalysts in fuel cell applications there is no common agreement on such a quantity for oxide-type OER catalysts in literature [1]. Therefore, the working electrode potential at a current density of 10 A/g was used for comparison within this study. Figure 2 displays ohmic drop corrected polarization curves for several IrO_2 catalysts used in this work. The resulting trend of decreasing overpotential with increasing total surface area is emphasized in Figure 3.

[1] ETH Zürich

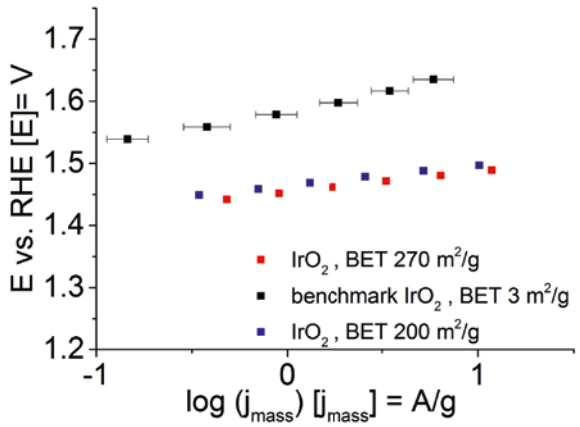

Figure 3: *IR-corrected polarisation curves for IrO_2 catalysts of different surface area.*

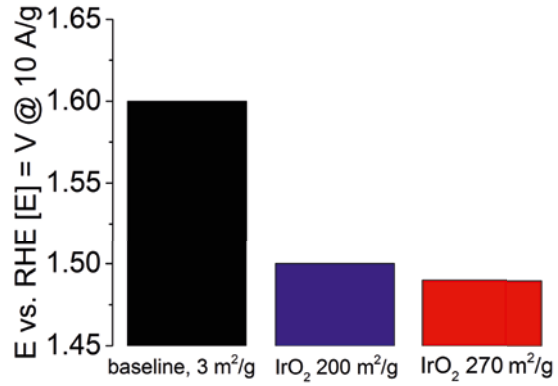

Figure 4: *Working electrode potential at 10 A/g for 3 different IrO_2 samples.*

The current regime of stable collection efficiency of the RRDE setup was determined by variations of the hydrogen peroxide concentration in the electrolyte.

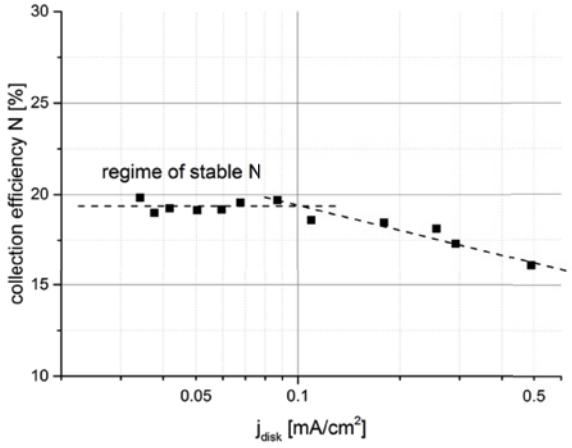

Figure 5: *Stability regime of collection efficiency up to 0.1 mA/cm².*

The current regime of stable collection efficiency is limited (Figure 5). Therefore, it defines an operational limit of 0.1 mA cm^{-2} for oxygen evolution current densities in RRDE experiments determining faradaic current efficiencies.

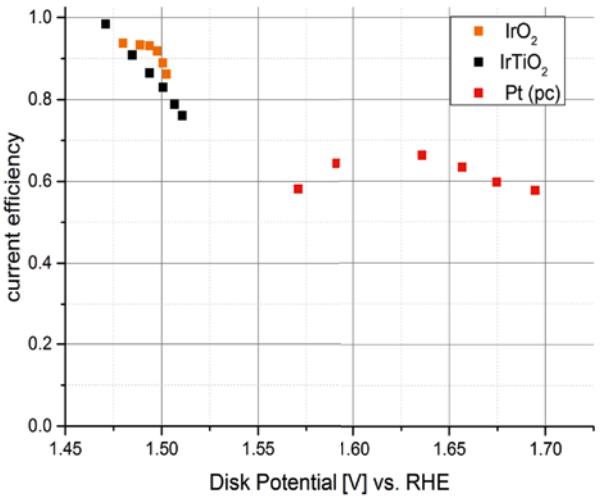

Figure 6: *Faradaic current efficiencies of three catalysts determined in the RRDE setup within the regime of stable collection efficiency.*

Discussion

The observed trend between a decreasing electrode potential to drive a certain fixed current and higher total surface area can be explained by an increased number of active reaction sites due to a larger electrode/electrolyte interface or, respectively, a larger electrochemically active surface area. It is to be elucidated if an increasing number of micropores, inaccessible to the electrolyte, cause the oxygen evolution reaction rate and therefore the activity of the catalysts to saturate with respect to the total surface area as determined by N_2 adsorption/desorption measurements.

The RRDE setups collection efficiency was investigated and a maximum current regime with stable collection efficiency determined. Within this regime of stability current efficiency measurements can be performed. On three model catalysts a decrease in current efficiency with the applied potential is observed (Figure 6). In the absence of impurity oxidation, the decreasing current efficiency is a clear sign of corrosion processes taking place at the catalyst under investigation. Since the valence state of the corrosion product is unknown, a more quantitative evaluation is not possible at the moment.

Acknowledgement

The authors would like to acknowledge funding from the Competence Center Energy & Mobility Switzerland, the Swiss Competence Center for Energy Research Heat & Electricity Storage, the Swiss Federal Office of Energy (SFOE) and Swiss Electric Research. Umicore AG & Co KG is acknowledged for the supply of $IrTiO_2$ samples.

References

[1] E. Fabbri, A. Habereder, K. Waltar, R. Kötz, T.J. Schmidt, *Catal. Sci. Technol.* **4** (11), 3800–3821 (2014).
[2] R. Kötz, S. Stucki, *Electrochim. acta* **31** (10), 1311–1316 (1986).
[3] J. Cheng, H. Zhang, G. Chen, Y. Zhang, *Electrochim. Acta* **54** (26), 6250–6256 (2009).

THE ELECTROCHEMISTRY LABORATORY

Facts & Figures

STRUCTURE 2014

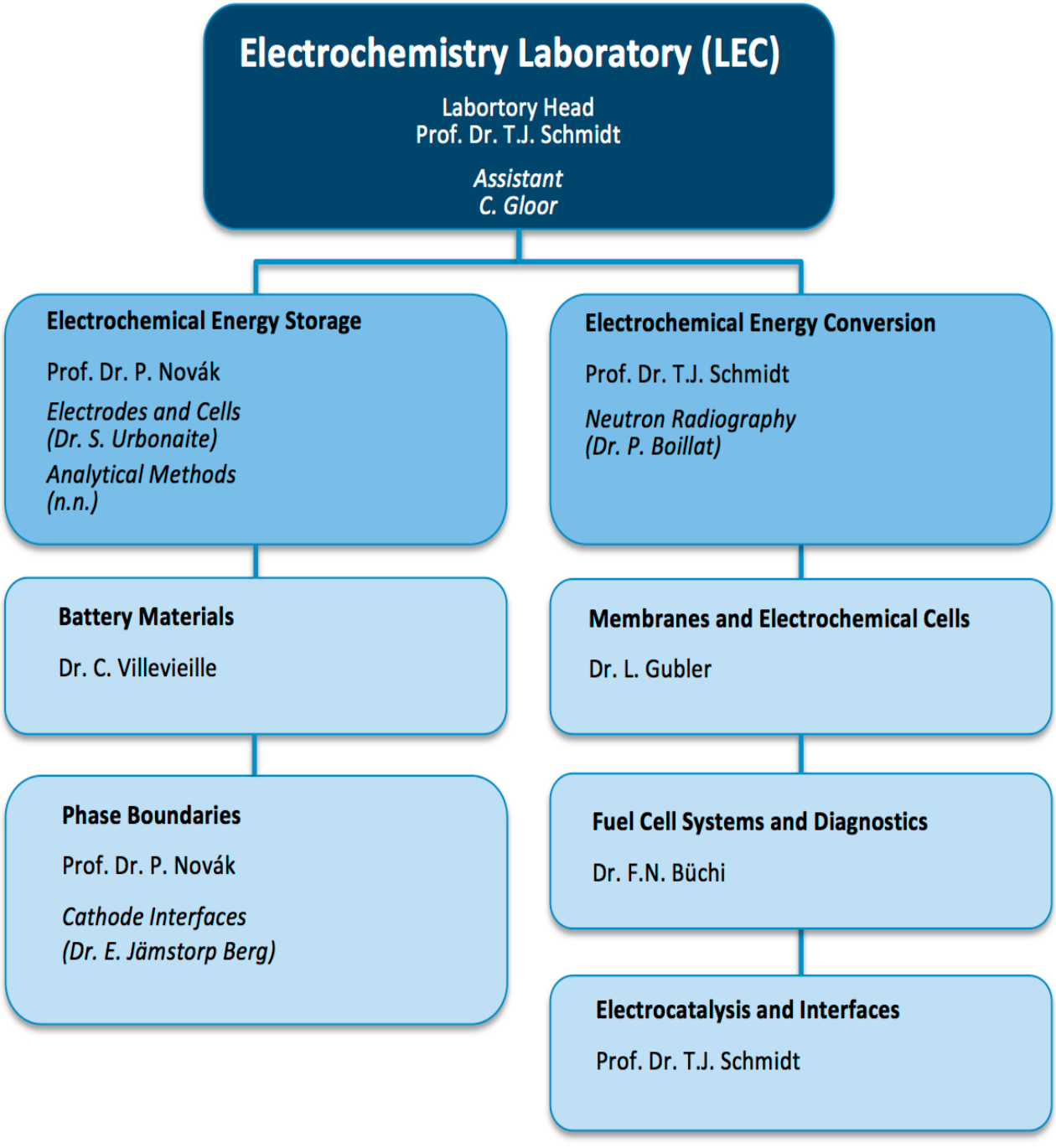

PERSONNEL 2014

Staff

Martin AMMANN (Technician)
Felix BERNAUER (Engineer)
Dr. Pierre BOILLAT (Project Leader)
Lukas BONORAND (Engineer)
Dr. Felix N. BÜCHI (Group Leader)
Dr. Christa BÜNZLI (Post Doctoral Researcher)
Dr. Elias CASTEL (Post Doctoral Researcher)
Dr. Xi CHENG (Post Doctoral Researcher)
Dr. Magali COCHET (Scientist)
Dr. Julien Durst (Scientist)
Dr. Mario EL KAZZI (Scientist)
Dr. Jens ELLER (Scientist)
Dr. Emiliana FABBRI (Scientist)
Dr. Maria GEORMEZI (Post Doctoral Researcher)
Cordelia GLOOR (Assistant)
Thomas GLOOR (Technician)
Dr. Juan Luis GÓMEZ-CÁMER (Post Doctoral Researcher)
Dr. Lorenz GUBLER (Group Leader)
Dr. Aurélie GUÉGUEN (Scientist)
Dr. Juan HERRANZ SALANER (Post Doctoral Researcher)
Dr. Marcel HOFER (Engineer)
Dr. Erik JÄMSTORP BERG (Post Doctoral Researcher)
Christoph JUNKER (Technician)
Hermann KAISER (Technician)
Dr. Rüdiger KÖTZ (Group Leader)
Dr. Adrien LAMIBRAC (Post Doctoral Researcher)
Christian MARMY (Technician)
Prof. Dr. Petr NOVÁK (Section Head)
Dr. Tiphaine POUX (Post Doctoral Researcher)
Dr. Mehtap ÖZASLAN (Scientist)
Dr. Alexandra PĂTRU (Post Doctoral Researcher)
Christian PETER (Engineer)
Dr. Rosa ROBERT SANCHEZ (Scientist)
Florian RUNTSCH (Engineer)
Dr. Sébastien SALLARD (Scientist)
Prof. Dr. Thomas J. SCHMIDT (Laboratory Head)
Dr. Daniel STREICH (Post Doctoral Researcher)
Jürg THUT (Technician)
Dr. Sigita URBONAITE (Scientist)
Dr. Claire VILLEVIEILLE (Group Leader)

PhD Students

Albert ALBERT
Tobias BINNINGER
Johannes BIESDORF
Peter BLEITH
Lucien BOULET-ROBLIN
Yves BUCHMÜLLER
Joanna CONDER
Sebastian EBERHARDT
Tom ENGL
Giulio FERRARESI
Antoni FORNER-CUENCA
Anja HABEREDER
Minglong HE
Immanuel MAYRHUBER
Olga NIBEL
Patrick LANZ
Yohan PARATCHA
Hai-Jung PENG
Annett RABIS
Martin REICHARDT
Sebastian SCHMIDT
Jakub SEWERYN
Véronique SPROLL
Michel SUERMANN
Susan TAYLOR
Sandra TEMMEL
Simon TSCHUPP
Leonie VOGT
Kay WALTAR
Zhuoxiang ZHANG

The Electrochemistry Laboratory, April 2014.

Fuel Cells Systems and Diagnostics Group, April 2014.

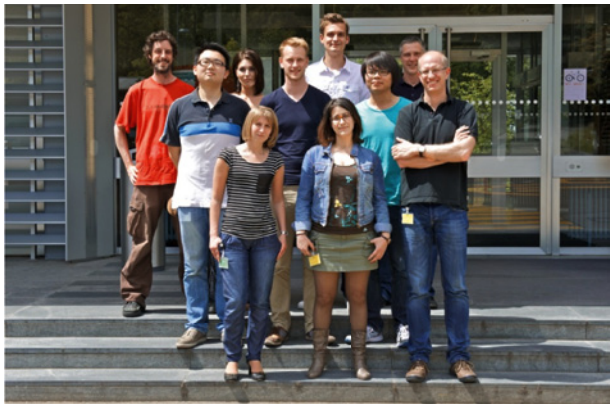

Membranes and Electrochemical Cells Group, April 2014.

Electrocatalysis and Interfaces Group, April 2014.

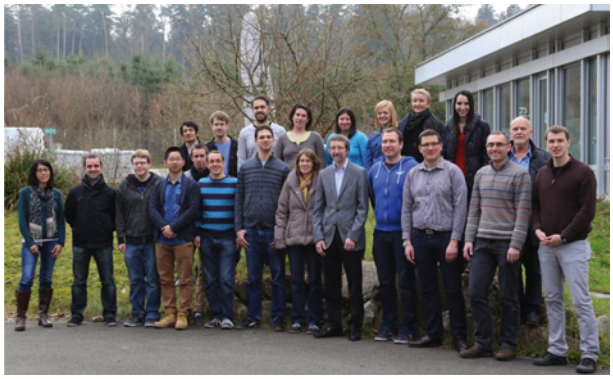

Energy Storage Group, January 2014.

DISSERTATIONS 2014

Dr. Yves Buchmüller

Antioxidants in radiation grafted membranes for fuel cells

Ph.D. Thesis No. 22075, ETH Zürich, June 2014.

Examiners: Prof. Dr. A. Wokaun, PSI Villigen/ETH Zürich
Prof. Dr. T.J. Schmidt, PSI Villigen/ETH Zürich
Prof. Dr. R. Nesper, ETH Zürich
Dr. L. Gubler, PSI Villigen

Dr. Zhuoxiang Zhang

Chemical degradation of radiation grafted membranes for fuel cells

Ph.D. Thesis No. 22197, ETH Zürich, September 2014.

Examiners: Prof. Dr. A. Wokaun, PSI Villigen/ETH Zürich
Prof. Dr. T.J. Schmidt, PSI Villigen/ETH Zürich
Dr. L. Gubler, PSI Villigen

Dr. Peter Bleith

Elucidation of the reaction mechanism of $M_{0.5}TiOPO_4$ upon lithiation and delithiation

Ph.D. Thesis No. 22295, ETH Zürich, October 2014.

Examiners: Prof. Dr. P. Novák, PSI Villigen/ETH Zürich
Prof. Dr. M. Kovalenko, ETH Zürich
Dr. C. Villevieille, PSI Villigen

Dr. Patrick Lanz

In situ characterization of electrode materials for lithium-ion batteries by Raman and IR microscopy

Ph.D. Thesis No. 22294, ETH Zürich, October 2014.

Examiners: Prof. Dr. P. Novák, PSI Villigen/ETH Zürich
Prof. Dr. M. Kovalenko, ETH Zürich

EXCHANGE STUDENTS, DIPLOMA THESES, SUMMER STUDENTS, GUEST SCIENTISTS

Tim Lochner
Ostbayrische Technische Hochschule Amberg-Weiden, Germany

In situ and ex situ characterization of aging phenomena in components for fuel cells and water electrolyzers
January – September 2014 (Membranes and Electrochemical Cells).

Muriel Siegwart
ETH Zürich

Effects of gas diffusion layer compression on the performance of a polymer electrolyte fuel cell
February – May 2014 (Neutron Radiography).

Ceren Yilmaz
ETH Zürich

Electrochemical investigations of high-surface area pure Pt and bimetallic Pt_xPd_{1-x} aerogels for the oxygen reduction reaction
February – July 2014 (Electrocatalysis and Interfaces).

Iris Kovácsovics
ETH Zürich

Synthesis of $LiFeBO_3$ and «$NaFeBO_3$» as insertion materials for Na-ion batteries
March – May 2014 (Battery Materials).

Prof. Kohei Miyazaki
Kyoto University, Kyoto, Japan

Electrochemical CO_2 reduction followed by differential electrochemical mass spectrometry
March – August 2014 (Electrocatalysis and Interfaces).

Jörn Käse
Ostbayrische Technische Hochschule Amberg-Weiden, Germany

Charakterisierung von Hochtemperatur Polymerelektrolyt-Brennstoffzellen
October 2013 – March 2014 (Membranes and Electrochemical Cells).

Miloš Toulec
Institute of Chemical Technology Prague, Czech Republic

Analyzing X-ray tomographic images
August 2013 – April 2014 (Fuel Cell Systems and Diagnostics).

Roger Staubli
ETH Zürich

Start – Stop strategies for H_2/O_2 PEFC systems
May – December 2014 (Fuel Cell Systems and Diagnostics).

Muriel Siegwart
ETH Zürich

Statistical analysis of cold start behavior of polymer electrolyte fuel cells
June – August 2014 (Neutron Radiography).

Heidi Thuv
Norwegian University of Science and Technology, Trondheim, Norway

Electrochemical study of Si/C composites with particulate and fibrous morphology as negative electrodes for lithium-ion batteries
June – August 2014 (Battery Materials).

Yuji Chino
University of Yamanashi, Kofu, Japan

Pt nanoparticles supported on oxide thin films: model electrodes for application in polymer electrolyte fuel cells
June – November 2014 (Electrocatalysis and Interfaces).

Sylvain Rigal
Institut National Polytechnique de Toulouse, Toulouse, France

Fuel cell flowfield simulation
June – August 2014 (Fuel Cell Systems and Diagnostics).

Ahmet O. Tezel Norwegian University of Science and Technology, Trondheim, Norway	*SEI forming reactions on graphitic anodes in li-ion batteries: Effect of anion receptor and $NaPF_6$ addition* July 2014 – July 2015 (Battery Materials).
Stefan Harms Faserinstitut Bremen, Germany	*Characterization of low and high temperature polymer electrolyte fuel cells using CO_2 containing H_2 as fuel* August – November 2014 (Membranes and Electrochemical Cells).
Rhiyaad Mohamed University of Cape Town, South Africa	*Synthesis and characterization of conductive oxide supports for Pt nanoparticles as cathode materials for polymer electrolyte fuel cells* August – December 2014 (Electrocatalysis and Interfaces).
Patricia Gröninger ETH Zürich	*Internal contact angle measurement of gas diffusion layers* September – October 2014 (Neutron Radiography).
Alice Gillen Trinity College, Dublin, Ireland	*Investigation of the early stages of the surface layer formation on cycled HE-NCM vs. LTO electrodes using XPS and SEM* September – December 2014 (Battery Materials).
Iris Kovácsovics ETH Zürich	*Electrochemical studies of Mg or Ca doped HE-NMC as insertion material in Li-ion half- and full-cells* September 2014 – January 2015 (Battery Materials).
Maximilian Tornow ETH Zürich	*Synthesis of tunable porous carbons and their application in batteries* September – December 2014 (Battery Materials).
John Boland Trinity College, Dublin, Ireland	*Finding the perfect carbon for Li-S batteries* September – December 2014 (Battery Materials).
Polychronis Patapis ETH Zürich	*Fuel cell characterization: hardware and software implementation and single cell testing* October 2014 – March 2015 (Membranes and Electrochemical Cells).

SEMINAR, INVITED SPEAKERS

Dr. Matthew Brown Institute for Chemical and Bioengineering, ETH Zürich	*X-ray photoelectron spectroscopy at the liquid-nanoparticle interface* January 15, 2014.
Dr. Katherine Ayers Proton OnSite, Wallingford, CT, USA	*Research needs and progress for megawatt scale PEM electrolysis* May 8, 2014.
Prof. Kohei Miyazaki Kyoto University, Kyoto, Japan	*Electrocatalysts and ion conductors for alkaline fuel cells* May 14, 2014.
Prof. Peter N. Pintauro Vanderbilt University, Nashville, TN, USA	*Nanofiber particle/polymer electrodes for hydrogen/air fuel cells* June 2, 2014.
Prof. Peter N. Pintauro Vanderbilt University, Nashville, TN, USA	*Multicomponent space-charge ion uptake and transport models for Nafion® membranes* June 3, 2014.
Prof. Makoto Uchida University of Yamanashi, Takeda, Kofu, Japan	*Research and development on high performance polymer electrolyte fuel cell materials in the HiPer-FC project* June 4, 2014.
Dr. Donat Adams Empa, Dübendorf	*Impedance and modelling for battery diagnostics* July 2, 2014.
Prof. Peter Strasser TU Berlin, Germany	*The oxygen evolution reaction during water electrolysis* July 15, 2014.
Dr. Nenad Markovic Argonne National Laboratory, Lemont, IL, USA	*Tailoring the future of surface electrochemistry* September 8, 2014.
Dr. habil. Klaus-Dieter Kreuer Max-Planck-Institut für Festkörperforschung, Stuttgart, Germany	*Ion containing polymers for fuel cells and batteries: Where polymer-chemistry meets electrochemistry* September 10, 2014.
Dr. Rangachary Mukundan Sensors and Electrochemical Devices, Los Alamos National Laboratory, USA	*Water management and durability of PEM fuel cells for automotive applications* October 2, 2014.

Dr. Marisa Medarde
Laboratory for Developments and Methods (LDM), Paul Scherrer Institut, Villigen

Ion conductors between two worlds: from fundamental physics to energy applications
November 26, 2014.

Prof. Stefano Passerini
European Editor of the Journal of Power Sources, Helmholtz Institute Ulm, Karlsruhe Institute of Technology, Ulm, Germany

Materials for sodium-ion batteries
December 17, 2014.

AWARDS

Mehtap Özaslan

Umicore Scientific Award 2014

For her PhD work in the field of *Catalytic properties of cathode fuel cell electrocatalysts.*

Bruxelles, Belgium, March 12, 2014.

Moritz M. Hantel

ETH Medaille 2014

For his excellent PhD thesis *Graphite oxide and graphene oxide based electrode materials for electrochemical double layer capacitors.*

Zürich, April 10, 2014.

Tom Engl

Best Poster Award
T. Engl, T.J. Schmidt, L. Gubler

Think different! Novel carbon corrosion mitigation strategy in high temperature PEFC.

3rd International Seminar on Green Energy Conversion, Yamanashi, Japan, August 25–27, 2014.

Albert Albert

Best Poster Prize Winner
A. Albert, T.J. Schmidt, L. Gubler

Radiation grafted polymer electrolyte membranes for water electrolysis cells – characterization of key membrane properties.

65th Annual Meeting of the International Society of Electrochemistry, Lausanne, August 31–September 5, 2014.

Peter Bleith

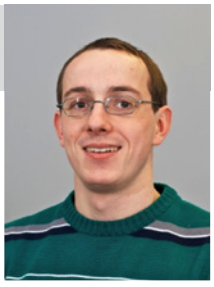

Best Poster Prize Winner
P. Bleith, H. Kaiser, P. Novák, C. Villevieille

Combined in situ XRD and XAS studies on materials for Li-ion batteries.

65th Annual Meeting of the International Society of Electrochemistry, Lausanne, August 31–September 5, 2014.

CONFERENCES – SYMPOSIA

30th PSI Electrochemistry Symposium May 7, 2014.

Oxygen: Airborne Energy Conversion and Storage

Organizers:
Thomas J. Schmidt, Cordelia Gloor

Contributions from (in order of appearance):
Hubert A. Gasteiger, TU München, Germany
Pascal Häring, Renata Batteries, Itingen
Jennifer Rupp, ETH Zürich
Jan Rossmeisl, DTU Lyngby, Denmark
Peter Strasser, TU Berlin, Germany
Katherine Ayers, Proton OnSite, Wallingford, CT, USA

From left to right: Jennifer Rupp, Hubert A. Gasteiger, Felix N. Büchi, Lorenz Gubler, Katherine Ayers, Thomas J. Schmidt, Peter Strasser, Jan Rossmeisl, Petr Novák (not shown on the picture: Pascal Häring).

The Assistants during the event (from left to right): Ursula Ludgate (SCCER), Cordelia Gloor (Electrochemistry Laboratory), Hannelore Krüger (Atmospheric Laboratory).

Pascal Häring (speaker) and Rüdiger Kötz (retired ECL group leader Electrocatalysis & Interfaces).

Talks, …

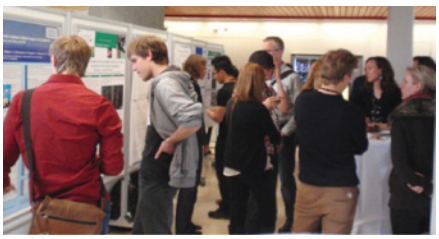

… poster session, …

… lunch and discussions.

REVIEW ACTIVITIES OF THE LABORATORY

Journals

A Advanced Functional Materials ♦ Angewandte Chemie International Edition ♦ Applied Surface Science

C Chemistry of Materials ♦ ChemSusChem

E ECS Electrochemistry Letters ♦ Electrochemistry Communications ♦ Electrochimica Acta

F Fuel Cells

I International Journal of Hydrogen Energy

J Journal of the American Chemical Society ♦ Journal of the Electrochemical Society ♦ Journal of Fuel Cell Science and Technology ♦ Journal of Membrane Science ♦ Journal of Physical Chemistry ♦ Journal of Power Sources ♦ Journal of Solid State Electrochemistry ♦ Journal of Synchrotron Radiation

N Nature Materials

P Physical Chemistry Chemical Physics

R RSC Advances

Organisations

A Agence National de Recherche, France ♦ Alexander von Humboldt-Stiftung, Germany

D Danish Council of Strategic Research

E ETH Zürich Research Commission

F FFG Österreichische Forschungsförderungsgesellschaft

N National Sciences and Engineering Research Council of Canada ♦ National Science Foundation, USA

S SNF (Schweizerischer Nationalfonds) ♦ Society in Science

T The Research Council of Norway

Q Qatar National Research Fund

External Dissertations: Review Activities

Thomas J. Schmidt:

- Z. Jovanov, DTU Lyngby, Denmark
- T. Poux, University of Strasbourg, France
- J. Hofer, ETH Zürich

Felix N. Büchi:

- Zhixue Zheng, Université de Franche-Comté, France

Lorenz Gubler:

- Assma El Kaddouri, Université de Grenoble, France
- Luis Felipe Rodrigues Castanheira, Université de Grenoble, France

Petr Novák:

- Ch. Karlsson, Uppsala University, Sweden

INDUSTRIAL PARTNERS

Collaborations with Industrial Partners

The Laboratory had the pleasure to collaborate with the following industrial partners during the year 2014:

B BASF SE, Ludwigshafen, Germany ♦ Belenos Clean Power Holding, Biel/Bienne

C Cellera, Caesarea, Israel

E ElringKlinger, Dettingen, Germany

I IBM Zürich Research Laboratory, Rüschlikon ♦ IMERYS Graphite & Carbon, Bodio

S Saft SA, Bordeaux, France

U UMICORE AG & Co. KG, Hanau, Germany

DOCUMENTATION

Project Collaborations with External Partners

BFE

P. Boillat Project leader	*In situ study of water transport processes in polymer electrolyte electrolysers with neutron imaging*
F.N. Büchi Project leader	*High Pressure Polymer Electrolyte Electrolysis* with Belenos Clean Power Holding, Biel/Bienne
F.N. Büchi Project leader	*S_Chain Fundamentals* with ZHAW Winterthur and Belenos Clean Power Holding, Biel/Bienne
L. Gubler Project leader	*Lebensdauer Limitierungen von Brennstoffzellen-Membranen: Mechanismen, Methoden und Innovationen*
T.J. Schmidt Project leader	*Renewable Energies in Future Energy Supply (RENERG^2)*

CCEM

C. Bach, T.J. Schmidt Project leaders	*RENERG^2 (Renewable Energies in Future Energy Supply)* with ETH Zürich, Empa Dübendorf, EPF Lausanne, ZAHW Winterthur
F.N. Büchi Project leader	*ADMIST (Advanced Understanding of Micro Structures in Fuel Cells and Batteries through X-ray Imaging)* with Laboratory for Nanoelectronics ETH Zürich
L. Gubler	*Hy-Form: Formic acid – chemical storage of electrical energy and on-site hydrogen production for use in PEM fuel cells* with EPF Lausanne, Granit Technologies SA, ZHAW Winterthur
C. Villevieille	*SLIB (All solid state Li-ion batteries based on new ceramic Li-ion electrolytes)* with ETH Zürich, Empa Dübendorf
T.J. Schmidt Project leader	*DURACAT (Highly durable oxide-based catalysts for polymer electrolyte fuel cells)* with ETH Zürich, CSEM Neuchâtel, University of Southampton UK and Umicore AG & Co KG.
T.J. Schmidt	*From tailored CO_2 -sorbent to optimized CO_2 electrochemical reduction catalyst: building tools for converting waste CO_2 to valuable chemicals* with ETH Zürich

EU

P. Boillat	*H_2FC (Integrating European infrastructure to support science and development of hydrogen- and fuel cell technologies towards European strategy for sustainable competitive and secure energy)*
F.N. Büchi, P. Boillat	*Auto-Stack CORE (Automotive Fuel Cell Stack Cluster Initiative for Europe)*
L. Gubler	*NOVEL (Novel materials and system designs for low cost, efficient and durable PEM electrolysers)*

KTI

T.J. Schmidt Director	*Swiss Competence Center for Energy Research – Heat & Electricity Storage*
C. Villevieille	*SCCER Heat & Electricity Storage: materials, systems, and modelling (sodium batteries work package)*

PSI Research Commission

T.J. Schmidt Co-Project leader	*Improved Insight into Catalysis Mechanisms via Nanopatterned Metal Structures (Nanocat)* Cross Initiative with Prof. J. Gobrecht; Prof. J.A. van Bokhoeven
L. Gubler Co-Project leader	*Structure-Property Correlations of Ion-Containing Polymers for Fuel Cells* Cross Initiative with Dr. U. Gasser; Dr. S. Balog, Université de Fribourg

SNSF

P. Boillat Project leader	*Synthesis and characterization of porous materials with patterned wettability for advanced fuel cell water management strategies*
F.N. Büchi	*Designing multifunctional materials for proton exchange membrane fuel cells* with ZHAW Winterthur NFP70 project
E. Fabbri Project leader	*Designing novel electrocatalysts for fuel cells and electrolyzers by tailoring perovskite surface properties* SNSF Ambizione project
L. Gubler Project leader	*Antioxidant strategies for the stabilization of fuel cell membranes against oxidative stress*
L. Gubler Project leader	*Lithium conducting polymer electrolytes with polysulphide barrier properties*
P. Novák Project leader	*In situ research on new generation of electrochemical capacitors* (Polish-Swiss research programme)
S. Sallard Project leader	*Hybrid organic-inorganic lithium metal diphosphonates and derivatives, new insertion materials for Li-ion batteries*
T.J. Schmidt Project leader	*Designing nano-extended multimetallic aerogel fuel cell catalysts for oxygen reduction reaction* with TU Dresden, Germany
T.J. Schmidt, L. Gubler	*Redox flow electrochemistry for power delivery and cooling (REPCOOL)* with IBM Research, ETH Zürich, Università della Svizzera Italiana SNF Synergia project
C. Villevieille Project leader	*Surface and interface investigations of high density energy electrodes for sodium-ion batteries*

Industry

P. Boillat Project leader	*Diagnostics of polymer electrolyte fuel cells* Automotive Industry
F.N. Büchi Project leader	*Stack and system development* Belenos Clean Power Holding, Biel/Bienne
J.L. Gómez-Cámer Project leader	*Graphite für Lithiumionen-Batterien* Imerys Graphite & Carbon, Bodio
P. Novák Project leader	*Forschungsnetzwerk «Elektrochemie und Batterien»* BASF SE, Ludwigshafen, Germany
T.J. Schmidt Project leader	*Advanced degradation studies on PBI/H_3PO_4 based MEAs for high temperature PEFCs* BASF SE, Ludwigshafen, Germany
T.J. Schmidt Project leader	*S_Chain* Belenos Clean Power Holding, Biel/Bienne
T.J. Schmidt Project leader	*Strained Pt/Perovskites as a novel class of oxygen reduction electrocatalysts* Dysenos
C. Villevieille Project leader	*Study of full cell reaction mechanism of lithium-ion batteries using 5 V spinel materials* Saft SA, Bordeaux, France

Teaching Activities

University Level Teaching

Prof. Dr. P. Novák	*Elektrochemie* ETH Zürich, HS 2014
Prof. Dr. T.J. Schmidt,	*Renewable Energy Technologies II, Energy Conversion and Storage* ETH Zürich, SS 2014
Prof. Dr. T.J. Schmidt, Prof. Dr. H.-J. Wörner	*Advanced Kinetics* ETH Zürich, SS 2014

Lecture Courses at Other Schools

J. Biesdorf	*Imaging and quantifying water in fuel cells with neutrons: latest methodological improvements* European Technical School on Hydrogen and Fuel Cells 2014.

Contributions to Courses at Universities, FHL, and other Institutes

L. Gubler	*Renewable Energy Technologies II, Energy Conversion and Storage* ETH Zürich, May 6, May 13, May 20, May 27, 2014.

Publications

Books and Reviewed Book Chapters

H.A. Gasteiger, H. Uchida, F.N. Büchi, K. Swider-Lyons, D.J. Jones, V. Ramani, T.J. Schmidt, A. Weber, J.M. Fenton, Y. Meas, K. Shinohara, M. Edmunson, K.A. Perry, C. Coutanceau, S. Mitsushima, P. Strasser, R. Mantz, T. Fuller, S.R Narayanan

Polymer Electrolyte Fuel Cells 14, ECS Transactions **64** (3), The Electrochemical Society, Pennington, NJ (2014). ISBN 978-1-62332-183-3

M. Inaba, T.J. Schmidt Editors

Fuel Cell Section, in Encyclopedia of Applied Electrochemistry, G. Kreysa, K. Ota, R.F. Savinell (Eds.), Springer, New York (2014). ISBN 978-1-4419-6995-8

C. Gloor, L. Gubler, T.J. Schmidt

PSI Electrochemistry Laboratory Annual Report 2013
doi: 10.3929/ethz-a-007047464, ISSN 1661-5379

Book Chapters

P. Rodriguez, T.J. Schmidt

Platinum-Based Anode Catalysts for Polymer Electrolyte Fuel Cells, in Encyclopedia of Applied Electrochemistry, Springer Science + Business Media LLC, New York, R.F. Savinell, K. Ota, G. Krysa (Eds.), 3, 1606–1617 (2014).

E. Fabbri, T.J. Schmidt

Platinum-Based Cathode Catalysts for Polymer Electrolyte Fuel Cells, in Encyclopedia of Applied Electrochemistry, Springer Science + Business Media LLC, New York, R.F. Savinell, K. Ota, G. Krysa (Eds.), 2, 1617–1626 (2014).

G. Neophytides, T.J. Schmidt

High-Temperature Polymer Electrolyte Fuel Cells, in Encyclopedia of Applied Electrochemistry, Springer Science + Business Media LLC, New York, R.F. Savinell, K. Ota, G. Krysa (Eds.), 2, 996–1004 (2014).

Peer Reviewed Papers

S. Balog, U. Gasser, L. Gubler, K. Jetsrisuparb, G.G. Scherer

Structure of the aqueous phase and its impact on the conductivity of graft copolymer ionomers at saturation
doi: 10.1016/j.polymer.2014.05.004, Polymer **55**, 3026–2036 (2014).

J. Biesdorf, P. Oberholzer, F. Bernauer, A. Kaestner, P. Vontobel, E. H. Lehmann, T. J. Schmidt, P. Boillat

Dual spectrum neutron radiography: Identification of phase transitions between frozen and liquid water
doi: 10.1103/PhysRevLett.112.248301, Phys. Review Letters **112**, 248301, (2014).

J. Biesdorf, P. Oberholzer, T.J. Schmidt, P. Boillat

Influence of hydrophobic coating of gas diffusion layers on the performance of water transport inside PEFC
doi: 10.1149/06403.0467ecst, ECS Trans. **64** (3), 467–475 (2014).

T. Binninger, E. Fabbri, R. Kötz, T.J. Schmidt

Determination of the electrochemically active surface area of metal-oxide supported platinum catalyst
doi: 10.1149/2.055403jes J. Electrochem. Soc. **161**, H121–H128 (2014).

P. Bleith, M. Valla, P. Novák, C. Villevieille
Elucidation of the reaction mechanism upon lithiation and delithiation of $Cu_{0.5}TiOPO_4$
doi: 10.1039/C4TA01627K, J. Mater. Chem. A **31**, 12513–12518 (2014).

P. Boillat, J. Biesdorf, P. Oberholzer, A. Kästner, T.J. Schmidt
Evaluation of neutron imaging for measuring phosphoric acid distribution in high temperature PEFCs
doi: 10.1149/2.023403jes, J. Electrochem. Soc **161**, F192–F198 (2014).

Y. Buchmüller, Z. Zhang, A. Wokaun, L. Gubler
Antioxidants in non-perfluorinated fuel cell membranes: prospects and limitations
doi: 10.1039/c4ra09792k, RSC Adv. **4**, 51911–51915 (2014).

Y. Buchmüller, A. Wokaun, L. Gubler
Polymer-bound antioxidants in grafted membranes for fuel cells
doi: 10.1039/c3ta15321e, J. Mater. Chem. A **2**, 5870–5882 (2014).

F.N. Büchi, M. Hofer, C. Peter, U.D. Cabalzar, J. Bernard, U. Hannesen, T.J. Schmidt, A. Closset, P. Dietrich
Towards re-electrification of hydrogen obtained from the power-to-gas process by highly efficient H_2/O_2 polymer electrolyte fuel cells
doi: 10.1039/C3RA47899H, Communication, RSC Adv. **4**, 56139–56146 (2014).

E. Castel, E.J. Berg, M. El Kazzi, P. Novák, C. Villevieille
Differential electrochemical mass spectrometry study of the interface of $xLi_2MnO_{3\cdot(1-x)}LiMO_2$ (M = Ni, Co, and Mn) material as a positive electrode in Li-ion batteries
doi: 10.1021/cm502201z, Chem. Mater. **26**, 5051–5057 (2014).

S.H. Eberhardt, F. Marone, M. Stampanoni, F.N. Büchi, T.J. Schmidt
Quantifying phosphoric acid in high-temperature polymer electrolyte fuel cell components by X-ray tomographic microscopy
doi:10.1107/S1600577514016348, J. Synchrotron Rad. **21**, 1319–1326 (2014).

T. Engl, J. Käse, L. Gubler, T.J. Schmidt
On the positive effect of CO during start/stop in high-temperature polymer electrolyte fuel cells
doi: 10.1149/2.0011407eel, ECS Electrochem. Lett. **3**, F47–F49 (2014).

T. Engl, K. Waltar, L. Gubler, T.J. Schmidt
Second cycle is dead: advanced electrode diagnostics for high-temperature polymer electrolyte fuel cells
doi: 10.1149/2.072404jes, J. Electrochem. Soc. **161**, F500–F505 (2014).

J. Eller, F.N. Büchi
Polymer electrolyte fuel cell performance degradation at different synchrotron beam intensities
doi: 10.1107/S1600577513025162, J. Synchrotron Rad. **21**, 82–88 (2014).

J. Eller, J. Roth, F. Marone, M. Stampanoni, A. Wokaun, F.N. Büchi
Implications of polymer electrolyte fuel cell exposure to synchrotron radiation on gas diffusion layer water distribution
doi: 10.1016/j.jpowsour.2013.07.025, J. Power Sources **245**, 796–800 (2014).

E. Fabbri, A. Habereder, K. Waltar, R. Kötz, T.J. Schmidt
Developments and perspectives of oxide-based catalysts for the oxygen evolution reaction
doi: 10.1039/c4cy00669k, Catal. Sci. Technol. 4, 3800-3821 (2014).

E. Fabbri, R. Mohamed, P. Levecque, O. Conrad, R. Kötz, T.J. Schmidt
Composite electrode boosts the activity of Ba0.5Sr0.5Co0.8Fe0.2O3-δ perovskite and carbon toward oxygen reduction in alkaline media
dx.doi.org/10.1021/cs400903k, ACS Catalysis 4, 1061–1070 (2014).

E. Fabbri, A. Rabis, R. Kötz, T.J. Schmidt
Pt nanoparticles supported on Sb-doped SnO2 porous structures: developments and issues
doi: 10.1039/c4cp00238e, Phys. Chem. Chem. Phys. 16, 13672-13681 (2014).

E. Fabbri, A. Pâtru, A. Rabis, R. Kötz, T.J. Schmidt
Advanced cathode materials for polymer electrolyte fuel cells based on Pt/metal oxides: From model electrodes to catalyst systems
doi:10.2533/chimia.2014.217, Chimia **68**, 217–220 (2014).

E. Fabbri, S. Taylor, A. Rabis, P. Levecque, O. Conrad, R. Kötz, T.J. Schmidt	*The effect of Pt nanoparticle distribution on oxygen electroreduction activity and selectivity* doi: 10.1002/cctc.201300987, ChemCatChem. **6**, 1410–1418 (2014).
E. Fabbri, R. Mohamed, P. Levecque, O. Conrad, R. Kötz, T.J. Schmidt	*$Ba_{0.5}Sr_{0.5}Co_{0.8}Fe_{0.2}O_{3-\delta}$ perovskite activity towards the oxygen reduction reaction in alkaline media* doi: 10.1002/celc.201300157, ChemElectroChem. **1**, 338–342 (2014).
E. Fabbri, R. Mohamed, P. Levecque, O. Conrad, R. Kötz, T.J. Schmidt	*Unraveling the oxygen reduction reaction mechanism and activity of d-band perovskite electrocatalysts for low temperature alkaline fuel cells* doi: 10.1149/06403.1081ecst, ECS Trans. **64**, 1081–1093 (2014).
L. Gubler	*Polymer design strategies for radiation grafted fuel cell membranes* doi: 10.1002/aenm.201300827, Adv. Energy Mater. **4**, 1300827 (2014).
D. Henkensmeier, L. Gubler	*Shape memory effect in radiation grafted ion exchange membranes* doi: 10.1039/c4ta01467g, J. Mater. Chem. A **2**, 9482–9485 (2014).
A. Iranzo, P. Boillat	*Liquid water distribution patterns featuring back-diffusion transport in a PEM fuel cell with neutron imaging* doi: 10.1016/j.ijhydene.2014.08.042, J. Hydrog. Energy. **39**, 17240–17245 (2014).
A. Iranzo, P. Boillat, F. Rosa	*Validation of a three dimensional PEM fuel cell CFD model using local liquid water distributions measured with neutron imaging* doi: 10.1016/j.ijhydene.2014.02.115, J. Hydrog. Energy. **39**, 7089–7099 (2014).
A. Iranzo, P. Boillat, J. Biesdorf, E. Tapia, A. Salva, J. Guerra	*Liquid water preferential accumulation in channels of PEM fuel cells with multiple serpentine flow fields* doi: 10.1016/j.ijhydene.2014.07.101, J. Hydrog. Energy. **39**, 15687–15695 (2014).
A. Iranzo, P. Boillat, P. Oberholzer, J. Guerra	*A novel approach coupling neutron imaging and numerical modelling for the analysis of the impact of water on fuel cell performance* doi: 10.1016/j.energy.2014.03.014, Energy. **68**, 971–981 (2014).
K. Jetsrisuparb, S. Balog, C. Bas, L. Perrin, A. Wokaun, L. Gubler	*Proton conducting membranes prepared by radiation grafting of styrene and various co-monomers* doi: 10.1016/j.eurpolymj.2014.01.021, Eur. Polym. J. **53**, 75–89 (2014).
K. Jetsrisuparb, H. Ben youcef, A. Wokaun, L. Gubler	*Radiation grafted membranes for fuel cells containing styrene sulfonic acid and nitrile comonomers* doi: 10.1016/j.memsci.2013.08.037, J. Membr. Sci. **450**, 28–37 (2014).
P. Lanz, P. Novák	*Combined in situ Raman and IR microscopy at the interface of a single graphite particle with ethylene carbonate/dimethyl carbonate* doi: 10.1149/2.0021410jes, J. Electrochem. Soc. **161**, A1555–A1563 (2014).
P. Lanz, C. Villevieille, P. Novák	*Ex situ and in situ Raman microscopic investigation of the differences between stoichiometric $LiMO_2$ and high-energy $xLi_2MnO_{3\cdot(1-x)}LiMO_2$ (M = Ni, Co, Mn)* doi: 10.1016/j.electacta.2014.03.004, Electrochim. Acta **130**, 206–212 (2014).
R. Mohamed, E. Fabbri, P. Levecque, R. Kötz, T.J. Schmidt, O. Conrad	*Understanding the influence of carbon on the oxygen reduction and evolution activities of BSCF/Carbon Composite Electrodes in alkaline electrolyte* doi: 10.1149/05836.0009ecst, ECS Trans. **58**, 9–18 (2014).
A. Rabis, D. Kramer, E. Fabbri, M. Worsdale, R. Kötz, T.J. Schmidt	*Catalyzed SnO2 thin films: Theoretical and experimental insights into fabrication and electrocatalytic properties* dx.doi.org/10.1021/jp4120139, J. Phys. Chem. C **118**, 11292–11302 (2014).

R. Robert, C. Villevieille, P. Novák	*Enhancement of the high potential specific charge in layered electrode materials for lithium-ion batteries* doi: 10.1039/C3TA12643A, J. Mater. Chem. A **2**, 8589–8598 (2014).
S. Urbonaite, P. Novák	*Importance of ‹unimportant› experimental parameters in LiS battery development* doi: 10.1016/j.jpowsour.2013.10.095, J. Power Sources **249**, 497–502 (2014).
C. Villevieille, T. Sasaki, P. Novák	*Novel electrochemical cell designed for operando techniques and impedance studies* doi: 10.1039/C3RA46184J, RSC Adv. **4**, 6782–6789 (2014).
C. Villevieille, P. Lanz, C. Bünzli, P. Novák	*Bulk and surface analyses of ageing of a 5 V-NCM positive electrode material for lithium-ion batteries* doi: 10.1039/C3TA13112B, J. Mater. Chem. A **2**, 6488–6493 (2014).
C. Villevieille, J.L. Gómez-Cámer, M. Heβ, P. Novák	*Reducing mass transfer effects on the kinetics of 5 V HE-NCM electrode materials for Li-Ion batteries* doi: 10.1149/2.067405jes, J. Electrochem. Soc. **161** (6), A871–A874 (2014).
Z. Zhang, R. Chattot, L. Bonorand, K. Jetsrisuparb, Y. Buchmüller, A. Wokaun, L. Gubler	*Mass spectrometry to quantify and compare the gas barrier properties of radiation grafted membranes and Nafion®* doi: 10.1016/j.memsci.2014.08.020, J. Membr. Sci. **472**, 55–66 (2014).

Talks

Invited Talks

F.N. Büchi	*Local gas analysis in polymer electrolyte fuel cells* 56. WE Heraeus-Seminar, Analytical tools for fuel cells and batteries, Bad Honnef, Germany, March 23–26, 2014.
E. Fabbri	*Advanced cathode materials for polymer electrolyte fuel cells based on Pt-oxide systems: from model electrodes to catalyst systems* MANA Alumni reunion, Tsukuba, Japan, March 3, 2014.
E. Fabbri	*Perovskite oxides as electrocatalyst materials for low temperature alkaline fuel cells and electrolyzers* Swiss-Japan Energy Technology Research Workshop, Gstaad, March 8, 2014.
E. Fabbri	*Pt/metal-oxide catalyst systems for application as cathode materials in polymer electrolyte fuel cells (PEFCs)* Workshop on Material Challenges in Devices for Fuel Solar Production and Employment, Trieste, Italy, May 21, 2014.
E. Fabbri	*Unraveling the oxygen reduction reaction mechanism and activity of d-band perovskite electrocatalysts for low Temperature alkaline fuel cells* 226th Meeting of the Electrochemical Society (ECS), Cancun, Mexico, October 7, 2014.
E. Fabbri	*Low temperature fuel cell developments for a sustainable hydrogen-based-economy* Materials Research Society (MRS) Fall Meeting, Boston, Massachusetts, USA, December 2, 2014.
L. Gubler	*Membrane degradation, radical attack and mitigation via regenerative radical scavengers* 11th Symposium on Fuel Cell and Battery Modeling and Experimental Validation (ModVal 11), Winterthur, March 19, 2014.

L. Gubler	*Radiation grafted fuel cell membranes: radical attack and mitigation using polymer-bound antioxidants* 11th Meeting of the Ionizing Radiation and Polymers Symposium (IRaP 2014), Jeju Island, Korea, October 8, 2014.
L. Gubler	*Radiation grafting: tailoring of ion-conducting membranes for electrochemical applications* Donghua University, College of Environmental Science and Engineering, Shanghai, China, October 13, 2014.
E. Jämstorp Berg	*Development and application of differential electrochemical mass spectrometry (DEMS) for Li-O_2 and Li-ion batteries* Seminar at the Technical University of Munich, München, Germany, August 27, 2014.
P. Novák	*In situ look into reactions of battery electrodes* Karlsruhe Institute of Technology, Karlsruhe, Germany, January 14, 2014.
P. Novák	*In situ structural analysis of battery materials with X-rays and neutrons* 556th Wilhelm and Else Heraeus Seminar - Analytical Tools for Fuel Cells and Batteries, Bad Honnef, Germany, March 25, 2014.
P. Novák	*In situ look on working lithium battery electrodes: do we see the strain?* 2014 MRS Spring Meeting & Exhibit, San Francisco, CA, USA, April 22, 2014.
P. Novák	*Raman microscopy, IR microscopy, and differential electrochemical mass spectrometry – what we can learn by combining in situ methods* 2014 MRS Spring Meeting & Exhibit, San Francisco, CA, USA, April 24, 2014.
P. Novák	*Interplay of bulk and surface – the primary challenge of battery materials* Seminar at the IBM Research, Almaden, CA, USA, April 28, 2014.
P. Novák	*Batteries, materials, structures – the in situ look* Symposium Novel Exciting Solid Phases, Energy Materials & Reactions, ETH Zürich, June 26, 2014.
P. Novák	*Oxides & co. – old new materials to store lithium* Bunsen Colloquium 2014 Lithium in Solids: Structure and Dynamics, Leibnitz University Hannover, Hannover, Germany, October 7, 2014.
P. Novák	*Lithiumionen-Batterien – Elektrochemische Energiespeicher für mobile Anwendungen* Leibnitz University Hannover, Hannover, Germany, October 8, 2014.
P. Novák	*The relationship between bulk and surface of battery materials* Seminar at the University of Uppsala, Uppsala, Sweden, October 30, 2014.
P. Novák	*Spektroskopie oder Diffraktometrie? Für Batteriematerialien beides!* Symposium Angewandte Elektrochemie in der Materialforschung, Fraunhofer-Institut für Keramische Technologien und Systeme, Dresden, Germany, December 5, 2014.
T.J. Schmidt	*The specific surface area: Key descriptor in electrocatalysis* Technical University of Denmark, Physics Department, Lyngby, Denmark, January 12, 2014.
T.J. Schmidt	*New insights into PEFCs and their materials* University of Strasbourg, Institut des Chimie et Procédé pur l'Énergie, l'Environnement et la Santé, Strasbourg, France, January 27, 2014.

T.J. Schmidt	*Electrochemical energy conversion: fuel cells, electrolyzers and more* Workshop Japan-Switzerland Energy Technology Research, Gstaad, March 9–12, 2014.
T.J. Schmidt	*Electrocatalysis in energy conversion devices: From fundamentals to applications* Symposium on Electrocatalysis, Helmholtz Institute Erlangen-Nürnberg, Erlangen, Germany, April 4, 2014.
T.J. Schmidt	*High temperature PEFCs: Recent findings using advanced diagnostics tools* Deutsches Zentrum für Luft und Raumfahrt, Institut für Technische Thermodynamik, Stuttgart, Germany, June 12, 2014.
T.J. Schmidt	*Catalyst and durability issues of polymer electrolyte fuel cells* CIMTEC 2014, 6th Forum on New Materials, Montecatini Terme, Italy, June 16–19, 2014.
T.J. Schmidt	*Advanced in situ diagnostics for HT-PEFCs: Approaching the unknowns* 14th Ulm Electrochemical Talks, Ulm, Germany, June 23–26, 2014.
T.J. Schmidt	*Oxide supported catalysts for polymer electrolyte fuel cell cathodes* Technical University of Denmark, Department of Energy Conversion and Storage, Risoe, Denmark, July 29, 2014.
T.J. Schmidt	*The Swiss competence center for energy research: Heat & Electricity Storage* 2. Berner Cleantech Treff – Erneuerbare Energien und Versorgungssicherheit – Wie geht das? Bern, August 12, 2014.
T.J. Schmidt	*Electrochemical energy research* ETH Industry Day 2014, Zürich, August 26, 2014.
T.J. Schmidt	*Durability of PEFC cathode catalysts: Challenges, new concepts and solutions* 65th Meeting of the International Society of Electrochemistry, Symposium 4: Electrochemical Energy Conversion and Storage: Fuel Cells and Electrolyzers, Lausanne, August 31–September 5, 2014.
T.J. Schmidt	*Technical options for energy storage* Studiengruppe Energieperspektiven, Baden, September 3, 2014.
T.J. Schmidt	*Approaches to overcome catalyst limits in electrochemical energy conversion devices* Materials Science and Engineering Conference 2014, Darmstadt, Germany, September 23–25, 2014.
T.J. Schmidt	*Polymer electrolyte fuel cells* Short Course at the 226th ECS Meeting, Cancun, Mexico, October 5, 2014. (with H.A. Gasteiger, TU Munich)
T.J. Schmidt	*Electrocatalysis for the future energy system: Fuel cells, electrolyzers and more…* Symposium on Advances in Surface Chemistry, Ulm University, Germany, November 6, 2014.
T.J. Schmidt	*Electrochemistry and the energy system: What the future may bring!* University of Cape Town, Chemical Engineering Department, Cape Town, South Africa, November 24, 2014.
T.J. Schmidt	*Imaging of polymer electrolyte fuel cells* Workshop Current Topics in Polymer Electrolyte Fuel Cells and Electrolysis, Cape Town, South Africa, December 4, 2014.

Contributed Talks

B. Adams, R. Black, Z. Williams, R. Fernandes, M. Cuisinier, E.J. Berg, P. Novák, G.K. Murphy, L.F. Nazar	*Enhancing the stability of non-aqueous electrolytes for Li-O_2 batteries* 2014 ECS and SMEQ Joint International Meeting, Cancun, Mexico, October 5–9, 2014.
A. Albert, T.J. Schmidt, L. Gubler	*Radiation grafted polymer electrolyte membranes for water electrolysis cells – characterization of key membrane properties* European Materials Research Society (E-MRS) Spring Meeting, Lille, France, May 26–30, 2014.
E.J. Berg, P. Novák	*In situ gas analysis to study Li-O_2 battery cathode performance during multiple cycles* 65th Annual Meeting of the International Society of Electrochemistry, Lausanne, August 31–September 5, 2014.
J. Biesdorf, P. Oberholzer, T.J. Schmidt, P. Boillat	*Impact of PTFE content in GDLs on PEFC performance evaluated by neutron radiography combined with pulsed helox analysis* European Hydrogen Energy Conference, Sevilla, Spain, March 12–14, 2014.
J. Biesdorf, P. Oberholzer, T.J. Schmidt, P. Boillat	*Influence of hydrophobic coating of gas diffusion layers on the performance of water transport inside PEFC* 226th Meeting of the Electrochemical Society, Cancun, Mexico, October 5–9, 2014.
P. Bleith, P. Novák, C. Villevieille	*Combined in situ XRD and XAS studies on materials for Li-ion batteries* Conference Power our Future 2014 – The 2nd International Forum on Progress and Trends in Battery and Capacitor Technologies, Vitoria, Spain, April 2–4, 2014.
P. Boillat	*Distinction of liquid water and ice using dual spectrum neutron imaging* 6th NEUWAVE, Garching, Germany, April 6–9, 2014.
P. Boillat	*Accuracy and reproducibility of water quantification in fuel cells by neutron imaging* 10th World Conference on Neutron Radiography, Grindelwald, October 5–10, 2014.
Y. Buchmüller, A. Wokaun, L. Gubler	*Polymer-bound antioxidants in grafted membranes for fuel cells* Fuel Cells 2014 Science & Technology – A Grove Fuel Cell Event, Amsterdam, The Netherlands, April 3–4, 2014.
E. Castel, E. Jämstorp Berg, M. El Kazzi, P. Novák, C. Villevieille	*Advanced investigation of reaction mechanisms at high potentials during cycling of HE-NCM* Gordon Research Conference – Batteries: Advances in Characterization, Analysis, Theory, and Modeling of Basic Processes. Ventura, CA, USA, March 9–14, 2014.
J. Conder, S. Urbonaite, P. Novák, L. Gubler	*PP-based ion-exchange membrane for Li-S batteries prepared by plasma induced graft copolymerization* 65th Annual Meeting of the International Society of Electrochemistry, Lausanne, August 31–September 5, 2014.
S.H. Eberhardt, F.N. Büchi, T.J. Schmidt	*Localisation and quantification of phosphoric acid in HT-PEFCs* HT-PEFC Workshop, Lyngby, Denmark, January 15–16, 2014.
S.H. Eberhardt, F.N. Büchi, T.J. Schmidt	*Imaging phosphoric acid in high-temperature PEFC components by X-tay tomographic microscopy* ModVal 11, Winterthur, March 17–19, 2014.
S.H. Eberhardt, F.N. Büchi, T.J. Schmidt	*Imaging the redistribution of phosphoric acid in HT-PEFCs under dynamic operation by X-ray tomographic microscopy* CARISMA 2014, Cape Town, South Africa, December 1–3, 2014.

M. El Kazzi, E.J. Berg, C. Villevieille, P. Novák	*Electrochemical performance and electrodes surface analysis of HE NCM¦LTO cells – ionic liquid vs. carbonate based electrolytes* 2014 ECS and SMEQ Joint International Meeting, Cancun, Mexico, October 5–9, 2014.
T. Engl, L. Gubler, T.J. Schmidt	*Positive effect of CO during start/stop on high-temperature PEFCs* Joint DTU-FZ Jülich-PSI Workshop on Challenges in HT-PEFC, Lyngby, Denmark, January 15–16, 2014.
T. Engl, L. Gubler, T.J. Schmidt	*Anodic carbon corrosion during start/stop in high temperature PEFC* CARISMA 2014, Cape Town, South Africa, December 1–3, 2014.
A. Forner-Cuenca, L. Gubler, T.J. Schmidt, P. Boillat	*Towards gas diffusion layers with patterned wettability* 11th Symposium for Fuel Cell and Battery Modelling and Experimental Validation, ModVal11, Winterthur, March 17–19, 2014.
L. Gubler, T. Engl, T.J. Schmidt	*Think different! Novel carbon corrosion mitigation strategy in high temperature PEFC – a durability study* CARISMA 2014, Cape Town, South Africa, December 1–3, 2014.
A. Guéguen, E.J. Berg, P. Novák	*XPS study of the porous carbonaceous positive electrode interface in Li-O_2 batteries upon cycling* 2014 ECS and SMEQ Joint International Meeting, Cancun, Mexico, October 5–9, 2014.
A. Lamibrac, J. Roth, F. Marone, F.N. Büchi	*X-ray tomographic imaging of GDLs during pressure driven water imbibitions/drainages* ModVal 11, Winterthur, March 17–19, 2014.
A. Lamibrac, J. Roth, F. Marone, F.N. Büchi	*Investigation of pressure driven water imbibition/drainage of GDLs using X-ray tomographic imaging* 65th Annual Meeting of the International Society of Electrochemistry, Lausanne, September 1–5, 2014.
G. Nagy, V. Sproll, U. Gasser, S. Balog, L. Gubler	*Small-angle neutron scattering study of the structure and morphology of radiation-grafted proton-conducting membranes* Annual Meeting of the Swiss Physical Society, Fribourg, June 30–July 2, 2014.
G. Nagy, V. Sproll, U. Gasser, S. Balog, L. Gubler	*Structure-property correlations ofilon-containing polymers for fuel cell applications* 13th International Conference on Sustainable Energy Technologies, Geneva, August 25–28, 2014.
M. Oezaslan , M. Nachtegaal, C. Bonnaud, W. Liu, A.-K. Herrmann, M. Werheid, N. Gaponik, A. Eychmüller, T.J. Schmidt	*XAS investigations on unsupported extended Pt-Pd aerogels* GdCh Electrochemistry, Mainz, Germany, September 22–24, 2014.
M. Oezaslan , M. Nachtegaal, C. Bonnaud, W. Liu, A.-K. Herrmann, M. Werheid, N. Gaponik, A. Eychmüller, T.J. Schmidt	*Investigations on Pt-Pd aerogels for oxygen reduction reaction* 226th Meeting of the Electrochemical Society, Cancun, Mexico, October 5–10, 2014.
H.J. Peng, S. Urbonaite, C. Villevieille, H. Wolf, K. Leitner, P. Novák	*Cycling-related factors influencing electrolyte (de-)composition in EC/EMC binary solvent based battery system* Inorganic Chemistry Christmas Symposium, ETH Zürich, December 10, 2014.

C. Peter, M. Hofer, U. Hannesen, A. Closset, F.N. Büchi	*Durability tests of H_2/O_2 fuel cell stacks including fluoride emission rate (FER) measurement* International Workshop on PEMFC Stack and Stack Component Testing, Stuttgart, Germany, June 4, 2014.
C. Peter, M. Hofer, J. Bernard, U. Hannesen, A. Closset, M. Birrer, F.N. Büchi	*H_2/O_2 FC system with high power density and efficiency for UPS applications* World of Energy Solutions, Stuttgart, Germany, October 8, 2014.
M.J. Schmid, K.R. Bickel, P. Novák, R. Schuster	*Microcalorimetric measurement of entropy changes upon electrochemical lithium bulk deposition and intercalation into graphite* Electrochemistry 2014, Mainz, Germany, September 23, 2014.
S. Schmidt, P. Benedek, C. Villevieille, P. Novák, S. Sallard	*Les disphosphonates métalliques lithiés Li_2FePO_6R matériaux hybrides organiques-inorganiques* GFECI 2014, Ile d'Oléron, France, March 31–April 3, 2014.
S. Schmidt, M. Reichardt, C. Villevieille, P. Novák, S. Sallard	*Novel positive materials for Li-ion batteries* University of Oslo battery materials seminar, Oslo, Norway, November 20–21, 2014.
T.J. Schmidt , F.N. Büchi, M. Hofer, U. Cabalzar, J. Bernard, U. Hannesen, A. Closset, P. Dietrich	*On power density of H_2/O_2 polymer electrolyte fuel cell systems* Symposium on Polymer Electrolyte Fuel Cells 14, 226th ECS Meeting, Cancun, Mexico, October 5–9, 2014.
S. Temmel , E. Fabbri D. Pergolesi, T. Lippert, T.J. Schmidt	*New approach for developing Pt electrocatylysts by pulsed laser deposition* 10th European Symposium on Electrochemical Engineering, Sardinia, Italy, October 2, 2014.
L. Vogt, M. El Kazzi, S. Perez Villar, E.J. Berg, C. Villevieille	*Sn anode for Na-ion batteries: a bulk and interfacial study* 65th Annual Meeting of the International Society of Electrochemistry, Lausanne, August 31–September 5, 2014.
K. Waltar, E. Fabbri, R. Kötz, T.J. Schmidt	*Mechanistic investigations of oxygen evolution catalysts in acidic electrolyte* 10th European Symposium on Electrochemical Engineering, Sardinia, Italy, September 28–October 2, 2014.
Z. Zhang, Y. Buchmüller, A. Wokaun, L. Gubler	*Chemical degradation and mitigation strategies of radiation grafted membranes in polymer electrolyte fuel cells* 2nd International Conference on Clean Energy, Qingdao, China, April 13–16, 2014.

Patent Applications

P. Boillat, A. Forner-Cuenca, L. Gubler, C. Padeste, F.N. Büchi	*A method to produce a gas diffusion layer and a fuel cell comprising a gas diffusion layer* Patent Application No. EP 14184065.2, 2014.
D. Henkensmeier, S. Hink, L. Gubler, K.H. Juhn, J.H. Jang, E. Cho, S.W. Nam, S.P. Yoon, T.H. Lim	*Method to decrease the in-plane swelling of ion exchange membrane, ion exchange membrane prepared thereby and method for preparing catalyst coated ion exchange membrane using the same* Korean Patent Application 10-2014-0048347, 2014.

Posters

J. Biesdorf, P. Oberholzer, F. Bernauer, A. Kästner, E.H. Lehmann, T.J. Schmidt, P. Boillat	*Distinction of liquid water and ice based on dual spectrum neutron imaging* 10th World Conference on Neutron Radiography, Grindelwald, October 5–10, 2014.
T. Binninger, M. Garganourakis, J. Han, A. Patru, E. Fabbri, O. Sereda, R. Kötz, T.J. Schmidt	*Investigation of the size distribution of metal-oxide supported Pt nanoparticles by in situ anomalous SAXS* 65th Annual Meeting of the International Society of Electrochemistry, Lausanne, August 31–September 5, 2014.
P. Bleith, P. Novák, C. Villevieille	*Combined in situ XRD and XAS studies on materials for Li-ion batteries* 65th Annual Meeting of the International Society of Electrochemistry, Lausanne, August 31–September 5, 2014.
L. Boulet, P. Novák, C. Villevieille	*Etude de l'interface du système complet: 5V-NMC vs. graphite* GFECI 2014, Ile d'Oléron, France, March 31–April 3, 2014.
L. Boulet, M. El Kazzi, P. Novák, C. Villevieille	*Full cells HE-NCM vs. graphite: cycling rate effects* 65th Annual Meeting of the International Society of Electrochemistry, Lausanne, August 31–September 5, 2014.
F.N. Büchi, S.H. Eberhardt, T.J. Schmidt	*Imaging phosphoric acid redistribution in HT-PEFC* Gordon Research Conference «Batteries», Smithfield, RI, USA, August 1–5, 2014.
F.N. Büchi, I. Mayrhuber, J. Eller, J. Roth, F. Marone, M. Stampanoni	*Towards 3D imaging of transient saturation changes in gas diffusion layers of PEFC* 65th Annual Meeting of the International Society of Electrochemistry, Lausanne, August 31–September 5, 2014.
C. Bünzli, D. Cericola, T. Hucke, M. Spahr, P. Novák, J.L. Gómez-Cámer	*Electrode engineering of graphite/silicon electrodes* Gordon Research Conference – Batteries: Advances in Characterization, Analysis, Theory, and Modeling of Basic Processes. Ventura, CA, USA, March 9–14, 2014.
C. Bünzli, D. Cericola, T. Hucke, M.E. Spahr, P. Novák, J.L. Gómez-Cámer	*Electrochemistry of carbon/silicon electrodes* 65th Annual Meeting of the International Society of Electrochemistry, Lausanne, August 31–September 5, 2014.
C. Bünzli, D. Cericola, T. Hucke, M. Spahr, P. Novák, J.L. Gómez-Cámer	*Graphite-based negative electrodes: correlation of electrode expansion and cyclability* 2014 ECS and SMEQ Joint International Meeting, Cancun, Mexico, October 5–9, 2014.
E. Castel, E.J. Berg, P. Novák, C. Villevieille	*Gas evolution from Li_2MnO_3-stabilized $Li(Ni_xCo_yMn_z)O_2$ electrode materials at different cycling temperatures: a DEMS study* 65th Annual Meeting of the International Society of Electrochemistry, Lausanne, August 31–September 5, 2014.
J. Conder, S. Urbonaite, D. Streich, T. Poux, P. Novák, L. Gubler	*New design of a separator for the Li-S battery by plasma induced grafting of styrene sulfonate onto porous polypropylene* 3rd Workshop «Lithium-Sulfur-Batteries», Dresden, Germany, November 12–13, 2014.
J. Duic, L. Capone, J.O. Schumacher, J. Biesdorf, P. Boillat.	*Computer simulation of liquid water saturation in porous media of fuel cells* Mobility 1st Annual conference SCCER, ETH Zürich, September 11, 2014.
S.H. Eberhardt, F.N. Büchi, T.J. Schmidt	*Imaging phosphoric acid in HT-PEFC components by X-ray tomographic microscopy* Heraeus Seminar on Energy Conversion and Storage, Bad Honnef, Germany, March 23–26, 2014.

S.H. Eberhardt, F. Marone, F.N. Büchi, T.J. Schmidt	*Imaging phosphoric acid in HT-PEFC by X-ray tomographic microscopy* 65th Annual Meeting of the International Society of Electrochemistry, Lausanne, August 31–September 5, 2014.
M. El Kazzi, E. Jämstorp Berg, C. Villevieille, P. Novák	*Electrochemical performance and XPS surface analyses of HE NCM/LTO cells in (LP30 vs. IL) electrolytes* 65th Annual Meeting of the International Society of Electrochemistry, Lausanne, August 31–September 5, 2014.
A. Forner-Cuenca, J. Biesdorf, L. Gubler, T.J. Schmidt, P. Boillat	*Advance water management strategies: gas diffusion layers with patterned wettability.* Mobility 1st Annual conference SCCER, ETH Zürich, September 11, 2014.
A. Guéguen, E. Jämstorp Berg, P. Novák	*XPS study of the evolution upon cycling of the interface layers on porous graphite electrodes for Li-O_2 batteries* 65th Annual Meeting of the International Society of Electrochemistry, Lausanne, August 31–September 5, 2014.
M. He, P. Novák, E. Jämstorp Berg	*Gas evolution reactions on conductive carbon additives in lithium-ion batteries* 65th Annual Meeting of the International Society of Electrochemistry, Lausanne, August 31–September 5, 2014.
M. Heβ, C. Villevieille, R. Nesper, P. Novák	*Investigating the phase transitions of graphite by in situ neutron diffraction* 17th International Meeting on Lithium Batteries, Como, Italy, June 23–28, 2014.
A. Lamibrac, J. Roth, M. Toulec, F. Marone, F.N. Büchi	*XTM Imaging of GDLs during pressure driven water imbibition and drainage* 1st Annual Conference SCCER Mobility, Zurich, September 11, 2014.
P. Lanz, P. Novák	*Combined in situ Raman and IR microscopy of electrode materials for lithium-ion batteries* IBA 2014 – International Battery Association Meeting, Brisbane, Australia, March 3–7, 2014.
I. Mayrhuber, T.J. Schmidt, F.N. Büchi	*Discrimination of ice and water in PEFC* Heraeus Seminar on Energy Conversion and Storage, Bad Honnef, Germany, March 23–26, 2014.
P. Novák, P. Lanz	*Combined IR and Raman in situ microscopy on single particles - a new tool for interface studies* 17th International Meeting on Lithium Batteries, Como, Italy, June 23–28, 2014.
M. Oezaslan, M. Nachtegaal, W. Liu, A.-K. Herrmann, C. Laugier Bonnaud, M. Werheid, N. Gaponik, A. Eychmüller, T.J. Schmidt	*XAS degradation studies on unsupported Pt-Pd aerogels* 65th Annual Meeting of the International Society of Electrochemistry, Lausanne, August 31–September 5, 2014.
H.J. Peng, C. Villevieille, S. Urbonaite, H. Wolf, K. Leitner, P. Novák	*Influence of electrolyte on the performance and lifetime of NCM family materials* 65th Annual Meeting of the International Society of Electrochemistry, Lausanne, August 31–September 5, 2014.
Y Paratcha, J. Durst, J. Herranz, T.J. Schmidt	*Electrochemical setup for online FTIR and differential electrochemical mass spectrometry studies of CO_2-electroreduction on model metal surfaces* SCCER H&E Storage Annual Symposium, Paul Scherrer Institut, Villigen, November 4, 2014.
N.I. Prasianakis, R. Sui, J. Mantzaras, F.N. Büchi	*Microscopic modeling of evaporative heat and mass transfer in the diffusion layer of PEFCs* 1st Annual Conference SCCER Mobility, Zurich, September 11, 2014.

A. Rabis, E. Fabbri, D. Kramer, M. Worsdale, R. Kötz, T.J. Schmidt	*Oxygen reduction on Pt/SnO_2 catalysts: Influence of the oxide surface and Pt loading* 65th Annual Meeting of the International Society of Electrochemistry, Lausanne, August 31–September 5, 2014.
A. Rabis, E. Fabbri, R. Kötz, T.J. Schmidt	*Oxygen reduction on Pt/SnO_2 catalysts: A model electrode study* Annual Meeting of the Swiss Chemical Society, Zürich, September 11, 2014.
M. Reichardt, C. Villevieille, P. Novák, S. Sallard	*Lithium chromium pyrophosphate as new insertion material for Li-ion batteries* 65th Annual Meeting of the International Society of Electrochemistry, Lausanne, August 31–September 5, 2014.
R. Robert, P. Novák	*Electrochemical and in situ XRD studies on the Li(Ni,Co,Al)O_2 system* 556th Wilhelm and Else Heraeus Seminar – Analytical Tools for Fuel Cells and Batteries, Bad Honnef, Germany, March 22–26, 2014.
S. Sallard, E. Castel, C. Villevieille, P. Novák	*One-pot synthesis by anhydrous sol-gel chemistry of mixtures of greigite and magnetite, and their use for electrodes in Li-ion batteries* 65th Annual Meeting of the International Society of Electrochemistry, Lausanne, August 31–September 5, 2014.
M.J. Schmid, K.R. Bickel, P. Novák, R. Schuster	*Microcalorimetric measurements of entropy changes upon electrochemical lithium deposition* 556th Wilhelm and Else Heraeus Seminar – Analytical Tools for Fuel Cells and Batteries, Bad Honnef, Germany, March 22–26, 2014.
S. Schmidt, P. Benedek, C. Villevieille, P. Novák, S. Sallard	*Lithium iron diphosphonates, organic-inorganic hybrid materials as new positive electrode materials for Li-ion batteries* 65th Annual Meeting of the International Society of Electrochemistry, Lausanne, August 31–September 5, 2014.
D. Streich, E. Jämstorp Berg, M. Özaslan, P. Novák	*FTIR spectroscopy tools for the characterization of electrode/electrolyte interfaces in Li-air and Li-ion batteries* 14th Ulm Electrochemical Talks, Ulm, Germany, June 23–26, 2014.
M. Suermann, T.J. Schmidt, F.N. Büchi	*Experimental investigation of mass transport losses in polymer electrolyte electrolysis cells* Electrochemistry 2014, Mainz, Germany, September 22–24, 2014.
S. Urbonaite, P. Novák	*High specific charge and long cycle life of simple Li-S batteries* 17th International Meeting on Lithium Batteries, Como, Italy, June 23–28, 2014.
S. Urbonaite, P. Novák	*Importance of ‹unimportant› experimental parameters in Li-S battery development* 65th Annual Meeting of the International Society of Electrochemistry, Lausanne, August 31–September 5, 2014.
C. Villevieille, P. Novák	*Dual performance electrodes for Li-S and Li-ion batteries* 17th International Meeting on Lithium Batteries, Como, Italy, June 23–28, 2014.
L. Vogt, P. Novák, C. Villevieille	*MSn_2 (M = Fe, Co, Mn) intermetallics as anode materials for Na-ion batteries* 65th Annual Meeting of the International Society of Electrochemistry, Lausanne, August 31–September 5, 2014.
S.A. Tschupp, W. Karim, M. Özaslan, J.A. van Bokhoven, J. Gobrecht, T.J. Schmidt, Y. Ekinci	*From light to catalysis: Well-defined nanostructures for electrochemistry* Swiss Nanoconvention 2014, FHNW Campus, Brugg-Windisch, May 21–22, 2014.

S.A. Tschupp, W. Karim, M. Özaslan, J.A. van Bokhoven, J. Gobrecht, Y. Ekinci, T.J. Schmidt	*Extreme ultraviolet lithography for the fabrication of nanoscale Pt model catalysts* Summer School on Surface Electrochemistry: Towards Energy Research, Eurotel Victoria, Villars-sur-Ollon VD, August 25–29, 2014.
S.A. Tschupp, W. Karim, M. Özaslan, J.A. van Bokhoven, J. Gobrecht, Y. Ekinci, T.J. Schmidt	*Fabrication of high-resolution and large-area platinum nanoparticles for model electrocatalytic systems* 40th International Conference on Micro and Nano Engineering, EPFL Lausanne, September 22–26, 2014.
K. Waltar, D. Lebedev, E. Fabbri, A. Fedorov, C. Coperet, T.J. Schmidt	*Insights into the application of the rotating ring disk electrode technique for the oxygen evolution reaction* 65th Annual Meeting of the International Society of Electrochemistry, Lausanne, August 31–September 5, 2014.
K. Waltar, D. Lebedev, E. Fabbri, A. Fedorov, C. Coperet, T.J. Schmidt	*High-surface area catalysts for the anodic oxygen evolution reaction in PEM electrolyzers* 1st Annual Symposium SCCER Heat & Electricity Storage, Villigen, November 4, 2014.

Conferences & Workshops Organizations

F.N. Büchi	*Electrochemical Energy Conversion and Storage: Fuel Cells and Electrolysers* at the 65th Annual Meeting of the International Society of Electrochemistry, Lausanne, August 31–September 5, 2014. Symposium Organizer
F.N. Büchi, T.J. Schmidt	*Polymer Electrolyte Fuel Cells PEFC 14* 226th ECS Meeting, Cancun, Mexico, October 5–10, 2014. Co-Organizers
E. Fabbri	*Symposium S: Advances in Materials Science, Processing, and Engineering for Fuel Cells and Electrolyzers* MRS Fall meeting 2014, Boston, Massachusetts, USA, November 29–December 5, 2014. Lead Organizer
P. Novák	*1st International Symposium on Energy Challenges and Mechanics* Member of Scientific Committee
P. Novák	*Symposium zur angewandten Elektrochemie in der Materialforschung* Member of Advisory Board
P. Novák	*Electrochemical Energy Conversion and Storage: Batteries* at the 65th Annual Meeting of the International Society of Electrochemistry Lausanne, August 31–September 5, 2014. Symposium Organizer
P. Novák	*CIMTEC 2014* Member of International Advisory Board
T.J. Schmidt	*65th Annual Meeting of the International Society of Electrochemistry* Lausanne, August 31–September 5, 2014. Symposium Organizer

T.J. Schmidt	*Synergizing theory and experiment in electrochemistry: State-of-the-art developments* at the 65th Annual Meeting of the International Society of Electrochemistry, Lausanne, August 31–September 5, 2014. Symposium Organizer
T.J. Schmidt	*State-of-the-art tutorial on durability in low temperature fuel cells* at the 225th Electrochemical Society Meeting, Orlando, FL, USA, May 2014. Co-Organizer
T.J. Schmidt	*30th PSI Electrochemistry Symposium – Oxygen: Airborne* Energy Conversion and Storage; Paul Scherrer Institut, Villigen, May 7, 2014. Lead Organizer

Members in external committees

L. Gubler	*Agence Nationale de la Recherche, France* Expert Evaluator
L. Gubler	*National Science Foundation, USA* Expert Evaluator
P. Novák	*The Northeastern Center for Chemical Energy Storage (NECCES)* Member of Scientific Advisory Board
T.J. Schmidt	*Competence Center Energy & Mobility Switzerland* Steering Board
T.J. Schmidt	*4M Centre – Mechanisms, Materials, Manufacturing and Management – Interdisciplinary Fundamental Research to Promote commercialization of HT-PEMFC* Technical University of Denmark, Lyngby, Denmark Technical Steering Committee
S. Urbonaite	*The Research Council of Norway* Member of Peer Review Panel
S. Urbonaite	*Qatar National Research Fund (QNRF)* Expert Evaluator
C. Villevieille	*Agence Nationale pour la Recherche française (ANR)* Expert Evaluator

Editorial Work

T.J. Schmidt	Associate Editor of the Electrochemistry Society Journals *(Journal of the Electrochemical Society, ECS Electrochemistry Letters)*
T.J. Schmidt	Member Editorial Advisory Board of *Electrocatalysis (Springer)* and *Energy Technology (Wiley)*

Paul Scherrer Institut :: 5232 Villigen PSI :: Switzerland :: Tel. +41 56 310 21 11 :: Fax +41 56 310 21 99 :: www.psi.ch